Aston University

Some pages of this thesis may have been removed for copyright restrictions.

If you have discovered material in AURA which is unlawful e.g. breaches copyright, (either yours or that of a third party) or any other law, including but not limited to those relating to patent, trademark, confidentiality, data protection, obscenity, defamation, libel, then please read our Takedown Policy and contact the service immediately

An investigation of thin amorphous carbon-based sputtered coatings for MEMS and micro-engineering applications

Gavin Malcolm Wilson

Doctor of Philosophy

Aston University – June 2008

This copy of the thesis has been supplied on condition that anyone who consults it is understood to recognise that its copyright rests with its author and that no quotation from the thesis and no information derived from it may be published without proper acknowledgement.

An investigation of thin amorphous carbon-based sputtered coatings for MEMS and micro-engineering applications Gavin Malcolm Wilson

Summary

The work presented in this thesis describes an investigation into the production and properties of thin amorphous C films, with and without Cr doping, as a low wear / friction coating applicable to MEMS and other micro- and nano-engineering applications. Firstly, an assessment was made of the available testing techniques. Secondly, the optimised test methods were applied to a series of sputtered films of thickness 10 – 2000 nm in order to: (i) investigate the effect of thickness on the properties of coatings/coating process (ii) investigate fundamental tribology at the nano-scale and (iii) provide a starting point for nanotribological coating optimisation at ultra low thickness.

The use of XPS was investigated for the determination of sp^3/sp^2 carbon bonding. Under C 1s peak analysis, significant errors were identified and this was attributed to the absence of sufficient instrument resolution to guide the component peak structure (even with a high resolution instrument). A simple peak width analysis and correlation work with C KLL D value confirmed the errors. The use of XPS for sp^3/sp^2 was therefore limited to initial tentative estimations. Nanoindentation was shown to provide consistent hardness and reduced modulus results with depth (to < 7nm) when replicate data was suitably statistically processed. No significant pile-up or cracking of the films was identified under nanoindentation. Nanowear experimentation by multiple nanoscratching provided some useful information, however the conditions of test were very different to those expect for MEMS and micro- / nano-engineering systems. A novel 'sample oscillated nanoindentation' system was developed for testing nanowear under more relevant conditions.

The films were produced in an industrial production coating line. In order to maximise the available information and to take account of uncontrolled process variation a statistical design of experiment procedure was used to investigate the effect of four key process control parameters. Cr doping was the most significant control parameter at all thicknesses tested and produced a softening effect and thus increased nanowear. Substrate bias voltage was also a significant parameter and produced hardening and a wear reducing effect at all thicknesses tested. The use of a Cr adhesion layer produced beneficial results at 150 nm thickness, but was ineffective at 50 nm. Argon flow to the coating chamber produced a complex effect. All effects reduced significantly with reducing film thickness.

Classic fretting wear was produced at low amplitude under nanowear testing. Reciprocating sliding was produced at higher amplitude which generated three body abrasive wear and this was generally consistent with the Archard model. Specific wear rates were very low (typically $10^{-16} - 10^{-18}$ $m^3N^{-1}m^{-1}$). Wear rates reduced exponentially with reduced film thickness and below (approx.) 20 nm, thickness was identified as the most important control of wear.

Keywords: DOE; Nanoindentation; Nanotribology; Nanowear.

Acknowledgements

I would like to express enormous thanks to my supervisor Professor John Sullivan for providing me with excellent support and friendship during my time at Aston and for creating a first-rate research group that I am proud to have been a part of. I would also like to thank Mr. Andrew Abbot, Dr. Sayah Saied, Dr. Baogui Shi, Mr. Mihai Ursu and Dr. Teodor Zaharia for their practical assistance, invaluable discussions and support.

I thank Teer Coatings Ltd and particularly Dr. Dennis Teer, Dr. Kevin Cooke and Ms. Susan Field for providing all film specimens and for contributing great assistance to this thesis. I also thank Micro Materials Ltd and particularly Dr. Jim Smith and Dr. Ben Beake for giving me the opportunity to work with and develop the Nano-Fretting system as well as giving me an excellent source of ideas and information.

I would like to thank DTI, EPSRC and Teer Coatings Ltd for providing the funding for this work.

Finally, I must thank my wife Sharon, my parents Kathleen and Malcolm and all family members for their support and encouragement during the last three years.

1 Introduction 19

1.1 Background to the project 19
1.2 Micro-/nano-scale engineering and Micro-electro-mechanical-systems 19
1.2.1 Surface/tribology issues affecting micro- / nano-engineering and MEMS development 24
1.3 Amorphous carbon-based coatings 28
1.3.1 Bonding and properties of C 28
1.3.2 Production of amorphous C coatings 31
1.4 Statistical design of experiment (DOE) 41
1.5 Low wear / low friction thin film analysis techniques 45
1.5.1 Chemical composition and structure 45
1.5.1.1 X-ray photoelectron spectroscopy (XPS) 45

1.5.1.2 Auger electron spectroscopy (AES) 53

1.5.2 Physical properties 54
1.5.2.1 Atomic force microscopy (AFM) 54

1.5.3 Mechanical properties 56
1.5.3.1 Nanoindentation 56

1.5.3.2 Nanoscratch 69

1.5.4 Nanotribological properties 70
1.5.4.1 General theories of tribology 70

1.5.4.2 The tribology of amorphous C coatings 76

1.5.4.3 The nanotribology of amorphous C coatings 80

1.6 Summary of the programme of research 85
2 Experimental 86

2.1 Test Materials 86
2.1.1 Substrates and pre-coating preparation 86
2.1.2 Coating process 86
2.1.2.1 Equipment 86

2.1.2.2 Coating procedure 88

2.1.2.3 Coating process control parameters 90

2.2 Low wear / low friction thin film analysis techniques 92
2.2.1 Chemical composition and structure 92
2.2.1.1 X-ray photoelectron spectroscopy (XPS) 92

2.2.1.2 Auger electron spectroscopy (AES) 93

2.2.2 Physical properties 94
2.2.2.1 Optical microscopy 94

2.2.2.2 Atomic force microscopy 94

2.2.2.3 Scanning electron microscopy 94

2.2.2.4 Profilometry 94

2.2.3 Mechanical properties 95
2.2.3.1 Nanoindentation 95

2.2.3.2 Nanoscratch 99

2.2.4 Nanotribological properties 100
2.2.4.1 Friction 100

2.2.4.2 Wear 100

2.3 Experimental design 104
2.3.1 Experiments to investigate the tribologically important properties of a-C coatings 104
2.3.1.1 Experiment to investigate Cr doping in a-C coatings at the nano- and macro-scale with 1 to 3 μm coatings 104

2.3.1.2 Experiment to investigate the effects of pulsed substrate biasing with 150 nm coatings 105

2.3.1.3 Experiment to investigate four key coating process parameters with 150 nm coatings 108

2.3.1.4 Experiment to investigate four key coating process parameters with 50 nm coatings ... 110

2.3.1.5 Experiment to investigate a range of film thicknesses (2000 nm to 10 nm) ... 111

2.3.2 Experiments to investigate the nanotribology of a-C films ... 112

2.3.2.1 Characterisation of the sample oscillated nanoindentation nanowear process ... 112

2.3.2.2 Experiment to investigate the nanowear of a matrix of 150 nm coatings and the effect of four key coating process parameters ... 114

2.3.2.3 Experiment to investigate the nanowear of a matrix of 50 nm coatings and the effect of four key coating process parameters ... 115

2.3.2.4 Experiment to investigate the nanowear of a range of film thicknesses (2000 nm to 10 nm) ... 116

3 Results ... 119

3.1 Low wear / low friction thin film analysis techniques ... 119

3.1.1 Experiment to investigate the use of XPS for the determination of sp^3/sp^2 bonding ratio in a-C ... 119

3.1.2 Investigation of material pile-up and cracking during nanoindentation experiments ... 122

3.1.3 Investigation of ISE with nanoindentation experiments ... 124

3.2 Experiments to investigate the tribologically important properties of a-C coatings ... 127

3.2.1 Experiment to investigate Cr doping in a-C coatings at the nano- and macro-scale with 1 to 3 μm coatings ... 127

3.2.2 Experiment to investigate the effects of pulsed substrate biasing with 150 nm coatings ... 134

3.2.3 Experiment to investigate four key coating process parameters with 150 nm coatings ... 140

3.2.4 Experiment to investigate four key coating process parameters with 50 nm coatings ... 142

3.2.5 Experiment to investigate a range of film thicknesses (2000 nm to 10 nm).. ... 145

3.3 Experiments to investigate the nanotribology of a-C films ... 151

3.3.1 Characterisation of the sample oscillated nanoindentation nanowear process ... 151

3.3.1.1 Dynamic depth measurements with the sample oscillated nanoindentation system 151

3.3.1.2 Low amplitude nanowear mode (experiments 1-9) 152

3.3.1.3 High amplitude nanowear mode (experiments 10-42) 153

3.3.1.4 High amplitude nanowear contact conditions 161

3.3.2 Experiment to investigate the nanowear of a matrix of 150 nm coatings and the effect of four key coating process parameters 162

3.3.2.1 Measurement of specific wear rates and analysis of the complete data set 162

3.3.2.2 Statistical analysis of the effect of the four key process parameters using ANOVA 165

3.3.2.3 Correlations with the tribologically important properties of the coatings 166

3.3.3 Experiment to investigate the nanowear of a matrix of 50 nm coatings and the effect of four key coating process parameters 169

3.3.3.1 Measurement of specific wear rates and analysis of the complete data set 169

3.3.3.2 Statistical analysis of the effect of the four key process parameters using ANOVA 171

3.3.3.3 Correlations with the tribologically important properties of the coatings 171

3.3.4 Experiment to investigate the nanowear of a range of film thicknesses (2000 nm to 10 nm) 174

4 Discussion 178

4.1 Low wear / low friction thin film analysis techniques 178

4.1.1 Experiment to investigate the use of XPS for the determination of sp^3/sp^2 bonding ratio in a-C 178

4.1.2 Investigation of material pile-up and cracking during nanoindentation experiments 179

4.1.3 Investigation of ISE with nanoindentation experiments 180
4.2 Experiments to investigate the tribologically important properties of a-C coatings 180
4.2.1 Experiment to investigate Cr doping in a-C coatings at the nano- and macro-scale with 1 to 3 μm coatings 180
4.2.2 Experiment to investigate the effects of pulsed substrate biasing with 150 nm coatings 185
4.2.3 Experiment to investigate four key coating process parameters with 150 nm coatings 188
4.2.4 Experiment to investigate four key coating process parameters with 50 nm coatings 190
4.2.5 Experiment to investigate a range of film thicknesses (2000 nm to 10 nm).. 192
4.3 Experiments to investigate the nanotribology of a-C films 193
4.3.1 Characterisation of the sample oscillated nanoindentation nanowear process 193
4.3.1.1 Dynamic depth measurements with the sample oscillated nanoindentation system 193
4.3.1.2 Low amplitude nanowear mode (experiments 1-9) 194
4.3.1.3 High amplitude nanowear mode (experiments 10-42) 194
4.3.1.4 High amplitude nanowear contact conditions 197
4.3.2 Experiment to investigate the nanowear of a matrix of 150 nm coatings and the effect of four key coating process parameters 198
4.3.2.1 Measurement of specific wear rates and analysis of the complete data set 198
4.3.2.2 Statistical analysis of the effect of the four key process parameters using ANOVA 199
4.3.2.3 Correlations with the tribologically important properties of the coatings 200
4.3.3 Experiment to investigate the nanowear of a matrix of 50 nm coatings and the effect of four key coating process parameters 204
4.3.3.1 Measurement of specific wear rates and analysis of the complete data set 204

4.3.3.2 Statistical analysis of the effect of the four key process parameters using ANOVA 204

4.3.3.3 Correlations with the tribologically important properties of the coatings 205

4.3.4 Experiment to investigate the nanowear of a range of film thicknesses (2000 nm to 10 nm) 206

5 Conclusions and further work 210

5.1 Assessment and development of an array of test methods for low wear / low friction ultra thin a-C films relevant to MEMS and micro- / nano-scale engineering systems 210

5.1.1 Chemical composition and structure 210

5.1.2 Physical properties 211

5.1.3 Mechanical properties 211

5.1.4 Nanotribology 211

5.2 Application of the test methods to a series of SIP a-C and Cr doped a-C coatings 212

5.2.1 Use of DOE with commercially produced ultra thin coatings 212

5.2.2 Investigation of the effect of thickness on the properties of coatings/coating process 212

5.2.3 Investigation of fundamental tribology at the nano-scale 214

5.2.4 Optimisation of a-C films for nanowear 216

5.3 Further work 217

5.3.1 Determination of sp^3/sp^2 ratio by XPS C 1s peak analysis 217

5.3.2 Nanotribology 217

6 Appendix – Publications 239

Figure 1.1 Process sequence for the production of a Si bridge by SMM. 22

Figure 1.2 SEM image of a MEMS accelerometer [11]. 23

Figure 1.3 SEM image of one element from the Texas Instruments Digital Micro-mirror Device™ [11]. 24

Figure 1.4 The three types of hybridised C bond [45]. 29

Figure 1.5 Atomic structure of (a) graphite (b) diamond and (c) amorphous C [51]. 31

Figure 1.6 Diagram showing magnetic field lines and plasma distribution of a conventional and unbalanced magnetron arrangement. 34

Figure 1.7 Plan view of a typical CFUBMSIP chamber arrangement. 35

Figure 1.8 Thornton's two parameter structure zone diagram [103]. 40

Figure 1.9 Kelly and Arnell's three parameter structure zone diagram [63]. 41

Figure 1.10 Cross-section of a hemispherical sector analyser [51]. 48

Figure 1.11 XPS C 1s peak fitted with sp^3/sp^2 and C-O components. 51

Figure 1.12 As collected XPS C KVV spectrum (upper) and the derivative showing the D value (lower). 53

Figure 1.13 AFM defection/force sensor [51]. 55

Figure 1.14 AFM system with feedback circuit and ceramic piezoelectric drives []. 55

Figure 1.15 A schematic diagram of an elastic-plastic indentation [51]. 57

Figure 1.16 Typcial load-displacement curve from an elastic-plastic indentation [51].....57

Figure 1.17 Diagram of a Berkovich indenter showing contact depth h_c, projected area of contact A_c and semi-angle θ [153]. 59

Figure 1.18 SEM micrograph of an indentation into TiN/SiN showing both pile-up and cracking [174]. 66

Figure 1.19 Side-wall tribometer. Electrostatic actuators pull the suspended beam into contact with the centre post while a second set oscillates the beam back and forth [11]. 84

Figure 1.20 The 'inchworm' nanotractor device [11]. 84

Figure 2.1 Schematic diagram of the CFUBMSIP chamber arrangement showing (a) graphite targets (b) Cr targets (c) rotating support (d) location of specimen. 88

Figure 2.2 Diagram of the basic operation of the NanoTest nanoindentation unit. 96

Figure 2.3 Photograph of the micro-scale sample oscillation unit (with labels). 102

Figure 2.4 Basic operation of the NanoTest unit showing oscillated sample effect. 103

Figure 3.1 Peak fitting results for the same C 1s data with (a) sp^3 dominant and (b) sp^2 dominant. 120

Figure 3.2 A single asymmetric sp^2 component (based on Ar^+ ion etched graphite) fitted to the same C 1s data as Figure 3.1. 120

Figure 3.3 C 1s data produced by a Thermo Electron ESCALAB 250. 121

Figure 3.4 Correlation between sp^3/sp^2 ratios determined from C KLL D value and C 1s peak fitting analysis. 121

Figure 3.5 (a) C KLL spectra for three different a-C films with similar D values labelled as a, b and c (b) C 1s data for films a, b and c along with data for etched graphite. 122

Figure 3.6 AFM scans of indentations into coating P11S1 (a) 1000 nm maximum indentation depth (b) data from a single AFM pass through the 1000 nm indentation (c) 500 nm maximum indentation depth (d) 250 nm maximum indentation depth. 123

Figure 3.7 AFM scan of an indentation to a maximum depth of 1000 nm into silicon... 124

Figure 3.8 Plots of all (a) hardness and (b) modulus data with indentation depth. 124

Figure 3.9 (a) a single load-unload curve at the lowest depth (b) replicated low depth load-unload curves superimposed. 125

Figure 3.10 Plots of mean (a) hardness and (b) modulus data with indentation depth.... 126

Figure 3.11 Plot of median hardness with indentation depth. 126

Figure 3.12 (a) ARXPS results for P1S1 (b) depth profile results for P1S1 (c) ARXPS results for P1S2 (the Cr and Ar results are coincident) (d) depth profile results for P1S2 (e) ARXPS results for P1S3 (f) Depth profile results for P1S3. The ARXPS analysis depths have been calculated by geometry from the maximum probe depth. 128

Figure 3.13 Differentiated Auger spectra for diamond, graphite and P1S1. 130

Figure 3.14 Comparison of C 1s peaks from P1S1 and P1S2 samples 131

Figure 3.15 (a) C 1s peak of P1S3 before any Ar ion etching (b) C 1s peak of P1S3 etched to a depth of 9 nm with Ar ions (c) C 1s peak of P1S3 etched to a depth of 27 nm with Ar ions (d) C 1s peak of P1S3 etched to a depth of 63 nm with Ar ions. Note: the C-C bonding has been interpreted as two symmetrical sp^3 and sp^2 components but could equally have been represented by a single broader asymmetric C-C peak (see section 3.1.1). 132

Figure 3.16 Cr 2p peaks of P1S3 with and without Ar ion etching. 133

Figure 3.17 Multipass nanoscratch wear test results. 134

Figure 3.18 Coefficient of friction values for the three coatings after each wear pass with the standard error range. 134

Figure 3.19 Optical microscopy photograph of the nanoscratch test results from (a) film P3S9 (b) film P3S3. 136

Figure 3.20 AFM scan of the surface of (a) film P3S5 (b) film P3S11. 136

Figure 3.21 Optical microscope images of nanoscratch tests with film thickness (a) 2000 nm (b) 150 nm (c) 50 nm (d) 20 nm (e) 10 nm (f) ion etched uncoated Si. In all cases the scratches were separated by 50 μm. 148

Figure 3.22 Scratch and topography depth-displacement plots from the nanoscratch tests with film thickness (a) 2000 nm (b) 150 nm (c) 50 nm (d) 20 nm (e) 10 nm (f) ion etched uncoated Si. 149

Figure 3.23 XPS depth profile results of (a) P11S1 (b) P11S2 (c) P11S3 (d) P11S4 and (e) P11S5. 150

Figure 3.24 Results of an investigation into depth changes due to thermal drift under nanowear testing when all components have reached thermal equilibrium 151

Figure 3.25 AFM micrograph of wear scars (a) after 72000 oscillations at 200 mN (b) after 360000 oscillations at 10 mN. 152

Figure 3.26 AFM micrograph of wear scars (a) after 18000 oscillations (test 27) (b) after 72000 oscillations (test 28) (c) after 144000 oscillations (test 29) (d) after 216000 oscillations (test 30). 154

Figure 3.27 Scatter plot of wear scar widths against mean depths for measured data and the theoretical values derived from the shape of the counter-body. 155

Figure 3.28 Scatter plot of all mean wear scar depths and group averages against number of oscillations. 155

Figure 3.29 Optical microscopy images of wear scars (a) after 18000 oscillations (test 27) (b) after 72000 oscillations (test 28) (c) after 144000 oscillations (test 29) (d) after 216000 oscillations (test 30). 156

Figure 3.30 (a) SEM image of wear scar outer debris (a) AES spectra of the unworn coating (b) AES spectra of an outer debris particle. 157

Figure 3.31 AFM micrographs of wear scar from test 10 with software shading to enhance the qualitative detail. 158

Figure 3.32 (a) AFM scan of the surface of the ruby ball (b) comparison of the surface topography of: a - untested P5S7; b – ruby ball; c – wear scar from test 10; d – wear scar from test 38. 158

Figure 3.33 Optical microscopy image of debris and transfer film on the spherical ruby counter-body. 159

Figure 3.34 (a) SEM image of the central region of transfer film on the counter-body surface (b) AES analysis of the transfer film (c) XPS analysis of the transfer film (d) XPS analysis of the clean ruby surface. 160

Figure 3.35 Optical microscopy image showing catastrophic failure of the Si substrate after total wear removal of the coating. 161

Figure 3.36 Scatter plot of mean wear depth against clean area radius. 162

Figure 3.37 Histogram of all specific wear rate data for 150 nm coatings. 163

Figure 3.38 Boxplots showing the distribution of specific wear rate data against number of oscillations for 150 nm coatings. The box is defined by the 25th to 75th percentile range. The whiskers are defined by the 5th to 25th and 75th to 95th percentile ranges. The full data range is shown by the lined crosses. The median and mean are indicated by a horizontal line and small square respectively. 164

Figure 3.39 Scatter plot of individual specific wear rate measurements against group averages for each coating at 150 nm. 165

Figure 3.40 150 nm correlation plots fitted with a linear regression between mean specific wear rate and tribologically important coating properties (a) hardness (b) reduced

modulus (c) H/E_r ratio (d) critical load (e) surface roughness Ra and (f) coating thickness......167

Figure 3.41 150 nm correlation plots fitted with a linear regression between mean specific wear rate and coating constituents (a) carbon (b) chromium (c) oxygen (d) argon (e) silicon......168

Figure 3.42 Histogram of all specific wear rate data with 50 nm films......169

Figure 3.43 Boxplots showing the distribution of specific wear rates against number of oscillations at 50 nm. For a definition of terms see the caption to Figure 3.38.......170

Figure 3.44 Scatter plot of individual specific wear rate measurements against group averages for each coating at 50 nm......170

Figure 3.45 50 nm correlation plots fitted with a linear regression between mean specific wear rate and tribologically important coating properties (a) hardness (b) reduced modulus (c) H/E_r ratio (d) critical load (e) surface roughness Ra and (f) coating thickness......172

Figure 3.46 50 nm correlation plots fitted with a linear regression between mean specific wear rate and bulk coating constituents (a) carbon (b) chromium (c) oxygen (d) argon (e) silicon......173

Figure 3.47 Boxplots showing the distribution of specific wear rates against number of oscillations. For a definition of terms see the caption to Figure 3.38......174

Figure 3.48 (a) boxplots showing the effect of applied load on all wear rate data (b) scatter plot showing applied load versus mean wear rate with standard error bars (c) boxplots showing the effect of thickness on all wear rate data (d) scatter plot showing thickness versus mean wear rate with standard error bars. For a definition of boxplot terms see the caption to Figure 3.38......175

Figure 3.49 Optical microscopy image of Si wafer after a two hour wear test at 1.0 mN. 176

Figure 3.50 3 μm x 3 μmAFM scans of wear scars (a) 0.1 mN load for 2 hours (b) 0.1 mN load for 6 hours (c) 10 mN load for 1 minute (d) 10 mN load for 5 minutes. 177

Figure 4.1 (a) Mean specific wear rate versus film thickness data fit with the expression in Equation 4.3 (b) Time or slid distance to failure versus film thickness expressed as t/w_r from Equation 4.2. 207

Table 1.1 Likely ranges for some operating conditions of MEMS [11,,,].........................27

Table 2.1 Identified independent and dependent process control variables. 91

Table 2.2 Parameter settings for 1 to 3 μm films...104

Table 2.3 DOE settings for substrate bias experiment with 150 nm films. 106

Table 2.4 Pulse parameters for substrate bias experiment with 150 nm films. 107

Table 2.5 DOE settings for key parameter experiment with 150 nm films. 109

Table 2.6 DOE settings for key parameter experiment with 50 nm films. 110

Table 2.7 Parameter settings for 2000 to 10 nm coatings..112

Table 2.8 Test conditions for nanowear characterisation experiment. 113

Table 2.9 Nanowear test conditions for experiment with 150 nm coatings.....................114

Table 2.10 Nanowear test conditions for experiment with 50 nm coatings....................115

Table 2.11 Nanowear test conditions for experiment with 2000 to 10 nm coatings. 117

Table 3.1 Hardness and elastic modulus results. 133

Table 3.2 150 nm bias tests. Mean values of measurements with standard errors bracketed. Surface composition data is bracketed for ease of interpretation...........135

Table 3.3 150nm bias tests. Main effects results from ANOVA, regression and t-tests. 138

Table 3.4 150 nm bias tests. Primary interaction effects from the ANOVA analysis.....139

Table 3.5 150 nm tests. Mean values of measurements with standard errors bracketed. Surface composition data is bracketed for ease of interpretation. 140

Table 3.6 150 nm tests. Main effects results from ANOVA and t-test analysis.............141

Table 3.7 150 nm tests. Primary interaction effects from the ANOVA analysis............ 142

Table 3.8 50 nm tests. Median values of hardness and modulus and means of other measurements with standard errors bracketed. Surface (s) and bulk (b) composition data is bracketed for ease of interpretation. 143

Table 3.9 50 nm tests. Main effects results from ANOVA and t-test analysis............... 144

Table 3.10 50 nm tests. Primary interaction effects from the ANOVA analysis............ 145

Table 3.11 Thickness range expt. Mean / median values of hardness and modulus and means of other measurements with standard errors bracketed. Surface (s) and bulk (b) composition data is bracketed for ease of interpretation.................................. 146

Table 3.12 Calculated contact radius and mean contact pressure values. 153

Table 3.13 Main effects results from ANOVA analysis at 150nm................................ 165

Table 3.14 Primary interaction effects from the ANOVA analysis at 150 nm............... 165

Table 3.15 Main effects results from ANOVA analysis at 50nm.................................. 171

Table 3.16 Primary interaction effects from the ANOVA analysis at 50 nm................. 171

Table 3.17 Calculated contact radius and mean contact pressure values. 174

Table 4.1 Comparison of nano-scale tests with micro/macro-scale tests. 182

1 Introduction

1.1 Background to the project

The work presented in this thesis formed part of a larger DTI funded Basic Technologies for Industrial Applications (BTIA) LINK project entitled 'Creation of Nano-Tribological Advanced Coating Technology' (CONTACT) [1]. The overall aim of the CONTACT project was to address nanotribological issues currently limiting the development of micro-electro-mechanical-systems (MEMS) and other micro- and nano-scale mechanical devices. The strategy of the CONTACT project was to investigate the use of industrial plasma enhanced chemical vapour deposition (PECVD) and physical vapour deposition (PVD) technologies for the production of thin nanotribological coatings. An exploration of suitable methods of coating characterisation and measurement was also required for the progress of the project to be successful.

The work detailed in this thesis focussed on the use of industrial non-hydrogenated amorphous C and Cr doped amorphous C coatings as a tribological coating effective at the nano-scale. An assessment was made of the techniques available for testing the relevant properties of thin films; the purpose was to assess the reliability of the techniques and where appropriate, to develop a method for working with ultra low thickness films. The optimised suite of test methods was then applied to selected arrays of films in order to: investigate the effect of reducing thickness on the properties of the coatings/coating process; produce fundamental knowledge of tribology at the nano-scale and provide a starting point for nanotribological coating optimisation.

1.2 Micro-/nano-scale engineering and Micro-electro-mechanical-systems

Interest in the production of micro-scale machines has grown significantly over the past two decades following the demonstration of machine components and a simple electrostatic motor with μm scale dimensions in the late 1980's [2,3,4,5,6]. The production method for these devices was based on standard integrated circuit (IC) fabrication techniques and this has remained the primary manufacture route to the present day [7].

There are a number of characteristics of the IC fabrication method that make it very attractive for the commercialisation of micro-scale machines [8]: Batch processing means that millions of items can be produced simultaneously on the surfaces of many Si wafers. The materials and process steps have been optimised over many decades and international standards of quality control have been introduced. The high level of optimisation and control makes the IC industrial environment one of the cleanest and most carefully monitored. The planar process enables component features to be designed by computer and produced using photolithography with sub-micrometre control. IC fabrication computer aided design packages have evolved greatly with the capability to perform pre-production device modelling and offer a standard communication route for diverse groups of designers and engineers.

The generic IC process has been refined for micro-scale engineering and innovative developments patented by a number of industrial companies, each with certain advantages. To date, there are three major (generic) production methods and they are normally categorised as: surface micromachining (SMM), silicon-on-insulator technology (SOI) and electroforming. SMM begins with a Si substrate and builds upon this with additional layers, some of which will form permanent features of the device and some of which will have a temporary construction role. Photolithography is used to pattern the additional layers. The final stage involves etching away the sacrificial layers and releasing the free-standing features. In SOI, the starting point is to bond two Si wafers together with an oxide layer in between. One of the Si wafers is then patterned by photolithography and the desired shape cut by deep reactive ion etching [7,8] stopping at the buried oxide. Again, free-standing features are released by selectively etching the oxide layer and hence under-cutting the patterned Si. Electroforming involves plating metals onto a conductive surface onto which a mould has previously been formed by patterning a polymeric photo-sensitive resist using photolithography [9]. Typically, metals such as Ni, Cu and Au are used. With SMM and SOI, the free-standing features normally remain anchored to the substrate. The electroforming process is usually used to create individual parts that are released from the substrate and then require assembling into a finished component.

The production of a simple free-standing Si bridge by SMM will be considered as an example of a micro-engineering fabrication process sequence (Figure 1.1) [7]. The

starting point is a Si wafer substrate as shown in Figure 1.1(a). This is usually coated with a buffer/isolation passivation layer (Figure 1.1(b)), for example a 0.5 μm oxide layer formed by thermal treatment followed by 0.15 μm of silicon nitride deposited by low pressure chemical vapour deposition (LPCVD). The buffer/isolation layer can be patterned with a mask using photolithography and etched through to the Si wafer, if electrical contacts into the substrate are required. This may be achieved by plasma etching (for example with a SF_6 plasma) followed by wet etching with buffered HF to cut through the silicon nitride and oxide layers. The sequence in Figure 1.1 shows an example where connections through to the substrate are not required. The next step is to apply a SiO_2 sacrificial layer of thickness 2 μm by plasma enhanced chemical vapour deposition (PECVD) as in Figure 1.1(c). A furnace stage may be used to enhance the uniformity of subsequent etching of this layer. The sacrificial layer is then patterned by applying a photolithographic mask and wet etching to the buffer/isolation layer with buffered HF (Figure 1.1(d)). The revealed windows define the anchor points of the bridge to the substrate. The surface is then covered with a 2 μm conformal deposit of polysilicon using LPCVD (for example with SiH_4 gas at 600°C). This layer is the structural material of the bridge (Figure 1.1(e)). At this stage the package may be annealed at (for example) 1000°C to reduce stress in the structure. Figure 1.1(f) shows the final release step, where the sacrificial layer is removed by etching with HF thus producing a free-standing Si bridge of thickness 2 μm suspended 2 μm above the substrate with two anchor points. More complex three dimensional shapes can be produced by building and patterning multiple layers of sacrificial SiO_2 and polysilicon.

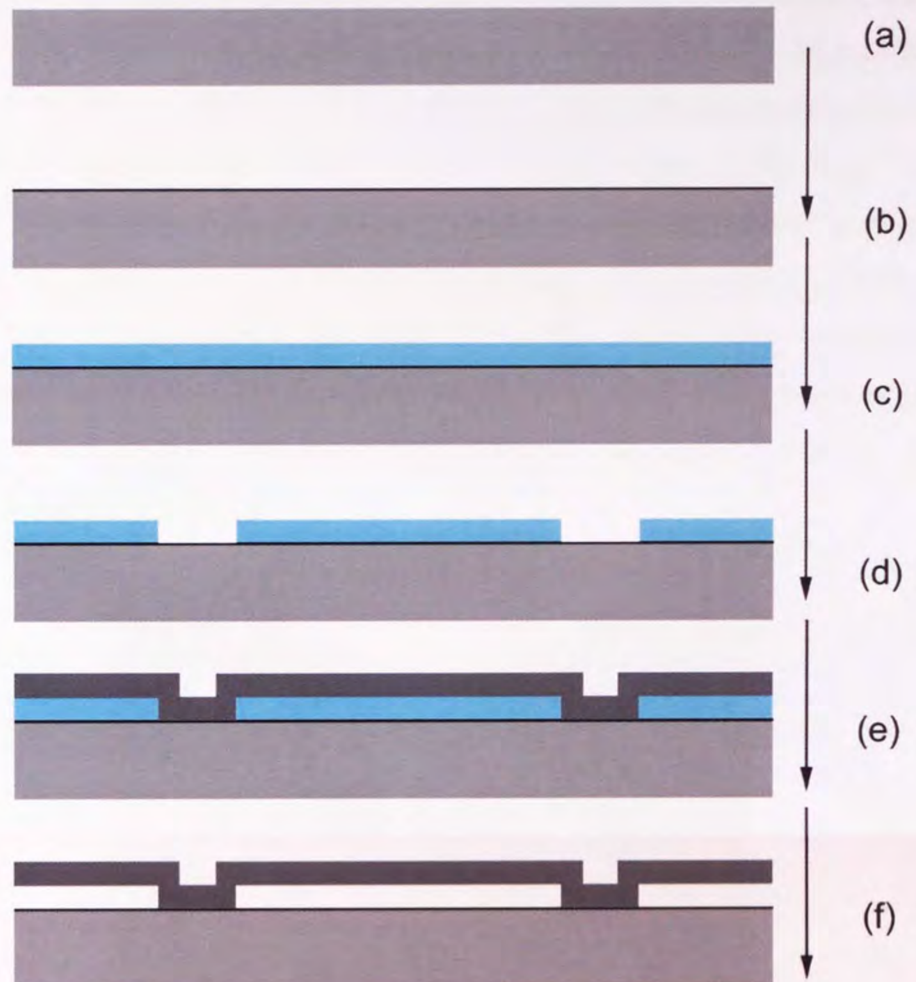

Figure 1.1 Process sequence for the production of a Si bridge by SMM.

IC electronic functionality can be incorporated into the Si device along with the mechanical function, which is a further advantage of using the IC fabrication process. The term micro-electro-mechanical-system or MEMS was coined as a short hand for such systems, although the term is now often applied to many micro-scale mechanical devices. MEMS devices with more sophisticated moving components, analogous to conventional machines, are often designated as moving mechanical assemblies (MEMS-MMA). As an extension to the MEMS name the term NEMS has been introduced to refer to devices with dimensions below 1 μm.

A large amount of research has been devoted to the construction of MEMS devices since the inception of this technology and there have been some major successes. The most

notable is the accelerometer used to deploy automobile airbags in the event of a crash [10]. This is a very simple MEMS device, manufactured by IC fabrication technology; however there are now numerous incarnations of the initial design. In general terms, the magnitude of vehicle acceleration is measured by changes in capacitance between the elements of a micro-fabricated 'comb'. The inter-leaved fingers of the comb alternately form part of the base of the device and also part of a micro-fabricated suspended mass (Figure 1.2). Acceleration causes movement of the suspended mass relative to the base of the device which in turn changes the degree of overlap of the comb elements and thus affects the capacitance. It is clear that the device involves both mechanical and electronic functionality and so it can be described as a true MEMS device. There are no contacting surfaces under normal operation.

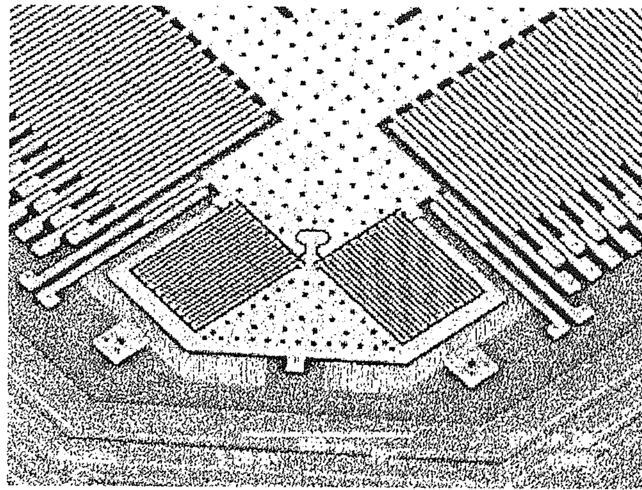

Figure 1.2 SEM image of a MEMS accelerometer [11].

An example of a MEMS device based on the IC fabrication process that involves contacting surfaces can be found in certain high definition projectors and televisions, which contain a large array of tiny light modulating units [12]. Each element of the array is an individual Al mirror mounted on a torsional hinge that can tilt to direct light toward or away from a screen thus forming one pixel of the projected image (Figure 1.3). Each mirror can be individually electronically addressed and rotated by electrostatic force. After each tilt movement, the mirrors contact a landing tip to maintain the correct position.

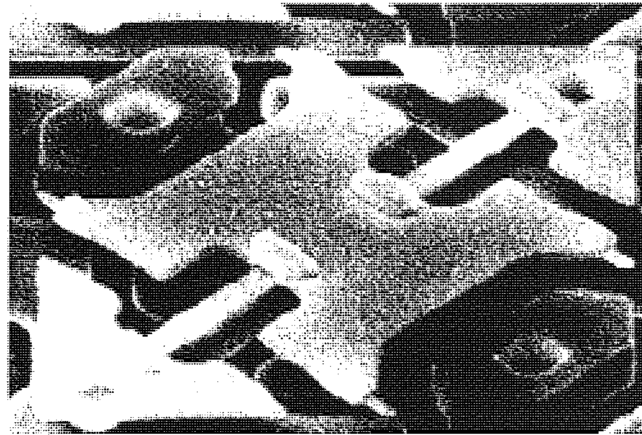

Figure 1.3 SEM image of one element from the Texas Instruments Digital Micro-mirror Device™ [11].

A further example is the high density magnetic data recording head [13]. The manufacture method of thin film heads is closely related to the IC fabrication process: thousands of heads are batch produced by building patterned layers on to a wafer substrate by PECVD. In use the electro-magnetic read/write function is not accompanied by direct movement of any individual components within the head. However accessing each piece of data involves rapid movement of the magnetic media just below the head.

1.2.1 Surface/tribology issues affecting micro- / nano-engineering and MEMS development

To date, commercially successful MEMS devices have no (or very limited) moving parts. There are many more potentially useful and interesting applications of MEMS that would involve more significant moving, touching and rubbing surfaces. These include: gears, motors and more general MEMS-MMAs with mechanical functions measured at the micro- and nano-scale. However, the effects of adhesion, friction and wear of the main materials of construction (notably Si) are seriously limiting the development and commercialisation of these sophisticated MEMS devices [14,15]. Machines at the micro-scale have large surface to volume ratios when compared with their macro-scale counterparts. This means that mass and inertia are small relative to the forces involved in surface interactions and hence the surface effects tend to dominate.

There is a significant problem with 'release stiction' during the final stages of MEMS production, as free-standing elements are under-cut and released. The surfaces of movable

elements can adhere to an adjacent surface due to interfacial forces such as: electrostatic attraction; van der Waals forces and capillary effects [16,17,18]. The elastic restoring force of the free-standing element may not be great enough to overcome the effect of stiction due to the large surface area relative to the mass or volume and hence a device failure can occur. This is a particular problem if the final production stages involve rinsing the wafer with water where capillary bridges may form between released elements, pulling surfaces together upon evaporation. A number of strategies have been developed to mitigate the effect of release stiction: Freeze-drying or supercritical CO_2 drying methods can be used as a final step to reduce the formation of capillary bridges [19,20]. Mono-molecular films can be applied at the final stage of manufacture to render the (normally hydrophilic) oxidised Si surfaces hydrophobic and hence reduce the capillary action. A number of groups have published research into the use of self assembled monolayers based on silane molecules for this purpose [21,22]. Another solution has been developed where the free-standing elements are partially undercut and then a temporary polymer support layer is deposited [23]. The sacrificial layer can then be etched and the device dried with no opportunity for the structure to collapse. A final dry plasma etch removes the support.

Stiction can also be a problem with a device in-use where contact between surfaces is a necessary consequence of operation. Micro-machined actuators may not be able to provide enough actuation force to overcome the adhesion of contacted surfaces. Surfaces may be roughened or dimpled to reduce the effective contact area [24]. As with release stiction, the use of self assembled monolayers provides a potential solution [25,26,27] by rendering the surface hydrophobic thus preventing water condensation from atmospheric humidity and hence capillary induced stiction.

Particular challenges are faced when considering the friction and wear of micro- and nano-scale machines involving sliding surfaces (the term nanotribology is often applied as tribological effects are occurring at the nano-scale). For example strong interfacial interactions operative at this scale can induce greater friction and wear than may be expected [15,28]. The low available activation forces mean that small amounts of wear and debris formation can completely arrest the movement [14,29]. The tribological properties of Si are poor [15,28,30] and render many MEMS designs (that make use of

sliding surfaces) unworkable. Wear of the outer SiO_2 layer, exposes the Si surface with dangling bonds. Without rapid passivation of the dangling bonds chemical junctions can form between two rubbing Si surfaces resulting in catastrophic wear [31]. In dry air, passivation is fast enough to prevent this catastrophic wear mechanism [32] although material loss continuously occurs ultimately leading to rapid wear and device failure [31]. In humid air, adsorbed water can have a significant but contradictory effect on friction and wear. The presence of water can induce tribochemical reactions and increase wear with single asperity situations [33,34]. However it has also been shown that with a MEMS actuator, the adsorbed water layer can improve the device lifetime [35]. Application of conventional macro-tribological solutions at the micro-scale can be inappropriate. For example, the use of fully-flooded lubrication methods based on viscous fluids when applied to MEMS can be disadvantageous to movement due to the high shear friction of the lubricant and the small shear stresses generated by the device [28]. High capillary forces with partially-flooded fluidic lubrication can overwhelm the available activation forces rendering devices useless [36]. Any surface treatments and coatings must be carefully chosen to conform to the micro- and nano-scale device features. This is usually achieved by restricting coating thicknesses to the nm scale. The use of silane based self assembled monolayers (normally applied for adhesive force reduction) can reduce friction [37] although the layers have a low durability. Research into mobile organic films and lubricant layers may provide solutions for some situations [38,39]. The layers can diffuse to re-cover regions that have undergone wear. However, further work is required before practical use can be made of this approach. Another option which has attracted attention is the use of hard coatings, particularly amorphous carbon-based films, applied by PVD or PECVD. The combination of a high hardness and elastic modulus coating tends to provide for both a low friction and hard wearing surface [40], although some very hard carbon coatings can be highly brittle, leading to low toughness.

It is interesting to consider the success of the MEMS devices discussed at the end of section 1.2 in light of the surface/tribology issues raised. The airbag accelerometer involves no contacting or sliding of surfaces, therefore no tribology solutions are required for in-use operation. Consideration need only be paid to the issue of release stiction during manufacture. The surfaces of the light modulating unit undergo no sliding, so the

usual problem of tribology is not applicable. However, surface contact does occur and consequently the contact area is kept to a minimum to reduce problems associated with adhesion. In addition, the mirrors have to be sealed within a controlled atmosphere during operation in order to counteract effects of wear caused by the contacting movements [41]. In the case of the high density magnetic data recording head there are no individual moving parts to suffer from stiction or friction/wear related seizure. However, the head is subject to a potential sliding contact due to the movement of magnetic media during reading/writing operations. For this reason low friction/high wear resistant hard coatings are routinely applied [13]. The preferred coating is a < 1 nm high hardness amorphous C film, devoid of pin-holes. It is clear that these MEMS devices have low susceptibility to the full range of potential surface/tribology issues discussed, due to the limited movement of component elements. This has certainly contributed to the successful commercialisation of these applications.

The nanotribology of any sliding element will depend strongly upon the conditions under which it operates. Key conditions relevant to tribology include: load, contact area, contact pressure, speed, oscillation displacement, total-lifetime distance travelled, mode of movement and environmental conditions. The operating conditions experienced will be governed by the particular application and there is expected to be a wide range of applications. Frequently, when discussing MEMS, one is referring to generic micro-scale motors and accompanying gear arrangements and MMAs. In these situations, rotation rates and oscillation frequencies are expected to be very high although displacements will be small. Applications involving occasional, slow movements are also likely. Table 1.1 gives an indication of the kind of ranges expected for some of the operating conditions of MEMS devices.

Table 1.1 Likely ranges for some operating conditions of MEMS [11,42,43,44].

Operating condition	Likely range
Mean contact area	nm^2 to μm^2
Mean contact pressure	<1 kPa to 400 MPa
Speed	0 to 250 mm/s
Displacement	nm to µm
Wear depth	Å - nm

It is apparent from the brief summary above that no single solution to the nanotribology issues associated with micro-/nano-engineering has yet been found. As device complexity increases and sizes are reduced still further, the challenges will become greater. This is certainly an area of on-going research.

One possible solution to the problems of nanotribology, namely the use of ultra thin hard amorphous C based coatings, formed the focus of the work discussed in this thesis.

1.3 Amorphous carbon-based coatings

It is a common feature of article manufacture that materials which have excellent bulk properties for construction offer poor surface attributes for interaction with the desired environment. Surface treatments have provided a solution to this perennial problem: from painting tar on wooden boats to providing biocompatible coatings on medical implants. The use of vapour deposition techniques has become a routine industrial process for achieving hard wearing, low friction, functional coatings at low thickness. Amorphous C coatings have evolved out of vapour deposition technology and offer some interesting and unique properties with great relevance to tribology.

1.3.1 Bonding and properties of C

C is a non-metal in group 14 of the periodic table of elements and is located near to the designated metal/non-metal boundary. The ground state electron configuration of C is: $[He].2s^2.2p^2$; hence the four valence electrons are distributed between both the 2s and 2p orbitals. C undergoes covalent bonding and during the bonding process can hybridise some or all of the valence orbitals to produce three types of hybridised bond: sp^1, sp^2 and sp^3 (see Figure 1.4).

As an example of the sp^1 hybridised bonded state: the 2s and the $2p_x$ orbitals are hybridised forming two sp^1 orbitals pointing in opposite directions along the x-axis which are available for σ-bonding. The remaining $2p_y$ and $2p_z$ orbitals, which point along the y- and z-axes, are unhybridised and are available for π-bonding. A simple example of sp^1 bonding can be found in acetylene (ethyne; C_2H_2) with a triple bond between the two C

atoms comprised of one hybridised sp^1 σ-bond and two unhybridised 2p π-bonds. The remaining hybridised sp^1 orbitals form σ-bonds with H.

In the sp^2 hybridised bonded state, the 2s, $2p_x$ and $2p_z$ orbitals are hybridised forming three sp^2 orbitals pointing trigonally along the x-z plane which are available for σ-bonding. The remaining $2p_y$ orbital, which points along the y-axis, is unhybridised and available for π-bonding. A simple example of sp^2 bonding can be found in ethene (ethylene; C_2H_4) with a double bond between the two C atoms comprised of one hybridised sp^2 σ-bond and the unhybridised $2p_y$ π-bond. The remaining hybridised sp^2 orbitals form σ-bonds with H.

Finally, the sp^3 hybridised bonded state is produced by hybridising all of the 2s and 2p orbitals to produce four tetrahedrally oriented sp^3 orbitals which are each available for σ-bonding.

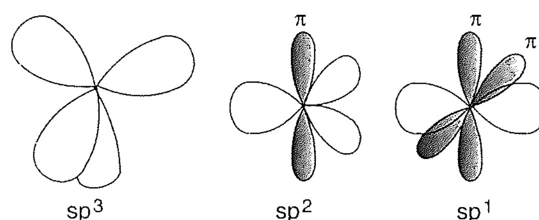

Figure 1.4 The three types of hybridised C bond [45].

C atoms will readily bond to other C atoms and will form large stable chains and networks of atoms. This fact, along with the hybridised bonding variants, means that C can exist in a large variety of stable crystalline and amorphous structures [46]. In nature, C tends to exist in three forms (or allotropes): diamond, graphite and amorphous C [47].

In diamond, all of the C atoms are bonded with sp^3 hybridised orbitals and hence each atom is σ-bonded to four near neighbours in tetrahedral formation. The tetrahedral arrangement is maintained over long ranges, thus diamond is crystalline with a face centred cubic structure (see Figure 1.5(b)). Diamond is an optically transparent, chemically inert dielectric, with an extremely high hardness and elastic modulus. The extreme properties derive from the strong, directional σ-bonds [48].

Graphite is an allotrope of C where all of the atoms are bonded together with sp^2 hybridised orbitals. Each atom is σ-bonded to three near neighbours producing two dimensional planes of hexagonally arranged atoms over long ranges. The unbonded electrons in the unhybridised 2p orbitals become delocalised around the plane, similar to metallic bonding, and hence graphite has some metallic characteristics [49]: electrical conductivity, slight metallic lustre. Graphite is composed of a stack of many of the described two dimensional layers (see Figure 1.5(a)). The layers are not chemically bonded but are held together by weak van der Waals forces. This means that the planes can slide relative to one another, providing graphite with anisotropic, lubricating properties.

Many commonly found examples of C are referred to as amorphous C, such as coal or soot, because they contain no long range ordering of the C atoms (as is present in diamond and graphite). The structure of amorphous C can be considered to be a random network of C atoms in a mix of (predominantly) the sp^3 and sp^2 hybridised states (see Figure 1.5(c)). Most naturally occurring amorphous C is not truly amorphous, but consists of crystallites of diamond and graphite held together with varying amounts of amorphous C, making them polycrystalline or nanocrystalline in nature [50]. The properties of the materials can be quite complex and will depend on the ratio of sp^3/sp^2 bonding and also on the size and distribution of any crystallites.

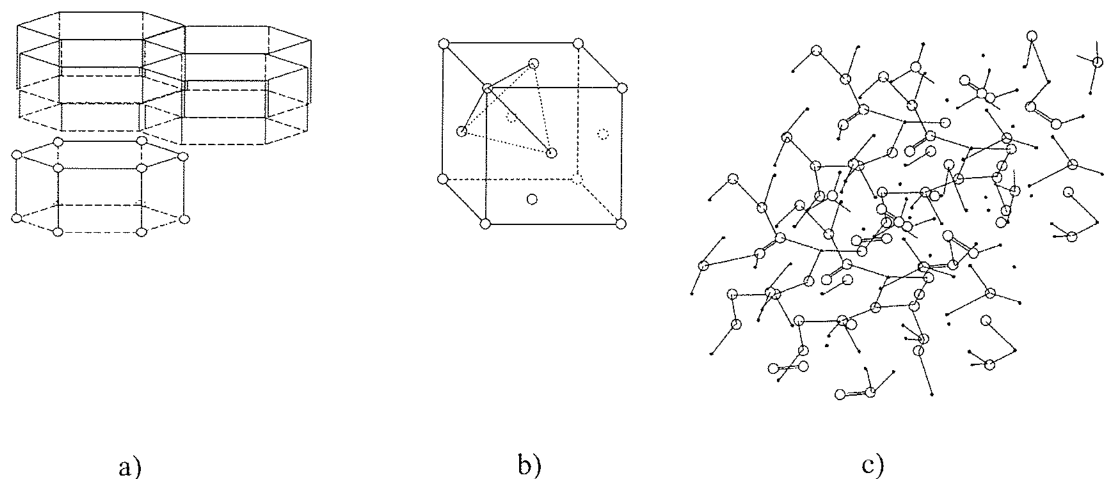

Figure 1.5 Atomic structure of (a) graphite (b) diamond and (c) amorphous C [51].

Synthetic amorphous C can be produced with a range of sp^3/sp^2 fractions, a greater or lesser degree of nanocrystalline nature and the inclusion of H (or other dopants) depending upon the method and conditions of production. The properties of the amorphous C will depend upon these variables. Materials with a high proportion of sp^3 bonding are normally referred to as diamond-like carbon (DLC) and will tend to exhibit properties similar to diamond (such as high hardness, high elastic modulus and optical transparency) [45]. Materials with a high proportion of sp^2 bonding may exhibit properties similar to graphite (such as possessing a lubricating nature and some electrical conductivity) [52]. However other factors (such as H content, for amorphous C produced from H containing C based gases) can also have a large effect on those properties [45]. By exploiting the diamond-like and graphite-like properties, amorphous C coatings have been used for many applications. The high hardness, high modulus and lubricating nature make it a good solution for certain tribology problems.

1.3.2 Production of amorphous C coatings

A number of production techniques have been developed to deposit amorphous C coatings, with a range of properties. The deposition methods normally make use of the plasma state. Plasma is considered to be the fourth state of matter and is a gas composed of neutral atoms, ions and electrons (and free-radicals in the case of molecular gases).

Plasma is usually created by introducing an electrical discharge into a low pressure gas. The electrical charge existing within the plasma enables a degree of energetic and positional control to be imparted on the plasma by the use of electrical and/or magnetic fields. Production methods tend to be divided into: those involving the formation / stabilisation of bonded species within the plasma prior to deposition, which are termed chemical vapour deposition (CVD); those involving negligible chemical changes within the plasma, where the coating properties are dominated by the physical process of deposition, which are termed physical vapour deposition (PVD).

With (simple) plasma enhanced chemical vapour deposition (PECVD) a C based gas is introduced into an evacuated coating chamber (along with a possible carrier gas) and a plasma is struck between a pair of electrodes. Simple, hydrocarbon gases are typically used as the source of C, such as methane, butane or acetylene. Dissociation of the gas occurs in the plasma and new species can be formed due to chemical reaction between breakdown products. The plasma species present will depend upon the gas and the conditions used to maintain the plasma. The greater mobility of the electrons within the plasma means that it acquires a positive charge. The charged species migrate and deposit upon the substrate which is attached to the cathode and form an amorphous C coating. The properties of the deposited coating will be influenced by such things as the nature / distribution of charged species and arrival energy. As hydrocarbons are used as the source of C, the dissociation products and consequently the coating will contain a relatively large proportion of chemically bonded H. It is common practise to abbreviate amorphous C to a-C and those films containing a significant H content to a-C:H. PECVD is commonly used in laboratories and there are many variations of the basic description given above [45].

Sputtering, which is a PVD process, is most commonly used for the industrial production of a-C coatings [45]. Basic sputtering involves the bombardment of a cathodic target material (graphite in the case of a-C coatings) by energetic ions in a glow discharge plasma (typically Ar) located in front of the target. The bombardment process causes the removal (or sputtering) of atoms from the target which can condense on a substrate thus producing a coating. Unlike PECVD, with sputter plating there is no H co-deposited with the C as the source of C atoms is from pure graphite. Secondary electrons are also

released during the sputtering process and collision between the escaping secondary electrons and atomic Ar maintains the plasma. The basic sputtering process has been used for many years to coat a range of materials. There are however, significant limitations to the process: low deposition rates; low ionisation efficiency in the plasma and high rates of substrate heating [53]. These issues have been overcome by the use of magnetron sputtering.

A magnetron is produced by incorporating an array of magnets behind the target, configured such that the magnetic field is parallel to the target surface. This constrains the ejected secondary electrons to a region close to the target (until the electrons are thermalised) which increases the chance of an ionising electron-atom collision [54] and hence produces a greater plasma density at the target [55]. This in turn increases the rate of sputtering and therefore the rate of film deposition [53]. The increased ionisation efficiency means that lower Ar pressures [56] and lower discharge voltages [57] can be used, increasing the chance of sputtered ions reaching the substrate without collision and reducing system heating [53].

The magnetron magnets are arranged such that one pole is at the central axis of the target and the second pole is formed by a ring of magnets around the outer edge. By strengthening the outer ring of magnets relative to the central pole not all of the magnetic field lines around the edge are closed by the central pole and some field lines are directed towards the substrate (see Figure 1.6). This configuration is called unbalanced magnetron sputtering. Some of the secondary electrons can follow the field lines directed toward the substrate which expands the region of plasma toward the substrate. This has the effect of providing a high rate of sputtered ions at the substrate and also a significant flux of bombarding Ar^+ ions. Substrate ion current densities an order of magnitude greater than conventional magnetrons have been reported [58,59,60]. The ion current drawn at the substrate and the deposition rate are both directly proportional to the target current [61]. For this reason, Kelly and Arnell were able to show that the ion-atom arrival ratio at the substrate remains constant with changes to target current [62,63]. The bombarding effect of the Ar^+ ions at the substrate can have a significant and useful modifying effect on the properties of the deposited films and this can be controlled by applying a bias voltage to the substrate.

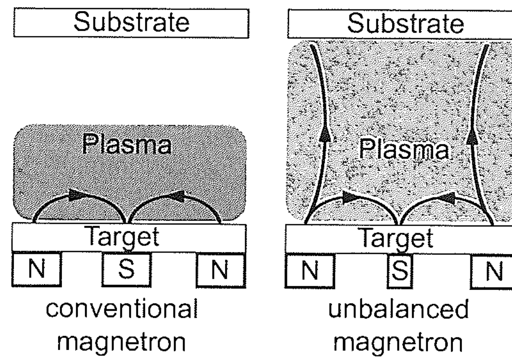

Figure 1.6 Diagram showing magnetic field lines and plasma distribution of a conventional and unbalanced magnetron arrangement.

A coating system based on one magnetron is insufficient when attempting to uniformly coat complex components at reasonable deposition rates. Therefore, in order to raise the capability of the technology for commercial applications, multiple magnetrons have been introduced. When building a coating chamber with an even number of multiple magnetrons, the magnetic arrangement of adjacent magnetrons can be configured with either like (mirrored) or unlike poles (closed field) next to one another. By selecting the latter option, the field lines between adjacent magnetrons are linked and few field lines are lost to the chamber walls (in contrast with the former option). The effectiveness of the closed field arrangement has been shown by Kelly and Arnell [64]. Ion-atom ratios incident at the substrate are 2-3 times that obtained with single unbalanced or mirrored configurations and the difference increases at greater target-substrate separations. Ion-atom ratio plays an important role in the properties of the deposited film [61,62,65]. The closed field arrangement has been adopted, developed and patented by Teer Coatings Ltd [66] and is referred to as closed field unbalanced magnetron sputter ion plating (CFUBMSIP). It is this established commercial coating process that was the method of film production used in this thesis. A schematic diagram of a typical arrangement is given in Figure 1.7.

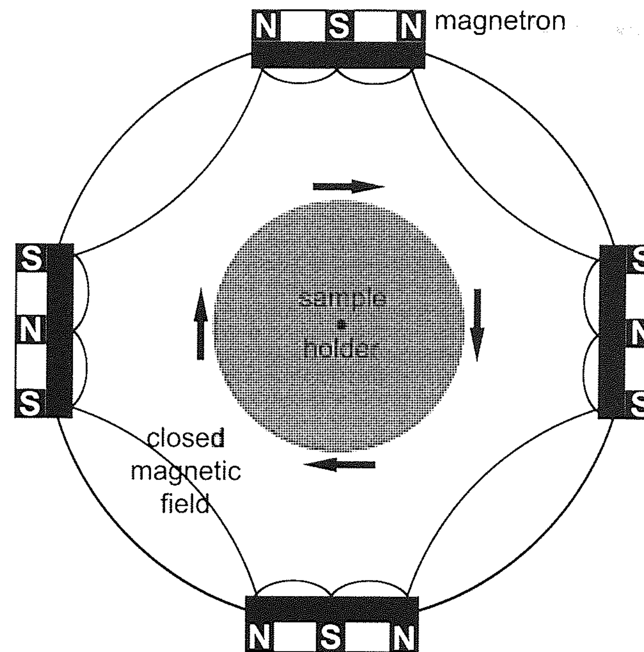

Figure 1.7 Plan view of a typical CFUBMSIP chamber arrangement.

There are a number of coating-system design and control factors associated with the type of chamber used in this work which influence the sputtering, coating-material-transfer and deposition processes and this ultimately affects the properties of the depositing film.

The size, shape and magnetron configuration of the coating chamber will have a complex effect on the size, shape and density of the generated plasma. Commercial coating chambers are available in a range of shapes and sizes to cater for the diversity of articles requiring coating. In most applications, a chamber is chosen so as to provide a significant and uniform distribution of plasma and incident atoms at the substrate, in order to produce a coating with uniform properties.

The geometry, degree of unbalance and strength of the magnet arrangement within the magnetrons has a major influence on the distribution and density of the plasma [55], which in turn controls the sputtering and arrival of particles at the substrate [53]. Teer Coatings have shown with TiN that by optimising the magnetic arrangement, ion current densities at the substrate can be increased significantly [67].

For a given coated article, the choice of chamber and the location of the substrate in the chamber will determine the target-substrate distance. Kelly and Arnell have shown (with Al, Zr and W) that by increasing the target-substrate distance the deposition rate and

temperature at the substrate decreases [62,65]. This is to be expected, as with a greater distance to travel there is more chance of a collision between sputtered atoms and Ar atoms prior to reaching the substrate, reducing the energy of the sputtered atoms and causing some to be deflected back in the direction of the targets [53]. Kelly and Arnell also found that increasing target-substrate separation had more of an effect on the rate of incident coating atoms than incident ions (when using a substrate bias voltage); this lead to a rise in ion-atom ratio at the substrate with increasing distance [61,62,65].

In order to improve coating uniformity it is common practise to include a rotating substrate holder at the centre of the chamber. This may be a simple rotating platen or it may include individually rotating location points built into a rotating platen. The choice of the mode of rotation and rate of rotation is made depending upon the shape and morphology of the article to be coated. Some commercial a-C coatings include dopants to modify the properties of the film. In the case of solid dopant materials, this is achieved by replacing one of the graphite targets by the dopant material. A careful choice of rotation rate and distance from the centre of rotation is required in order to provide a homogeneously doped coating [68]. Rigato et al. found the concentration of the dopant Cr to decrease with increasing rotation rate [69]. By optimising the rotation rate, target substrate distance and target currents it is possible to create 'nano-structured' layers in the coating, as the rotated substrate alternately passes close to the different target materials [68,70,71,72].

A key control parameter of the CFUBMSIP system is the electrical power supplied to the magnetron. Power supplies normally allow an operator to dial in a required ion current or voltage to the magnetron. The sputter rate is proportional to the total power at the magnetron and hence so is the deposition rate [53]. Large increases of ion current are achieved by raising the magnetron voltage which in turn increases the number and average energy of sputtered atoms [73]. Sputter yields (ratio of the number of sputtered atoms to incident Ar^+ ions) tend to be low, so only a relatively small proportion of the total power being drawn by the target is lost through sputtering. For example, Berg and Katardjiev [74] compute a sputter yield of <0.5 for C with 300 eV incident Ar^+ ions. Therefore the magnetrons may generate a large amount of heat. Sophisticated water cooling systems are used to remove the heat from the magnetrons to stop them being

damaged and to control the amount of heat being radiated into the chamber. When working with targets made from materials with low electrical conductivity, localised charge build up and arcing events can occur [75,76,77,78,79]. This results in particulate matter being released into the chamber and destabilisation of the coating process parameters, with detrimental effects on the coating quality. The use of a medium frequency pulsed voltage supply has been found to alleviate this problem [75,76,77,78,79]. The pulsing conditions have also been found to modify the plasma state [80,81,82,83,84,85] and can provide a useful method of coating quality control. Arcing can be a problem when sputtering graphite at very high power, although magnetron pulsing is not routinely used due to the additional complexity that this can add to the coating system.

The application of a negative bias voltage to the substrate provides a further process control. The positive Ar^+ ions and any ionised sputtered atoms will be accelerated toward the negatively charged substrate increasing the ion current and also the energy of incoming ions [53,61]. This has a bombarding action on the developing film which, given enough energy, may result in beneficial modifications to the film. This action can be greatly enhanced by the addition of a dedicated ion beam source to provide a controllable flow of high energy bombarding ions at the substrate [86]. Under most sputtering conditions films grow as three dimensional island structures on the substrate. With little migration of deposited atoms, the islands will shadow the substrate and further incoming atoms will preferentially adhere to the islands, producing columns separated by voids [87,88]. Migration of atoms on the surface can occur and depends on their surface mobility, which increases with both atom energy and the thermal energy due to the surface temperature. Atoms will move on both the surface and in the bulk, with an activation energy proportional to the melting point T_m [53]. The ion bombardment, induced by the bias voltage, causes surface heating which provides energy for migration and individual collision events can lead directly to migration. This has a densifying effect, producing a more uniform coating without voids and a less distinct columnar structure [87,89,90,91]. For a-C, the action of a substrate bias could increase sp^3 bonding within the coating. Models of subplantation proposed by Robertson [45] and Lifshitz [92] suggest that the arrival of any C^+ ions or knock-on collisions from arriving Ar^+ ions above a

threshold energy level can subplant C atoms deeper into the bulk, increasing the coating density in that region. Stabilisation of the dense region is achieved by formation of sp^3 bonds. Robertson calculates a minimum penetration energy of ~ 32 eV for incoming ions to produce sp^3 bonding by subplantation.

When depositing films that are not very conductive (such as a-C) a pulsed cathodic bias voltage is normally used to eliminate possible arcing, similar to that used with magnetron voltage. This provides further variables for controlling the bias voltage: (1) average supplied voltage (2) reverse phase going positive (bipolar) or reverse phase going to ground (unipolar) (3) frequency (4) duty factor (ratio of forward signal time to reverse signal time). Previous work has been performed to investigate the effects of these parameters on the coating process. Part of the work in this thesis examined the effect of these parameters on the properties of deposited a-C, at very low thickness. Pulsing the substrate bias voltage has been found to significantly increase the ion current drawn at the substrate [93]. In magnetron sputtering the ion current drawn at the substrate usually saturates with a bias voltage of approximately -100 V [94]. Work done by Teer has shown that by pulsing the substrate voltage, not only is the magnitude of the ion current greater than with a DC case, but the ion current drawn continues to increase as the voltage goes below -100 V [61]. The ion current at the substrate has been shown to increase with increasing pulse frequency [93,95].

The chamber pressure is determined by a balance between the rate of gas removal of the diffusion pump and the rate of Ar being fed into the chamber. The diffusion pump is usually run to allow the chamber pressure to fall to a set starting value to minimise atmospheric contamination and then the Ar flow is introduced. The chamber pressure is controlled by making adjustments to the Ar flow whilst the diffusion pumping is fixed. The effect of chamber pressure on the coating system is quite complex. At low chamber pressure, there are fewer Ar atoms present meaning that there are slightly fewer Ar ionisations and thus reduced plasma density. From this one would expect reducing Ar pressure to reduce the target current [53] (in constant magnetron voltage mode) thus reducing the sputtering rate and the deposition rate. In constant current mode, the voltage must increase to maintain the current and hence the magnetron power would increase, producing a greater sputtering rate. These effects are pressure dependent [56] and will be

limited when taking the Ar pressure a long way from normal operating conditions. At pressures where sputtered atoms undergo frequent collisions with Ar during material transfer, reducing pressure results in increased deposition rate for a constant sputtering rate [96,97]. This is because the mean free path before collision increases with reducing pressure, resulting in fewer deflecting (and reflecting) collisions of the sputtered atoms [53]. However, as discussed above, altering the pressure will also alter the magnetron power and even if this is held constant a change of magnetron voltage is likely to occur with some accompanying change of sputter yield [53,98].

Substrate temperature has been alluded to in the discussion about substrate bias voltage: increasing bias voltage increases the substrate temperature [62,65,99]. It has also been shown that: increasing the target current increases the substrate temperature [62,65,99]; increasing the chamber pressure [62,65,99] and increasing the target-substrate distance both reduce the substrate temperature [53,99]. This is to be expected as increasing the bias voltage will raise the average energy of particles reaching the substrate and increasing the target current will provide a greater number. This in turn provides the heating mechanism. With a higher chamber pressure and greater distance to the substrate there is more chance of collision on route to the substrate, resulting in a reduced flux of energy. The substrate will also gain heat from the plasma/chamber temperature and by radiation from the magnetrons. By allowing some heating of the substrate, atomic migration and hence densification of the coating is promoted. However, damage to the substrate may occur if the temperature gets to high. Also, any thermal mismatch between the coating and the substrate may result in unacceptable stresses being produced upon cooling to room temperature. Colligon et al. using a dual ion beam assisted deposition method showed TiN/S_3N_4 films to exhibit increased film hardness with increased temperature to a maximum, which when exceeded, produced film delamination and/substrate breaking due to excessive stress [100]. Gago et al. have shown graphitisation of a-C:H (conversion of sp^3 to sp^2 bonding) to occur at raised temperature with a PECVD system [101] and Nakazawa et al. have reported the same with both hydrogenated and non-hydrogenated films when annealed under an atomic H atmosphere [102]. Independent heating of the substrate is not usually required but removal of excess heat is. This is achieved by water cooling the magnetrons and the chamber walls.

It is clear from this brief description that CFUBMSIP is a complex system and that many of the design/control parameters and their subsequent effects on the sputtering/transfer/coating process are inter-related. Attempts have been made to bring together the effect of some of the main parameters on the structure of films. Thornton [103] summarised the relationship between chamber pressure and the homologous substrate temperature with respect to coating structure in a structure zone diagram, from studies of thick metal films (Figure 1.8). Homologous temperature T_h is defined as the ratio between substrate temperature T and the melting point of the coating T_m:

Equation 1.1

$$T_h = \frac{T}{T_m}$$

The diagram shows zones of different coating structure as pressure and/or T_h is changed, with increasing T_h and decreasing pressure producing a more dense structure. Four zones are allocated: zone I is dominated by shadowing during formation and is low density, with voids and a rough surface; zone II is dominated by surface migration and is fully dense with slight columnar structure and a rough surface; zone III results from significant atomic diffusion in the bulk and is of epitaxial form; zone T is a transitional region between I and II. The surface diffusion is great enough to prevent voids although there is significant columnar structure and the surface is relatively smooth.

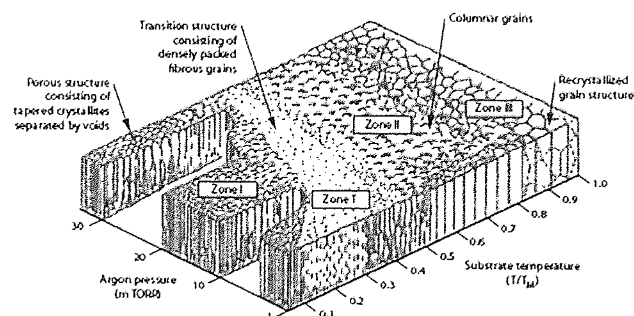

Figure 1.8 Thornton's two parameter structure zone diagram [103].

Kelly and Arnell [62] extended the structure zone diagram concept to three dimensions and proposed: substrate bias voltage; ion-to-atom ratio and T_h to be more pertinent drivers of coating structure (Figure 1.9).

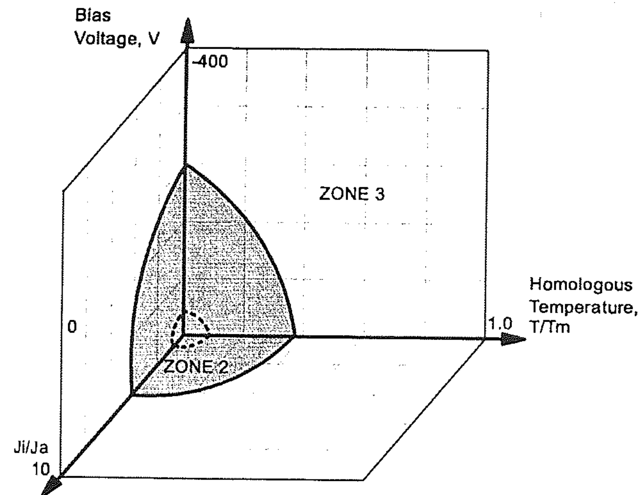

Figure 1.9 Kelly and Arnell's three parameter structure zone diagram [63].

Amorphous C coatings have found many tribological applications at thicknesses of ~ 1 - 3 μm and there has been significant research in this area, which will be reviewed in section 1.5.4.2. Very low thicknesses are required when considering the use of a-C coatings for micro- / nano-scale engineering and MEMS; much less work has been devoted to this. This will also be discussed in section 1.5.4.2 . To successfully produce and control the properties of very thin sputtered a-C films there is a need to re-evaluate the current understanding of the coating process but under conditions of very low thickness. Industrial processes must be considered if one is to achieve commercially viable a-C coatings at very low thickness. To address these points, part of the aim of this work was to look at the changing relationship between: the key sputter coating control parameters and the properties of the deposited a-C film, as a function of thickness, with an existing industrial process. The Teer Coating Ltd Graphit-IC™ [104] coating system was chosen as a 'test vehicle' for this work. It is a Cr doped sputtered non-hydrogenated a-C coating that has a proven history in tribological applications and it is expected that these excellent properties will be maintained at very low thickness. In addition there is a significant body of research about this coating at thicknesses of ~ 1 - 3 μm for comparison purposes.

1.4 Statistical design of experiment (DOE)

The focus of the work reported here is on the properties of the deposited films. Much of the research into the CFUBMSIP process has been concerned with understanding the

effect of certain process control parameters on the coating system; for example: how target current affects: plasma density, substrate ion current and substrate temperature (as discussed in 1.3.2). Other work has looked at 'key influences' on the coating properties (particularly structure); as an example, for Thornton and Kelly/Arnell [62,103] this has been: chamber pressure, substrate temperature, substrate bias voltage and ion/atom ratio (also discussed in 1.3.2). Practically, however, one does not have direct control of all of the key influences on the coating properties. One cannot simply adjust the ion/atom ratio reaching the substrate or (usually) the substrate temperature. In addition, a number of the key influences are inter-related: changes to the bias voltage will affect the substrate temperature and ion/atom ratio; changes to the chamber pressure can affect many of the other coating conditions. The coating process controls that are available may have an effect on more than one of the key influences, either directly or through inter-relationships between key influences. Therefore, the impact of a process control change on the properties of the film is potentially complex. For this reason, in order to understand the relationships between the available process controls on the one hand and the properties of the deposited thin films on the other and to investigate the interactions between the process controls in terms of film properties, a statistical design of experiment methodology (DOE) was used. This also provides a starting point for future optimisation of the CFUBMSIP system for specific ultra thin film applications.

Conventionally, when deciding to test and model the behaviour of a measured response R in terms of an input I, an attempt is made to hold all other variables constant whilst controlling I over a range of settings and measuring R at each setting, thus establishing the R-I relationship. Quite a lot of information can be gained about the R-I relationship with a manageable number of experiments. With a more complex process, as is the case in this work, there are a number of interesting inputs (I_1, I_2, I_3 and I_4) to be tested and modelled and it is suspected that some or all may influence one another's effects. The R-I_1, R-I_2, R-I_3 and R-I_4 relationships could be established individually, at specific settings of the other 3 inputs, but this does not account for changing relationships when any of the other inputs are altered (i.e. interactions between the inputs). In order to establish an R-I relationship what should the other 3 inputs be set to and does it matter if they are changed? In order to fully test the R-I relationships and answer this question the number

of experiments can become unmanageable. For example, if each input is set to 6 different values, then 1296 (6^4) individual experiments are required for a full factorial design (every combination of the 4 inputs at 6 different settings) with no repeats. If all 1296 experiments were run, then the four R-I relationships and all of the R-I-I, R-I-I-I and R-I-I-I-I inter-relationships would be known. True multi-level optimisation of the system could be achieved and specific I values could be dialled-up to produce a desired R. The quantity of experiments required is clearly unmanageable when considering an industrial sputter coating process.

Another difficulty when working with an industrial process is uncontrolled variation or noise. This is less of a problem with laboratory work where equipment can be better isolated and dedicated to just the experiments in hand. The problem of noise can be mitigated to some degree by producing repeated coatings, however this pushes up the number of experiments further. This is in addition to the replicated testing of each coating that will be required when quantifying the properties of films at very low thickness.

The use of DOE offers a solution to these issues, with some trade-offs. The aim of DOE is usually to test for the basic trend of multiple inputs over a desired range, with just 2 or 3 settings. All input settings are changed within one experiment and few repeated experiments can be used. From this, the magnitude and direction of the response for each input can be quantified and hence the most important inputs and interactions between inputs can be identified. The results provide an overall 'snapshot' of the various inputs and interactions of a complex system with no detailed information about each input-response relationship. If a more detailed understanding of the system is required for modelling and optimisation, then further experimentation can be run with just the most important inputs and by controlling the most important interactions. DOE can hence provide the first stage of modelling and optimising a complex process such as sputter coating [105,106].

Even though there may be few identically repeated experiments, the designs are symmetrical (or orthogonal arrays), such that there are the same number of experiments at each input setting. A statistical procedure is required to analyse the data and this normally involves analysis of variance (ANOVA). The ANOVA analysis procedure gives statistical

significance values to the effects observed for the inputs. The most important value is the probability statistic 'P' which quantifies the likelihood of the observed variation, which is suspected to have been produced by a particular input, being due to chance alone. An α level is chosen (typically of 0.05) which means that if the P statistic is less than 0.05 then the input is said to be statistically significant with 95% confidence. The P statistic is derived from an 'F' value which in turn is a measure of the variance (or effect) caused by a particular input, in comparison with the variance within replicated tests. The mean values for a particular input setting are derived from replicated testing and also from samples that had different settings of the other inputs; therefore they are subject to variance (random errors) from within the replicated group and variance caused by the differences in the other input settings. The ANOVA procedure separates the two levels of variation and produces the probability P values described above [105,106,107].

The DOE method and statistical analysis can still provide useful results with fractional rather than full factorial designs. This means that the number of experiments can be reduced significantly. There will be some loss of information concerning certain interaction combinations, therefore the fractional design must be carefully chosen based upon pre-existing knowledge of the system under test and the aim of the work. There are many fractional designs or orthogonal arrays available. The most famous are probably those used in the Taguchi designs. Taguchi designs are used for 'robust parameter design', in which the primary goal is to find input settings that minimise response variation, while adjusting or keeping a process on target. Consequently, Taguchi designs are a particularly useful tool for reducing component variation in a production line [105,106].

Full factorial and fractional DOE was used in this work to: identify the most important process control parameters (and any interactions) and show the magnitude and direction of the effect on the coating properties; hence providing a 'picture' of the complex coating process in terms of process control parameters and film property. The changing relationship between: the key sputter coating control parameters and the properties of the deposited a-C film, as a function of thickness, was investigated by repeating this work with coatings of reducing thickness. DOE has been used by some researchers to investigate sputter coating processes at conventional thickness [62,65,99,108]. It was

important in the work here to consider whether the DOE procedure is capable of providing useful information when working with the demanding requirements of ultra thin coatings (150 - 10 nm).

1.5 Low wear / low friction thin film analysis techniques

Robust procedures for testing and analysing the properties of deposited films are a necessary requirement of any research work into surface coatings for tribological applications. When moving toward very thin coatings the challenge of effective testing becomes significant. This section does not include an exhaustive list of applicable techniques but reviews the principle ones used in thesis. The theory of the testing technique is summarised and then consideration is given to potential problems arising which are pertinent to this work, particularly as a result of the very low coating thickness. Details of the specific equipment used in this work are given in section 2.2.

1.5.1 Chemical composition and structure

1.5.1.1 X-ray photoelectron spectroscopy (XPS)

XPS makes use of the photoelectric effect. A sample is irradiated by X-rays of known energy $h\upsilon$ causing core level photoelectrons to be emitted. The intensity of the emitted electrons is measured as a function of electron kinetic energy with a detector and displayed as a spectrum (which is usually expressed as counts/s versus eV). [109,110].

A simple spectrum consists of a series of peaks superimposed onto a background. Each peak corresponds to the electrons occupying a specific energetic orbital in a specific atom type. The kinetic energy (KE) of the electrons contributing to a particular peak is known from the spectrum. The energy of the X-ray photons is known ($h\upsilon$). Therefore the binding energy (BE) of the photoelectrons in the atom can be determined:

Equation 1.2

$$BE = h\upsilon - KE - W$$

Where W is the work function of the spectrometer. The core electrons of each element have characteristic binding energies and generate fingerprint patterns of peaks in spectra

at those energies. Electrons occupying the same orbital of the same atom type which are excited and escape without energy loss contribute to the characteristic peak in the spectrum. Those electrons which undergo inelastic scattering and suffer energy loss contribute to the background of the spectrum. The peak intensity depends on the X-ray intensity, the atomic photoemission cross-section, and the transmission characteristics of the analyser (which is a function of electron energy). Energy resolution ΔE is defined by peak width, which is often measured by the full width at half maximum (FWHM). ΔE is governed by the natural width of the core level ionisation ΔE_n, the X-ray photon source line width ΔE_p and the electron analyser resolution ΔE_a:

Equation 1.3

$$\Delta E = \sqrt{(\Delta E_n^2 + \Delta E_p^2 + \Delta E_a^2}$$

XPS testing is performed under conditions of ultra-high vacuum (UHV) which is in the range 10^{-8} to 10^{-10} mbar. This maximises the spectral intensity and minimises noise by reduction/elimination of photoelectron scattering. More importantly, the UHV environment is necessary to maintain a 'clean' sample surface for extended periods because of the surface sensitivity of XPS. [110].

X-rays are generated by bombarding an anode material with high energy electrons. The electrons are emitted from a thermal source and accelerate toward the anode, which is held at a high positive electrical potential of typically ~ 10- 15 kV. There are normally two anode materials available within the X-ray gun: Al and Mg; providing AlKα or MgKα photons of energy 1486.6 eV and 1253.6 eV respectively. Increased performance can be achieved with the use of a monochromator, where a very narrow X-ray line can be produced by reflecting the X-rays on a (typically quartz 1010) crystal face and making use of Bragg diffraction to effectively filter the incoming wavelengths. Some of the benefits of using a monochromator are:

- Reduced X-ray line width, for example, from 0.9 eV to approximately 0.25 eV for AlKα.

- Removal of unwanted regions of the X-ray spectrum where other minor lines may exist.
- The sample can be set further away from the X-ray gun meaning less exposure to radiant heat from the source.
- It is possible to focus the X-rays using the monochromator for small area XPS analysis.

For high resolution electron detection a hemispherical sector analyser (HSA) is used (Figure 1.10). The HSA consists of a pair of concentric hemispherical electrodes between which there is a gap for the electrons to pass. There is usually a series of lenses between the sample and the HSA which (amongst other things) serve to retard the incoming electrons for increased resolution. A potential difference is applied across the two hemispheres with the outer hemisphere being more negative than the inner. Electrons entering the gap will only reach the detector with an energy E given by:

Equation 1.4

$$E = e\Delta V\left(\frac{R_1 R_2}{R_2^2 - R_1^2}\right)$$

Where e is the charge on the electron, ΔV is the potential difference between the hemispheres and R_1 and R_2 are the radii of the inner and outer hemispheres respectively. By scanning the voltage between the hemispheres a scan of incoming electron energies can be achieved. [110].

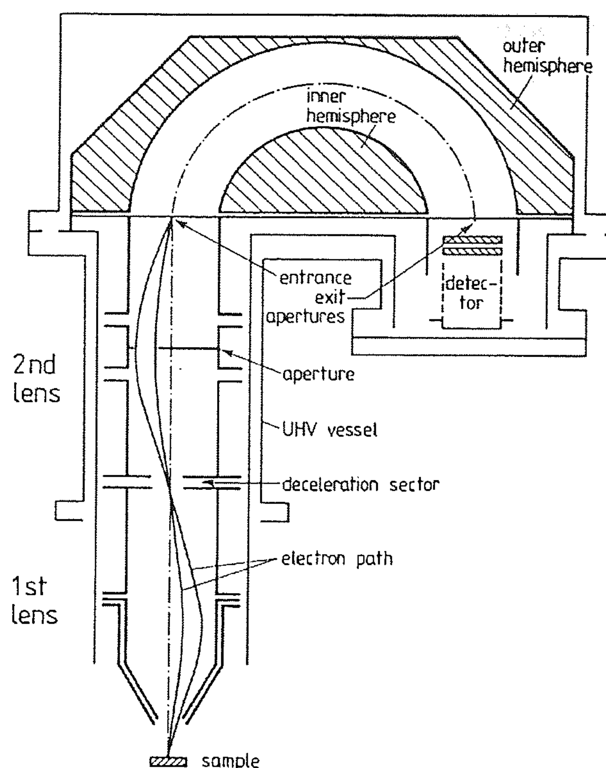

Figure 1.10 Cross-section of a hemispherical sector analyser [51].

The XPS signal is composed of a combined contribution from photoelectrons that have escaped from the surface and bulk of the sample without undergoing an inelastic collision. The chance of a photoelectron meeting this criterion reduces exponentially with depth below the sample surface, making XPS a very surface sensitive technique. Three times the attenuation length of a photoelectron is widely taken to be the limit of XPS probe depth [109]. Attenuation length is a function of the energy of the electron and type of material and various equations have been suggested to model this relationship; for example the Cumpson and Seah CS2 equation [111]. For a film of C under typical conditions of XPS analysis, an attenuation length of ~ 2.5 nm can be derived from the CS2 equation, making the approximate analysis depth 7.5 nm. The analysis depth can be reduced further by tilting the angle of the sample relative to the electron detector. By progressively tilting the sample angle with respect to the photoelectron analyser away from the position normal to the sample surface, XPS becomes progressively more sensitive to the outer layers of the surface [109]. Therefore elements that show an increased concentration at higher angles will be more localised near to the surface. This technique is usually referred to as angle resolved XPS (ARXPS) and provides a useful

method of looking at the distribution of elements over the outer few layers of the surface. Depth profiling can also be achieved with in situ ion etching of the sample.

When considering the investigation of doped a-C films for tribological applications, XPS offers an important method of identifying and quantifying the elements present in films down to ~ 10 nm thickness with little interference from the substrate. Information can be gained about the distribution of elements through the coating thickness, with angle-resolved XPS and depth profiling.

1.5.1.1.1 The use of XPS for the determination of sp^3/sp^2 bonding ratio in a-C

Small changes in the electron energy as a result of the chemical environment of the emitting atoms (chemical shifts) can be detected by XPS and provide an insight into the bound state of atoms. The existence of un-equivalent C atoms in a-C, that is sp^3 and sp^2 bonding, leads to the expectation of different binding energies for the associated C 1s electrons. This provides the theoretical basis for studies of the C 1s peak shape with a-C coatings; which has been found to be broad and asymmetric when compared with diamond and graphite [112].

In the first analyses derived from a-C, the C 1s peak was described in terms of a superposition of two symmetrical components relating to sp^3 and sp^2 hybrids with component peaks derived simply from measurements of graphite and diamond [113,114]. Schafer et al. [115] suggested a model based on two components relating to the number of coordinated atoms, analogous to the shift observed with 3-coordinated atoms on the clean surface of diamond relative to the 4-coordinated bulk [116,117]. Later work [118,119,120] proposed a model for the mechanism of the two component charge shift based on final state effects of the ionised C atoms. The lower binding energy of the sp^2 component being understood in terms of more effective core-hole screening by the slightly delocalised π electrons associated with the sp^2 bonds. This contrasts with the poor core-hole screening provided by the highly localised σ electrons at the sp^3 sites. Computational and experimental work by Haerle et al. [121,122] returned to the concept of atomic coordination with a two component model based on 3 and 4 coordinate C

systems; with both initial state effects due to bond length and final state effects due to π electron screening contributing to the chemical shift.

Although the C 1s peak broadening of a-C can be understood as a simple sp^3/sp^2 two component system, a more complex situation is possible. Intermediate hybridisations may exist with a-C due to strained configurations [123] or loss of planar symmetry for sp^2 clusters [124,125,126,127].

When attempting to synthesise a C 1s into two components there are a number of choices with regard to the separation and shape of the synthetic peaks. Early work [113,114] involved the use of symmetrical peaks simulated by a combination of Gaussian and Lorentzian functions with separations typically in the range 0.7 – 1.0 eV. Recognising the fact that graphite produces an asymmetrical C 1s peak, Diaz et al. and then other researchers [128,129,130,131] established the use of a Gaussian function convoluted with a Doniac-Sunjic function [132] to provide the necessary asymmetry. This method has been previously used successfully to interpret the asymmetric shape of metallic core electron XPS lines [133] and it is proposed that the metallic nature of graphite produces the asymmetry [134]. Work with molecules based on networks of hexagonal benzene rings has shown asymmetry of the C 1s peak when network size is greater than ~ 10 – 22 Å [135]. Few reports of all component peak parameters used for quantifying sp^3/sp^2 ratio are given in the literature; where quoted, component peak widths tend to fall in the range 1.00 – 1.30 eV [114,128,129,130,131]. The width of the component peaks is generally higher than expected from instrument broadening alone and this is understood in terms of disorder of the amorphous state [136]. Additional peaks need to be assigned to the synthetic fit when the surface has been exposed to the atmosphere to account for C-O bonding or when the coating has been doped. A typical example of an XPS C1s peak fitted with three components is given in Figure 1.11.

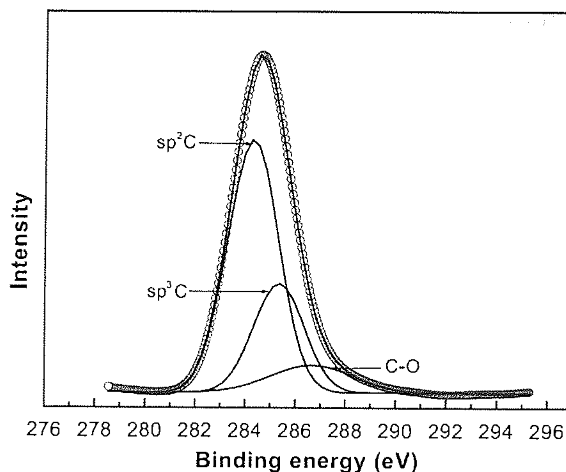

Figure 1.11 XPS C 1s peak fitted with sp^3/sp^2 and C-O components.

Electron energy loss spectroscopy (EELS) has been used widely to determine the sp^3/sp^2 fraction in a-C films [45]. The technique involves passing an electron beam through a detached film [45] and is not considered here. However, low loss EELS information, associated with the C 1s peak, can be observed on XPS spectra of un-detached a-C films. The EELS spectral peaks are termed plasmon loss features and are located at a BE around 30 – 40 eV higher than the C 1s peak. They arise when outgoing electrons excite collective oscillations in the conduction band electrons of a solid and thus suffer a discrete energy loss. Haq et al. [137] showed that the plasmon features of diamond are dominated by a 'bulk plasmon' peak located at a BE ~ 35 eV greater than the C 1s peak and graphite is dominated by a peak at a BE ~ 28 eV above C 1s. It has been proposed that the Plasmon features of a-C films can be synthesised into component peaks relating to diamond/graphite and a semi-quantitative 'diamond content' value can be produced by taking the ratio of the peak areas of the C 1s line to the diamond bulk plasmon. Speranza and Laidani [138,139] adopted this procedure and applied it to a series of sp^3/sp^2 containing samples. It was reported that the method was not very reliable owing to ambiguity in fitting the component peaks as a result of the large overlap of the proposed components.

Once a core photoelectron has been emitted as a result of the XPS procedure, the ionised atom must relax by some process. This is achieved by an internal transition of an electron from a higher energy shell to fill the vacancy in the core shell. In order to conform to the principle of energy conservation, the atom must release energy (approximately) equal to

the change brought about by the electron transition. This can be achieved by the emission of an X-ray photon (X-ray fluorescence) or by the emission of an electron from the higher energy shell. This is termed an Auger electron and the technique of interpreting these electrons is called X-ray induced Auger electron spectroscopy (XAES). From this description, it can be seen that the energy of the emitted Auger electrons is linked to the transitions of electrons within the atom rather than the energy of the XPS X-ray source. Consequently, the Auger electron spectrum of each element will occupy the same KE region of the spectrum irrespective of X-ray source energy. [109,110].

In the case of C, the 2 core electrons occupy the K shell and the remaining 4 electrons occupy the L shell. Auger electrons are brought about as a result of a transition from the L to K shell and then the emission of an electron from the L shell. The distribution of emitted Auger electron energies is therefore termed the C KLL spectrum. For C, the electrons in the L shell are also valence electrons, so the Auger spectrum involves transitions between core and valence and emission of valence electrons i.e. C KVV. It has been found that KVV Auger spectra contain a superposition of the degenerate valence band structure onto the shape of the Auger peak(s). This means that KVV Auger spectra can have quite complex shapes and due to the involvement of core electrons in the Auger emission the shape is influenced by the chemical environment of the emitting atom, although not with discrete chemical shifts seen with XPS core levels. [109,110].

Use has been made of the C KVV valence band structure to estimate sp^3/sp^2 fraction [138,139,140,141,142]. A large number of component peaks are fitted to the valence band structure of both diamond and graphite and then this arrangement is applied to the C KVV spectra of an a-C sample with adjustments to the peak heights until the optimum fit is found. An estimate of sp^3/sp^2 fraction is derived by determining the ratio of the area of all component peaks associated with diamond and graphite.

A popular method of sp^3/sp^2 estimation in a-C films involves peak width estimation of C KVV spectra [112,113,129,143]. The width of the main C KVV peak (D value) is estimated, normally by determining the energy difference between the primary maximum and minimum on the derivative of the C KVV spectrum. D values of ~ 22 and 14 eV are typically found for diamond and graphite respectively. As with valence band fitting, the

method assumes that the spectrum of an unknown a-C film can be approximated by a linear combination of the spectra from graphite and diamond, thus an estimate of sp^3/sp^2 fraction can be produced. A typical example is given in Figure 1.12.

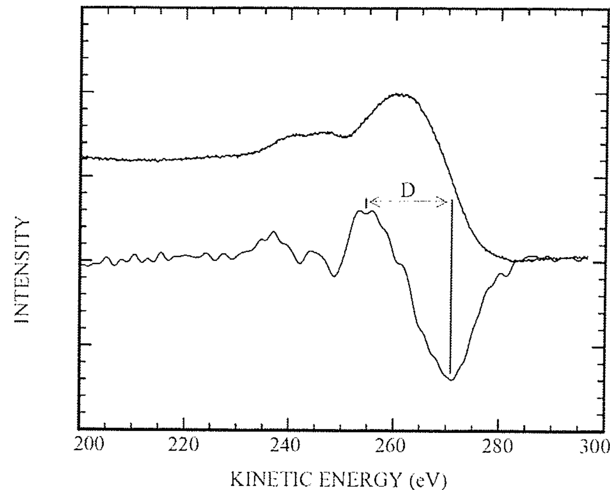

Figure 1.12 As collected XPS C KVV spectrum (upper) and the derivative showing the D value (lower).

There are a number of potential problems with the use of C KVV spectra. Particularly pertinent for the work reported here is the interference effects that first row transition elements can have on the spectra [144]. A further interference is attributed to O, whose presence in the coating has been found to negatively correlate with D value [145]. Questions have been raised with regard to the degree of disorder in the film significantly affecting the region of C KVV spectra where D values are derived [136]. The surface sensitivity of all XPS methods for sp^3/sp^2 estimation means that probe depths are restricted to a region that may be structurally different to the bulk [146].

1.5.1.2 Auger electron spectroscopy (AES)

The principle of AES is very similar to XPS but instead of irradiating the sample with X-rays, an electron beam is used. The emitted core electrons (secondary electrons) possess a range of energies and do not contain any analytical information, however Auger electrons are also emitted and these can be spectrally analysed by a hemispherical sector analyser as with XPS. [109,110].

Hot field emitters have become a popular source of electron beam in recent years. The source consists of a single crystal tungsten wire coated with ZrO_2. The coating lowers the work function of the emitter and increases the emission current. It also provides a self-cleaning, self-healing surface. Heat and the application of a large electrostatic field to the small emitting surface produces an electron beam which is then passed through a lens arrangement. [109,110].

The lens system enables a very small electron beam spot size to be produced (< 10 nm) and provides the ability to scan the beam. It is relatively simple to couple scanning electron microscopy (SEM) with AES by rastering the electron beam and collecting the emission of low energy secondary electrons. Together, this makes a powerful technique, providing high resolution topographical and elemental scans of surfaces. [109,110].

Many of the issues raised in the discussion about XPS apply to AES due to the close similarity between the techniques, particularly concerning the C KVV spectrum. It is worth noting that structural modifications have been reported with a-C:H when irradiating with electron beams [147,148,149].

1.5.2 Physical properties

1.5.2.1 Atomic force microscopy (AFM)

AFM is a type of scanning probe microscopy. A very sharp Si tip attached to a flexible cantilever is brought close to the surface under test. When the distance between the atoms at the Si tip and those of the surface is small enough, a repulsive force is experienced and the flexible cantilever will bend according to Hooke's Law: $F = -kx$, where F is the force, x is cantilever displacement and k is the spring constant of the cantilever. If the tip is brought closer to the surface, the repulsive force increases and so the cantilever will bend further. A laser beam is reflected onto the cantilever and then into the face of a four-section photodetector; hence the cantilever deflection (and therefore repulsive force) can be monitored as a function of light intensity (Figure 1.13).

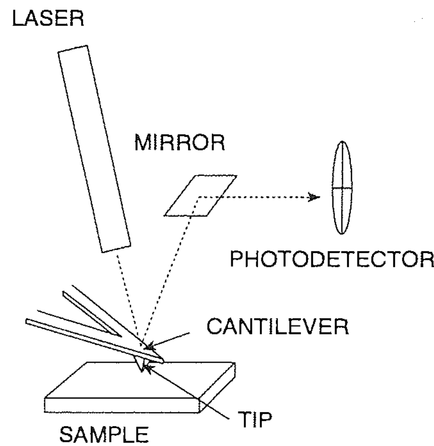

Figure 1.13 AFM defection/force sensor [51].

Feedback circuitry is linked to both the photodetector output and a piezoelectric ceramic z-axis drive attached to the cantilever. A repulsive force can be chosen by the AFM user and this force is maintained by the feedback circuitry as the tip is moved across a sample surface, by making z-axis (height) adjustments of the tip. When a surface peak is approached, the tip-surface distance decreases and hence the repulsive force / cantilever deflection increases. This results in a change of light at the photodetector sections which causes a voltage change at the z-axis drive via the feedback circuitry; hence raising the tip to maintain the user defined force.

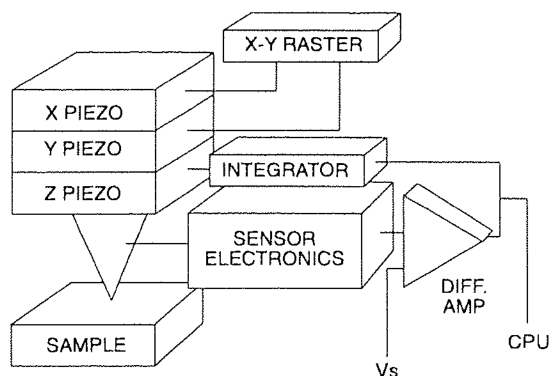

Figure 1.14 AFM system with feedback circuit and ceramic piezoelectric drives [150].

Piezoelectric drives are also supplied for x- and y-axis movement, so the tip can be rastered across a chosen surface area (Figure 1.14). By suitable calibration of the

feedback voltage and x- / y-axis drives, quantified topographical scans can be produced. Vertical resolutions of < 1 Å are achievable. Lateral resolutions are governed by the tip radius / side-wall angle and the degree of pixelation of the image. [150,151,152].

It is possible to apply excessive tip force to perform surface scratching, effectively from a single asperity. This will be discussed in more detail in section 1.5.4.3.

1.5.3 Mechanical properties

1.5.3.1 Nanoindentation

Important mechanical properties of tribological coatings, such as hardness and elastic modulus have been determined by indentation methods for many years; where a hard material with known physical/mechanical properties is pushed into a softer unknown material under controlled force. It is crucial in the quantification of hardness and elastic modulus that the area of contact between the indenter and sample is known. Conventionally, this is estimated by optical examination of the residual impression left in the sample surface. Nanoindentation is an indentation test in which the penetration depths are measured in nanometers rather than microns / millimetres as with indentation testing. Nanometer depth testing is important when working with thin coatings to avoid interference from the substrate. The residual impression left following nanoindentation is of micron scale and too small to be conveniently measured directly. By continuously measuring the applied load and indentation depth a load-displacement curve is produced. From this the contact area at full load can be indirectly determined and hence the hardness and reduced elastic modulus can be estimated. [153,154].

Doerner and Nix were the first to produce a comprehensive method for determining hardness and modulus from nanoindentation load-displacement data [155]. This was modified by Oliver and Pharr [156] and this method now forms the basis of international standards for nanoindentation [157]. The method of analysing load-displacement data from a load-unload nanoindentation cycle is derived from the original Hertz theory describing the linear elastic contact between two parabolic bodies [158]. This was extended to cover a number of other geometries, the most important for nanoindentation being the cylindrical and conical indenters on a flat surface [159,160,161]. A schematic

diagram of a load-unload cycle is shown in Figure 1.15 and the resulting load-displacement data is given in Figure 1.16.

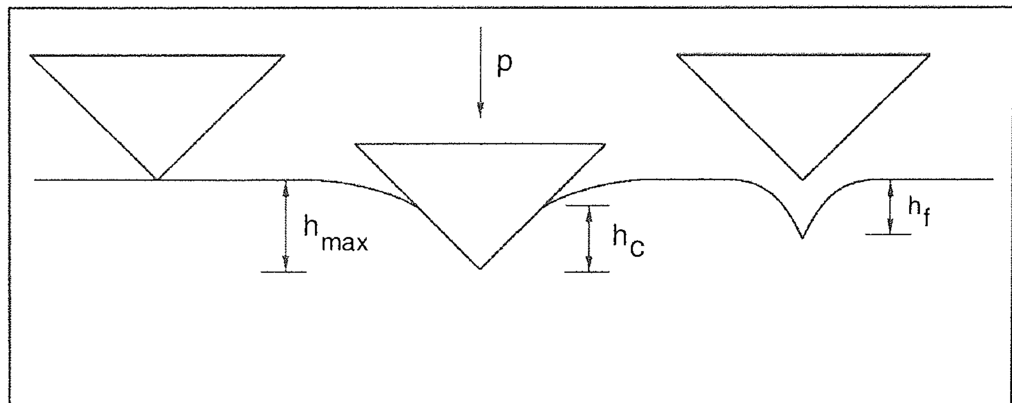

Figure 1.15 A schematic diagram of an elastic-plastic indentation [51].

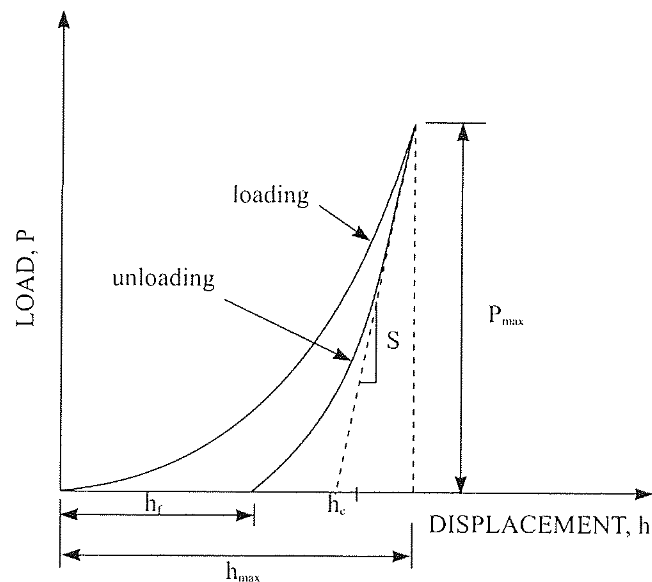

Figure 1.16 Typcial load-displacement curve from an elastic-plastic indentation [51].

Most nanoindentation tests involve both plastic and elastic deformations. The loading portion of the cycle can be generally divided into three stages: the first being fully elastic, where the mean contact pressure is too low to generate stresses that are sufficient to produce plastic flow. If the load were to be removed in this zone, the unload curve would coincide with the load curve and no residual impression would be left in the material. In the second zone, stresses are sufficient to produce plastic deformation beneath the surface

but it is constrained by the surrounding elastic material or material flow limitations. The final stage is fully plastic and the mean contact pressure can no longer be increased. The plastic region extends to the surface and continues to grow in size such that the indentation contact area increases at a rate that gives little or no increase in mean contact pressure. The maximum mean contact pressure (P_m) has been reached and this is designated as the indentation hardness (H) [153]. From this definition it can be seen that:

Equation 1.5

$$H = P_m = \frac{P_{\max}}{A_c}$$

where A_c is the projected contact area at maximum load P_{max}. The value of P_{max} is known from the load-unload plot, therefore one need only calculate A_c and an estimate of H can be made.

It can be shown by geometry [153] that for a cone with apex angle α, the projected area of contact A_c at maximum indentation load is given by:

Equation 1.6

$$A_c = \pi h_c^2 \tan^2 \alpha$$

where h_c is the maximum contact depth between indenter and surface. It is usual with nanoindentation work to use a Berkovich three sided pyramidal diamond indenter, as this geometry enables a particularly sharp tip to be readily manufactured. It can be shown by geometry [153] that for a tetrahedral indenter with semi-angle θ, the projected area of contact A_c at maximum indentation load is given by:

Equation 1.7

$$A_c = 3\sqrt{3} h_c^2 \tan^2 \theta$$

The semi-angle of a Berkovich indenter is 65.3°, therefore:

Equation 1.8

$$A_c = 24.5h_c^2$$

A diagram showing the relationship between A_c and h_c for a Berkovich indenter is given in Figure 1.17. It is convenient to treat data produced by a Berkovich indenter as though is was from a conical indenter with the same area-depth relationship, as this enables the use of convenient axial-symmetric elastic equations. The equivalent cone for a Berkovich indenter has an apex angle of 70.2996° [153].

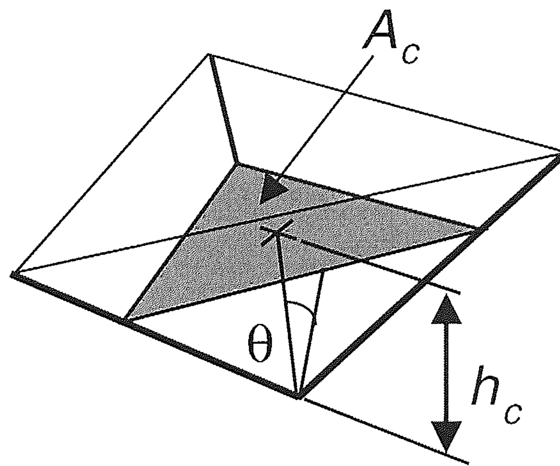

Figure 1.17 Diagram of a Berkovich indenter showing contact depth h_c, projected area of contact A_c and semi-angle θ [153].

The material recovers elastically during the unloading portion of the cycle. If the contact area remained constant during the full unloading sequence (and hence all elastic recovery was just located in the curved material surface) the load-displacement curve would follow the dotted line in Figure 1.16 and h_c would simply be given by the intersection of the linear unload curve with the displacement axis:

Equation 1.9

$$h_c = h_{max} - \frac{P_{max}}{S}$$

where S is the slope (stiffness) of the unload curve. This situation is effectively the same as an elastic contact between a cylindrical flat punch and a flat surface where the unloading response is given by [153]:

Equation 1.10

$$P = 2aE_r h$$

Where P and h are the load and depth at any point during the unload sequence, a is the radius of contact and E_r is the reduced modulus given by:

Equation 1.11

$$\frac{1}{E_r} = \frac{(1-\upsilon^2)}{E} + \frac{(1-\upsilon_i^2)}{E_i}$$

Where E and v are the elastic modulus and Poisson's ratio for the specimen surface and E_i and v_i are the elastic modulus and Poisson's ratio for the indenter. Equation 1.10 includes a reduced modulus term to take account of the combined elastic behaviour of both the surface under test and the indenter.

Differentiating Equation 1.10 with respect to h yields the slope of the unload curve (or stiffness) S and by substituting the circular area of contact A_c for a and rearranging:

Equation 1.12

$$E_r = \frac{1}{2} S \frac{\sqrt{\pi}}{\sqrt{A_c}}$$

It can be seen from Figure 1.16 that the unloading curve does not follow a straight line in practice. This is because all of the elastic recovery is not confined to the surface curvature. There is elastic recovery within the contact zone and hence the contact area is not constant and reduces during unloading. Doerner and Nix [155] assumed that the initial portion of the unloading curve was linear (i.e. the contact area remained constant and the flat punch approximation was valid) and hence made use Equation 1.12 in their analysis by manual linear extrapolation of the initial portion of unloading data. Oliver and Pharr

[156] noted that few if any real materials showed an initially linear unloading curve and therefore questioned the use of a flat punch approximation. They proposed a method whereby a simple power law fit was made to the unloading curve (by least square fitting) of the form:

Equation 1.13

$$P = A(h - h_f)^m$$

where P and $(h - h_f)$ are the load and depth terms (adjusted for the final depth h_f) and A and m are constants. The initial unloading slope S was found by analytically differentiating the derived function and evaluating the derivative at the peak load and displacement. Also an amendment to Equation 1.9 was needed to include a geometric constant, derived from work by Sneddon [159], to account for the deflection of the surface at the contact point being influenced by the geometry of the indenter:

Equation 1.14

$$h_c = h_{max} - \varepsilon \frac{P_{max}}{S}$$

By calculation, ε is equal to 0.72 for a conical indenter (the elastic contact calculations assume a Berkovich indenter to be a conical indenter with equivalent area-depth relationship). Oliver and Pharr found ε to be 0.75 experimentally and attributed the difference to be as a result of none ideal shape, particularly at the tip. Others propose that ε can be considered as a function, dependent upon the power law fit applied to the unloading data [162,163]. The effect of ε is marked on the displacement axis in Figure 1.16.

The use of Equation 1.12 is still valid for the determination of E_r with the Oliver-Pharr method as the initial unloading slope S derives from an infinitely small change of depth resulting in an infinitely small change of contact area. However an extra geometric term β is included to take account of the non-symmetrical pyramidal shape of a Berkovich indenter:

Equation 1.15

$$E_r = \frac{1}{2} S \frac{1}{\beta} \frac{\sqrt{\pi}}{\sqrt{A_c}}$$

The value of β is usually taken to be 1.034 for a Berkovich indenter [164]. Hay et al. introduced an additional correction factor γ to take account of deviations from the ideal Sneddon model [165]. Troyon and Huang [166] combined β and γ into one factor identified as α, which was shown to be dependent upon the size of the indenter tip and the tested material.

In summary, by generating a simple power function to fit the unload curve, its initial slope can be calculated S. Inserting this value into Equation 1.14 provides the contact depth h_c. From this, A_c can be calculated using Equation 1.8, leading to a determination of H using Equation 1.5 and E_r using Equation 1.15.

There are however some potential errors that need to be addressed when dealing with experimental nanoindentation data:

1.5.3.1.1 Instrument compliance

Depth measurements of a typical nanoindentation system include elastic displacements of the equipment (instrument compliance) in addition to the expected plastic penetration of the indenter into the sample and elastic contact between the indenter/sample. The instrument compliance C_f (which is the inverse of stiffness) must be measured and accounted for in the analysis. This is dealt with by assuming the instrument compliance to be a spring attached in series to the indenter/sample. Consequently, the instrument stiffness $1/C_f$ must be deducted from the initial slope of the load-unload curve dP/dh in order to derive the sample/indenter stiffness term S for use in Equation 1.14 and Equation 1.15:

Equation 1.16

$$S = \frac{dP}{dh} - \frac{1}{C_f}$$

Oliver and Pharr [156] determined C_f by making use of Equation 1.15 and inserting Equation 1.16 and re-arranging to give:

Equation 1.17

$$\frac{dh}{dP} = \frac{\sqrt{\pi}}{2\beta E_r} \frac{1}{\sqrt{A_c}} + C_f$$

Therefore a plot of initial unload slope against projected contact area for a range of indents made into a specimen of known, depth-independent, E_r will yield C_f as the intercept. There is an error associated with the function used to derive the contact area (Equation 1.8) which will be discussed below and since this method relies upon knowledge of the area function, an iterative procedure was used to converge upon both the best C_f and area function. This is the method favoured by the ISO 14577 standard [157].

If deep indents are used then the error associated with the area function, which is most likely as a result of tip blunting, is reduced and convergence upon the best C_f value is expedited [167].

Direct measurement of frame compliance has been undertaken, where loads are applied through a flat contact of the instrument indenter / specimen holders [168].

1.5.3.1.2 Indenter geometry

The area function, which relates depth to projected contact area of the indenter, given in Equation 1.8 is for an ideal Berkovich shape. Practically, however, Berkovich indenters will have some blunting of the tip and may also deviate from the ideal shape due to crystal anisotropy of diamond, therefore an adjustment to the ideal function is required.

Oliver and Pharr [156] addressed this issue as part of the instrument compliance determination (see above). The first estimate of instrument compliance was made by assuming an ideal Berkovich shape. This estimate was then used to re-calculate the contact area values (with Equation 1.17) which were then fitted to a polynomial function describing the depth/projected area relationship. The polynomial area function was then

applied to the indentation data to produce a second estimate of instrument compliance. This sequence was re-iterated until a reasonable convergence of instrument compliance and polynomial area function occurred.

Indenter area functions have been produced by direct examination with AFM [167,169], although this method is rather inconvenient and susceptible to AFM calibration errors.

1.5.3.1.3 Material creep

Creep is exhibited by some materials, where plastic deformation does not occur instantaneously. It can be observed most clearly when the load on the indenter is held constant and the depth readings increase, as the indenter slowly sinks into the surface. If this occurs unexpectedly during a nanoindentation experiment then full plasticity may not have occurred when the unloading cycle begins, resulting in apparently high material hardness and interference with the initial unloading stiffness. A specific creep test may be performed at constant load in order to investigate the material under test. If a specimen exhibits creep, a delay can be introduced at maximum load to enable full plasticity to develop prior to unloading. Loading and unloading rates should be carefully chosen to provide enough time for full plasticity to develop. Excessively long tests may expose the experiment to significant thermal drift. Amorphous C coatings generally show only a small degree of material creep. Sanchez-Lopez et al. demonstrated some creep behaviour with hydrogenated a-C films which reduced with reducing H content [170].

1.5.3.1.4 Thermal drift

Nanoindentation equipment is very sensitive to system expansion/contraction as a result of thermal changes. This is interpreted as a change of depth. A degree of thermal isolation is typically designed into the equipment to minimise the problem. A correction for thermal drift is normally made by halting the unloading sequence at a relatively low load (so that interference by any additional material creep is unlikely to occur) and recording depth for a set time period. A thermal drift rate can be derived from the depth/time data and applied to the load-unload depth data.

1.5.3.1.5 Initial penetration depth

The indenter must first make contact with the specimen surface prior to beginning a nanoindentation cycle to provide a datum for depth measurements. This first contact is usually made at a very low load; however some penetration of the indenter into the surface will occur. Therefore all subsequent depth measurements, taken relative to this datum, will have a systematic error equal to the initial penetration depth. A method of extrapolating the initially elastic portion of the load/depth data back to zero load is usually undertaken to estimate the initial penetration depth and then all depth data is offset by this amount.

1.5.3.1.6 Material pile-up and cracking

It is an assumption of the Oliver-Pharr analysis that the surface around the area of contact elastically sinks and the region of contact is at or below the original unstrained surface as shown in Figure 1.15. However, with certain materials, plastic flow at the surface can result in pile-up around the indenter, above the original surface height. The tendency of a material to show pile-up is related to the ratio of elastic modulus to yield stress and also the strain-hardening properties [153]. Bolshakov et al. [171,172] investigated this phenomenon by finite element methods and showed that the Oliver-Pharr analysis can significantly underestimate the true contact area when pile-up is occurring. A convenient, experimentally measurable parameter was shown to offer an indication of a materials tendency to exhibit pile up under indentation [173]. The parameter is the ratio of the final indentation depth h_f to the indentation depth at peak load h_{max}. The amount of pile-up is large only when $h_f{:}h_{max}$ is close to one and the amount of work-hardening is small. When $h_f{:}h_{max} < 0.7$, very little pile-up is found no matter what the work-hardening behaviour of the material is.

It is assumed with any hardness measurement that permanent deformation occurs only as a result of plastic flow. Errors will result in the H and E_r values derived by the Oliver-Pharr method if material cracking occurs, which contributes to a permanent deformation or affects the elastic response of the indenter/surface. When determining area of contacts by optical means, any cracking will be apparent. With nanoindentation, no viewing of the

indentation is normally made, however sudden changes or discontinuities in the depth data can indicate that a crack has occurred. Rabe et al. were able to demonstrate some correlation between discontinuities in the depth data and coating cracking by imaging with a novel SEM compatible nanoindentation device [174]. An example from Rabe et al. of an indentation into TiN/SiN showing both pile-up and cracking is given in Figure 1.18.

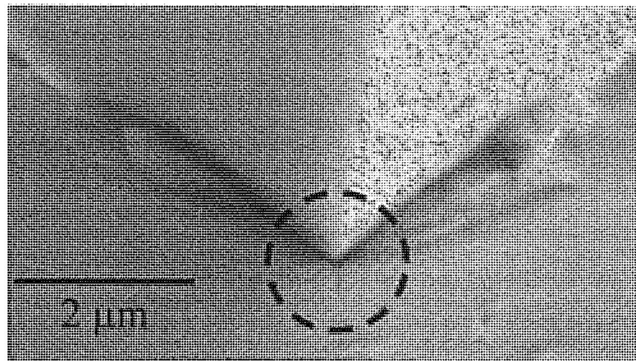

Figure 1.18 SEM micrograph of an indentation into TiN/SiN showing both pile-up and cracking [174].

1.5.3.1.7 Surface roughness

The effect of surface roughness is to reduce the mean contact pressure by increasing the contact radius which, without correction, will reduce the computed E_r and increase H. It is proposed [153] that surface roughness can be quantified by a roughness parameter α where:

Equation 1.18

$$\alpha = \frac{\sigma_s R}{a_0^2}$$

In Equation 1.18 σ_s is approximately equal to the maximum asperity height, R is the indenter radius and a_0 is the contact radius for a smooth surface at the same load. Surface roughness is said to have a significant effect when $\alpha > 0.05$ [153]. It is clear from Equation 1.18 that the roughness parameter increases with increasing surface roughness and with decreasing indenter load/depth, which is the case when testing very thin films. Significant surface roughness is likely to add to the error measurement of replicated tests, due to there being a random distribution of asperity size across the specimen surface. It is

possible that a polishing treatment to reduce the surface roughness may alter the surface structure, induce stresses in the outer layers and/or leave contaminants embedded in the coating.

1.5.3.1.8 Low coating thickness

Nanoindentation is usually used for investigating coating properties, where influence from the substrate must be avoided. To ensure this it is common to restrict indentations to no more than 10% of the film thickness [153,175,176], although there does not appear to be a physical basis for this rule [177]. For specimens with soft, elastic films on hard, stiff substrates the 10% value may be increased and vice versa for hard, stiff films on soft, elastic substrates [178,179,180]. Work has been undertaken to model the changing 'composite' hardness and reduced modulus of a coated system as the substrate influence increases with indentation depth [181]. This is particularly effective when there is a marked difference between the properties of the coating and substrate.

It has been suggested that particular difficulties may arise when working with indentations below about 20 nm due to area function inaccuracies arising from indenter tip rounding [182] and a more detailed definition of the area function below this depth is required [183].

1.5.3.1.9 Indentation size effect (ISE)

Values of hardness and modulus can vary with depth even when performing indentations into a homogeneous isotropic material. There are a large number of possible reasons for this, for example:

The presence of oxide layers with substantially different mechanical properties to the bulk.

An inaccurate determination of the initial contact depth may have occurred; which has a greater relative effect at lower depth.

Errors in the diamond area function.

Changes in coating stress near the surface and/or changes in the degree of material cracking with indentation depth.

ISE can still be seen in some materials even when all other possible reasons are ruled out. It has been proposed that the conditions for plastic flow in these materials depend not only on the strain, but also on the magnitude of any strain gradients present. ISE has been modelled for crystalline materials using the concept of geometrically necessary dislocations [184]. In general, the indentation hardness is observed to increase with decreasing depth for soft strain-hardenable materials but this is not evident with hard, finely structured materials [185].

Reported hardness and modulus results from nanoindentation tests with amorphous C coatings frequently show ISE, however the effect is inconsistent and the mechanism is not clear:

Huang et al. reported results from 2.5 μm DLC coatings on Ti-Al-V alloy which showed rapidly increasing hardness and reduced modulus values with increasing indentation depth, in a range up to 150 nm [186]. This was attributed to: water adsorption on the film surface; elastic deformation of both the tip and surface; and intrinsic errors with the equipment. Lemoine et al. also showed increasing hardness and modulus values with increasing depth to approx. 10 – 20 nm indentation range with 10 – 50 nm a-C:H coatings on Al_2O_3-TiC substrate [187]. A number of the possible causes listed above were mentioned, however the effect was mainly attributed to elastic deformation dominating the low indentation range. Martinez et al. again demonstrated increasing hardness and modulus with increasing depth up to 10 nm indentations with 100 nm a-C coatings on Si and this was also seen with fused silica [188]. No mechanism was proffered.

A contrary response was found in work by Lin et al. with N doped a-C:H films of thickness 50 – 300 nm on Si, which showed a rapidly decreasing hardness and modulus with increasing depth to approximately 60 nm indentations [189]. This trend was also observed to a depth of approximately 20 nm by Bhushan and Koinkar [190] using a range of 5 – 25 nm DLC coatings on magnetic disks and by Beake and Lau [191] up to 50 nm

indentations into a-C coatings of thickness 5 – 80 nm on Si. No mechanism was proffered.

Li et al. [192] reported no ISE down to 10 nm indentations, with 5 – 20 nm DLC coatings on Al_2O_3-TiC substrate.

1.5.3.2 Nanoscratch

Scratch tests have been used for a number of years to provide a measurement of coating/substrate adhesion. Typically, a diamond stylus is drawn across a sample surface under a ramped load until an adhesion failure event occurs. The load to failure is designated as the critical load (L_c) and provides a method of comparing samples.

Nanoindentation systems are commonly adapted for performing nanometer scale scratch tests, which are applicable for thin coatings. A diamond sphero-conical indenter is usually used as the stylus. The detection of critical load can be made with a number of techniques: optical microscopy; dynamic depth measurement; acoustic emission; changes in measured friction. In general, at low load, the nanoscratch is dominated by elastic contact between the stylus and the surface, until the yield stress is reached and plastic deformation occurs. Eventually, a (or possibly multiple) critical load event(s) may occur which can be due to a number of possible failure mechanisms: through-thickness cracking; coating detachment; chipping within the coating; chipping within the substrate [193]. Beake et al. working with TiN/Si_3N_4 coatings on Si were able to identify four distinct critical loads: (i) elastic-to-plastic transition; (ii) first cohesive failure (edge or parallel cracking); (iii) onset of external transverse cracks; (iv) total failure occurring in front of the probe [194].

The measurement of critical load is complicated by its dependence on a number of test parameters such as: scratching speed, loading rate, stylus tip radius, substrate hardness, film thickness, surface roughness and coefficient of friction [153,195]. Consequently, the physical meaning of critical load results is questionable. It has primarily been used as a comparison between films tested under the same conditions.

Park and Kwon [196] working with DLC and WC-Co films showed critical load to increase with increased tip radius and decrease with increased film thickness and scratch speed. An attempt to give physical significance to the results was made by estimating the work of adhesion through stress analysis in the region ahead of the indenter. This showed reasonably constant results irrespective of film thickness or scratch speed. However, Bull and Berasetegui [193] concluded from working with finite element modelling that the stresses around the moving indenter are too complicated to be predicted accurately and therefore the stresses driving coating failure are not predictable. Beake et al. [197] testing Si doped a-C:H on glass, found critical load to be independent of scratching speed, loading rate and increase of load per unit scratch distance (LPUSD) if LPUSD is kept below 1 N/mm. A slight dependence was found with LPUSD in the range 1 – 5 N/mm. In contrast, Lin et al. reported critical load to be dependent upon scratching speed and loading rate with 100 nm N doped a-C:H films on Si, although the dependency diminished at low loading rate/scratching speed [198].

1.5.4 Nanotribological properties

1.5.4.1 General theories of tribology

Tribology can be defined as 'the science and technology of interacting surfaces in relative motion and of related subjects and practices' [199]. The phenomena of friction, wear and the associated chemical and physical changes affecting the surfaces involved is of particular interest. This has been driven primarily by the need to mitigate or control the effects of friction and wear in engineering applications.

1.5.4.1.1 Friction

Friction is the resistance to motion which occurs whenever one surface slides against another. Friction force is the resistive force which acts in a direction opposite to the direction of motion. The friction force which must be overcome to initiate sliding is known as the static friction force and that required to maintain sliding is known as the kinetic friction force. Kinetic friction is usually lower than static friction.

Amontons proposed two laws of friction in 1699 based on experimental observations [200]. The first states that friction is independent of the apparent area of contact between the two surfaces and the second that the friction force is proportional to the normal load between them. Coulomb proposed a third law in 1785 [201] which states that the kinetic friction is almost independent of the sliding speed. These general laws are entirely empirical and no physical laws are violated in situations where the laws are not obeyed. The first two laws are generally well obeyed but deviation from the third is common. Friction force will often show a slight reducing trend with increasing sliding speed [202].

Bowden and Tabor [203] brought the friction laws together with a simple adhesion theory. This model of friction is based on forces of adhesion existing between plastically deformed, 'cold welded', contacting asperities formed between the two sliding surfaces. There will also be a large number of elastic contacts, where the stresses are not sufficient for plastic yield to occur. These points are assumed not to contribute to friction. The friction force F is proportional to the real area of contact between the surfaces A (which is composed of the sum of the individual plastically deformed contact areas) and to the force required to cause shear failure of a unit area of asperity junction s. Therefore:

Equation 1.19

$$F = A.s$$

The real area of contact does not depend on the apparent area of contact when asperity heights are randomly distributed. The real area of contact A is proportional to the load between the surfaces W and inversely proportional the yield pressure of the softer of the two surfaces, which can be approximated to the indentation hardness H such that:

Equation 1.20

$$A = \frac{W}{H}$$

Combining Equation 1.19 and Equation 1.20:

Equation 1.21

$$\mu = \frac{F}{W} = \frac{s}{H} \approx \frac{k}{H}$$

where μ is the coefficient of friction for the combination of two surfaces. For the case of failure in the softer material, we can approximate s as being equal to the critical shear stress of this material k. There are some deficiencies with the simple model. Experimentation shows that real values of μ do not just depend on the properties of the softer material and also tend to be significantly higher than those calculated from values of H and k. A more complex model is required which takes account of other friction contributions. The simple model does however provide a useful tool for making basic analyses of friction systems.

It is clear from the above that susceptibility to plastic deformation is an important parameter of friction. This is reflected by the inverse relationship between μ and H in Equation 1.21. Greenwood and Williamson [204] introduced a plasticity index ψ which is indicative of the degree of plastic deformation for a surface:

Equation 1.22

$$\psi = \left(\frac{E_r}{H}\right) \cdot \left(\frac{\sigma}{\beta}\right)^{0.5}$$

where E_r is the reduced modulus, H is the hardness, β is the asperity radius and σ is the standard deviation of the surface peak height distribution. When the index is greater than 1, surface deformation is largely plastic. When the index is less than 0.6, the deformation is largely elastic. The index is independent of load, as long as the asperities deform independently.

Surface roughness does not appear in the adhesion model of friction, other than indirectly by asperity radius and height distribution contributing to the surface plasticity index. Therefore it can be concluded that friction coefficients are independent of roughness. This is an oversimplification, as very smooth surfaces will tend to show higher friction forces due to the intimate contact raising the real area of contact. Very rough surfaces will

produce an increase of friction force due to the force needed to lift one surface over the roughness of the other. [202].

If a hard surface with a sharp point is slid over a soft surface, it will dig into the soft surface and produce a groove. Extra force is required to create the groove which is not accounted for by the adhesion model of friction. A ploughing term can be introduced to account for this which will be related to the size and shape of the point. For a conical asperity with semi-angle θ the coefficient of friction ploughing term is given by [199]:

Equation 1.23

$$\mu = 2\frac{\cot\theta}{\pi}$$

Other, more subtle, friction contributions need to be considered for a complete model, such as: deformation of asperities during sliding; adhesive force at the asperity contacts; asperity junction growth due to the combined effects of normal and tangential stresses; plastic shear stresses at elastic contact points; effects of work hardening, fatigue of asperities; temperature effects and physical/chemical changes of the materials.

Due to the complex array of mechanisms contributing toward the coefficient of friction value, which are also likely to depend upon the sliding system being investigated, it is often not considered to be an intrinsic material property. Experimental methods are still generally used for determining μ. The methods normally rely upon knowledge of the applied normal load and accurate determination of the total resisting frictional force during a sliding sequence. The value of μ is then calculated from Equation 1.21.

1.5.4.1.2 Wear

Wear is the progressive loss of substance from the operating surface of a body occurring as a result of relative motion at the surface. As with friction, there is no reliable way of predicting wear from knowledge of the two materials and the proposed rubbing conditions. Coefficients of friction for pairs of materials usually fall in the range 0.1 – 1. This is due in part the ratio k/H being fairly constant for most materials (Equation 1.21). Small changes of friction can often be accommodated in engineering systems, resulting in

a slight increase of power consumption. Unlike friction, wear rates can vary over many orders of magnitude and may change catastrophically due to a small change in operating conditions. The mechanism of wear is often divided into separate categories [205]:

(i) Adhesive wear. The theory of adhesive wear has the same basis as the adhesion theory of friction. Material is transferred, normally from the softer to the harder surface, because some of the strongly adhered asperity contacts shear within the softer material rather than at the junction between them. Archard [206] derived a theoretical expression for the adhesive wear rate:

Equation 1.24

$$Q = K.\frac{W}{H}$$

where Q is the total wear volume per unit sliding distance of a surface, W is the load, H is the yield pressure or indentation hardness and K is the wear coefficient of the surface, which expresses the fraction of asperity interactions resulting in the formation of a wear particle. Equation 1.24 is often condensed to:

Equation 1.25

$$Q = CW$$

where the wear constant C can be determined experimentally without measurement of H and is equal to the ratio of K to H.

(ii) Abrasive wear occurs when a soft surface is ploughed by a relatively hard material. This can be two-body abrasive wear, which occurs when a rough hard surface slides against a relatively soft opposing surface or three-body abrasion, where rough hard particles trapped between the two sliding surfaces cause one or both to be abraded. By modelling abrasive wear with the assumption of simple conical indenters, equations of exactly the same form as Equation 1.24 and Equation 1.25 are produced. In this case K represents the fraction of ploughing events resulting in material loss.

(iii) Fatigue wear. During sliding or rolling between surfaces the contacting asperities are exposed to a range of contact stresses due to their height distribution. Truly elastic stresses will cause no damage, while those above the fracture stress of the material will cause the formation of a wear particle. At intermediate stresses, above the fatigue limit but below the fracture stress, the asperity will undergo a single fatigue cycle. Such cycles accumulate, until the formation of a wear particle occurs by local surface fatigue fracture. During the initial stages of a typical sliding process, plastic deformation and hence adhesive wear may dominate, as the highest asperities make contact which have the greatest chance of producing high localised stresses above the material yield stress (again the Greenwood and Williamson analysis is a useful guide to estimating the dominating mode of contact, Equation 1.22). After a period of 'running in', when the asperity height has reduced due to plastic deformation and/or fracture, the contact may move toward a more elastically dominated regime. However, if the elastic deformation produces stresses greater than the fatigue limit in a significant number of asperities, then wear will occur due to fatigue fracture. Again, the equation describing fatigue wear [207,208] takes the form of the Archard model (Equation 1.24), where K can be interpreted as the inverse of the number of fatigue cycles to wear particle generation. H is replaced by a mechanical constant defining the load capacity, but given that in elastic contact most of the asperities are close to their yield stress, this can be approximated to H [199]. Particles thus produced may go on to contribute to three-body wear.

(iv) Corrosive wear. When sliding takes place in a corrosive environment then chemical reactions may take place, producing reaction products at the contact. The resulting products may be more easily removed than the un-reacted surfaces, accelerating the wear rate. The most likely corrosive reactant to be encountered is atmospheric oxygen, although wear-reducing protective oxide films can occur in some systems.

(v) Other minor types of wear: Delamination wear [209,210] describes a fatigue mechanism whereby cyclic loading leads to sub-surface cracking and ultimately the production of plate-like wear particles. Similar to this is fretting wear, when the slid distance is small in comparison to the contact area. Full sliding may occur; it may be limited to just the edge of the contact or there may be no true sliding at all. Wear can be the result of a complex combination of the previous mechanisms discussed.

It can be shown that all forms of wear can be represented by a generic form of the Archard model (Equation 1.24) [199]. In each case, the volume of material worn is proportional to both the slid distance and load and inversely proportional to a mechanical constant defining the load capacity (H in the case of adhesion/abrasion/fatigue). The mechanism of wear in real situations is normally quite complex and will likely contain contributions from many of the mechanisms discussed above, with complicating factors not accounted for in the simple model such as: plasticity index of the surface; the properties of both sliding surfaces; work hardenening; surface microstructure; temperature changes; the design of sliding system and the formation of new species at the contact (tribo-chemistry). As with friction, experimental systems are normally used for determining wear constants. The methods typically involve the use of Equation 1.25 by estimation of the volume of material lost along with knowledge of both the applied load and slid distance. The values thus arrived at are often referred to as 'specific wear rates' and will be within this thesis.

1.5.4.2 The tribology of amorphous C coatings

The effects of friction and wear are routinely controlled or mitigated in machine applications by the use of liquid lubrication. This can be under conditions of boundary lubrication, where a low shear strength coating is produced on the solid surfaces, reducing the force required to separate any contacted asperities. Alternatively, with elastohydrodynamic lubrication, the solid surfaces are completely separated by a thin film of fluid, which is capable of transmitting the normal loads between the surfaces, while allowing sliding to occur in the transverse direction.

There are certain situations that preclude the use of liquid lubrication. For example: when extreme temperature changes occur that may degrade the lubricant; where cleanliness is essential or conversely in corrosive environments that are damaging to the fluid and when the lubricated mechanism is inaccessible after assembly. More significantly for MEMS and micro- / nano-engineering systems, the use of fluidic lubrication methods can be disadvantageous to movement, due to the low shear stresses generated by the devices and the relatively high capillary forces formed by the liquid, as discussed in section 1.2.1.

A key solution is the use of solid lubricants. The mechanism is similar to the use of liquid lubrication in that the surfaces are completely separated, even under high normal load, while sliding is ameliorated by using a material with low shear strength. Graphite can provide this type of lubrication. Graphite readily forms a strongly-adhered transfer film on the opposing sliding surface, so that after a short period of 'running in' movement is between two lubricating surfaces. It is thought that the low shear strength between the parallel atomic sheets is an important contribution to lubrication. However, atmospheric condensable vapours are required or graphite will wear quite rapidly. The vapour is believed to saturate any dangling bonds formed as new surfaces appear under shearing action, thus stopping strong adhesion between neighbouring unsaturated C atoms [211]. The effectiveness of the condensable vapour seems to depend upon the molecular size, with water vapour and long-chain hydrocarbons providing a significant effect in contrast to single atoms such as N [199].

Related to solid lubrication is the use of hard coatings. It can be seen from Equation 1.21 and Equation 1.24 that there is an inverse relationship between both friction and wear and surface hardness. That is, friction and wear will generally reduce as the interaction between the sliding surfaces becomes dominated more by an elastic contact. The plasticity index (Equation 1.22) shows that an elastic regime is favoured as the ratio H/E increases. Consequently, use has been made of coatings with very high hardnesses for certain mechanical applications. However, hardness is often associated with brittleness and low impact strength, so a balance may need to be struck between competing properties.

There has been a keen interest in the use of a-C:H and a-C coatings for tribological applications as the films can address both of the points raised above: i.e. production of a lubricating graphite-like transfer film whilst providing diamond-like load support. Tribological coatings based on a-C:H and a-C have been used for a number of applications such as: magnetic storage read-write heads, razor blades and engine parts [212]. Film thicknesses with magnetic heads are normally just a few nm but for applications involving significant sliding contact a few μm is common.

A large amount of research has been undertaken to study the tribology of a-C:H and a-C coatings. This is usually performed with a pin-on-disk (POD) tribometer. The POD test involves engaging a hard spherical counter body (with a diameter of several mm) against the test coating at a controlled position from the centre of rotation and applying a controlled load of a few N or tens of N. The sample is then rotated at a controlled rate and the friction force at the pin is monitored with a transducer. Wear rates are determined by approximating the material loss in the worn groove.

Friction coefficients of a-C:H films are typically found in the range 0.01 to > 0.5 depending on the nature of the film and the conditions of test [213]. Reported wear constants span a range of many orders of magnitude, with the lower values typically around 10^{-16} $m^3N^{-1}m^{-1}$ [213,214,215]. The wide range of results reflects the numerous variables that contribute to an experiment for the determination of friction and wear. These include the mechanical, physical and chemical properties of the coating (which are ultimately governed by the coating parameters) and the tribological test conditions. Rarely are all of these variables reported, due to the large number, which makes generalised correlations to tribological properties difficult [213].

The primary controlling influence on the tribology of a-C:H is generally attributed to the formation of a transfer film and accompanying tribo-chemical effects [213,216,217]. The transfer film has been reported as having a graphite-like and/or disordered graphitic structure [217,218,219] and the presence of hydrocarbon macromolecules has also been shown [220]. It is thought that the transfer film behaves as a low shear strength lubricant operating between the opposing surfaces [213,221]. The conditions of tribology testing, such as load and velocity, can significantly alter the properties of the transfer film [212], thus affecting the tribology results. Work by Ronkainen et al. [222] showed the friction coefficient between DLC and steel or alumina pins to decrease with increasing load and speed, in opposition to the standard models of friction and wear. The environmental conditions can also affect the transfer film and hence the tribological results. The friction coefficient of a-C:H is low in humid air or nitrogen and very low in dry nitrogen or UHV as long as there is sufficient H present [223,224225]. The role of H is attributed to the passivation of any dangling bonds at the sliding interface. Donnet and Grill [224] have shown higher friction coefficients with hard, low H containing DLC coatings compared

with softer, high H content films under conditions of UHV, in opposition to the standard models of friction and wear.

The tribological mechanism of a-C coatings is generally considered to be similar to that of a-C:H. The formation of a graphitised transfer film is the primary control of tribology, but there is a greater sensitivity to the absence of condensable vapours, due to there being no H to passivate any dangling bonds. An increase of friction coefficient has been reported when moving from ambient to UHV conditions [226,227]. The tribology of sputtered a-C coatings has not been studied as widely as a-C:H but reports have shown films of a-C and doped a-C to have excellent tribological properties [228,229,230].

The work reported in this thesis involves variations of Graphit-IC™ [104,228] which is a Cr doped a-C sputter coating developed by Teer Coatings Ltd. The standard coating includes a thin Cr adhesion layer between the substrate and main coating which improves adhesion to metallic surfaces [61,228]. The change from adhesion layer to main coating is produced as a graded change, so that no definite boundary is created which could act as a plane of adhesion failure [228]. The coating is reported to have an amorphous structure [231]. Low wear and friction has been reported for this coating under POD testing with typical wear constants and coefficients of friction quoted around 10^{-18} to 10^{-16} $m^3N^{-1}m^{-1}$ and 0.08 to 0.16 respectively [228,231]. Camino et al. [228] reported with POD testing that wear rate increased with increasing load, consistent with the Archard wear model. A repeated set of tests under different conditions showed little change of specific wear rate with load. Coefficient of friction was reported to fall at high load, deviating from the Bowden and Tabor model of friction. Work by Yang et al. [231] to investigate the effect of certain coating parameters using POD testing showed a falling and then rising response of both wear rate and friction coefficient to increasing hardness. Friction coefficient was shown to decrease with applied load but wear rate exhibited a complex effect. Wear rate was shown to increase with increasing sliding speed whilst the friction coefficient decreased. Additional work by Yang and Teer [232] to review the effect of increasing Cr concentration using POD testing revealed a response similar to that reported previously for hardness. Therefore an intermediate level of Cr doping was shown to provide beneficial tribological properties and an optimum doping level was found. Friction coefficient was again shown to decrease with applied load. Wear rate was little affected

by applied load when Cr was present but was significantly affected in the absence of Cr. Further work by Yang et al. [233] reported a falling coefficient of friction during the early stages of the POD test which was attributed to the development of a transfer film and this was confirmed to be present on the counter-body. Re-orientation of the outer surface of the coating under rubbing action and the development of a transfer film were proposed as the primary controls of the coating tribology.

1.5.4.3 The nanotribology of amorphous C coatings

The use of POD testing has proved to be a valuable tool in the development of amorphous C coatings under conditions relevant to macro- and micro-scale tribological applications, where loads of tens of Newtons, contact areas of many μm^2 or mm^2, distances of several m and wear depths of μm scale are considered. This has also provided fundamental knowledge of the tribology of such systems, as discussed in the previous section. When considering MEMS and micro- / nano-scale engineering, it is important for fundamental research and coating development to be undertaken under conditions of nanotribology relevant to the potential applications (summarised in Table 1.1). In this case the macro- / micro-scale testing regime may not be appropriate [234]. As discussed in section 1.2.1, when the scale of mechanical devices is reduced so the relative effects of the fundamental forces alter, which means that new design rules have to be considered. It follows that as the scale is reduced so the tribological behaviour may change, demanding a fresh consideration of the effects of: the applied mechanical conditions (loads, displacements, speeds etc.); material properties (hardness, elastic modulus, roughness etc.); and environmental conditions (temperature, humidity, atmospheric composition etc.) upon the nanotribology.

Extensive use of AFM has been made for nanotribological investigations. Sundararajan and Bhushan [235] used a sharp pyramidal diamond indenter attached to an AFM cantilever to produce multiple linear nano-scale scratches in a series of thin DLC coatings. Coefficients of friction were calculated indirectly from surface height measurements at low load, along with knowledge of the indenter geometry. Wear was estimated from the scratch depths. Coefficients of friction were reported in the range 0.02 – 0.08 and wear depths typically 2 – 25 nm after 30 cycles. It was concluded that the

load-bearing capacity of the films diminished with reducing thickness. Friction and wear were shown to increase with decreasing film thickness. This work was extended to two dimensional 'wear maps' by Bhushan and Koinkar [190] and then by Tambe and Bhushan [236] with Si_3N_4 AFM tips. The range of reported coefficients of friction was approximately 0.1 – 0.8 and wear depths 20 to 80 nm after 30 cycles. The earlier work suggested a trend of reducing wear rate with lower thickness DLC films. In the later work, friction force was shown to fall at high tip velocity. Qualitative wear investigations were interpreted as showing a dependency on tip load, tip velocity and the number of sliding cycles. It was speculated that a graphitised layer was formed during high load sliding cycles. Martinez et al. [188] used an AFM with a pyramidal diamond tip to produce nano-scale linear scratches on a-C coatings. Wear was estimated from the depth of the wear scars. Typical depths were in range 2 – 10 nm after 100 cycles. Wear rate was shown to increase with applied load and number of sliding cycles and decrease with increasing coating hardness. A similar protocol was adopted by Tsuchitani et al. [237] and again it was reported that wear rate increased with applied load and number of sliding cycles. Wear rate was also shown to increase with both humidity and scan speed. Typical wear depths were 0.3 – 0.8 nm after 20 cycles. A study by Wei and Komvopoulos [238] with DLC films between 5 and 25 nm thickness reported enhanced wear resistance with increasing DLC film thickness and hardness.

The nanoscratch facility of a nanoindentation unit has been used for nanotribology research. Beake and Lau [191] used the nanoscratch technique to report values of friction coefficient in the range 0.1 – 0.3 with a-C films of thickness 5 – 80 nm. Thicker films were shown to provide a greater load support. Lin et al. [198] used a single nanoscratching sequence with N containing a-C:H coatings and estimated wear volume by topographical scans of the scars. Typical wear volumes of between 0.001 and 100 μm^2 were reported. Wear rates were shown to increase with film thickness and applied load and decrease with scan velocity. Wear rate also decreased with increasing hardness and modulus.

There are a number of difficulties with the use of AFM and nanoscratch work when investigating nanotribology relevant to MEMS-type systems, notably: the slow scanning speed compared with the sliding speed of many potential MEMS; the high contact

pressures produced due to a (almost) single asperity contact; and the difficulty of relating single asperity results to larger contact situations containing arrays of asperities moving together, complicated by factors such as adhesive/abrasive material transfer, fatigue events, heat formation and corrosion. Estimations of mean contact pressure for the work reported above fall in the range of 2 – 30 GPa and the wear scars were formed with just a few tens of sliding cycles. It is clear that the mode of wear under AFM/nanoscratch testing is dominated by high pressure (almost) single asperity interactions producing predominantly ploughing and plastic deformation. This fundamental work provides an insight into tribological processes operative at all scales, since all tribo-interactions involve a combination of many single asperity interactions. However it is unlikely that a complete understanding of the wear behaviour of materials relevant to MEMS-type systems can be derived from this fundamental work.

Some researchers have gone some way to address this by the use of a low load sliding-reciprocating tribometer. Gupta and Bhushan and others [192,239,240] performed a series of tests on a range of DLC coatings with a 3 mm sapphire ball oscillated at 0.1 Hz, using a stroke length between 2 and 7 mm and an applied load between 10 and 200 mN. Frictional forces were measured with an attached strain gauge and wear was estimated qualitatively by optical examination of the wear scar. Coefficients of friction were typically reported in the range 0.2 – 0.6. Particles of wear debris were observed. It was concluded that the amount and size of debris was independent of coating thickness. Huang et al. [186] tested a series of DLC coatings with an oscillated 10 mm Al_2O_3 ball at 10 Hz, 1 N and 100 μm stroke length. Coefficients of friction were reported between 0.05 and 1.0. Increased humidity produced a decreased coefficient of friction. Achanta et al. [234] reported the use of a micro-tribometer with a DLC coating. A Si_3N_4 ball of diameter 5 mm oscillated at 0.2 Hz was used as the counter body. Loads between 100 and 200 mN were applied over a stroke length of between 300 and 400 μm for 1000 – 5000 cycles. Coefficients of friction were reported in the range 0.08 – 0.10. The resulting wear scars were examined by AFM. The surface roughness was shown to reduce in the wear scar due to the inter-asperity spaces being filled by wear material. A small amount of wear debris was observed outside the wear track. Following ultrasonic cleaning the wear debris was

removed and the wear scar showed only slight flattening of the asperities. No measurable wear was produced.

Estimations of the mean contact pressure and mean contact radius for the above reported work are in the ranges: 200 – 500 MPa and 4 – 11 μm respectively. These test conditions are more relevant to MEMS-type systems than the reported AFM and nanostratch work (Table 1.1). However the information currently available, particularly for wear, is quite limited. There has been little quantified wear data published due to the difficulty of measuring such small volume losses.

A testing technique which is guaranteed to provide conditions relevant to MEMS is to use a MEMS device as the nanotribometer. Lim et al. [241] were one of the first to produce a MEMS device specifically designed to measure friction between polysilicon surfaces. It was based on an electrostatically driven comb-drive. It was concluded that as the applied load was reduced the friction coefficient remained higher than in a macroscopic system, due to a significant adhesion contribution to the applied load. Senft and Dugger [242] were the first to develop a device to measure continuous kinetic friction between MEMS sidewall contacts (Figure 1.19). The device is controlled by electrostatic actuators and measurements are indirectly made by capturing images of the movement portion of the device. 230 MPa was estimated as the contact pressure at the contacts with this device [42]. Results suggest that the tribology of these types of devices is influenced by environmental conditions (such as humidity) and a combined contact pressure-velocity parameter [11,42]. An 'inchworm' nanotractor device was reported by de Boer et al. [243] for both friction and wear measurements (Figure 1.20). The motion of the nanotractor was achieved by sequentially actuating and releasing a central driving plate while clamps on each side of the plate are alternately held in place using electrostatic potentials. Friction was estimated by reducing the clamping force until slipping events occurred and wear was assessed by examining wear scars with AFM and determining the number of 'steps' to device failure.

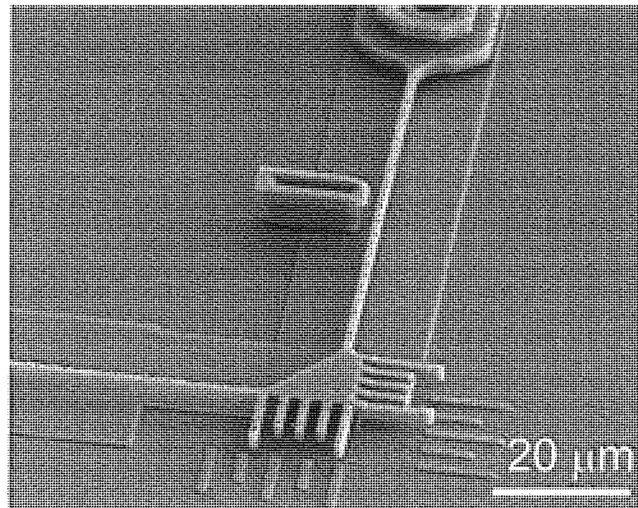

Figure 1.19 Side-wall tribometer. Electrostatic actuators pull the suspended beam into contact with the centre post while a second set oscillates the beam back and forth [11].

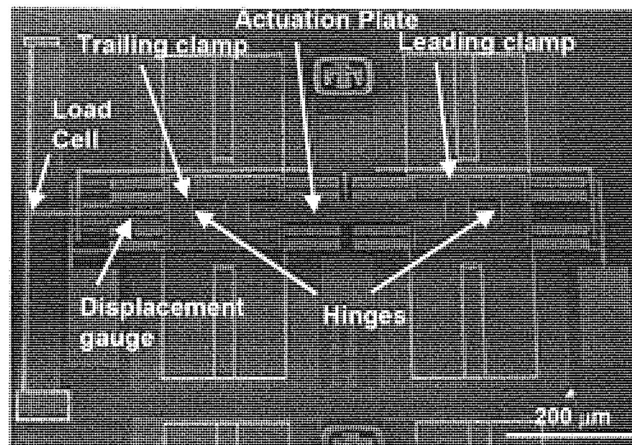

Figure 1.20 The 'inchworm' nanotractor device [11].

Although the applicability of nanotribological testing with real MEMS devices is without question, there are some significant problems. The MEMS test devices require specialised manufacturing and control technology, therefore the availability is mainly limited to organisations specialising in MEMS production. The design of the systems are such that the test conditions can be varied, however the tribology is likely to be significantly influenced by the intrinsic conditions arising as a result of the mode of movement. The use of real MEMS systems may prove to be prohibitively expensive, in terms of time and resources, when attempting to test and compare the tribology of a large array of surface treatments; particularly when considering that wear measurements usually involve

destroying the device. This probably explains the relatively limited work so far in this area and the fact that minimal results for amorphous C coatings have been reported. There is clearly a requirement for simple nanotribological testing relevant to MEMS that is analogous to the macro- / micro-scale POD test; one that allows surfaces to be tested and results analysed relatively quickly and test conditions to be easily altered and span the range of interest. This would allow fundamental nanotribology to be investigated, as well as providing a procedure for coating development and optimisation.

1.6 Summary of the programme of research

The aims of this project were two-fold: Firstly, to develop a suite of testing protocols capable of providing fundamental information about ultra thin a-C films (to 10 nm thickness) suitable for nanotribological situations. An assessment was made of some of the techniques available for testing relevant properties of thin films. The purpose was to identify the reliability of the techniques and where appropriate to develop the technique to meet the needs of the project. Three aspects of thin film testing were investigated: (i) the use of XPS C 1s peak analysis for determining the proportion of sp^3/sp^2 C bonding in a-C and Cr doped a-C coatings (ii) the use of nanoindentation to measure H and E_r with ultra low thickness films and (iii) the development of a rapid nano-scale wear system with capability relevant to MEMS and micro- / nano-scale engineering systems.

The second aim of the project was to apply the optimised test methods to a series of SIP a-C and Cr doped a-C coatings in order to: (i) investigate the effect of thickness on the properties of coatings/coating process (ii) investigate fundamental tribology at the nano-scale and (iii) provide a starting point for nanotribological coating optimisation at ultra low thickness, from (i) and (ii). This was achieved using arrays of a-C coatings produced at thickness: 1-3 μm, 150 nm, 50 nm, 20 nm and 10 nm from an industrial CFUBMSIP production process at Teer Coatings Ltd. DOE was extensively used for this part of the project work as it provides an efficient methodology for understanding the effects and interactions of variables in a complex industrial process that may be affected to some degree by uncontrolled external influences. It was also important to consider whether the DOE procedure was capable of providing useful information when working with the demanding requirements of ultra thin coatings (150 - 10 nm).

2 Experimental

2.1 Test Materials

2.1.1 Substrates and pre-coating preparation

All coating tests were performed using Si wafer substrates. The wafers were sourced from Compart Technology Ltd, with specification: 150 mm diameter, single-side polished, single side etched, <100> orientation, 0.645 mm thickness. A mixture of both n/Phosphorous and p/Boron doped wafers were used.

The Si wafers were cut to approximate 10 – 20 mm square pieces prior to coating. Each test piece was cleaned firstly by rinsing with acetone and then by immersion in an ultrasonically agitated hot proprietary aqueous cleaning solution. The wafers were then thoroughly rinsed with de-ionised water and dried by evaporation in a warm air flow. Finally the wafers were inserted into the test chamber without delay.

2.1.2 Coating process

2.1.2.1 Equipment

All test films were produced at Teer Coatings Ltd in a Teer Coatings UDP 650 FOD closed field unbalanced magnetron sputter ion plating coating system [52,66]. A schematic diagram of the chamber arrangement is given in Figure 2.1.

The cylindrical chamber was connected to a diffusion pumping system to maintain reduced pressure. Ar gas was supplied to the chamber from a compressed gas cylinder via a flow control unit. Chamber pressure was continuously monitored with a Penning gauge. The usual method of controlling the chamber pressure was to adjust the Ar flow rate while maintaining a constant diffusion pump rate. The chamber and coating process was controlled by computer using bespoke software which also provided a method of continuous chamber monitoring.

Four water-cooled magnetrons were used in a closed field arrangement. Two of the targets were made of copper backed graphite and two were made of Cr and the arrangement was such that like materials were in opposite facing positions. The test coded P1S3 (test identification will be given in section 2.3) was coated with all four magnetrons active. All other tests were performed with both of the graphite and just one Cr magnetron active. The magnetrons were powered by Advanced Energy Pinnacle DC electrical supplies such that a specific current could be selected for each magnetron and maintained for the duration of the coating process. The targets used for coating preparation were standard 'production' targets that had been used for previous coating work. The same targets were used for one experimental run but these may have been changed between experimental runs. Targets with similar and moderate surface wear were chosen for all experiments.

The Si samples to be coated were fixed to a rotating support at the centre of the chamber. The rotation rate could be varied but was set at 5 revolutions per minute for all tests (this was checked by a stopwatch). A similar location on the support was used for all tests to maintain a constant target-substrate distance of approximately 160 mm. These are the standard conditions for the Teer Coatings Ltd Graphit-IC™ process [104] which produces a hard, dense, uniform, amorphous structure [68,231]. The starting position of rotation was the same for each test. This meant that for a given thickness each sample will have experienced the same number of C and Cr target passes. Unipolar pulsed negative substrate biasing was used for all tests with an Advanced Energy Pinnacle Plus pulsed electrical power supply. The pulse system supplies nominally square pulses of negative substrate biasing with a 0 V off-time between the pulses. The magnitude of the voltage pulses is varied as a time averaged voltage value [95] and all values quoted in this work refer to the time averaged voltage unless otherwise stated. The frequency of the pulses and the duration of the off-time (referred to as pulse width) can also be varied. The pulse system has a minimum duty factor of 50% which means that the off-time must be less than or equal to the duration of the voltage pulse [95]. This further means that for a given pulse width setting, the full frequency range may not be available and vice versa. High and low values of average voltage, frequency and pulse width were chosen such that within these ranges the three factors can be independently varied, which is required for a

DOE treatment and is useful for any subsequent optimization procedure. In order to maintain a constant time averaged pulse voltage at different frequency and pulse width settings, the magnitude of the pulses must vary with frequency and pulse width. Table 2.4 includes calculations of the peak voltage to maintain the time averaged bias voltage which indicates that the magnitude of the pulses must increase as frequency and pulse width increase.

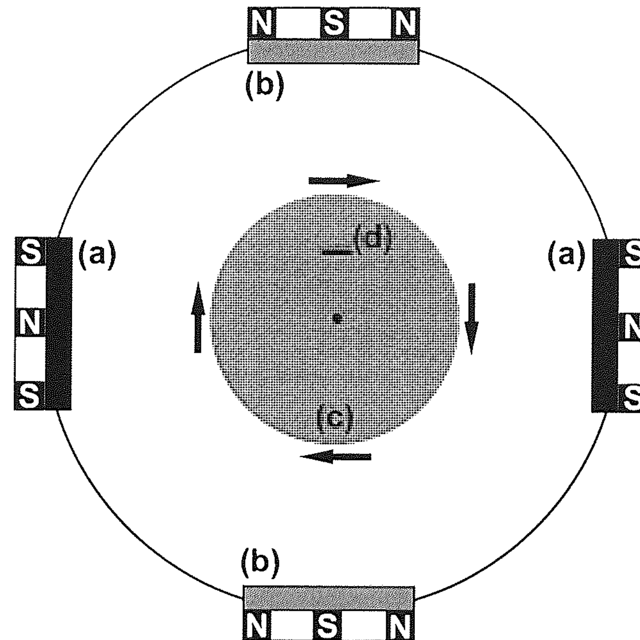

Figure 2.1 Schematic diagram of the CFUBMSIP chamber arrangement showing (a) graphite targets (b) Cr targets (c) rotating support (d) location of specimen.

2.1.2.2 Coating procedure

(i) Target/support cleaning.

Prior to inserting the substrate into the coating chamber, the targets and rotating support were sputter cleaned. This was performed as a separate operation as there were no shutters in the system to protect the substrate. This was accomplished by closing the chamber, pumping down to a starting pressure of 4.0 x 10^{-5} mbar and then applying the Ar gas flow. A high cathodic voltage was applied to the magnetrons which produced a plasma and sputtered the surface of the targets with a high rate of material removal. In addition a high cathodic voltage was initially applied to the support to produce sputter cleaning of the surface.

(ii) Si sample loaded.

The chamber was brought to atmospheric pressure and the pre-cleaned Si substrates were attached to the support such that the polished surface was used as the test surface. In most cases, along with the main test pieces, a further Si substrate was inserted which had been half covered with a Kapton (polyimide) based masking tape with good thermal tolerance. This was used for coating thickness determination.

(iii) Ion cleaning.

The chamber was closed and pumped down to the starting pressure of 4.0 x 10^{-5} mbar and then the Ar flow was introduced. A low sputter current of 0.3 and 0.2 A was established on the Cr and C magnetrons respectively. A high cathodic pulsed bias of -450 V was applied to the substrate with a frequency of 250 kHz and pulse width of 500 ns. This promotes a large degree of ion bombardment at the substrate resulting in sputtering of the Si surface. This has the effect of cleaning the substrate and promoting adhesion of the subsequent coating layers [244]. The duration of the ion cleaning stage was 30 minutes.

(iv) Adhesion/ramp layer.

For those tests involving no adhesion/ramp layer, stage (iv) was omitted. For all others, a sputter current of 4 A was established on one Cr magnetron (in current controlled mode), with all others at zero. The cathodic pulsed bias voltage, frequency and pulse width were set to -120 V, 250 kHz and 500 ns respectively. This produced a Cr adhesion layer on the Si surface with relatively high (negative) bias voltage to encourage a degree of Cr penetration and mixing into the Si surface for improved adhesion. The duration of this stage was adjusted to produce a Cr layer that was approximately 3% of the total coating thickness. At the end of the adhesion layer stage, all pulsed bias parameters were abruptly adjusted to the desired test conditions (as given in the section 2.3). The sputter currents on the magnetrons were then ramped to the desired currents for the test (as given in the section 2.3). The duration of the ramp stage was such that the total thickness of the adhesion/ramp layers was approximately 10% of the total coating thickness.

(v) Main coating.

The conditions for each test are detailed in section 2.3. All magnetrons were run in current controlled mode. The nominal coating thickness was achieved by adjustment of the coating duration. Some initial thickness tests were run in order to optimise the coating duration prior to the main experiments. At the end of the coating stage the magnetron sputter currents and bias voltage were abruptly reduced to zero. The Ar flow and pumping was stopped and the chamber was brought to atmospheric pressure.

(vi) Removal, storage and preparation for thin film testing.

The coated samples were removed from the chamber and individually wrapped in Al foil prior to storage in plastic grip-seal bags. No attempt was made to protect them from the ambient atmosphere. Prior to thin film testing, the coated samples were scored with a diamond cutter and broken into smaller parts using clean vinyl gloves. All effort was made to avoid any contact with the coated surfaces.

2.1.2.3 Coating process control parameters

In order to have the capability to optimise a thin coating for a particular tribological application, an understanding of the available process controls is required. For this reason a review of the coating process was made at Teer Coatings Ltd in order to identify the independent process control variables (those which are under the control of a process operator, albeit with possible difficulty) and the dependent process control variables (those which vary as a result of the independent variables and are therefore not under the direct control of an operator). A list of the identified variables is given in Table 2.1.

Table 2.1 Identified independent and dependent process control variables.

INDEPENDENT VARIABLES	DEPENDENT VARIABLES
• **Magnetron currents.**	• Target voltages.
• **Substrate bias voltage.**	• Substrate ion current density.
• **Substrate bias frequency.**	• Chamber running pressure.
• **Substrate bias pulse width.**	• Substrate temperature.
• **Argon flow.**	• Water vapour concentration.
• **Adhesion layer time.**	• Adhesion layer thickness/mass.
• **Coating layer time.**	• Ramp layer thickness/mass.
• Carrier gas type.	• Coating layer thickness/mass.
• Chamber design.	• Adhesion layer composition.
• Rotation mode.	• Ramp layer composition.
• Rotation rate.	• Coating layer composition.
• Target-substrate distance.	• Ar plasma energy.
• Level of target wear.	• Coating atom energy.
• Chamber-floor cooling.	• Density of coating vapour clusters.
• Chamber starting pressure.	• Size of coating clusters.
• Magnetron magnetic strength.	• Deposition rate.
• Magnetron degree of unbalance.	• Plasma temperature.
• Magnetron magnetic geometry.	• Quantity of sputtered +ve ions.
• Target crystal grain size/orientation.	• Energy of sputtered +ve ions.
	• Quantity of sputtered –ve ions.
	• Energy of sputtered –ve ions.
	• Power going to substrate.
	• Distribution of angles of incoming species.
	• Ion/atom ratio at substrate.

The key control parameters were chosen for investigation following the process review and a review of the Graphit-IC^{TM} expertise available at Teer Coatings Ltd. The variables selected are marked in bold. The parameters were chosen such that they could be readily controlled in the standard coating system design and were known to play a significant role with tribologically important coating properties. The Cr target current controls the amount of co-deposited dopant which has been shown to significantly influence the tribological properties at the micro- macro-scale [232]. Substrate bias voltage and frequency have also been shown to influence the coating tribology [231]. Bias pulse width has been shown to significantly affect the coating system [95]. The flow-rate of Ar into the chamber is a readily governable factor which regulates the chamber pressure. Although other factors will contribute to the pressure such as: outgassing from materials in the chamber and the pumping effect of depositing atoms trapping gases on the chamber walls. The potentially significant effects of chamber pressure on the coating process and hence the properties of the depositing film have been discussed in section 1.3.2. The use of an adhesion layer is

frequently made for improved coating attachment at thicknesses of µm scale. This is achieved by providing a transition in elastic modulus and displacing any peak shear stresses away from the substrate-coating interface. It is interesting to investigate this importance with reduced thickness. The other independent variables were either not easily controllable, would have required a significant re-design of the system or were believed to have less influence on tribologically important coating properties. They were recognised as a potential source of noise and were held as constant as possible.

2.2 Low wear / low friction thin film analysis techniques

2.2.1 Chemical composition and structure

2.2.1.1 X-ray photoelectron spectroscopy (XPS)

During the early stages of the project, XPS work was performed with a VG Scientific ESCALAB 200D spectrometer equipped with a hemispherical electron energy analyser and Al Kα X-ray source. The analysed area was approximately 2 x 3 mm for each sample and the base pressure was less than 5×10^{-9} mbar. The generated data was analysed using Eclipse Datasystem software version 2.0. During the latter stages of the project, XPS work was performed with a Thermo Electron Corporation ESCALAB 250 spectrometer equipped with a hemispherical electron energy analyser and monochromated X-ray source. The analysed area was approximately 1 x 1 mm for each sample and the base pressure was less than 5×10^{-10} mbar. The generated data was analysed using Avantage software version 3.19. The specific equipment settings used for each experiment are given in section 2.3.

A sample piece was cut from the coated Si wafer and this was attached to a sample stub with conductive fixing tape suitable for UHV conditions. A wide scan spectrum was first produced and each spectral peak was identified. Multiple narrow scans were then produced for each peak present, a Shirley background was removed and relative atomic concentrations were quantified with the respective software and the Schofield library of elemental sensitivity factors.

Where specified in section 2.3, ARXPS was used, by adjusting the angle of the sample relative to the electron detector such that measurements were made at the following angles (between the line normal to the sample surface and the detector): 0, 15, 30, 45 and 60°. The other XPS conditions were maintained at the values specified above.

Where specified in section 2.3, computer controlled depth profiling was used such that the sample surface was etched by Ar^+ bombardment for a set period of time and then stopped, during which time the multiple narrow scans were produced. Etch times were chosen and the above process was repeated until the full coating thickness was tested.

2.2.1.1.1 Experiment to investigate the use of XPS for the determination of sp^3/sp^2 bonding ratio in a-C

A discussion of the use of XPS to determine sp^3/sp^2 bonding ratio in a-C films has been given in section 1.5.1.1.1 with particular emphasis on the analysis of C 1s peaks and differentiated XAES spectra. Both of these methods were applied to the XPS spectra produced from coatings coded: P1S1, P1S2 and P1S3 with the Eclipse Datasystem software.

An investigation into the reliability of the methods was undertaken from ESCALAB 200D and ESCALAB 250 XPS data, collected from some of the coatings listed in section 2.3 along with graphite, diamond and data that had been previously collected from a range of a-C coatings. The coatings in this group were a mixture of hydrogenated and non-hydrogenated a-C coatings prepared by C sputter deposition, butane based CVD and acetylene based CVD.

2.2.1.2 Auger electron spectroscopy (AES)

Auger electron spectroscopy was undertaken with a Thermo Electron Corporation Microlab 350 unit equipped with a hemispherical electron energy analyser. The electron beam energy and current was 10 keV and 1 nA respectively. The analyser was set to a constant retard ratio of 10; step size of 1 eV and dwell time of 50 ms. The base pressure was less than 5×10^{-9} mbar. The collected data was analysed using Avantage software version 3.19.

2.2.2 Physical properties

2.2.2.1 Optical microscopy

An Olympus BH optical microscope fitted with 10x, 25x, 40x and 65x objectives and a 10x eyepiece was used to investigate the surface of the coatings and wear scars. The microscope was equipped with a Nikon Coolpix 4500 digital camera and this was used to produce all optical microscopy images. A graticule with a 1 mm scale subdivided into 10 μm divisions was used for the measurement of feature sizes.

2.2.2.2 Atomic force microscopy

A ThermoMicroscopes Autoprobe M5 atomic force microscope run in contact mode and fitted with Ultralever ULCT-AUMT-AB Au coated SiN probes was used extensively throughout this project to: characterise the surface roughness of the coatings (Ra); map nano-indents and map wear scars. The collected data was analysed using ThermoMicroscopes ProScan software (version 2.1). The size of scan area was set according to the feature of interest and this information along with any particular sample treatment is given in section 2.3.

2.2.2.3 Scanning electron microscopy

Scanning electron microscopy was undertaken with a Thermo Electron Corporation Microlab 350 unit equipped with a hemispherical electron energy analyser. The electron beam energy and current was 10 keV and 1 nA respectively. The analyser was set to a constant retard ratio of 10; step size of 1 eV and dwell time of 50 ms. The base pressure was less than 5×10^{-9} mbar. The collected image data was analysed using Avantage software version 3.19.

2.2.2.4 Profilometry

A Taylor-Hobson Talystep 223-27 profilometer was used for coating thickness measurements. Along with the main test pieces, a further Si substrate was inserted into the coating chamber which had been half covered with a polymer based masking tape. The masking tape was removed and the sample was levelled on the profilometer platform.

Coating thickness measurements were made by multiple profile passes across the step in the film formed by the masking tape.

2.2.3 Mechanical properties

2.2.3.1 Nanoindentation

All coating hardness and reduced modulus measurements were made with a NanoTest nanoindentation unit manufactured by Micro Materials Ltd and operated in 'indentation mode'.

The fundamental operation of the NanoTest unit is depicted in Figure 2.1 and is based around a vertically oriented pendulum which is free to rotate about a frictionless pivot. Forces are generated by applying a carefully controlled current to a coil and magnet arrangement, of which the coil is attached to the top of the pendulum. The resulting load is applied to the sample under test via an inter-changeable probe attached to the pendulum. The sample is located at the test probe be means of three DC motors driving micrometer stages set in an xyz configuration. Displacements of the probe into the sample surface are detected with a parallel plate capacitor, one plate of which is attached to the probe holder. The capacitor forms part of a balanced AC bridge circuit which is sensitive to small changes in plate separation. The limit stop defines the maximum outward movement of the pendulum. The equilibrium position of the pendulum, with zero load current, is adjusted with a movable balance weight.

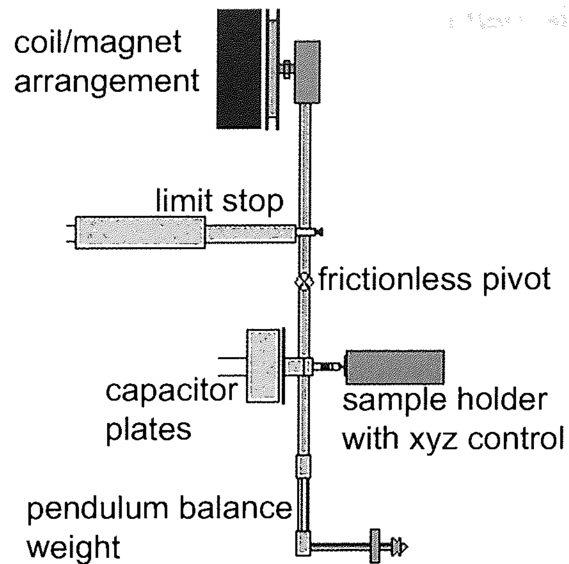

Figure 2.2 Diagram of the basic operation of the NanoTest nanoindentation unit.

Suitably sized coated samples were cut and attached to the sample holder by means of a cyanoacrylate adhesive. A Berkovich diamond indenter was inserted into the probe holder. The pendulum was balanced with adjustments to the movable weight, the capacitive bridge circuit was brought to balance by means of an adjustable circuit element and the sample holder was aligned with the indenter probe. Finally the system temperature was allowed to stabilise before the automated indentation sequence was initiated with the NanoTest software. Multiple tests were performed on each coating. The specific experimental settings are given in section 2.3. The resulting data was analysed with the NanoTest software using the Oliver-Pharr method in order to determine hardness and reduced modulus values. The potential errors discussed in section 1.5.3.1 and particular issues relevant to the NanoTest system were addressed as follows:

2.2.3.1.1 Instrument compliance

The instrument compliance was determined and checked at regular intervals during this project. There is a standard function available for this within the NanoTest software. The method involves making multiple deep indentations, at a relatively high load of 100 mN, into a fused silica calibration standard (which has a known compliance) using a Berkovich indenter with a well defined diamond area function (see below). The

instrument compliance is derived by subtracting the known fused silica compliance from the measured compliance.

2.2.3.1.2 Indenter geometry

The diamond area function for the indenter used in this work was produced indirectly by making a series of indentations into a standard fused silica sample. There is a standard procedure built into the NanoTest software for accomplishing this which is similar to the Oliver-Pharr iterative method. A total of 235 indentations were made covering a range of maximum indentation depths from 9 to 260 nm, with the majority of data points at very low depth, given that this work is focussed on very thin films. The condition of the indenter was checked daily with a small series of indentations into fused silica using a load of 0.5 mN. No significant change in the load-depth indentation curves was observed throughout the duration of this work.

2.2.3.1.3 Material creep

Previous experience by the author with the type of coatings used in this work suggests little or no creep effects. The loading and unloading rates were adjusted so that the total load and unload times were in the range 10 – 30 seconds for all tests. In addition a delay of 5 seconds was included at the end of the loading sequence to ensure that full plasticity was reached.

2.2.3.1.4 Thermal drift

Thermal drift was minimised by the use of a heated isolation cabinet. Samples were allowed to reach thermal equilibrium over a period of several hours prior to initiating the nanoindentation sequence. An account of thermal drift was made for each indentation cycle by halting the unloading sequence for 60 seconds once the load had reduced to 80% of the maximum value. The NanoTest software was used to correct the indentation data by applying a linear regression derived from the load-depth response during the final 40 seconds of the thermal drift test.

2.2.3.1.5 Initial penetration depth

Low forces were used to make the initial contact with the sample surfaces. However, when working at very small depths, the initial contact depth can still be significant. For each coating, the multiple load-unload curves were over-laid and inspected. An approximation of the initial penetration depth was made by manually extrapolating the curve back to the zero load point and then all data was shifted via the NanoTest zero load depth correction facility.

2.2.3.1.6 Material pile-up and cracking

It is an assumption of the Oliver-Pharr treatment that no material pile-up or cracking occurs. To investigate the condition of these assumptions within this work a series of indentations (to 1000, 500, 250, 150 and 100 nm depths) were made into the coating coded P11S1 with the Berkovich indenter and the resulting indents were examined by AFM. An uncoated Si wafer was also tested for comparison. The NanoTest unit was used in scanning mode to scratch the surface with a Rockwell diamond indenter to provide a location mark for ease of finding the indents.

2.2.3.1.7 Surface roughness

The effect of surface roughness is likely to become more significant with smaller indentations. Due to the random distribution of asperity sizes the impact is likely to add to the error measurement of replicated tests. The number of replicated indentation tests was increased with decreasing indent depth. No surface polishing treatments were used to eliminate the possibility of contamination or induced structural changes.

2.2.3.1.8 Low coating thickness

For all indentations the maximum penetration depth was limited to 10% of the coating thickness. The diamond area function was produced with particular emphasis on very low depth data. An 'ultra sharp' Berkovich indenter supplied by Micro Materials Ltd was chosen for the reported work so that the highest mean contact pressure could be delivered to the surface under test at very low indentation depth. This is a requirement if full

plasticity of the coating is to be achieved and hence true hardness measured at low depth. The effect of low coating thickness is linked to indentation size effect.

2.2.3.1.9 Indentation size effect (ISE)

A review of reported ISE with a-C coatings in section 1.5.3.1.9 shows that no universal pattern or mechanism seems to exist. For this reason an investigation specific to the work in this report was made. An experiment was performed with a Cr doped a-C film coated to 5000 nm thickness to investigate ISE; to test the reliability of the diamond area function and to look at surface roughness effects. The coating was tested with many replicates using the Berkovich indenter covering a range of maximum indentation depths from 7 to 300 nm.

2.2.3.1.10 Load measurement calibration

There is a procedure built into the NanoTest software for calibrating the generated loads against the current applied to the pendulum coil and this was performed regularly during this project.

2.2.3.1.11 Depth measurement calibration

There is a procedure built into the NanoTest software for calibrating the displacements of the pendulum against the x-axis motor driven micrometer stage and this was performed regularly during this project.

2.2.3.2 Nanoscratch

All nanoscratch measurements of coatings were made with a NanoTest nanoindentation unit manufactured by Micro Materials Ltd and operated in 'scanning mode'.

The basic operation of the NanoTest unit is described in section 2.2.3.1. In scanning mode, the stage holding the sample can be moved in either of two axes whilst the probe is in contact with the surface. Dynamic load and probe depth measurements are taken during the scan. Scan length and scan velocity can be defined by the instrument operator. Loads can be ramped or applied abruptly.

Suitably sized coated samples were cut and attached to the sample holder by means of a cyanoacrylate adhesive. A sphero-conical diamond indenter of nominal opening angle 60° and spherical end radius 4 μm was inserted into the probe holder. The pendulum was balanced by means of the movable weight, the capacitive bridge circuit was adjusted and brought to balance by means of an adjustable circuit element and the sample holder was aligned with the indenter probe. Finally the system temperature was allowed to stabilise before the automated scanning sequence, which is controlled by the NanoTest software, was initiated. Multiple tests were performed on each coating. The specific experimental settings are given in section 2.3. The resulting probe-depth versus scan-distance plots were reviewed and the scratches were examined by optical microscopy.

2.2.4 Nanotribological properties

2.2.4.1 Friction

Where friction measurements were undertaken, a friction probe manufactured by Micro Materials Ltd was added to the NanoTest unit. The probe is built around a torsion transducer which sits between the indenter and probe holder. When the NanoTest unit is used in scanning mode, frictional forces produce a slight bending of the transducer which is measured by the software controlled detection unit. Prior to each experiment, the probe was calibrated using the standard NanoTest function which involved adding a range of accurately known masses to the probe and hence producing a force versus output voltage calibration curve. The specific experimental settings are given in section 2.3.

2.2.4.2 Wear

2.2.4.2.1 Multipass nanoscratch wear test

The nanoscratch function of the NanoTest unit (as described in section 2.2.3.2) was used in 'multipass mode' to provide a simple nano-scale wear test. The multipass operation enabled the nanoscratch sequence to be repeated for a user defined number of cycles at the same location. A sphero-conical diamond indenter of nominal opening angle 60° and spherical end radius 4 μm was used for all tests and the specific experimental settings are given in section 2.3.

2.2.4.2.2 Sample oscillated nanoindentation nanowear test

In order to address the points raised in section 1.5.4.3 and provide a means of undertaking rapid nanotribological experiments at conditions relevant to MEMS and micro- / nano-scale engineering a novel nanowear device was produced. A micro-scale oscillation mechanism was designed and built to fit into the sample support system of the NanoTest nanoindentation unit. A photograph of the oscillation unit is given in Figure 2.3. Each coated Si sample was in turn attached to a standard Al sample holder by means of a cyanoacrylate adhesive. The sample holder was clamped to the oscillation unit (Figure 2.3(d)). The design of the oscillation unit was such that that it permitted (1) the sample to be brought into contact with the test probe of the NanoTest equipment (2) the sample plane to be oscillated in a direction perpendicular to the test probe axis and (3) the applied normal force and the resulting depth of penetration to be monitored continuously. The oscillator utilised a pivoted (Figure 2.3(b)) lever mechanism (Figure 2.3(c)) to magnify the oscillations of a piezoelectric stack (Figure 2.3(a)). The design incorporated a flexure (Figure 2.3(e)), which allowed the mounted sample to oscillate in just one plane (also shown in Figure 2.3). The oscillation signal was derived from an amplified signal generator capable of producing a wide range of amplitude and frequency parameters.

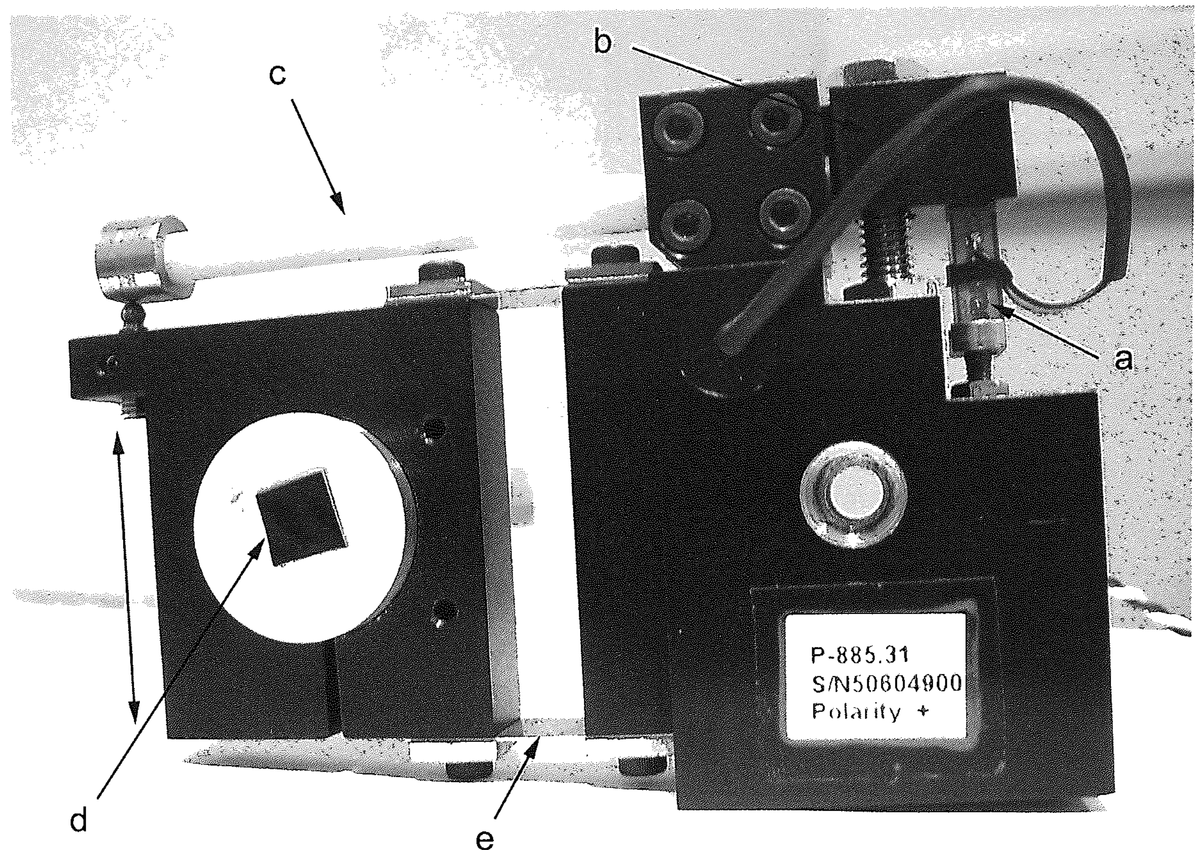

Figure 2.3 Photograph of the micro-scale sample oscillation unit (with labels).

In order to produce the desired low contact pressures a spherical ruby indenter was made by attaching an Edmund Optics 0.3 mm diameter ruby ball lens to an indenter holder with a cyanoacrylate adhesive. The ruby counter-body was examined by AFM. The basic sample oscillated nanoindentation effect is depicted in Figure 2.4.

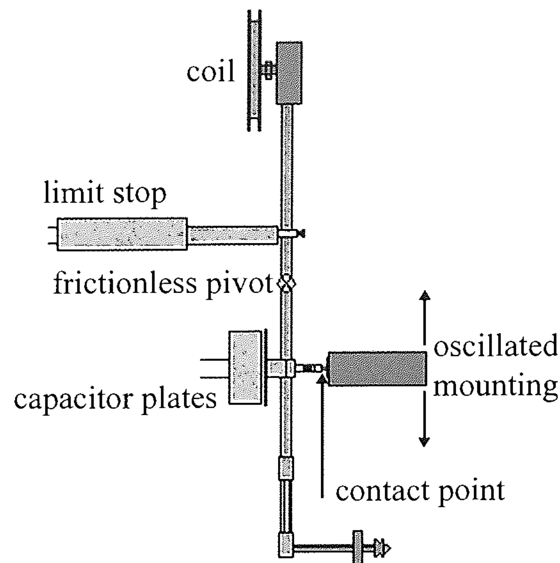

Figure 2.4 Basic operation of the NanoTest unit showing oscillated sample effect.

A number of experiments were run with the oscillated nanoindentation set-up in order to: (i) develop the technique to achieve the desired test conditions and to understand the capability (ii) observe and characterise the development of the nanowear process generated by the technique (iii) investigate the nanowear properties of the major coating arrays described in section 2.3. All tests were performed in a controlled atmosphere where temperature was maintained in the range 25.5 to 26.5 °C and relative humidity in the range 35 to 45 % unless otherwise stated.

Following the wear tests, each sample and the ruby sphere were examined by optical microscopy. The ruby sphere was then cleaned by wiping with 2-propanol and checked for any damage by optical microscopy prior to the next test. The test coating was washed and gently wiped with 2-propanol to remove the wear debris and the wear scar was scanned by AFM. Following certain experiments an examination of worn debris/transfer film was attempted by: AFM examination of the coating/ruby ball and AES/XPS examination of both the coating and counter-body prior to cleaning.

The conditions of the experiments relating to the use of the optimised nanowear test are listed in section 2.3.2.

2.3 *Experimental design*

2.3.1 Experiments to investigate the tribologically important properties of a-C coatings

2.3.1.1 Experiment to investigate Cr doping in a-C coatings at the nano- and macro-scale with 1 to 3 μm coatings

The purpose of this work was to test a series of μm scale thickness a-C and Cr doped a-C coatings for nano-scale mechanical and tribological properties and compare with the conclusions derived from previous work reported from a similar series of coatings tested and characterised at the macro-scale. In addition, the structure of the coatings was characterised, with particular emphasis on the outer regions for comparison with similar low thickness coatings. The coating process was set as for standard Graphit-IC™ with the exception of Cr target currents which were varied to generate a range of concentrations. There was also some variation of pulsed negative substrate bias voltage between the three samples; although previous work has suggested that within this range the bias voltage has little effect of the hardness and critical load of coatings at this thickness [231]. Substrate bias pulse frequency and pulse width were set to the standard 50 kHz and 1500 ns respectively for all tests. The coating times were varied such that the nominal coating thicknesses for samples coded P1S1, P1S2 and P1S3 were 1, 1 and 2.7 μm respectively. The key coating parameter settings are given in Table 2.2.

Table 2.2 Parameter settings for 1 to 3 μm films.

Code	Ar flow (sccm)	Adhesion layer	1st and 2nd C magnetron current (A)	Cr magnetron current (A)	Additional Cr magnetron current (A)	Substrate bias voltage (-V)
P1S1	20	Present	3.5	0	0	40
P1S2	20	Present	3.5	0.25	0	60
P1S3	20	Present	3.5	0.75	0.75	50

Chemical composition and structural information was determined with a VG Scientific ESCALAB 200D XPS spectrometer. The X-ray source was set to an excitation energy of 15 keV and emission current of 20 mA. The hemispherical analyser was run with pass energy of 20 eV, step size of 0.1 eV and dwell time of 100 ms. Multiple scans were

employed in order to achieve a satisfactory signal to noise ratio. ARXPS spectra were produced by tilting the angle of the sample relative to the electron detector. Depth profiling was achieved by Ar^+ ion bombardment of energy 3.5 keV and ion current of 1.5 μA. An etch rate of 0.3 nm per minute was determined at these settings by measuring the etch depth using AFM.

The mechanical properties of the coatings were determined by nanoindentation using a Micro Materials Ltd NanoTest unit. In each test the applied force was increased from a starting contact-force of 0.5 mN, the maximum depth was controlled to 50 nm and the test was repeated 12 times.

The nanotribological properties were undertaken using the multipass scanning mode of a Micro Materials Ltd NanoTest unit. Both wear tests and friction measurements were made using a sphero-conical diamond indenter with a nominal opening angle of 60° and spherical end radius of 4 μm and were repeated 3 times with a constant indenter velocity of 5.00 μms^{-1}. An initial contact load of 0.15 mN was applied during the first 30 μm of the scratch and then the load was increased abruptly to 100 mN for the remaining 70 μm of the scratch. One wear test involved 5 passes in the same location. The topography was measured after each pass using a low contact force of 0.15 mN. Frictional force measurements were made using a Micro Materials Ltd frictional force transducer attached to the diamond probe during the 100 mN scans.

Topographical information from surfaces and scratches was obtained using a ThermoMicroscopes Autoprobe M5 AFM fitted with ThermoMicroscopes ProScan Software (Version 2.1) operated in contact mode.

2.3.1.2 Experiment to investigate the effects of pulsed substrate biasing with 150 nm coatings

The purpose of this work was to investigate the effects and interactions of a small closely related group of substrate bias coating process parameters and identify the most important for the production of thin, hard, wear resistant coatings for very low load applications on Si. In addition, this provided information that helped in the selection process for the key parameters in a more detailed study. It also gave valuable information about the principle

of using the DOE approach under the demands of nano-scale work. The three available pulsed negative substrate bias control parameters investigated by statistical DOE were: average negative bias voltage, pulse frequency and (zero voltage) pulse width. A full factorial DOE was produced with bias voltage varied over three levels and frequency and pulse width over two levels. The levels were chosen such that they could be independently varied. Previous experience suggested that significant effects on the coating properties were to be expected over these ranges at the μm scale. All other parameters were set as with the standard Graphit-IC™ system. The coating time was set to produce a nominal thickness of 150 nm for all tests. The experimental design with the key process parameters is given in Table 2.3 and some related pulse values are given in Table 2.4.

Table 2.3 DOE settings for substrate bias experiment with 150 nm films.

Code	Ar flow (sccm)	Adhesion layer	1st and 2nd C magnetron current (A)	Cr magnetron current (A)	Substrate bias voltage (-V)	Substrate bias pulse frequency (kHz)	Substrate bias pulse width (ns)
P3S1	20	Present	3.5	0.25	30 (0.06)*	50	500
P3S2	20	Present	3.5	0.25	30 (0.07)*	50	2500
P3S3	20	Present	3.5	0.25	30 (0.06)*	150	500
P3S4	20	Present	3.5	0.25	30 (0.1)*	150	2500
P3S5	20	Present	3.5	0.25	60 (0.11)*	50	500
P3S6	20	Present	3.5	0.25	60 (0.12)*	50	2500
P3S7	20	Present	3.5	0.25	60 (0.15)*	150	500
P3S8	20	Present	3.5	0.25	60 (0.18)*	150	2500
P3S9	20	Present	3.5	0.25	90 (0.17)*	50	500
P3S10	20	Present	3.5	0.25	90 (0.22)*	50	2500
P3S11	20	Present	3.5	0.25	90 (N/A)*	150	500
P3S12	20	Present	3.5	0.25	90 (N/A)*	150	2500

* Recorded substrate bias current values (A)

Table 2.4 Pulse parameters for substrate bias experiment with 150 nm films.

Code	Duty cycle (%)	Fraction of period that bias is on (%)	Fraction of period that bias is off (%)	Peak V to maintain time average bias (-V)
P3S1	97.5	97.5	2.5	30.8
P3S2	87.5	87.5	12.5	34.3
P3S3	92.5	92.5	7.5	32.4
P3S4	62.5	62.5	37.5	48.0
P3S5	97.5	97.5	2.5	61.5
P3S6	87.5	87.5	12.5	68.6
P3S7	92.5	92.5	7.5	64.9
P3S8	62.5	62.5	37.5	96.0
P3S9	97.5	97.5	2.5	92.3
P3S10	87.5	87.5	12.5	102.9
P3S11	92.5	92.5	7.5	97.3
P3S12	62.5	62.5	37.5	144.0

Chemical composition and structural information was determined under the same conditions as given in section 2.3.1.1. No ARXPS or depth profiling was undertaken.

The mechanical properties of the coatings were determined as given in section 2.3.1.1, except the initial contact force was limited to 0.015 mN and the maximum depth of indentation to 15 nm. The indentation test was repeated 15 times per sample.

A nanoscratch test was run on each sample. Scratch tests were repeated 3 times with a constant indenter velocity of 0.5 μms^{-1}. An initial load of 0.05 mN was applied during the first 30 μm of the scratch and then the load was increased linearly to 100 mN over a further distance of 100 μm. The topography was measured after each pass using a low contact-force of 0.05 mN.

The complete nanoindentation and nanoscratch procedure detailed above was repeated five times on film P3S6 at five positions separated by tens of mm across the coating surface. This provided additional hardness, reduced modulus and critical load data which tested for coating variation across macro-scale distances.

Topographical measurements were made as section 2.3.1.1 at two 1 x 1 μm sample locations per specimen. The data was analysed using the ProScan software to determine two Ra values per sample at the two scan locations as a measure of the overall surface roughness. A more detailed analysis of the surface topography was made by measuring

the mean peak height relative to the overall mean surface height; repeated 24 times at positions evenly distributed across the two scan areas. The mean spacing between significant peaks was also determined in duplicate for each sample within the ProScan software.

Film thickness was determined by measuring the step height between the coating and a masked region of substrate at multiple locations with a Taylor-Hobson Talystep 223-27 profilometer.

2.3.1.3 Experiment to investigate four key coating process parameters with 150 nm coatings

This experiment was undertaken to investigate the effects and interactions of the four key coating process parameters that had been identified (section 2.1.2.3). An assessment of the properties that are beneficial to coating tribology was made in order to identify the most important parameters for the production of thin, hard, wear resistant coatings for very low load applications on Si. The four process control parameters investigated by statistical DOE were: Ar flow rate, the use of an adhesion layer, Cr magnetron current, average negative bias voltage. A full factorial DOE was produced and each factor was varied between two levels. Further investigation of bias voltage and the range chosen was stimulated by the results from the previous experiment. The selection of the Cr current range was influenced by previous work at μm scale [232] where significant improvements in coating tribology occurred at 0.75 A, in comparison with a Cr free film. The Ar flow range was chosen from previous knowledge with the coating system at μm thicknesses. Substrate bias pulse frequency and pulse width were set to 50 kHz and 1500 ns respectively for all tests. The coating time was set to produce a nominal thickness of 150 nm for all tests. The experimental design is given in Table 2.5.

Table 2.5 DOE settings for key parameter experiment with 150 nm films.

Code	Ar flow (sccm) {pressure (mBar)}	Adhesion layer	1st and 2nd C magnetron current (A)	Cr magnetron current (A)	Substrate bias voltage (-V)
P5S1	12 {5.1 x10^{-4}}	NONE	3.5	0	40 (0.09)*
P5S2	12	NONE	3.5	0	80 (0.19)*
P5S3	12	NONE	3.5	0.75	40 (0.21)*
P5S4	12	NONE	3.5	0.75	80 (0.39)*
P5S5	12	PRESENT	3.5	0	40 (N/A)*
P5S6	12	PRESENT	3.5	0	80 (0.17)*
P5S7	12	PRESENT	3.5	0.75	40 (0.25)*
P5S8	12	PRESENT	3.5	0.75	80 (0.38)*
P8S1	28 {1.5 x10^{-3}}	NONE	3.5	0	40
P8S2	28	NONE	3.5	0	80
P8S3	28	NONE	3.5	0.75	40
P8S4	28	NONE	3.5	0.75	80
P8S5	28	PRESENT	3.5	0	40
P8S6	28	PRESENT	3.5	0	80
P8S7	28	PRESENT	3.5	0.75	40
P8S8	28	PRESENT	3.5	0.75	80

* Recorded substrate bias current values (A)

In order to fully account for any uncontrolled variation that may affect the sputter coating process under DOE testing it was desirable to produce repeated films at each set of coating conditions and also to randomise the order of the tests. However, this was not possible due to the time constraints of working with an industrial production line. A single film (P5S7) was produced four times in separate process runs over a three month period, in order to provide some additional data to test for uncontrolled variation.

Chemical composition and structural information was again determined under the same conditions as given in section 2.3.1.1. No ARXPS or depth profiling was undertaken.

The conditions of mechanical property testing was as given in section 2.3.1.1, except the initial contact force was limited to 0.015 mN and the maximum depth of indentation to 15 nm. The indentation test was repeated 25 times per sample.

Friction tests were undertaken as given in section 2.3.1.1, except the test was repeated 3 times with a constant indenter velocity of 1 μms^{-1}. An initial load of 0.05 mN was applied during the first 1 μm of the scratch and then the load was increased abruptly to 20 mN over a further distance of 9 μm.

A nanoscratch test was run on each sample under the conditions given in section 2.3.1.2, except the load was increased linearly to 200 mN over a distance of 200 μm.

Topographical measurements were made as in section 2.3.1.2 but at three 1 x 1 μm locations per sample, with no analysis of peak height and peak separation.

Film thickness was also determined as in section 2.3.1.2.

2.3.1.4 Experiment to investigate four key coating process parameters with 50 nm coatings

This experiment was undertaken to investigate the effects and interactions of the four key coating process parameters (given in section 2.1.2.3) with 50 nm films. It is effectively a repeat of the work detailed in section 2.3.1.3 but at a further reduced film thickness. Again an assessment of the properties that are beneficial to coating tribology was made in order to identify the most important for the production of thin, hard, wear resistant coatings for very low load applications on Si. A half factorial DOE was produced and each factor was varied between two levels as before. Substrate bias pulse frequency and pulse width were set to 50 kHz and 1500 ns respectively for all tests. The coating time was set to produce a nominal thickness of 50 nm for all tests. The experimental design is given in Table 2.6.

Table 2.6 DOE settings for key parameter experiment with 50 nm films.

Code	Ar flow (sccm)	Adhesion layer	1st and 2nd C magnetron current (A)	Cr magnetron current (A)	Substrate bias voltage (-V)
P9S1	28	NONE	3.5	0	80
P9S2	12	NONE	3.5	0	40
P9S3	28	PRESENT	3.5	0	40
P9S4	12	NONE	3.5	0.75	80
P9S5	28	PRESENT	3.5	0.75	80
P9S6	12	PRESENT	3.5	0.75	40
P9S7	12	PRESENT	3.5	0	80
P9S8	28	NONE	3.5	0.75	40

Chemical composition and structural information was determined with a Thermo Electron Corporation ESCALAB 250 spectrometer equipped with a hemispherical electron energy analyser and monochromated X-ray source. The X-ray source was set to an excitation

energy of 15 keV and emission current of 6 mA. The hemispherical analyser was run with pass energy of 20 eV, step size of 0.1 eV and dwell time of 50 ms. Multiple scans were employed in order to achieve a satisfactory signal to noise ratio. Depth profiling was achieved by Ar^+ ion bombardment of energy 3 keV and ion current of 1 μA.

Mechanical property testing was performed as given in section 2.3.1.3, except an initial contact force of 0.01 mN was used and the indentations were limited to a maximum indentation load of 0.05 mN. The test was repeated 50 times per sample.

Friction tests were undertaken as given in section 2.3.1.1, except the test was repeated 3 times with a constant indenter velocity of 1 μms^{-1}. An initial load of 0.05 mN was applied during the first 2 μm of the scratch and then the load was increased abruptly to 20 mN over a further distance of 8 μm.

Nanoscratch testing was undertaken under the conditions given in section 2.3.1.2.

Topographical measurements were made at eight 1 x 1 μm locations per sample under the conditions given in section 2.3.1.2, with no analysis of peak height and peak separation.

Film thicknesses were measured via the same method as section 2.3.1.2.

2.3.1.5 Experiment to investigate a range of film thicknesses (2000 nm to 10 nm)

In order to more closely scrutinise the relationship between coating thickness and the resulting coating properties an experiment was run using the same coating formulation but deposited at a range of nominal thicknesses. The key coating parameters were set to the standard Graphit-IC^{TM} process and are given in Table 2.7. Substrate bias pulse frequency and pulse width were set to 50 kHz and 1500 ns respectively for all tests. The coating time was set to produce a nominal thickness of 2000, 150, 50, 20 and 10 nm respectively. The time of adhesion layer production was scaled by the same factor as the main coating time.

Table 2.7 Parameter settings for 2000 to 10 nm coatings

Code	Nominal thickness (nm)	Ar flow (sccm)	Adhesion layer	1st and 2nd C magnetron current (A)	Cr magnetron current (A)	Substrate bias voltage (-V)
P11S1	2000	20	PRESENT	3.5	0.25	60
P11S2	150	20	PRESENT	3.5	0.25	60
P11S3	50	20	PRESENT	3.5	0.25	60
P11S4	20	20	PRESENT	3.5	0.25	60
P11S5	10	20	PRESENT	3.5	0.25	60

Chemical composition and structure was examined under the same conditions as given in section 2.3.1.4.

Mechanical property testing was performed as given in section 2.3.1.3, except an initial contact force of 0.01 mN was used. The indentations were limited to: a maximum depth of 15 nm for P11S1 and P11S2; a maximum load of 0.05 mN for P11S3 and a maximum load of 0.03 mN for P11S4. The test was repeated 25 times for P11S1 and P11S2; 50 times for P11S3 and 100 times for P11S4.

Nanoscratch tests were performed under the same conditions given in section 2.3.1.2, except the load was increased linearly to 200 mN (500 mN for P11S1) over a distance of 200 μm (500 μm for P11S1).

Topographical measurements were made at four 1 x 1 μm locations per sample under the conditions given in section 2.3.1.2, with no analysis of peak height and peak separation.

2.3.2 Experiments to investigate the nanotribology of a-C films

2.3.2.1 Characterisation of the sample oscillated nanoindentation nanowear process

The purpose of this initial experiment was to look at the conditions of the sample oscillated nanoindentation nanowear test and understand the mechanism of nanowear operating over a range of oscillation amplitude and applied force.

Table 2.8 Test conditions for nanowear characterisation experiment.

	Coating	Normal force (mN)	Oscillation frequency (Hz)	Peak to peak voltage	Displacement amplitude (μm)	Number of oscillation cycles
1	P5S2	200	10	30	2	18000
2	P5S2	200	10	30	2	36000
3	P5S2	200	10	30	2	54000
4	P5S2	200	10	30	2	72000
5	P5S2	10	10	30	2	18000
6	P5S2	10	10	30	2	36000
7	P5S2	10	10	30	2	54000
8	P5S2	10	10	30	2	72000
9	P5S2	10	10	30	2	360000
10	P5S2	10	10	75	14	216000
11	P5S1	10	10	75	14	18000
12	P5S1	10	10	75	14	72000
13	P5S1	10	10	75	14	144000
14	P5S1	10	10	75	14	216000
15	P5S2	10	10	75	14	18000
16	P5S2	10	10	75	14	72000
17	P5S2	10	10	75	14	144000
18	P5S2	10	10	75	14	216000
19	P5S3	10	10	75	14	18000
20	P5S3	10	10	75	14	72000
21	P5S3	10	10	75	14	144000
22	P5S3	10	10	75	14	216000
23	P5S4	10	10	75	14	18000
24	P5S4	10	10	75	14	72000
25	P5S4	10	10	75	14	144000
26	P5S4	10	10	75	14	216000
27	P5S5	10	10	75	14	18000
28	P5S5	10	10	75	14	72000
29	P5S5	10	10	75	14	144000
30	P5S5	10	10	75	14	216000
31	P5S6	10	10	75	14	18000
32	P5S6	10	10	75	14	72000
33	P5S6	10	10	75	14	144000
34	P5S6	10	10	75	14	216000
35	P5S7	10	10	75	14	18000
36	P5S7	10	10	75	14	72000
37	P5S7	10	10	75	14	144000
38	P5S7	10	10	75	14	216000
39	P5S8	10	10	75	14	18000
40	P5S8	10	10	75	14	72000
41	P5S8	10	10	75	14	144000
42	P5S8	10	10	75	14	216000

2.3.2.2 *Experiment to investigate the nanowear of a matrix of 150 nm coatings and the effect of four key coating process parameters*

The matrix of coatings considered in section 2.3.1.3 were subjected to nanowear in order to further the fundamental knowledge of wear at the nano-scale and also to understand the rules of tribological coating optimisation at the nano-scale.

Table 2.9 Nanowear test conditions for experiment with 150 nm coatings.

	Coating	Normal force (mN)	Oscillation frequency (Hz)	Peak to peak voltage	Displacement amplitude (μm)	Number of oscillation cycles
1	P5S1	10	10	75	14	18000
2	P5S1	10	10	75	14	72000
3	P5S1	10	10	75	14	144000
4	P5S1	10	10	75	14	216000
5	P5S2	10	10	75	14	18000
6	P5S2	10	10	75	14	72000
7	P5S2	10	10	75	14	144000
8	P5S2	10	10	75	14	216000
9	P5S3	10	10	75	14	18000
10	P5S3	10	10	75	14	72000
11	P5S3	10	10	75	14	144000
12	P5S3	10	10	75	14	216000
13	P5S4	10	10	75	14	18000
14	P5S4	10	10	75	14	72000
15	P5S4	10	10	75	14	144000
16	P5S4	10	10	75	14	216000
17	P5S5	10	10	75	14	18000
18	P5S5	10	10	75	14	72000
19	P5S5	10	10	75	14	144000
20	P5S5	10	10	75	14	216000
21	P5S6	10	10	75	14	18000
22	P5S6	10	10	75	14	72000
23	P5S6	10	10	75	14	144000
24	P5S6	10	10	75	14	216000
25	P5S7	10	10	75	14	18000
26	P5S7	10	10	75	14	72000
27	P5S7	10	10	75	14	144000
28	P5S7	10	10	75	14	216000
29	P5S8	10	10	75	14	18000
30	P5S8	10	10	75	14	72000
31	P5S8	10	10	75	14	144000
32	P5S8	10	10	75	14	216000
33	P8S1	10	10	75	14	18000
34	P8S1	10	10	75	14	72000
35	P8S1	10	10	75	14	144000
36	P8S1	10	10	75	14	216000
37	P8S2	10	10	75	14	18000
38	P8S2	10	10	75	14	72000
39	P8S2	10	10	75	14	144000

40	P8S2	10	10	75	14	216000
41	P8S3	10	10	75	14	18000
42	P8S3	10	10	75	14	72000
43	P8S3	10	10	75	14	144000
44	P8S3	10	10	75	14	216000
45	P8S4	10	10	75	14	18000
46	P8S4	10	10	75	14	72000
47	P8S4	10	10	75	14	144000
48	P8S4	10	10	75	14	216000
49	P8S5	10	10	75	14	18000
50	P8S5	10	10	75	14	72000
51	P8S5	10	10	75	14	144000
52	P8S5	10	10	75	14	216000
53	P8S6	10	10	75	14	18000
54	P8S6	10	10	75	14	72000
55	P8S6	10	10	75	14	144000
56	P8S6	10	10	75	14	216000
57	P8S7	10	10	75	14	18000
58	P8S7	10	10	75	14	72000
59	P8S7	10	10	75	14	144000
60	P8S7	10	10	75	14	216000
61	P8S8	10	10	75	14	18000
62	P8S8	10	10	75	14	72000
63	P8S8	10	10	75	14	144000
64	P8S8	10	10	75	14	216000

2.3.2.3 Experiment to investigate the nanowear of a matrix of 50 nm coatings and the effect of four key coating process parameters

The matrix of coatings considered in section 2.3.1.4 was subjected to nanowear in order to further the fundamental knowledge of wear at the nano-scale and also to understand the rules of tribological coating optimisation at the nano-scale. This work also provided some information concerning the influence of coating thickness on the measured effects.

Table 2.10 Nanowear test conditions for experiment with 50 nm coatings.

	Coating	Normal force (mN)	Oscillation frequency (Hz)	Peak to peak voltage	Displacement amplitude (μm)	Number of oscillation cycles
1	P9S1	10	10	75	14	3000
2	P9S1	10	10	75	14	6000
3	P9S1	10	10	75	14	9000
4	P9S1	10	10	75	14	18000
5	P9S1	10	10	75	14	27000
6	P9S1	10	10	75	14	36000
7	P9S2	10	10	75	14	3000
8	P9S2	10	10	75	14	6000
9	P9S2	10	10	75	14	9000

10	P9S2	10	10	75	14	18000
11	P9S2	10	10	75	14	27000
12	P9S2	10	10	75	14	36000
13	P9S3	10	10	75	14	3000
14	P9S3	10	10	75	14	6000
15	P9S3	10	10	75	14	9000
16	P9S3	10	10	75	14	18000
17	P9S3	10	10	75	14	27000
18	P9S3	10	10	75	14	36000
19	P9S4	10	10	75	14	3000
20	P9S4	10	10	75	14	6000
21	P9S4	10	10	75	14	9000
22	P9S4	10	10	75	14	18000
23	P9S4	10	10	75	14	27000
24	P9S4	10	10	75	14	36000
25	P9S5	10	10	75	14	3000
26	P9S5	10	10	75	14	6000
27	P9S5	10	10	75	14	9000
28	P9S5	10	10	75	14	18000
29	P9S5	10	10	75	14	27000
30	P9S5	10	10	75	14	36000
31	P9S6	10	10	75	14	3000
32	P9S6	10	10	75	14	6000
33	P9S6	10	10	75	14	9000
34	P9S6	10	10	75	14	18000
35	P9S6	10	10	75	14	27000
36	P9S6	10	10	75	14	36000
37	P9S7	10	10	75	14	3000
38	P9S7	10	10	75	14	6000
39	P9S7	10	10	75	14	9000
40	P9S7	10	10	75	14	18000
41	P9S7	10	10	75	14	27000
42	P9S7	10	10	75	14	36000
43	P9S8	10	10	75	14	3000
44	P9S8	10	10	75	14	6000
45	P9S8	10	10	75	14	9000
46	P9S8	10	10	75	14	18000
47	P9S8	10	10	75	14	27000
48	P9S8	10	10	75	14	36000

2.3.2.4 Experiment to investigate the nanowear of a range of film thicknesses (2000 nm to 10 nm)

The matrix of coatings considered in section 2.3.1.5 was subjected to nanowear in order to further the fundamental knowledge of wear at the nano-scale and the effect of coating thickness.

Table 2.11 Nanowear test conditions for experiment with 2000 to 10 nm coatings.

	Coating	Normal force (mN)	Frequency (Hz)	Peak - peak voltage	Displacement amplitude (μm)	Number of oscillations
1	P11S1	10	10	75	14	600
2	P11S1	10	10	75	14	3000
3	P11S1	10	10	75	14	6000
4	P11S1	10	10	75	14	9000
5	P11S1	10	10	75	14	18000
6	P11S1	10	10	75	14	27000
7	P11S1	10	10	75	14	36000
8	P11S1	10	10	75	14	72000
9	P11S1	10	10	75	14	108000
10	P11S1	1	10	75	14	600
11	P11S1	1	10	75	14	3000
12	P11S1	1	10	75	14	6000
13	P11S1	1	10	75	14	9000
14	P11S1	1	10	75	14	18000
15	P11S1	1	10	75	14	27000
16	P11S1	1	10	75	14	36000
17	P11S1	1	10	75	14	72000
18	P11S1	1	10	75	14	108000
19	P11S1	0.1	10	75	14	72000
20	P11S1	0.1	10	75	14	144000
21	P11S1	0.1	10	75	14	216000
22	P11S2	10	10	75	14	600
23	P11S2	10	10	75	14	3000
24	P11S2	10	10	75	14	6000
25	P11S2	10	10	75	14	9000
26	P11S2	10	10	75	14	18000
27	P11S2	10	10	75	14	27000
28	P11S2	10	10	75	14	36000
29	P11S2	10	10	75	14	72000
30	P11S2	10	10	75	14	144000
31	P11S2	1	10	75	14	600
32	P11S2	1	10	75	14	3000
33	P11S2	1	10	75	14	6000
34	P11S2	1	10	75	14	9000
35	P11S2	1	10	75	14	18000
36	P11S2	1	10	75	14	27000
37	P11S2	1	10	75	14	36000
38	P11S2	1	10	75	14	72000
39	P11S2	1	10	75	14	144000
40	P11S2	0.1	10	75	14	72000
41	P11S2	0.1	10	75	14	144000
42	P11S2	0.1	10	75	14	216000
43	P11S3	10	10	75	14	600
44	P11S3	10	10	75	14	3000
45	P11S3	10	10	75	14	6000
46	P11S3	10	10	75	14	9000
47	P11S3	10	10	75	14	18000
48	P11S3	10	10	75	14	27000
49	P11S3	10	10	75	14	36000
50	P11S3	10	10	75	14	72000
51	P11S3	10	10	75	14	144000
52	P11S3	1	10	75	14	600
53	P11S3	1	10	75	14	3000
54	P11S3	1	10	75	14	6000
55	P11S3	1	10	75	14	9000
56	P11S3	1	10	75	14	18000

57	P11S3	1	10	75	14	27000
58	P11S3	1	10	75	14	36000
59	P11S3	1	10	75	14	72000
60	P11S3	1	10	75	14	144000
61	P11S3	0.1	10	75	14	72000
62	P11S3	0.1	10	75	14	144000
63	P11S3	0.1	10	75	14	216000
64	P11S4	10	10	75	14	600
65	P11S4	10	10	75	14	3000
66	P11S4	10	10	75	14	6000
67	P11S4	10	10	75	14	9000
68	P11S4	10	10	75	14	18000
69	P11S4	10	10	75	14	27000
70	P11S4	10	10	75	14	36000
71	P11S4	10	10	75	14	72000
72	P11S4	10	10	75	14	144000
73	P11S4	1	10	75	14	600
74	P11S4	1	10	75	14	3000
75	P11S4	1	10	75	14	6000
76	P11S4	1	10	75	14	9000
77	P11S4	1	10	75	14	18000
78	P11S4	1	10	75	14	27000
79	P11S4	1	10	75	14	36000
80	P11S4	1	10	75	14	72000
81	P11S4	1	10	75	14	144000
82	P11S4	0.1	10	75	14	72000
83	P11S4	0.1	10	75	14	144000
84	P11S4	0.1	10	75	14	216000
85	P11S5	10	10	75	14	600
86	P11S5	10	10	75	14	3000
87	P11S5	10	10	75	14	6000
88	P11S5	10	10	75	14	9000
89	P11S5	10	10	75	14	18000
90	P11S5	10	10	75	14	27000
91	P11S5	10	10	75	14	36000
92	P11S5	10	10	75	14	72000
93	P11S5	10	10	75	14	144000
94	P11S5	1	10	75	14	600
95	P11S5	1	10	75	14	3000
96	P11S5	1	10	75	14	6000
97	P11S5	1	10	75	14	9000
98	P11S5	1	10	75	14	18000
99	P11S5	1	10	75	14	27000
100	P11S5	1	10	75	14	36000
101	P11S5	1	10	75	14	72000
102	P11S5	1	10	75	14	144000
103	P11S5	0.1	10	75	14	72000
104	P11S5	0.1	10	75	14	144000
105	P11S5	0.1	10	75	14	216000

3 Results

3.1 Low wear / low friction thin film analysis techniques

3.1.1 Experiment to investigate the use of XPS for the determination of sp^3/sp^2 bonding ratio in a-C

Using the ESCALAB 200D spectrometer, the measured C 1s envelope from a range of (undoped) a-C and a-C:H coatings typically had a FWHM of 1.8 – 2.1 eV. During the peak synthesis procedure the separation between sp^2 and sp^3 component peaks was constrained to 0.7 – 0.9 eV and component peak widths to 1.5 – 1.8 eV. This compared with typically reported values of C 1s envelope FWHM of 1.5 – 1.9 eV with component separation and FWHM of 0.7 – 1.0 eV and 1.0 – 1.3 eV respectively [113,114,119,128,129,131,245,246,247].

There were 17 variables available when attempting to synthesise three components (Csp^2, Csp^3 and C-O) within the C 1s peak envelope using the VG Eclipse Data System peak fitting algorithm: energy separation between the sp^2 and sp^3 peaks; energy separation between the sp^2 and C-O peaks; sp^2 peak width, sp^2 peak shape (Gauss-lorentz ratio); sp^2 asymmetric tail height peak shape; sp^2 asymmetric exponential tail decay; sp^2 asymmetric ratio of tail height/exponential components; and the same for the sp^3 and C-O peaks. The absence of sufficient instrument resolution to guide the component peak structure meant that there was a large amount of freedom to fit, enabling many different component combinations to be synthesised from one C 1s peak. Consequently, repeated fittings on the same data under the same variable constraints produced variations of sp^3/sp^2 ratio of 50% or more. It was also noted that the 'fitter' could chose to 'lead' the fit toward an sp^3 dominant or sp^2 dominant result. Each fit was legitimate according to the variable constraints, however there was no basis on which to chose. An example of this is given in Figure 3.1.

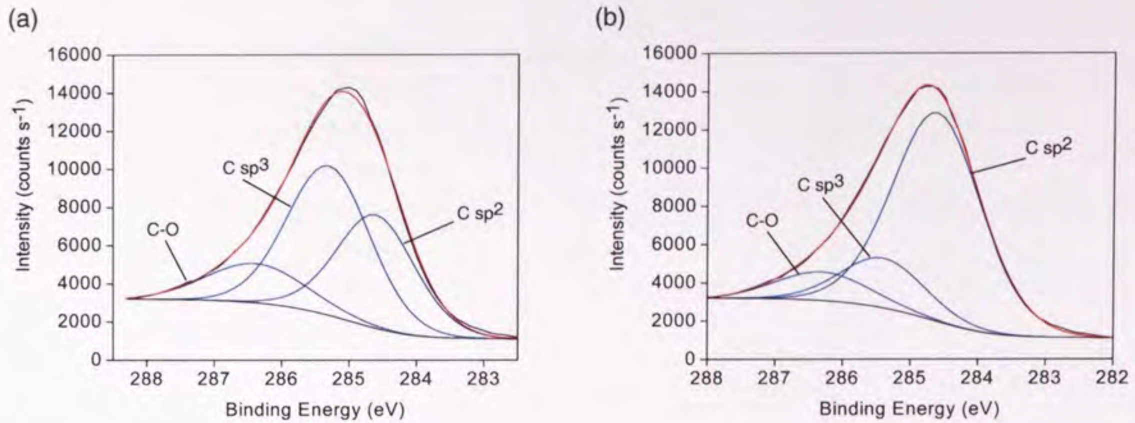

Figure 3.1 Peak fitting results for the same C 1s data with (a) sp^3 dominant and (b) sp^2 dominant.

Peak fitting was also attempted using an asymmetric sp^2 component. The component parameters were derived from XPS analysis of Ar^+ ion etched graphite. A reasonable fit was possible without the inclusion of an sp^3 component (Figure 3.2).

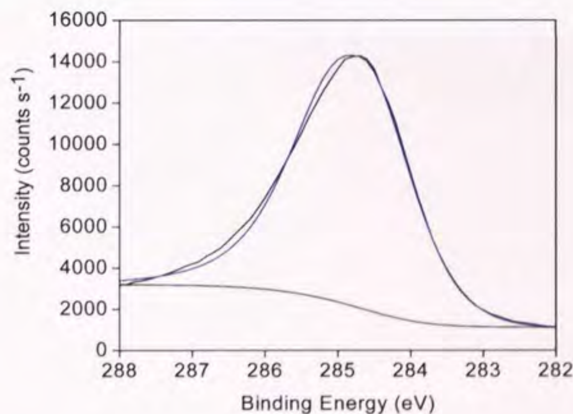

Figure 3.2 A single asymmetric sp^2 component (based on Ar^+ ion etched graphite) fitted to the same C 1s data as Figure 3.1.

A Thermo Electron Corporation ESCALAB 250 XPS spectrometer was also used to test a series of a-C coatings. The resolution of this equipment far exceeded that of the ESCALAB 200D. The measured C 1s envelope typically had a FWHM of 1.3 – 1.5 eV, however, no separation of the sp^3 and sp^2 components was detected. Consequently, as with the early work, there was no guide for component fitting which lead to a large uncertainty of any computed sp^3/sp^2 ratio. An example is given in Figure 3.3.

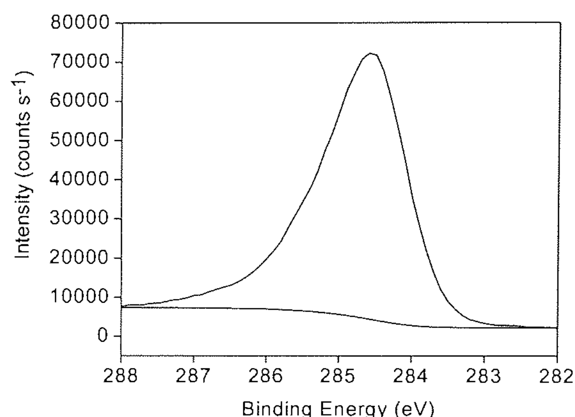

Figure 3.3 C 1s data produced by a Thermo Electron ESCALAB 250.

Data was also collected from the C KLL region of the spectrum and the ratio of sp^3/sp^2 bonding was calculated by D value method for the group of (undoped) a-C and a-C:H coatings. No correlation could be found between the results determined by C 1s analysis and those from D value method. An example is shown in Figure 3.4 where the sp^2 component was given the priority during the peak fitting sequence.

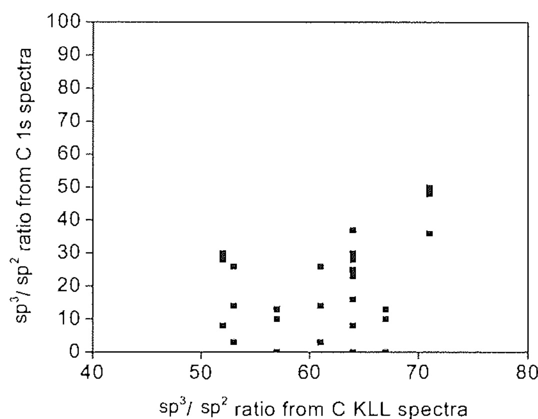

Figure 3.4 Correlation between sp^3/sp^2 ratios determined from C KLL D value and C 1s peak fitting analysis.

This is further demonstrated in Figure 3.5, where the C KLL spectra of three different films with similar D values and oxygen contents are shown. For each film the D value was determined to be 17 eV which equates to 63 % sp^3. The respective C 1s peaks are shown in Figure 3.5 (b) along with data collected for a sample of Ar^+ ion etched graphite.

Measurements of C 1s FWHM for a, b, c and graphite were 1.95, 1.93, 1.78 and 1.84 eV respectively. Similar sp^3/sp^2 ratios (as exhibited in the C KLL results) are expected to produce similar C 1s peaks, which is not the case here. Graphite which has no sp^3 component would be expected to show the lowest FWHM, again this is not the case here. This observation will be discussed more fully in section 4.1.1.

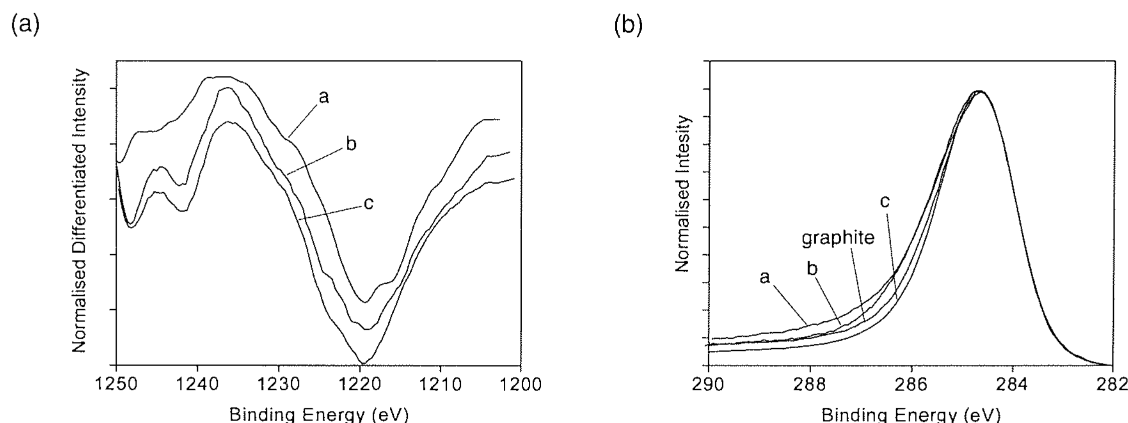

Figure 3.5 (a) C KLL spectra for three different a-C films with similar D values labelled as a, b and c (b) C 1s data for films a, b and c along with data for etched graphite.

3.1.2 Investigation of material pile-up and cracking during nanoindentation experiments

The h_f/h_{max} ratio was calculated from the nanoindentation results for all of the coatings tested. The mean value was 0.40 and the highest result was 0.61.

AFM scans of indentations to a maximum depth of 1000, 500 and 250 nm into coating P11S1 are shown in Figure 3.6, along with data from a single AFM pass through the centre of the 1000 nm indentation. It is clear that very little material pile-up was produced during the nanoindentation sequence and no cracking of the coating was observed. Indentations to a maximum depth below 250 nm could not be resolved from the surface topography.

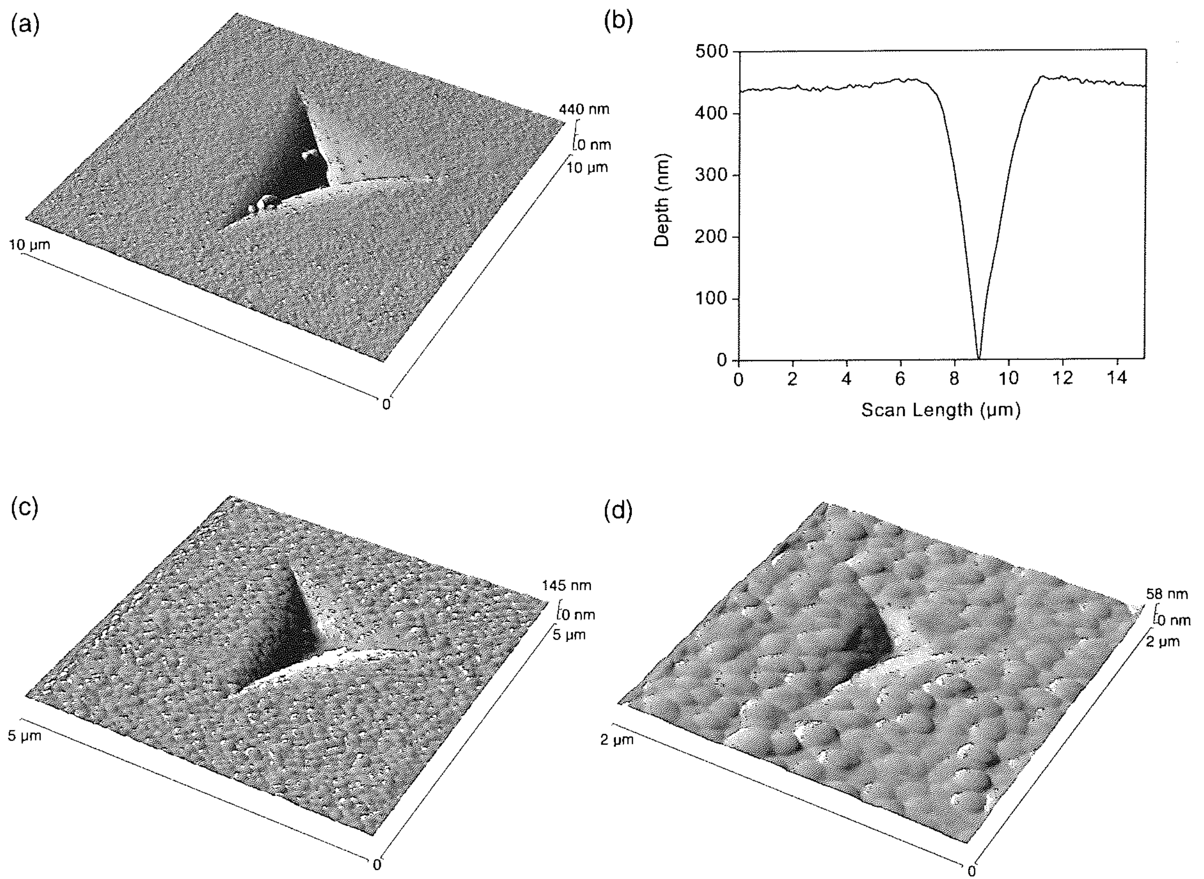

Figure 3.6 AFM scans of indentations into coating P11S1 (a) 1000 nm maximum indentation depth (b) data from a single AFM pass through the 1000 nm indentation (c) 500 nm maximum indentation depth (d) 250 nm maximum indentation depth.

An AFM scan of an indentation to a maximum depth of 1000 nm into a sample of uncoated silicon substrate is shown in Figure 3.7. Significant fracturing of the silicon was observed with all indentations. Cracking occurred at the corners of the indenter and the material fractured and rose up around the faces of the indenter.

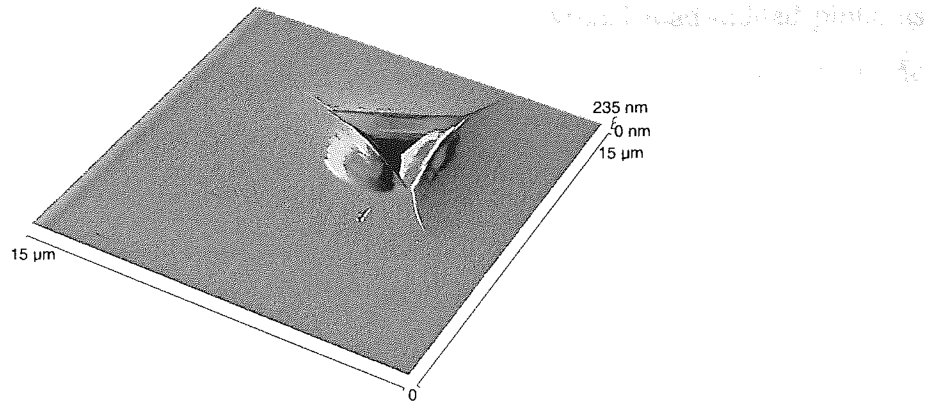

Figure 3.7 AFM scan of an indentation to a maximum depth of 1000 nm into silicon.

3.1.3 Investigation of ISE with nanoindentation experiments

Figure 3.8 shows hardness and reduced modulus results from a series of replicated indentations into the 5000 nm Cr doped a-C film. 130 separate indentations were performed over a range of depths from 6.7 nm to 280 nm.

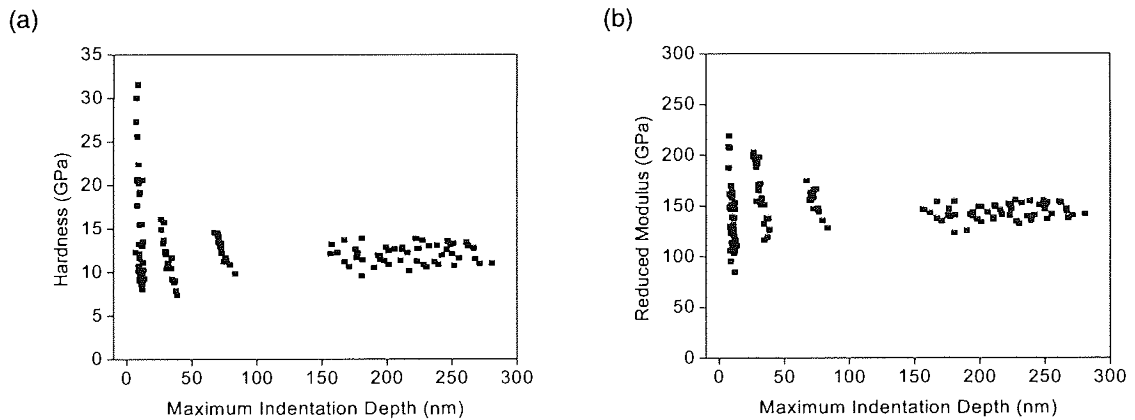

Figure 3.8 Plots of all (a) hardness and (b) modulus data with indentation depth.

The scatter of data increased as depth reduced. At low depths the results of replicated indentations tended to fall into bands. The bands lay on negative gradient slopes and the gradient reduced with increasing depth. At low depth, the scatter of hardness results was asymmetric with a long tail extending to high hardness values. The reduced modulus results were approximately symmetrically scattered over a (relatively) smaller range.

At the lowest depths there was significant noise on the individual load-unload plots, as expected. However, by superimposing all of the replicated curves it is clear that plastic deformation was occurring (Figure 3.9)

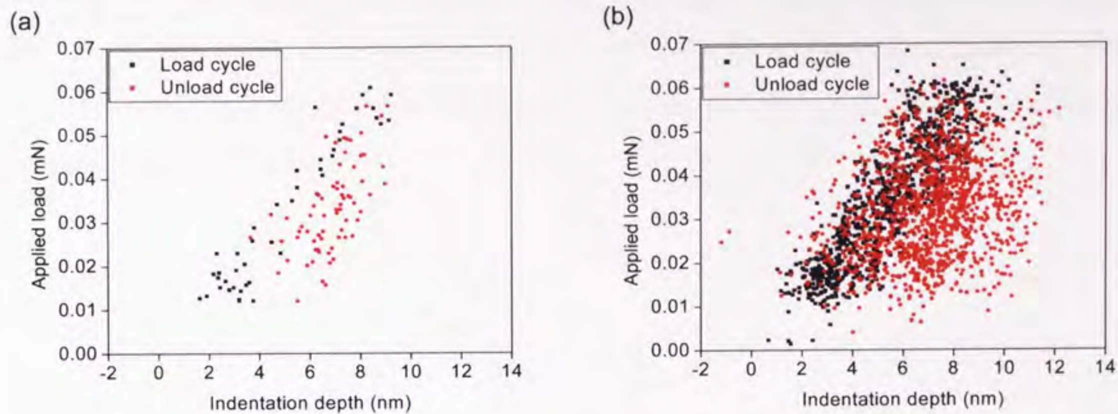

Figure 3.9 (a) a single load-unload curve at the lowest depth (b) replicated low depth load-unload curves superimposed.

Consideration was given to the expected effect of experimental random errors on hardness and reduced modulus values calculated through the Oliver-Pharr method. Three values are determined during the NanoTest indentation analysis procedure: maximum load P_{max}, maximum depth h_{max} and initial unloading stiffness S. Values of hardness and reduced modulus are then determined from these three values with Equation 1.14, Equation 1.5 and Equation 1.15. It was clear by inspection of many load-unload curves that very little error was associated with P_{max}. However at very low depths there was considerable error attached to the determined values of h_{max} and S due to the influence of noise from vibration. A theoretical analysis of the effect of random errors in h_{max} and S on the distribution of calculated hardness and reduced modulus was made by generating a normal distribution of typical h_{max} and S values. Calculated hardness values fell on an asymmetric distribution of the same form as that shown in Figure 3.8 for normal distributions of both h_{max} and S. Calculated reduced modulus values fell on an asymmetric distribution with h_{max} and a symmetrical distribution with S which in both cases spanned a much smaller relative range than hardness. Therefore the distribution and banding pattern of data observed here could be accounted for by the effect of noise on the measured h_{max} and S values.

In order to better observe the trends in Figure 3.8 with depth it is usual practise to find means of the replicated data. In the case of reduced modulus where the replicated data was symmetrically distributed the use of a mean accurately reflected the bulk location of the data. However, with hardness, the mean was shifted away from the bulk location of data due to the effect of a small number of very high hardness values in the asymmetric tail. This produced an apparent indentation size effect (ISE) with hardness at low depths as can be seen in Figure 3.10.

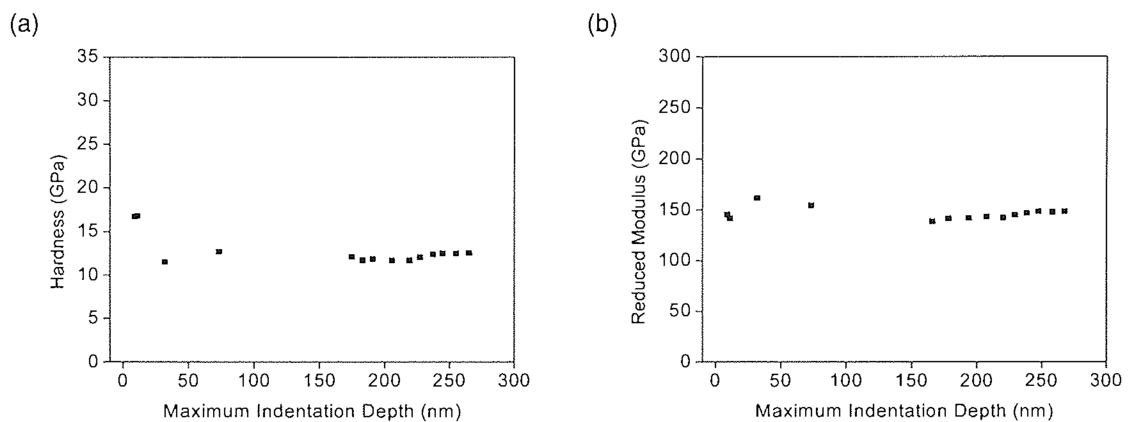

Figure 3.10 Plots of mean (a) hardness and (b) modulus data with indentation depth.

When dealing with asymmetrically distributed data it is preferable to use median values as this better reflects the bulk location of the data. This is shown for hardness in Figure 3.11.

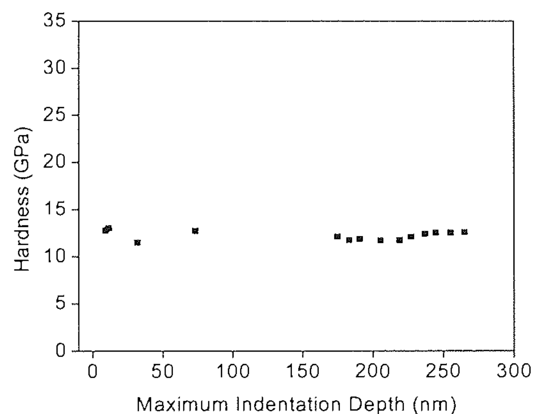

Figure 3.11 Plot of median hardness with indentation depth.

When the data was suitably processed it can be seen that there was negligible ISE apparent for both hardness and reduced modulus data down to < 7 nm indentations.

3.2 Experiments to investigate the tribologically important properties of a-C coatings

3.2.1 Experiment to investigate Cr doping in a-C coatings at the nano- and macro-scale with 1 to 3 μm coatings

3.2.1.1.1 XPS compositional analysis

The results of the XPS analysis are shown in Figure 3.12. As expected there was an increasing concentration of Cr with increasing current on the Cr sputter target. In addition there was an increasing concentration of O at the surface as the Cr content rose.

It should be noted that the samples were subject to normal atmospheric condition after removal from the coating chamber prior to analysis. The coating process was not initiated until the chamber pressure was lower than 4.7×10^{-5} mbar, which implies that the O content within the coating would be expected to be low and any oxidation of the surface is most likely to have occurred after exposure to the atmosphere.

The ARXPS results are sensitive to variations in relative atomic concentration (RAC) that occur over a very small depth range from the surface. The results for P1S1 showed a reduction of O content over this range which is probably due to a localised O layer on the surface. The P1S2 sample showed almost no RAC variation, therefore the O was evenly distributed over this depth range. The RAC results for P1S3 showed a slight increase in Cr and corresponding decrease in C with almost no change in O. Again this showed that the O was evenly distributed over the depth range.

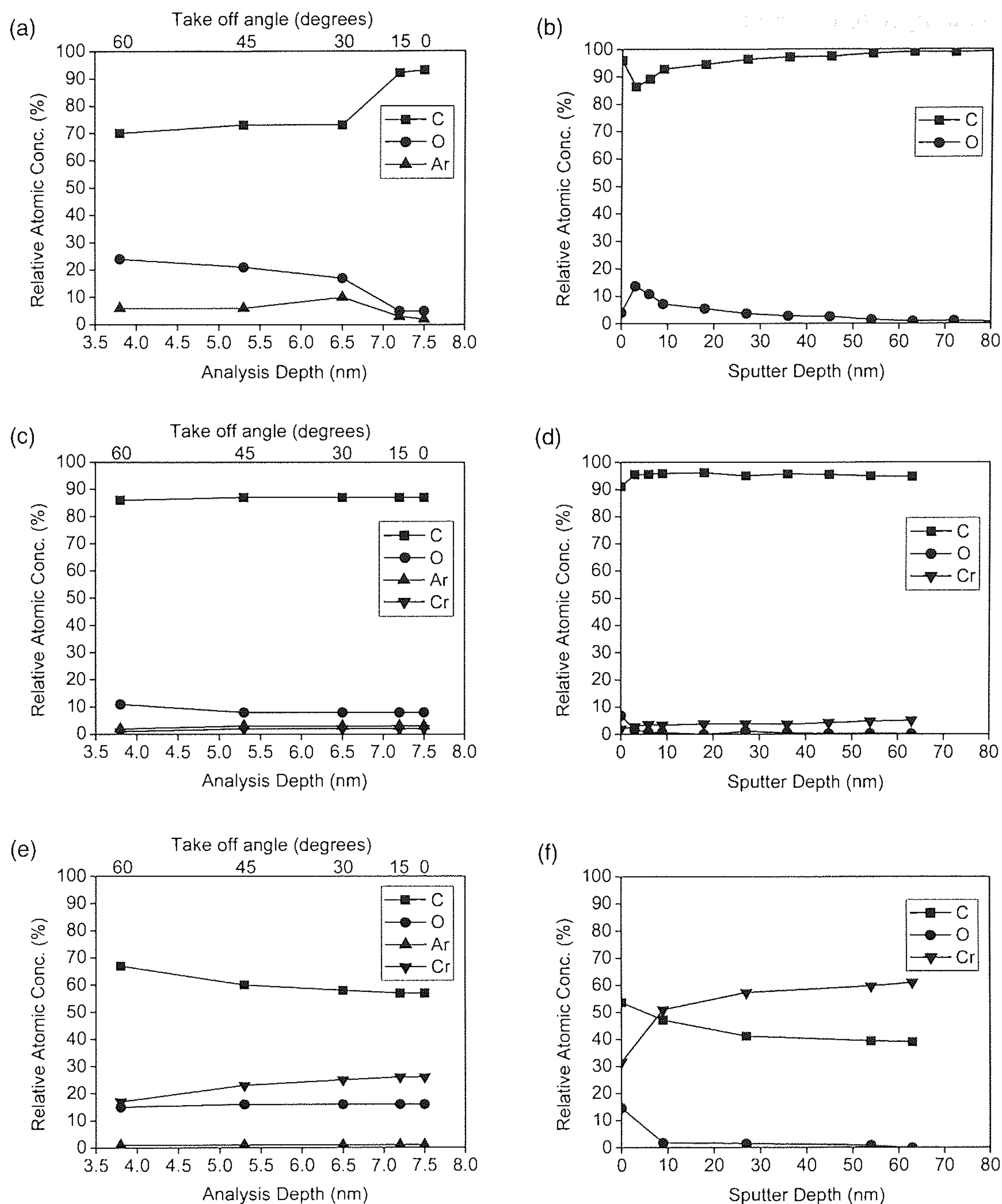

Figure 3.12 (a) ARXPS results for P1S1 (b) depth profile results for P1S1 (c) ARXPS results for P1S2 (the Cr and Ar results are coincident) (d) depth profile results for P1S2 (e) ARXPS results for P1S3 (f) Depth profile results for P1S3. The ARXPS analysis depths have been calculated by geometry from the maximum probe depth.

The depth profile measurements analyse variations of RAC over a much greater depth than the ARXPS (from the surface to a depth of about 80 nm). All samples showed that O was located predominantly near to the surface, which is consistent with adsorption of O from the atmosphere. However, in the case of P1S1, the depth profile results showed the highest concentration of O to be similar to that contained in the P1S3 coating, but located just below the outer layers. Also, the graph showed that O occurred within the P1S1 coating to a greater depth (50 – 60 nm) than the two Cr containing coatings. This could be due to O contamination in the chamber during deposition (although a leak check was performed prior to starting each coating run by testing for a rise in pressure after the high vacuum valve was closed, isolating the chamber from the pumping system) or a greater capacity for migration of Oxygen into the near surface regions. If O contamination had occurred during deposition it is difficult to explain the peak of concentration near to the surface. It therefore seems likely that P1S1 had a more attenuated amorphous structure associated with the outer layer during growth in comparison to the other coatings.

Both the ARXPS and depth profile results showed P1S2 to have a reasonably constant C and Cr concentration with depth. However, P1S3 exhibited a significantly lower concentration of Cr in the outer layers compared to the bulk. This may be due to the presence of adventitious carbon on the surface of the coating, although this would be expected to be of low thickness (< 1 nm). It is more likely to be due to a change in the relative flow of the C and Cr toward the coated specimen as a result of the coating shutdown procedure. As the P1S3 coating was milled away by Ar ion etching, the ratio of C:Cr tended towards a ratio of 2:3, suggesting that at this depth the coating may be in the form of Cr_3C_2.

3.2.1.1.2 XPS chemical analysis

A tentative analysis of both C KLL and C 1s XPS data was made for sp^3/sp^2 bonding. It should be noted that serious doubts have been raised about this type of analysis in section 3.1.1. The results given below were made in parallel with the work given in section 3.1.1 and are included for interest. No further use of KLL and C 1s XPS data for sp^3/sp^2 was made.

The C KLL Auger spectrum was collected for the P1S1 sample and compared with spectra previously collected for diamond and graphite. The spectra were differentiated using the Savitsky Golay smoothing algorithm set to average 17 data points. The results are shown in Figure 3.13. From these spectra it was possible to determine D values of: 14.5 eV, 22.4 eV and 18.8 eV for diamond, graphite and P1S1 respectively. By assuming a linear relationship between D value and percentage sp^3 bonding, a value of 46% was derived for the sp^3/sp^2 bonding in P1S1. No C KLL spectra were collected for P1S2 or P1S3 due to the reported interference from first row transition elements [144].

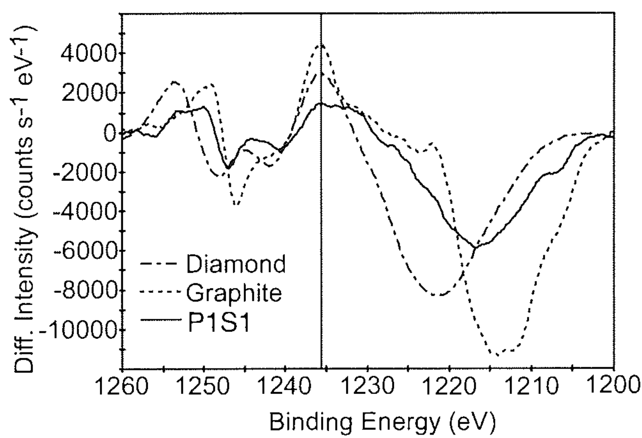

Figure 3.13 Differentiated Auger spectra for diamond, graphite and P1S1.

The XPS C 1s peaks for the P1S1, P1S2 and P1S3 samples had FWHM values of 2.0, 2.0 and 3.2 eV respectively. These results are significantly greater than FWHM values previously measured for diamond and graphite suggesting possible broadening of C 1s peak due to the presence of sp^3 and sp^2 bonding.

The C 1s peak shape of the P1S2 sample was very similar to that of P1S1 (see Figure 3.14). C-Cr bonding was expected to contribute very little to the C 1s peak as only about 2% of the atomic concentration was Cr. Therefore, C-C bonding in P1S2 may also be composed of both sp^2 and sp^3 bonding.

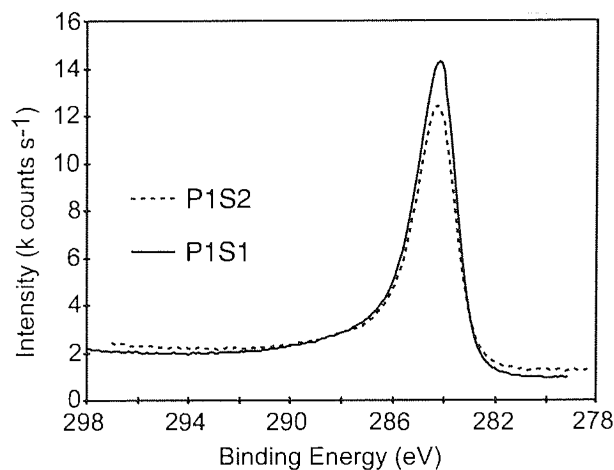

Figure 3.14 Comparison of C 1s peaks from P1S1 and P1S2 samples.

The C 1s peak shape of the P1S3 sample showed distinct regions which could be assigned to C-O, C-C and C-Cr bonding. C-O compounds (with C existing in a high oxidation state) have positive C 1s binding energy shifts (compared with adventitious C at 284.6 eV) of approximately 3.5 – 4.5 eV, which corresponded with the high energy region of the P1S3 peak shape (see Figure 3.15) [248]. C-Cr compounds have lower C 1s binding energy than adventitious C by approximately 1.5 – 2.0 eV, which corresponded with the low energy region of the P1S3 peak shape (see Figure 3.15) [248]. It was interesting to compare the P1S3 spectra during Ar^+ ion bombardment (see Figure 3.15). It was clear that the top layers of the coating were composed of a mixture of C-C, C-O and C-Cr bonding. Below the surface, there was a transition to predominantly C-Cr bonding. As the bonding tended to be dominated by C-Cr, the ratio of C:Cr concentration tended towards 2:3 (see Figure 3.12 (f)). This observation pointed to the fact that at the maximum etch depth the coating could be composed of Cr_3C_2. This is not necessarily contradicted by Figure 3.15 (d) where two peaks (C-Cr and C-C sp^2) have been synthesised. It may be the case that the properties of the C-Cr bonding produce an asymmetric peak.

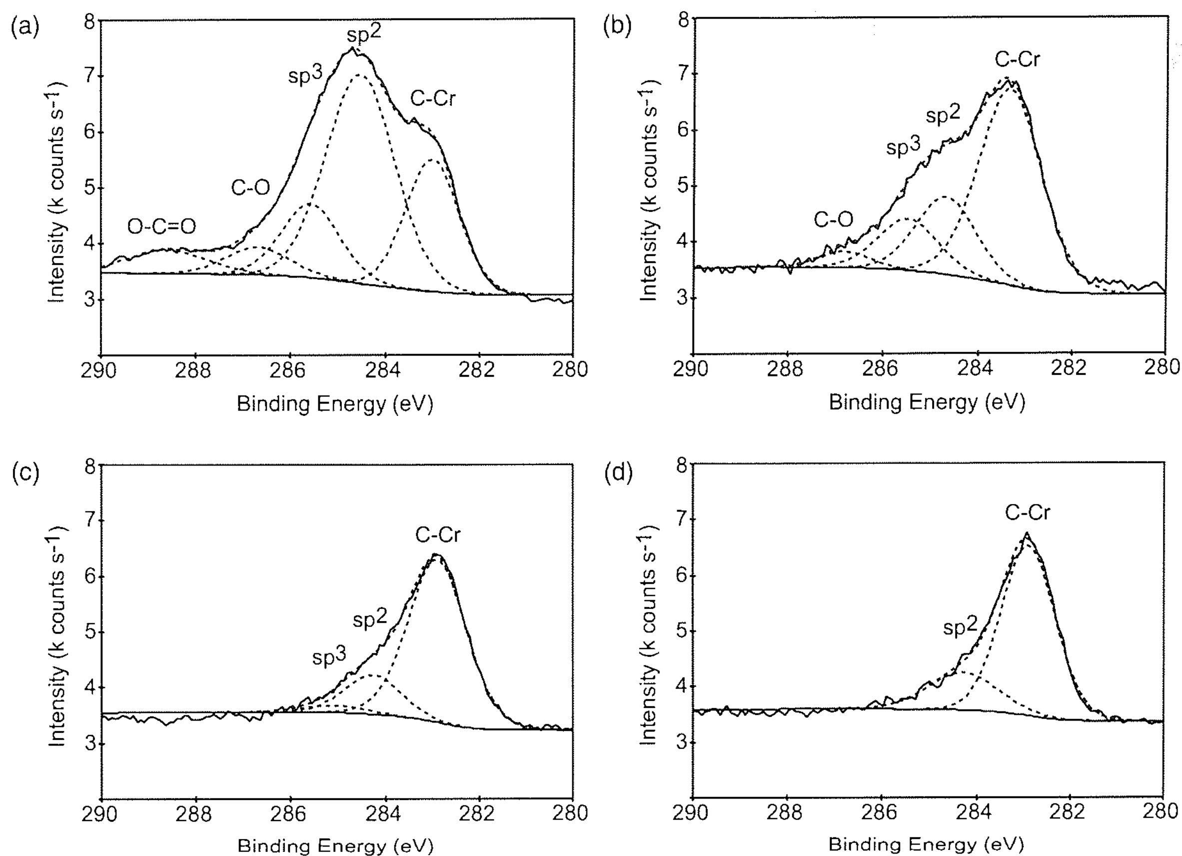

Figure 3.15 (a) C 1s peak of P1S3 before any Ar ion etching (b) C 1s peak of P1S3 etched to a depth of 9 nm with Ar ions (c) C 1s peak of P1S3 etched to a depth of 27 nm with Ar ions (d) C 1s peak of P1S3 etched to a depth of 63 nm with Ar ions. Note: the C-C bonding has been interpreted as two symmetrical sp^3 and sp^2 components but could equally have been represented by a single broader asymmetric C-C peak (see section 3.1.1).

The Cr 2p peaks of the P1S3 sample prior to Ar^+ ion etching and after 9 nm depth of etching, are shown in Figure 3.16. The surface result showed the Cr 1/2p and Cr 3/2p peaks to exist as overlapped doublets. The energy shift between the components of the doublets was determined to be 2.1 eV which is in agreement with the energy shift for Cr_2O_3 compared with elemental Cr [248]. Following the first etch depth, the 2.1 eV shifted component was no longer present, which corresponded with the loss of O from the relative atomic concentration (RAC) values (Figure 3.12 (f)) providing evidence that Cr was bonded to O in the outer layers.

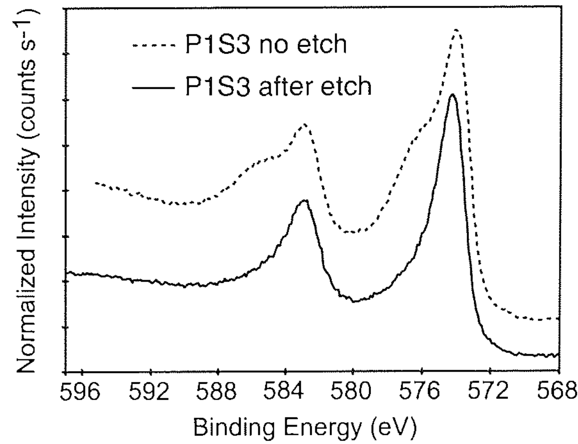

Figure 3.16 Cr 2p peaks of P1S3 with and without Ar ion etching.

3.2.1.1.3 Nanoindentation analysis

Hardness and elastic modulus results are given in Table 3.1. The P1S3 coating had a significantly lower hardness and higher elastic modulus than the other two coatings.

Table 3.1 Hardness and elastic modulus results.

	P1S1	P1S2	P1S3
Hardness (GPa)	11.5 +/- 1.0	11.2 +/- 0.8	8.4 +/- 0.5
Elastic modulus (GPa)	157 +/- 15	129 +/- 8	187 +/- 3

The results of the multipass nanoscratch wear test are given in Figure 3.17 as measured by the depth of the wear track. The depths were measured from the topography scans by determining the height difference between the minimal load and 100 mN load sections of the track. There may be contributions to this result from both wear and plastic deformation, but AFM scans across the tracks suggest that material wear was the greater contributor. It can be seen that the wear track depth increased with increasing Cr content, as one would expect from the relative hardness values.

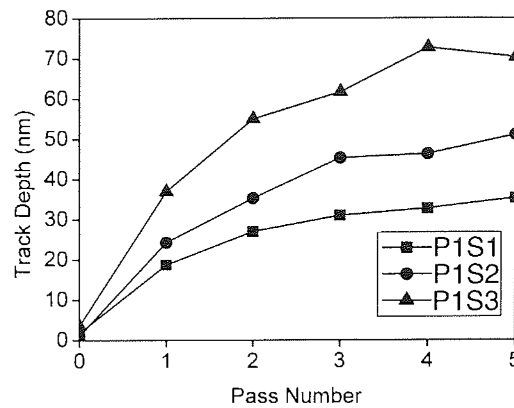

Figure 3.17 Multipass nanoscratch wear test results.

Frictional forces were measured during the series of wear tests. From this, the coefficient of friction was calculated. The results are given in Figure 3.18. Initially, the coefficient of friction decreased with Cr content, but after 4 or 5 passes there was no significant difference in the coatings.

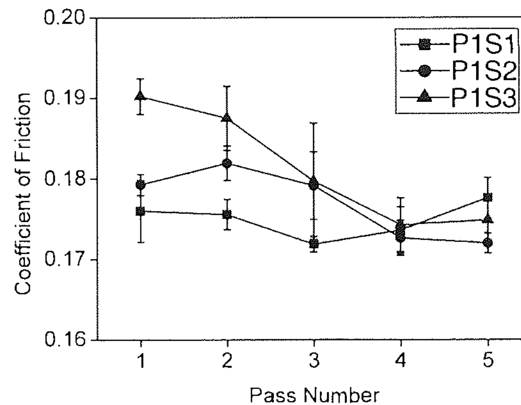

Figure 3.18 Coefficient of friction values for the three coatings after each wear pass with the standard error range.

3.2.2 Experiment to investigate the effects of pulsed substrate biasing with 150 nm coatings

The purpose of this experiment was to statistically analyse all of the results together in order to draw general inferences about the relationships between pulsed substrate biasing and coating quality. It is not practical to present all of the data and analysis work. Mean values and where appropriate standard errors of measurements are given in Table 3.2.

Typical examples of scratch test images and AFM scans are given in Figure 3.19 and Figure 3.20. These show clear differences in critical load and surface topography peak spacing. It can be seen that the critical load to complete failure of the coating was significantly lower with test P3S9 than with test P3S3. It can also be seen that the surface topography peak spacing of test P3S11 was significantly higher than test P3S5.

Table 3.2 150 nm bias tests. Mean values of measurements with standard errors bracketed. Surface composition data is bracketed for ease of interpretation.

	Hardness (GPa)	Reduced modulus (GPa)	Critical load (mN)	Surface roughness (nm) *	Coating thickness (nm)	Composition (%) (C)(Cr)(O)(Ar)(Si)
P3S1	12.3 (1.0)	154 (8)	100 (<1)	0.82[a] 65[b] 1.97(0.13)[c]	150	(82.6)(1.6)(10.2)(1.3)(4.1)
P3S2	12.4 (0.4)	183 (3)	100 (<1)	1.01[a] 60[b] 2.43(0.08)[c]	160	(87.1)(4.1)(5.9)(2.1)(0.8)
P3S3	13.9 (0.7)	169 (4)	93 (2)	1.19[a] 75[b] 2.85(0.06)[c]	140	(85.6)(4.7)(7.0)(2.4)(0.3)
P3S4	15.2 (0.5)	184 (6)	100 (<1)	0.53[a] 95[b] 1.14(0.05)[c]	145	(89.1)(2.6)(6.1)(1.9)(0.3)
P3S5	14.9 (1.1)	174 (6)	72 (<1)	1.13[a] 50[b] 2.91(0.13)[c]	150	(85.9)(4.3)(6.8)(3.1)(0.0)
P3S6	15.4 (0.4)	190 (2)	70 (3)	0.67[a] 50[b] 1.67(0.06)[c]	140	(90.6)(1.9)(4.5)(3.0)(0.0)
P3S7	15.4 (0.9)	182 (3)	68 (<1)	0.60[a] 85[b] 1.13(0.04)[c]	150	(83.7)(4.0)(8.0)(3.0)(1.4)
P3S8	15.3 (0.7)	183 (5)	92 (1)	0.98[a] 50[b] 2.31(0.13)[c]	160	(84.8)(2.7)(7.6)(2.4)(2.4)
P3S9	15.6 (1.0)	173 (9)	61 (1)	1.00[a] 75[b] 2.36(0.06)[c]	150	(85.9)(3.3)(5.8)(3.7)(1.3)
P3S10	17.5 (1.0)	218 (16)	91 (<1)	0.23[a] 60[b] 0.49(0.02)[c]	150	(87.8)(2.5)(5.3)(3.6)(0.8)
P3S11	17.1 (0.7)	215 (11)	91 (1)	0.66[a] 100[b] 1.08(0.05)[c]	180	(90.1)(1.7)(4.7)(2.7)(0.8)
P3S12	19.3 (0.5)	209 (4)	62 (2)	0.55[a] 70[b] 1.24(0.07)[c]	150	(89.3)(3.1)(4.0)(3.6)(0.0)
* a = Ra, b= peak spacing, c = peak height.						

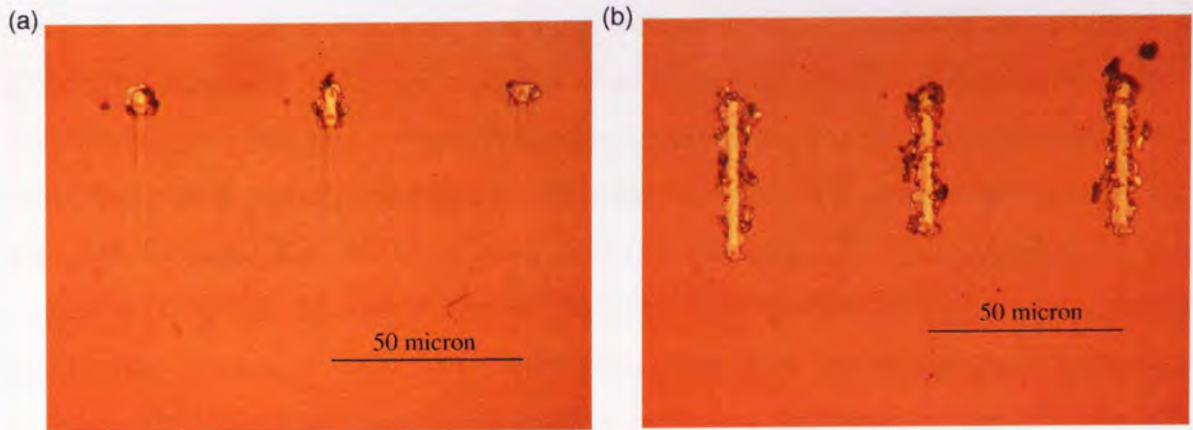

Figure 3.19 Optical microscopy photograph of the nanoscratch test results from (a) film P3S9 (b) film P3S3.

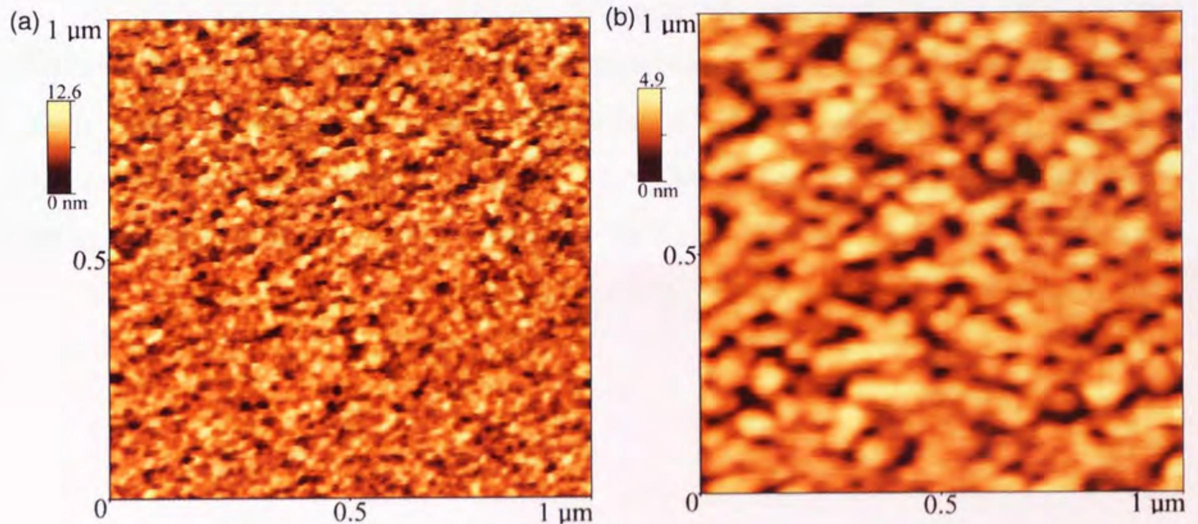

Figure 3.20 AFM scan of the surface of (a) film P3S5 (b) film P3S11.

The complete set of results from the nanoindentation and AFM tests were analysed using the analysis of variance (ANOVA) statistical procedure and the eighteen separate output plots and statistical analyses are summarised in Table 3.3 for ease of comparison. The columns show the three test parameters subdivided into the test values used. The results under the column headings were calculated by finding the mean of the total group of data that had that particular test parameter setting. The mean values are derived from replicated testing and also samples with different coating parameters so they are subject to random errors from within the replicated group and variation from differences in the other coating parameters, therefore it would be misleading to quote an error against these

numbers. The ANOVA procedure separates the two levels of variation and produces a probability statistic P and F value as described in section 1.4. The mean results simply demonstrate the effect that a particular parameter exerts and for ease of interpretation the values have been spatially positioned within the table cells to represent the shape of the main effects plots. The cells have been shaded to represent the significance of the test parameter as given by the P and F statistics: no shading indicating the greatest significance compared with the other parameters and darker shading indicating progressively less significance. The P and F statistics are displayed in brackets in the cell as a reference for the shading designation. Where there was no statistically significant effect caused by a particular test parameter the cells in the table have been shaded to the darkest level. The (average) standard deviation (s) for individual test measurements has been included in the first column for reference. A linear regression analysis was performed on the XPS elemental concentration results where voltage was varied over three levels. A two-sample t-test was used for the XPS results where frequency and pulse were varied over two levels. The mean values have been entered into the table and shading has been used in a similar manner to the ANOVA results. Values of R^2(adjusted) from the regression analysis and the probability statistic from the t-test have been included for reference.

Table 3.3 150nm bias tests. Main effects results from ANOVA, regression and t-tests.

	Bias voltage (V) 30	60	90	Bias frequency (KHz) 50	150	Bias Pulse width (ns) 500	2500
Hardness (GPa) (s = 3.0 GPa)	13.4	15.8	17.4	15.0	16.0	14.9	16.2
	(P=	0.000	F= 22)	(P= 0.038	F= 4)	(P= 0.006	F= 8)
Reduced modulus (GPa) (s = 25 GPa)	173	181	203	181	190	178	193
	(P=	0.000	F= 18)	(P= 0.036	F= 4)	(P= 0.000	F= 13)
Critical load (mN) (s = 1.6 mN)	99.0	82.4	74.5	87.2	83.4	82.0	88.6
	(P=	0.000	F= 385)	(P= 0.000	F= 26)	(P= 0.000	F= 83)
Ra (nm) (s = 0.073 nm)	0.888	0.843	0.608	0.810	0.750	0.897	0.662
	(P=	0.000	F= 16)	(P= 0.191	F= 2)	(P= 0.000	F= 30)
Mean peak height (nm) (s = 0.35 nm)	2.10	2.01	1.29	1.97	1.63	2.05	1.55
	(P=	0.000	F= 120)	(P= 0.000	F= 55)	(P= 0.000	F= 118)
Mean peak spacing (nm) (s = 6 nm)	74	60	76	61	79	75	65
	(P=	0.006	F= 8)	(P= 0.000	F= 27)	(P= 0.015	F= 8)
Thickness (nm) (s = 7 nm)	149	150	157	150	154	153	151
	(P=	0.088	F= 3)	(P= 0.223	F= 2)	(P= 0.461	F= 1)
C concentration (%)	86.1	86.3	88.3	86.7	87.1	85.6	88.1
	(R^2(ad)=		4.4%)	(P =	0.777)	(P =	0.096)
Cr concentration (%)	3.3	3.2	2.7	3.0	3.1	3.3	2.8
	(R^2(ad)=		0.0%)	(P =	0.780)	(P =	0.493)
O concentration (%)	7.3	6.7	5.0	6.4	6.2	7.1	5.6
	(R^2(ad)=		26.7%)	(P =	0.865)	(P =	0.143)
Ar concentration (%)	1.9	2.9	3.4	2.8	2.7	2.7	2.8
	(R^2(ad)=		68.6%)	(P =	0.774)	(P =	0.885)
Si concentration (%)	1.4	1.0	0.7	1.2	0.9	1.3	0.7
	(R^2(ad)=		0.0%)	(P =	0.689)	(P =	0.418)

The ANOVA analysis also produced a series of output plots and statistical analyses of the interactions between the three test parameters. As with the main effects analysis, F and P statistics are produced. The results are summarised in Table 3.4. The column headings show the three test parameters and the sub-headings define the primary interactions that can exist. Due to the complex interactions that existed within the 36 generated interactions plots, the results have been categorised into 3 groups. Where there was no statistically significant interaction between two parameters (for a given set of measurements) the corresponding cell has been shaded to the darkest level. Where there was an interaction but the general trend of the effect remained the same (where there was just a change in the gradient of the effects plot) the corresponding cell has been shaded to a medium level. Finally, where there was an interaction that inverts the trend of the effect or radically altered the shape, the corresponding cell has been left un-shaded. For reference, the P and F values for each potential interaction have been included.

Table 3.4 150 nm bias tests. Primary interaction effects from the ANOVA analysis.

	Bias voltage		Bias frequency		Bias pulse width	
	Frequency interaction	Pulse width interaction	Voltage interaction	Pulse width interaction	Voltage interaction	Frequency interaction
Hardness	P=0.02 F=3.80	P=0.55 F=0.61	P=0.02 F=3.80	P=0.70 F=0.15	P=0.55 F=0.61	P=0.70 F=0.15
Reduced modulus	P=0.46 F=0.78	P=0.29 F=1.26	P=0.46 F=0.78	P=0.01 F=8.05	P=0.29 F=1.26	P=0.01 F=8.05
Critical load	P=0.28 F=1.33	P=0.00 F=122	P=0.28 F=1.33	P=0.00 F=205	P=0.00 F=122	P=0.00 F=205
Ra	P=0.65 F=0.44	P=0.01 F=7.14	P=0.65 F=0.44	P=0.03 F=6.10	P=0.01 F=7.14	P=0.03 F=6.10
Mean peak height	P=0.00 F=5.75	P=0.00 F=27.7	P=0.00 F=5.75	P=0.00 F=66.4	P=0.00 F=27.7	P=0.00 F=66.4
Mean peak spacing	P=0.69 F=0.39	P=0.01 F=6.50	P=0.69 F=0.39	P=0.18 F=2.00	P=0.01 F=6.50	P=0.18 F=2.00

It is clear that bias voltage had the greatest effect on the coating properties, although significant effects and interactions involving frequency and pulse width were found. This will be examined in greater depth in the discussion section. The use of bias voltage was chosen for further investigation in the key coating parameter work.

3.2.3 Experiment to investigate four key coating process parameters with 150 nm coatings

The results of this experiment are displayed in a similar format to that given in section 3.2.2 and consequently the explanatory notes there are also applicable here. Mean values and where appropriate standard errors are given in Table 3.5.

Table 3.5 150 nm tests. Mean values of measurements with standard errors bracketed. Surface composition data is bracketed for ease of interpretation.

	Hardness (GPa)	Reduced modulus (GPa)	Critical load (mN)	Ra (nm)	Coefficient of friction	Thick ness (nm)	Composition (%) (C)(Cr)(O)(Ar)(Si)
P5S1	16.2 (0.3)	183 (5)	72 (3)	0.3 (<0.1)	0.18 (0.03)	125	(86.2)(0.0)(10.7)(2.0)(1.2)
P5S2	17.4 (0.5)	198 (3)	70 (1)	0.1 (<0.1)	0.26 (0.01)	97	(88.1)(0.0)(7.7)(3.2)(1.0)
P5S3	11.7 (0.3)	166 (5)	71 (2)	1.3 (0.2)	0.23 (0.03)	166	(73.4)(5.1)(16.7)(1.7)(3.1)
P5S4	13.2 (0.5)	186 (5)	58 (2)	0.5 (0.2)	0.20 (0.02)	151	(78.3)(6.6)(11.1)(2.9)(1.2)
P5S5	15.2 (0.5)	187 (5)	82 (1)	0.4 (0.1)	0.27 (0.03)	143	(87.7)(0.0)(9.8)(1.8)(0.7)
P5S6	19.4 (0.5)	204 (4)	79 (2)	0.3 (0.1)	0.24 (0.03)	155	(88.8)(0.0)(7.9)(3.0)(0.3)
P5S7	11.5 (0.2)	171 (3)	71 (2)	0.7 (0.1)	0.27 (0.01)	215	(79.0)(6.2)(11.1)(2.0)(0.8)
P5S8	14.6 (0.4)	210 (6)	73 (2)	1.0 (<0.1)	0.24 (0.01)	210	(75.6)(7.2)(14.4)(2.4)(0.5)
P8S1	16.4 (0.4)	170 (3)	76 (3)	0.2 (<0.1)	0.25 (0.00)	133	(83.6)(0.0)(10.8)(1.3)(3.1)
P8S2	18.4 (0.7)	194 (4)	78 (2)	0.1 (<0.1)	0.26 (0.01)	115	(86.7)(0.0)(9.0)(2.1)(2.2)
P8S3	13.0 (0.7)	160 (4)	85 (1)	1.0 (0.1)	0.24 (0.01)	167	(69.3)(6.3)(20.6)(1.3)(2.5)
P8S4	16.8 (0.8)	178 (5)	65 (1)	0.2 (<0.1)	0.22 (0.00)	146	(70.5)(7.4)(20.2)(1.8)(0.0)
P8S5	16.3 (0.6)	187 (5)	97 (4)	0.1 (<0.1)	0.23 (0.00)	136	(89.7)(0.0)(8.3)(2.0)(0.0)
P8S6	21.6 (0.6)	201 (4)	93 (3)	0.1 (<0.1)	0.26 (0.00)	133	(87.5)(0.0)(8.8)(2.1)(1.6)
P8S7	13.6 (0.8)	155 (4)	103 (4)	1.2 (n/a)	0.27 (0.00)	176	(67.1)(7.8)(22.3)(1.0)(1.8)
P8S8	15.6 (0.5)	177 (5)	106 (2)	0.6 (<0.1)	0.26 (0.00)	178	(68.6)(5.6)(22.3)(2.0)(0.0)

The complete set of results were analysed using the ANOVA statistical procedure and the results of this analysis are summarised in Table 3.6. The values have been spatially positioned and shaded to represent the shape of the main effects plots and the significance of the test parameter as in section 3.2.2. A two-sample t-test was performed on the XPS elemental concentration data and the results are displayed under the same criteria as given in section 3.2.2.

Table 3.6 150 nm tests. Main effects results from ANOVA and t-test analysis.

	Ar flow (sccm)		Adhesion Layer		Cr current (A)		Bias voltage (V)	
	12	28	None	Present	0.00	0.75	40	80
Hardness (GPa) (s = 2.4 GPa)	14.1	16.5	15.5	15.1	17.7	13.3	13.7	17.5
	(P=0.000	F=31)	(P=0.034	F=5)	(P=0.000	F=191)	(P=0.000	F=106)
Reduced modulus (GPa) (s = 20 GPa)	184	178	179	182	190	173	172	193
	(P=0.000	F=20)	(P=0.003	F=9)	(P=0.000	F=44)	(P=0.000	F=82)
Critical load (mN) (s = 3.7 mN)	71.7	87.9	71.8	83.5	81.3	76.7	79.3	77.8
	(P=0.000	F=155)	(P=0.000	F=160)	(P=0.161	F=2)	(P=0.002	F=11)
Ra (nm) (s = 0.11 nm)	0.58	0.37	0.47	0.50	0.21	0.78	0.60	0.37
	(P=0.008	F=8)	(P=0.128	F=2)	(P=0.000	F=130)	(P=0.000	F=30)
Coefficient of friction (s = 0.04)	0.24	0.24	0.22	0.25	0.23	0.24	0.24	0.24
	(P=0.757	F=0)	(P=0.007	F=8)	(P=0.632	F=0)	(P=0.773	F=0)
Coating thickness (nm) (s = 6 nm)	152	146	132	167	126	176	159	141
	(P=0.000	F=18)	(P=0.000	F=170)	(P=0.000	F=391)	(P=0.001	F=17)
C concentration (%)	82.1	77.9	79.5	80.5	87.3	72.7	79.5	80.5
	(P =	0.322)	(P =	0.819)	(P =	0.000)	(P =	0.813)
Cr concentration (%)	3.1	3.4	3.2	3.4	0	6.5	3.2	3.4
	(P =	0.888)	(P =	0.927)	(P =	0.000)	(P =	0.922)
O concentration (%)	11.2	15.3	13.3	13.1	9.1	17.3	13.8	12.7
	(P =	0.141)	(P =	0.934)	(P =	0.002)	(P =	0.694)
Ar concentration (%)	2.4	1.7	2.0	2.0	2.2	1.9	1.6	2.4
	(P =	0.025)	(P =	0.999)	(P =	0.348)	(P =	0.005)
Si concentration (%)	1.1	1.4	1.8	0.7	1.3	1.2	1.7	0.8
	(P =	0.611)	(P =	0.038)	(P =	0.964)	(P =	0.123)

ANOVA results relating to interactions between the four process control parameters are given in Table 3.7 and are displayed in a similar manner to that described in section 3.2.2.

Table 3.7 150 nm tests. Primary interaction effects from the ANOVA analysis.

Parameter:	Ar flow			Adhesion layer		Cr current
Interaction with:	Ad. Layer	Cr current	Bias volt	Cr current	Bias volt	Bias volt
Hardness	P = 0.926 F = 0	P = 0.110 F = 3	P = 0.182 F = 2	P = 0.106 F = 3	P = 0.007 F = 7	P = 0.338 F = 1
Reduced modulus	P = 0.235 F = 1	P = 0.015 F = 6	P = 0.430 F = 1	P = 0.639 F = 0	P = 0.452 F = 1	P = 0.105 F = 3
Critical load	P = 0.000 F = 35	P = 0.000 F = 18	P = 0.773 F = 0	P = 0.045 F = 4	P = 0.006 F = 9	P = 0.066 F = 4
Ra	P = 0.294 F = 1	P = 0.869 F = 0	P = 0.102 F = 3	P = 0.659 F = 0	P = 0.003 F = 11	P = 0.001 F = 14
Coefficient of friction	P = 0.269 F = 1	P = 0.411 F = 1	P = 0.915 F = 0	P = 0.929 F = 0	P = 0.443 F = 1	P = 0.404 F = 1
Thickness	P = 0.000 F = 43	P = 0.001 F = 14	P = 0.793 F = 0	P = 0.013 F = 7	P = 0.000 F = 21	P = 0.944 F = 0

Cr current was shown to have the greatest number of significant effects on the coating properties, although all of the tested coating parameters showed significance. A full analysis of the results will be given in the discussion section.

3.2.4 Experiment to investigate four key coating process parameters with 50 nm coatings

A summary of the results from this experiment is given in Table 3.8. Again a similar format is used to that in the previous sections. Hardness and modulus are quoted as median values due to an asymmetric distribution. Other values are given as mean results with standard errors as appropriate.

Table 3.8 50 nm tests. Median values of hardness and modulus and means of other measurements with standard errors bracketed. Surface (s) and bulk (b) composition data is bracketed for ease of interpretation.

	Hardness (GPa)	Reduced modulus (GPa)	Critical load (mN)	Ra (nm)	Coeff. friction	Thickness (nm)	Composition (%)* (C)(Cr)(O)(Ar)(Si)
P9S1	22.4	187	69 (5)	0.08 (0.01)	0.072 (0.001)	37 (1)	(88.3)(0.0)(6.9)(2.8)(2.0)s (94.8)(0.0)(0.7)(4.0)(0.4)b
P9S2	11.0	205	61 (2)	0.09 (0.01)	0.067 (0.002)	34 (2)	(89.5)(0.0)(8.3)(0.7)(1.5)s (95.8)(0.0)(1.4)(2.4)(0.2)b
P9S3	14.8	149	65 (2)	0.14 (0.01)	0.067 (0.002)	57 (2)	(88.4)(0.0)(8.6)(1.0)(2.0)s (95.7)(0.0)(1.3)(2.8)(0.0)b
P9S4	9.5	200	64 (2)	0.14 (0.02)	0.080 (0.005)	47 (3)	(80.0)(3.4)(11.5)(2.9)(2.1)s (80.6)(11.5)(1.7)(6.2)(0.0)b
P9S5	16.2	142	70 (1)	0.14 (0.01)	0.073 (0.005)	75 (1)	(71.9)(3.3)(19.7)(2.8)(2.4)s (81.7)(11.7)(1.2)(5.4)(0.0)b
P9S6	12.6	215	68 (2)	0.11 (0.01)	0.068 (0.003)	79 (3)	(79.6)(3.4)(11.3)(2.7)(3.1)s (80.4)(11.9)(1.5)(6.2)(0.0)b
P9S7	17.4	160	63 (1)	0.12 (0.01)	0.071 (0.003)	53 (2)	(88.5)(0.0)(7.6)(2.2)(1.7)s (95.7)(0.0)(1.2)(2.8)(0.0)b
P9S8	9.2	212	60 (2)	0.13 (0.01)	0.074 (0.003)	45 (1)	(77.9)(2.5)(14.9)(1.5)(3.2)s (82.3)(10.6)(2.2)(4.9)(0.0)b

* s = surface analysis, b = bulk analysis following 10 nm Ar ion etch.

The complete set of results were analysed using the ANOVA statistical procedure and the results of this analysis are summarised in Table 3.9. No significant effects were calculated for the hardness and reduced modulus data. However, the reliability of the ANOVA procedure is reduced when data diverges from a normal distribution, which is the case here as the low depth hardness and modulus data are asymmetrically distributed. For this reason the hardness and reduced modulus results were analysed by two-sample t-test along with the composition data. Again the values have been spatially positioned and shaded as described in section 3.2.2.

Table 3.9 50 nm tests. Main effects results from ANOVA and t-test analysis.

	Ar flow (sccm)		Adhesion Layer		Cr current (A)		Bias voltage (V)	
	12	28	None	Present	0.00	0.75	40	80
Hardness (GPa)	12.6	15.7	13.0	15.3	16.4	11.9	11.9	16.4
	(P =	0.389)	(P =	0.550)	(P =	0.179)	(P =	0.199)
Reduced modulus (GPa)	195	173	201	167	175	192	195	172
	(P =	0.321)	(P =	0.142)	(P =	0.461)	(P =	0.309)
Critical load (mN) (s = 6.2 mN)	64	66	63	66	64	65	64	66
	(P=0.119	F=2)	(P=0.098	F=3)	(P=0.563	F=0)	(P=0.119	F=2)
Ra (nm) (s = 0.03 nm)	0.11	0.12	0.11	0.13	0.11	0.13	0.12	0.12
	(P=0.432	F=1)	(P=0.026	F=5)	(P=0.021	F=6)	(P=0.527	F=0)
Coefficient of friction (s = 0.05)	0.072	0.071	0.073	0.070	0.069	0.074	0.069	0.074
	(P=0.971	F=0)	(P=0.154	F=2)	(P=0.070	F=4)	(P=0.046	F=5)
Coating thickness (nm) (s = 3 nm)	53	54	41	66	45	62	54	53
	(P=0.770	F=0)	(P=0.000	F=160)	(P=0.000	F=70)	(P=0.770	F=0)
C conc. (%) Surface	84	82	84	82	89	77	84	82
	(P =	0.596)	(P =	0.728)	(P =	0.009)	(P =	0.751)
C conc. (%) Bulk	88	89	88	88	96	81	89	88
	(P =	0.934)	(P =	0.996)	(P =	0.000)	(P =	0.956)
Cr conc. (%) Surface	1.7	1.4	1.5	1.7	0.0	3.2	1.5	1.7
	(P =	0.850)	(P =	0.896)	(P =	0.001)	(P =	0.890)
Cr conc. (%) Bulk	5.9	5.6	5.6	6.0	0.1	11.4	5.7	5.9
	(P =	0.952)	(P =	0.930)	(P =	0.000)	(P =	0.981)
O conc. (%) Surface	9.7	12.5	10.4	11.8	7.9	14.3	10.7	11.5
	(P =	0.429)	(P =	0.691)	(P =	0.048)	(P =	0.841)
O conc. (%) Bulk	1.5	1.3	1.5	1.3	1.2	1.6	1.6	1.2
	(P =	0.700)	(P =	0.528)	(P =	0.127)	(P =	0.218)
Ar conc. (%) Surface	2.1	2.0	2.0	2.2	1.7	2.4	1.5	2.7
	(P =	0.840)	(P =	0.802)	(P =	0.234)	(P =	0.078)
Ar conc. (%) Bulk	4.4	4.3	4.4	4.3	3.0	5.6	4.1	4.6
	(P =	0.914)	(P =	0.953)	(P =	0.003)	(P =	0.647)
Si conc. (%) Surface	2.1	2.4	2.2	2.3	1.8	2.7	2.5	2.0
	(P =	0.512)	(P =	0.870)	(P =	0.041)	(P =	0.408)
Si conc. (%) Bulk	0.1	0.1	0.2	0.0	0.2	0.0	0.1	0.1
	(P =	0.662)	(P =	0.219)	(P =	0.219)	(P =	0.662)

ANOVA results relating to interactions between the four process control parameters are given in Table 3.10 and are displayed in a similar manner to that described in section 3.2.2.

Table 3.10 50 nm tests. Primary interaction effects from the ANOVA analysis.

Parameter:	Ar flow			Adhesion layer		Cr current
Interaction with:	Ad. Layer	Cr current	Bias volt	Cr current	Bias volt	Bias volt
Critical load	P > 0.300 F = 0	P > 0.300 F = 0	P = 0.015 F = 6	P > 0.300 F = 0	P > 0.300 F = 0	P > 0.300 F = 0
Ra	P > 0.300 F = 0	P > 0.300 F = 0	P > 0.300 F = 0	P > 0.300 F = 0	P > 0.300 F = 0	P > 0.300 F = 0
Coefficient of friction	P > 0.300 F = 0	P > 0.300 F = 0	P > 0.300 F = 0	P > 0.300 F = 0	P > 0.300 F = 0	P > 0.300 F = 0
Thickness	P > 0.300 F = 0	P > 0.300 F = 0	P = 0.001 F = 16	P > 0.300 F = 0	P > 0.300 F = 0	P > 0.300 F = 0

Again Cr had the greatest number of significant effects. Adhesion layer also showed significance. The main effects trends were similar to that measured at 150 nm for many coating properties, for example hardness, roughness, thickness and composition. This was not the case for reduced modulus. A full analysis of the results will be given in the discussion section.

3.2.5 Experiment to investigate a range of film thicknesses (2000 nm to 10 nm)

A summary of the results from this experiment is given in Table 3.11. Again a similar format is used to that in the previous sections. Low depth hardness and modulus results are quoted as median values due to an asymmetric distribution. Other values are given as mean results with standard errors as appropriate.

Table 3.11 Thickness range expt. Mean / median values of hardness and modulus and means of other measurements with standard errors bracketed. Surface (s) and bulk (b) composition data is bracketed for ease of interpretation.

	Thickness (nm)	Hardness (GPa)	Reduced modulus (GPa)	Critical load (mN)	Ra (nm)	Composition (%)* (C)(Cr)(O)(Ar)(Si)
P11S1	2000	18.8 (0.9)	194 (6)	334 (9)	2.1 (0.1)	(83.9)(1.7)(10.9)(3.5)(0.0)s (90.4)(4.0)(0.3)(5.0)(0.0)b
P11S2	149	18.5 (1.4)	166 (8)	54 (3)	0.42 (0.01)	(85.2)(1.2)(9.9)(3.0)(0.7)s (91.7)(2.7)(1.8)(3.5)(0.0)b
P11S3	55	16.3	215	46 (1)	0.63 (0.02)	(86.5)(1.0)(9.3)(2.5)(0.7)s (90.5)(2.8)(2.6)(4.0)(0.0)b
P11S4	20	N/A	N/A	36 (3)	0.43 (0.03)	(84.2)(1.7)(11.1)(2.2)(0.7)s (91.7)(2.6)(1.7)(3.9)(0.1)b
P11S5	10	N/A	N/A	32 (1)	0.47 (0.05)	(79.4)(3.2)(13.0)(2.4)(2.1)s
Ion etch Si	N/A	11.6 (1.0)	134 (6)	37 (3)	0.29 (0.01)	N/A

* s = surface analysis, b = bulk analysis following Ar ion etch.

Care has to be taken when interpreting the hardness and reduced modulus trends due to the uncertainties associated with nanoindentation testing very thin coatings, in the absence of replicated films as employed in the previous results sections. There appears to be no clear trend of hardness or reduced modulus with coating thickness, which is in agreement with the results reported in section 3.2.3 and 3.2.4. It was not possible to undertake Oliver-Pharr analysis with films of thickness 20 nm and below due to the depth signal being inseparable from the vibrational noise, even with a large number of replicated indentations.

It can be seen that critical load reduced with reducing coating thickness. The mode of coating failure also changed with thickness. Optical images of the nanoscratch test results of the five film thicknesses are shown in Figure 3.21 along with a test on ion-etched uncoated Si substrate. A clear point of coating failure was identified with the 2000, 150 and 50 nm films. No such point was observed with the 20 and 15 nm films and Si. The load where debris first appeared alongside the scratch was chosen as the point of critical load for the 20 and 15 nm films and Si. It can be seen that the 20 and 15 nm films offered negligible protection under the nanoscratch test when the results are compared with uncoated Si substrate.

The change of mode of coating failure can also be observed by comparing the scratch and topography depth-displacement plots from the NanoTest software (Figure 3.22). A sudden 'stepped' increase in scratch depth was observed on the topography scans, coincident with the optically identified point of critical load with the 2000, 150 and 50 nm films. No sudden failure was observed with the 20 and 15 nm films or uncoated Si. There was no significant difference between the nanoscratch results from the 20 nm, 15 nm and uncoated Si samples.

Coating roughness increased significantly at high thickness. However, there was little change in roughness over the range 150 – 10 nm. All coatings had significantly greater roughness than the ion-etched uncoated Si substrate.

XPS depth profile results are given in Figure 3.23. There were no clear trends observed between the coating atomic composition and thickness. The composition and structure of the five coatings was similar. In all cases the Cr adhesion layer was detected. The adhesion layer results of P11S4 and the total coating results of P11S5 will be subject to interference from the substrate material due to the feature sizes approaching the probe depth of XPS.

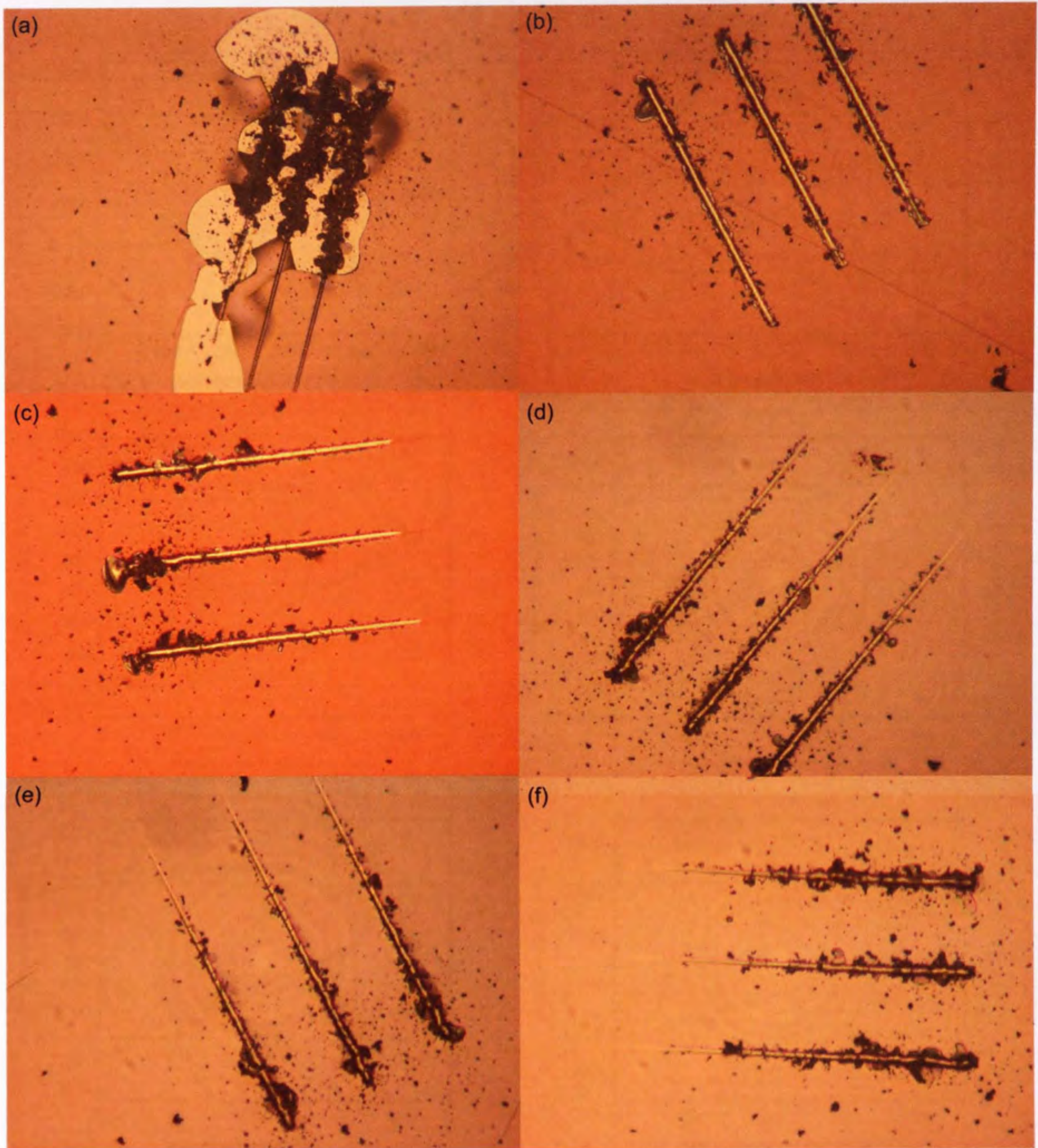

Figure 3.21 Optical microscope images of nanoscratch tests with film thickness (a) 2000 nm (b) 150 nm (c) 50 nm (d) 20 nm (e) 10 nm (f) ion etched uncoated Si. In all cases the scratches were separated by 50 μm.

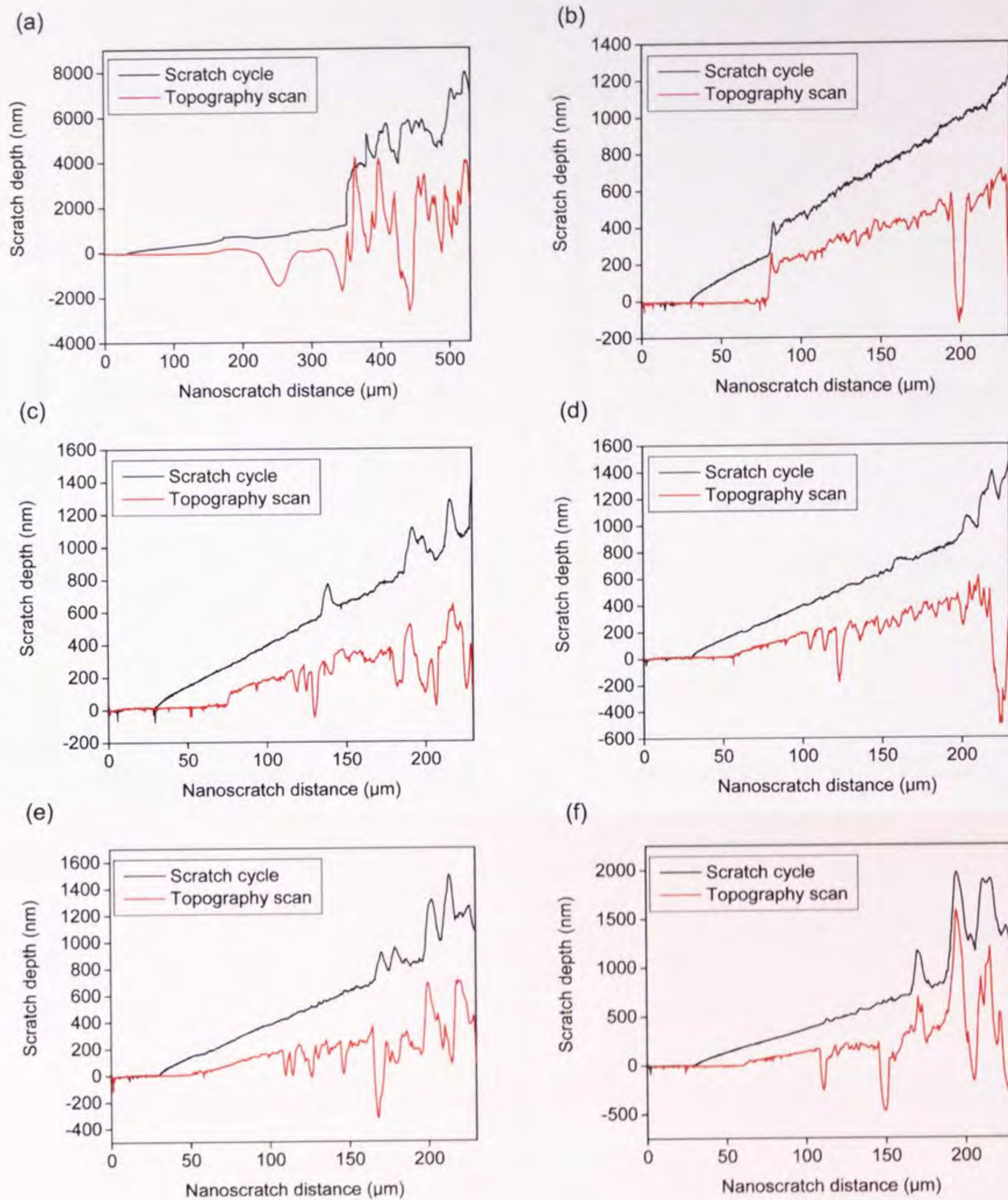

Figure 3.22 Scratch and topography depth-displacement plots from the nanoscratch tests with film thickness (a) 2000 nm (b) 150 nm (c) 50 nm (d) 20 nm (e) 10 nm (f) ion etched uncoated Si.

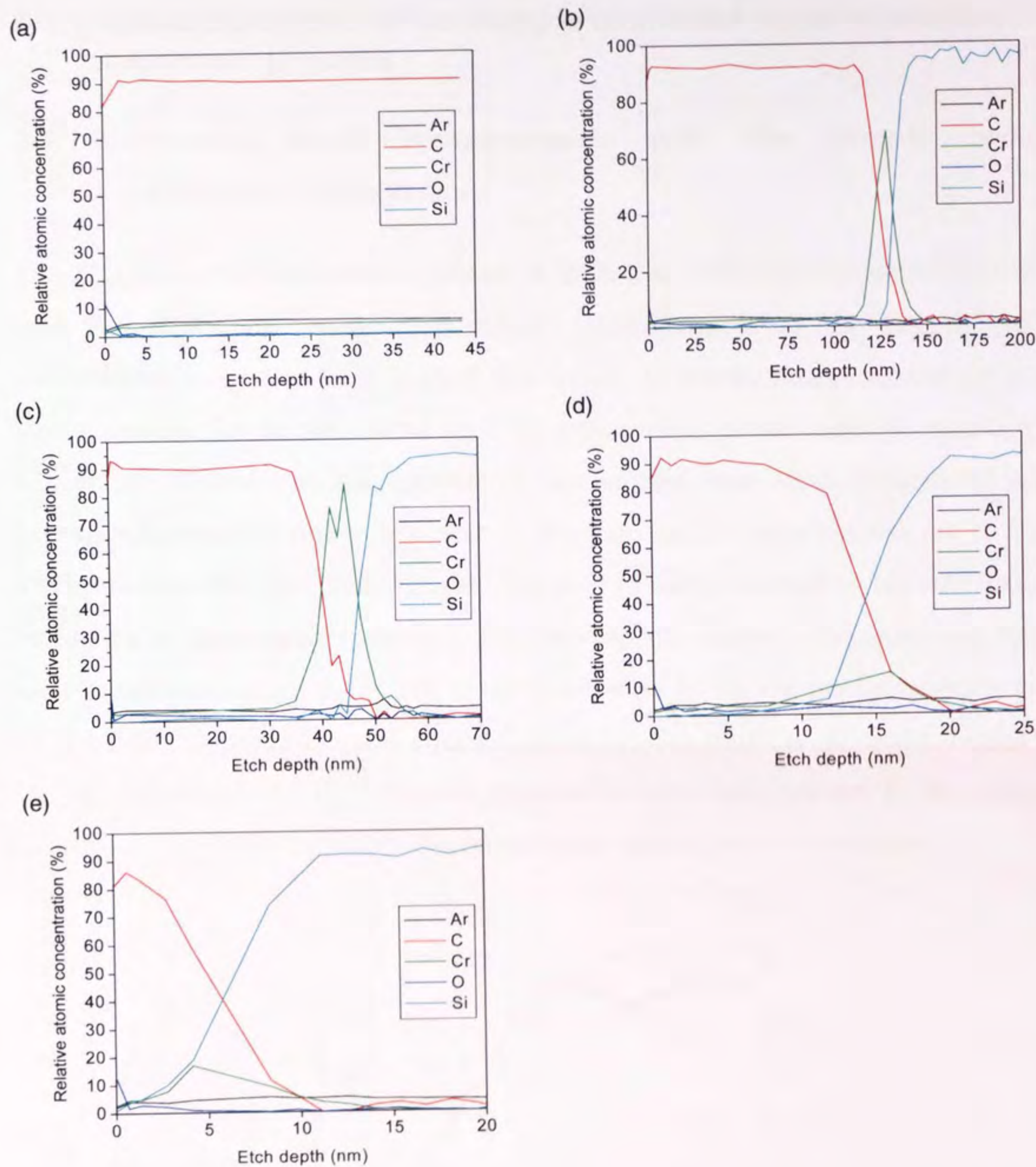

Figure 3.23 XPS depth profile results of (a) P11S1 (b) P11S2 (c) P11S3 (d) P11S4 and (e) P11S5.

3.3 *Experiments to investigate the nanotribology of a-C films*

3.3.1 Characterisation of the sample oscillated nanoindentation nanowear process

3.3.1.1 Dynamic depth measurements with the sample oscillated nanoindentation system

The design of a nanoindentation system is such that continuous measurements of both load and depth are made. A potentially useful aspect of the sample oscillated nanoindentation system is to exploit this feature to continuously monitor wear depth during testing. To be successful such an arrangement would need to maintain tight temperature control over long periods of time so that wear depth is measured and not expansion/contraction due to temperature changes. An investigation was run to monitor depth changes with time under typical conditions of nanowear testing, but with no sample oscillation. A temperature logging probe was installed, located a few mm away from the sample-indenter contact point. All components were left in the nanoindentation cabinet for 24 hours to reach thermal equilibrium. A typical result is shown in Figure 3.24. During the test period the recorded temperature remained constant to the instrument accuracy (+/- 0.05°C) and depth changes of many tens of nm were recorded.

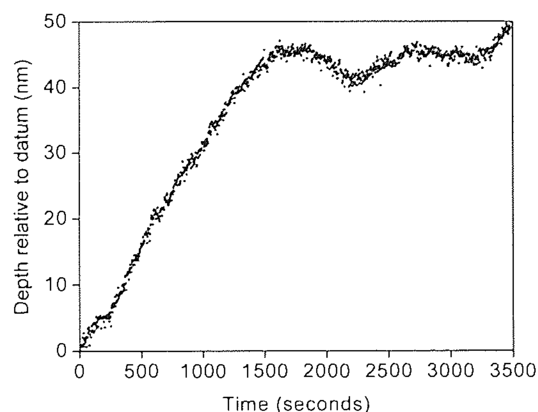

Figure 3.24 Results of an investigation into depth changes due to thermal drift under nanowear testing when all components have reached thermal equilibrium.

3.3.1.2 Low amplitude nanowear mode (experiments 1-9)

At high load (200 mN) a wear scar was present after an 18000 cycle test duration and progressively deepened to the final 72000 cycle test. All of the scars were circular, of approximate diameter 10 μm with a 'W' shaped cross-section (an example AFM micrograph is given in Figure 3.25(a)). The deepest region formed a circular trench around the edge of the wear scar. The depth of this trench was quite uneven but mean depths for the 18000, 36000, 54000 and 72000 cycle tests were measured at 10, 25, 35 and 40 nm respectively. A pattern was observed in the depth of the trenches such that the deepest regions were located at positions parallel to the direction of oscillation and the shallowest regions were located at positions perpendicular to the direction of oscillation. The difference between the depths at the parallel and perpendicular positions was a factor of approximately 1.5. At low load (10 mN) slight traces of wear debris could be observed for the 18000, 36000, 54000 and 72000 cycle tests, however after cleaning no scar could be identified by AFM. An extended duration 360000 cycle test was performed and an AFM micrograph is shown in Figure 3.25(b). The wear scar was similar in form to the high load although the trench was more irregular in shape and there was very little wear at the centre. The depth of the trench was more uneven with some points extending right through the total coating thickness. As with the high load test, the deepest regions tended to be located at positions on the contact that were parallel to the direction of oscillation.

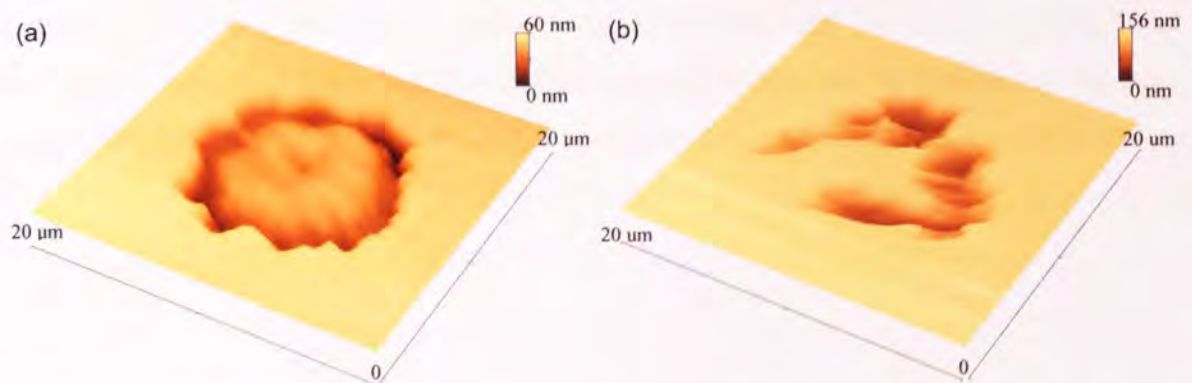

Figure 3.25 AFM micrograph of wear scars (a) after 72000 oscillations at 200 mN (b) after 360000 oscillations at 10 mN.

Calculations of initial contact radius and initial mean contact pressure based on the Hertzian contact theory are given in Table 3.12. Oscillation amplitude values have been estimated from the lengths of scratch lines visible in the early stages of wear scar development.

Table 3.12 Calculated contact radius and mean contact pressure values.

Test duration (minutes)	Normal load (mN)	Contact radius (μm)	Mean contact pressure (MPa)	Oscillation amplitude (μm)
0	200	5.4	2200	2
0	10	2	800	2

3.3.1.3 High amplitude nanowear mode (experiments 10-42)

At the higher oscillation amplitude a wear scar more typical of macro-scale reciprocating sliding conditions was produced as shown with AFM images of tests 27-30 in Figure 3.26.

An oscillation amplitude of 14 μm was estimated from the length of scratch lines visible in the early stages of wear scar development compared to about 2 μm in the fretting experiments. The wear scars typically show a 'U' shaped cross-section with considerable scoring and roughness. An approximation of the average depth at the centre of each 'U' shaped scar was made and this was plotted against the central scar width in order to analyse the contact pressures in more detail and understand the mode of wear. The measured results are plotted in Figure 3.27 along with the theoretical distribution for wear scar evolution that simply conforms to the geometric shape of the spherical counter-body.

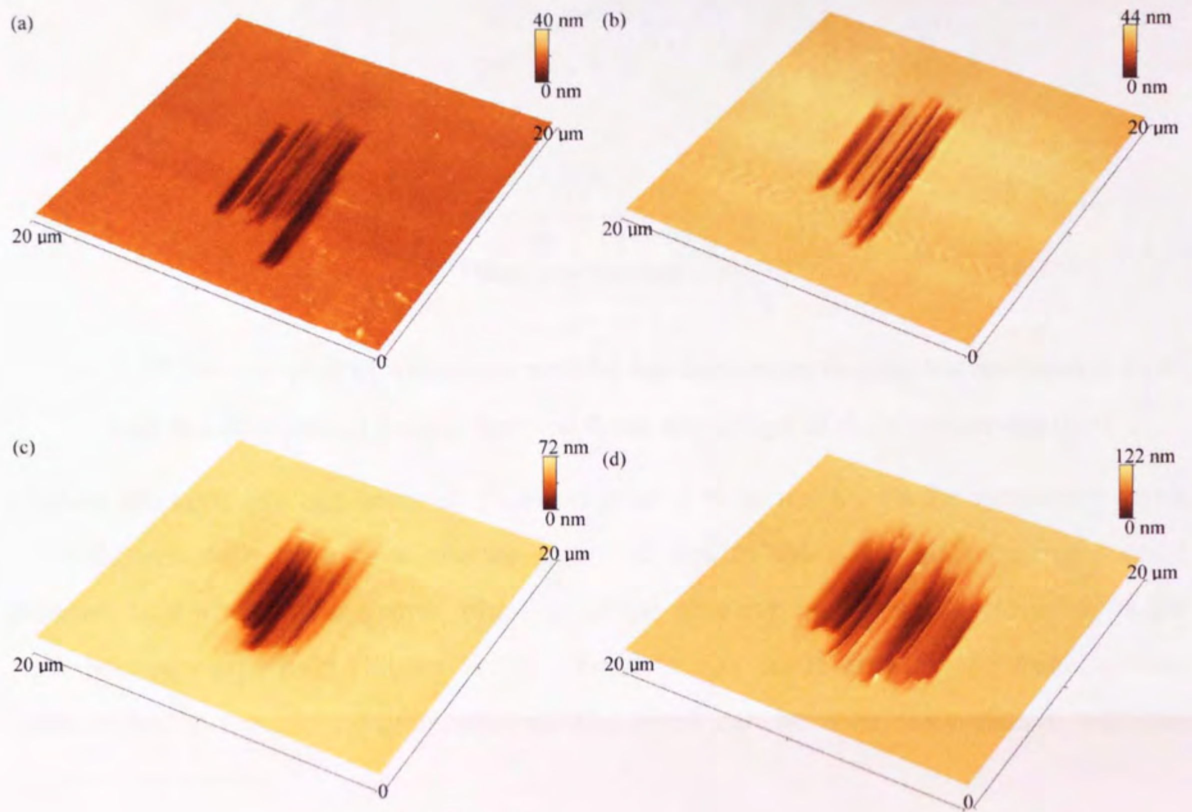

Figure 3.26 AFM micrograph of wear scars (a) after 18000 oscillations (test 27) (b) after 72000 oscillations (test 28) (c) after 144000 oscillations (test 29) (d) after 216000 oscillations (test 30).

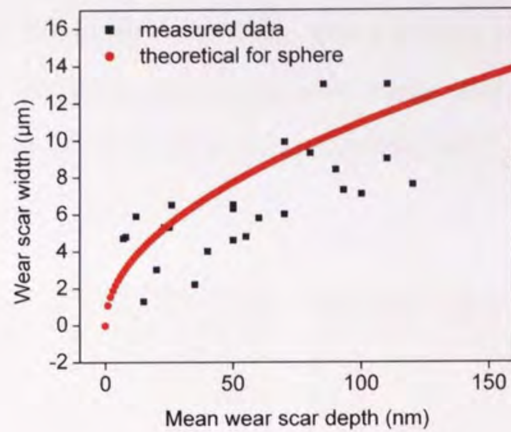

Figure 3.27 Scatter plot of wear scar widths against mean depths for measured data and the theoretical values derived from the shape of the counter-body.

Plotting the same average depth data against time of wear test shows the increasing depth trend flattens with time as would be expected due to the effect of reducing contact pressure as the wear scar grows, blunting of the abrasive particles and clogging of the gaps between asperities (Figure 3.28). The data has come from 9 different coating variants and is therefore quite scattered. The trend can be seen more clearly with the average data points.

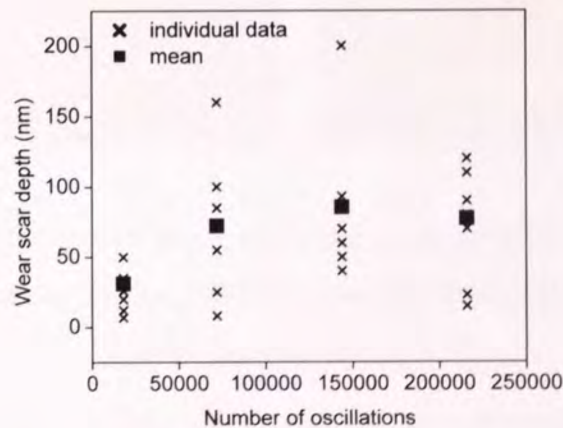

Figure 3.28 Scatter plot of all mean wear scar depths and group averages against number of oscillations.

Optical microscopy images of nanowear scar development prior to cleaning are shown in Figure 3.29 for tests 27-30. In all cases there was a central worn region, surrounded by a clean area of coating showing no measurable wear and a large amount of debris surrounding the entire area. The outer debris formed very quickly and increased only slightly with time.

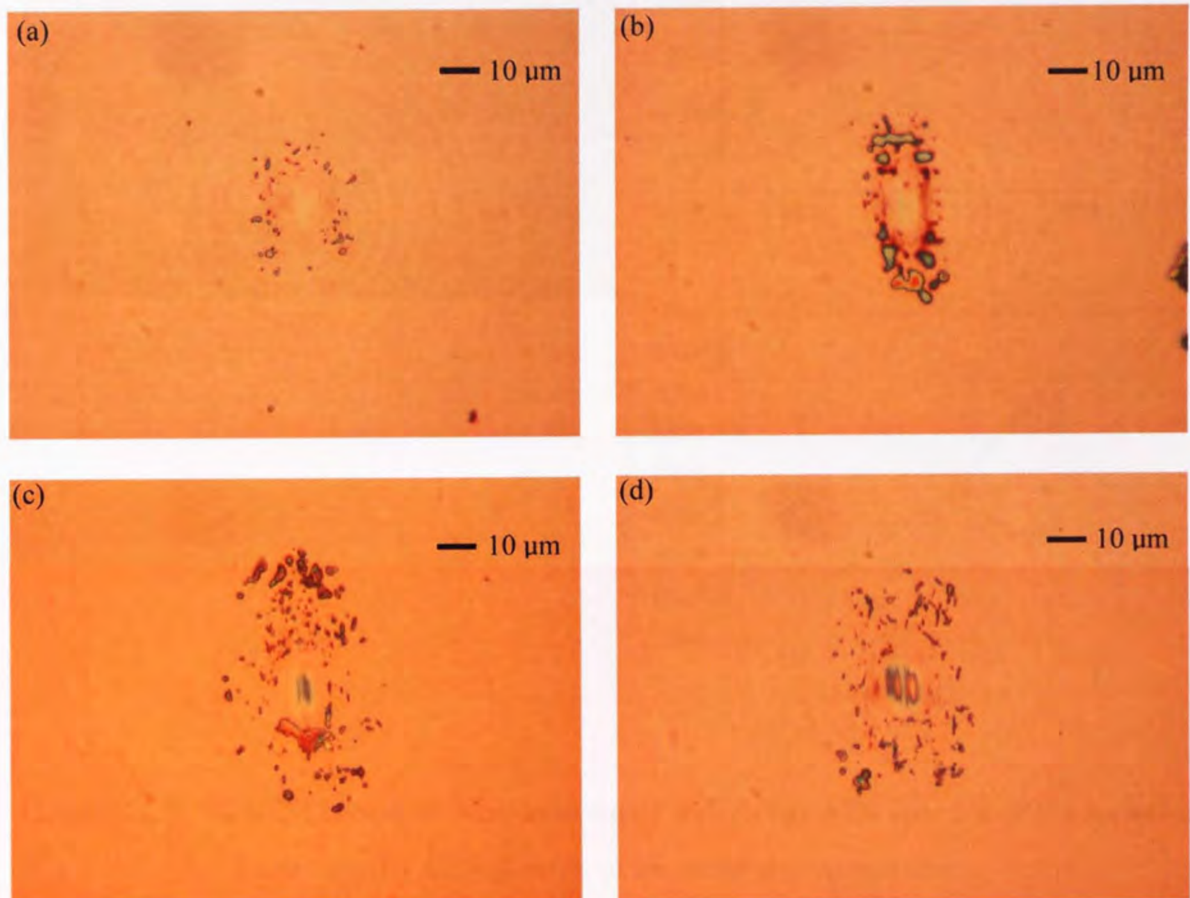

Figure 3.29 Optical microscopy images of wear scars (a) after 18000 oscillations (test 27) (b) after 72000 oscillations (test 28) (c) after 144000 oscillations (test 29) (d) after 216000 oscillations (test 30).

The outer debris from test 10 has been imaged by SEM and analysed by AES. The SEM images show the particles of debris to be very thin layers of material curled into tubes (Figure 3.30 (a)); such debris is often seen in macro-wear. From the Auger electron spectra, the only difference between the composition of the coating and that of the particles was the higher oxygen concentration in the latter which suggests post removal

oxidation (Figure 3.30 (b) and (c)). There was no Al present in the debris or wear scar showing that the ruby counter-body was not itself undergoing any wear.

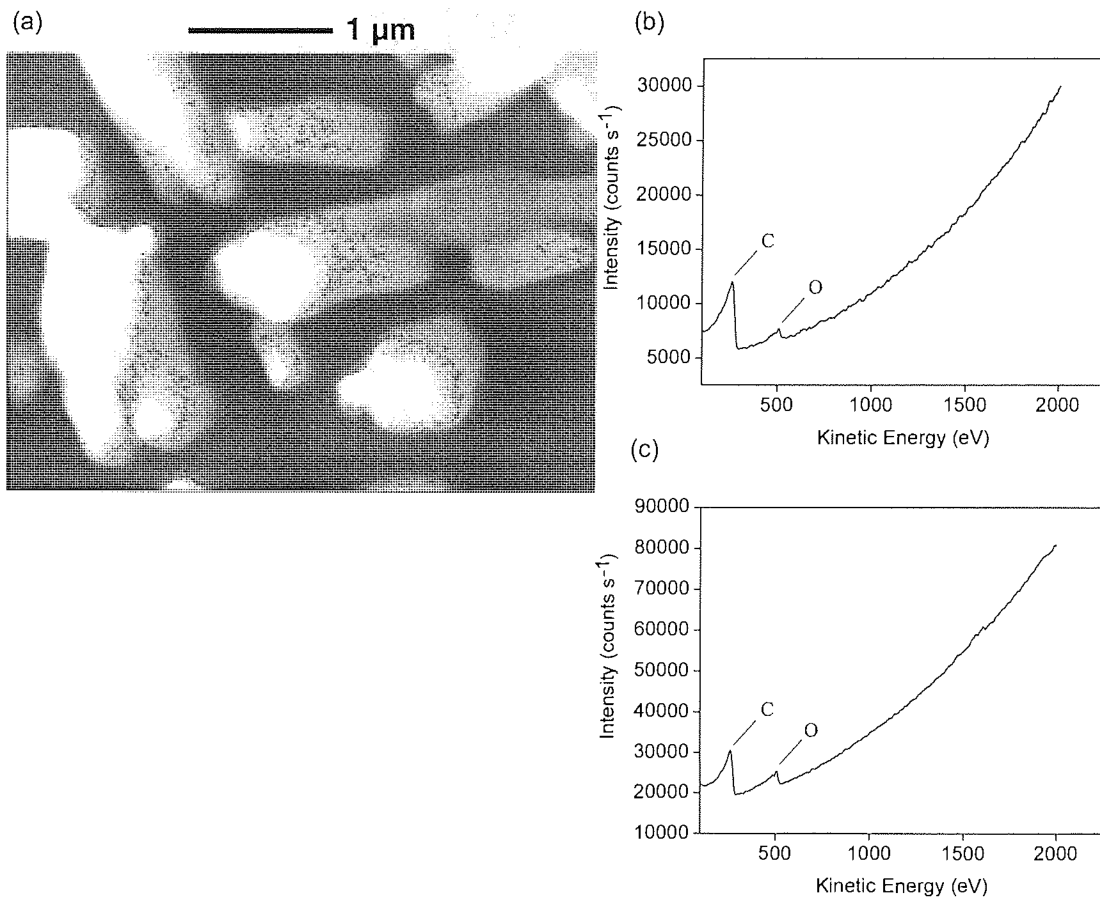

Figure 3.30 (a) SEM image of wear scar outer debris (a) AES spectra of the unworn coating (b) AES spectra of an outer debris particle.

Figure 3.31 shows small area AFM images of a region of the wear scar of test 10, with software shading in order to highlight the detail of the surface. The surface is clearly scored and there are some entrapped particles of debris within the wear tracks with similar dimensions to the tracks. Typical depths in the grooves below the unworn surface were 60 nm and groove widths 100 – 200 nm.

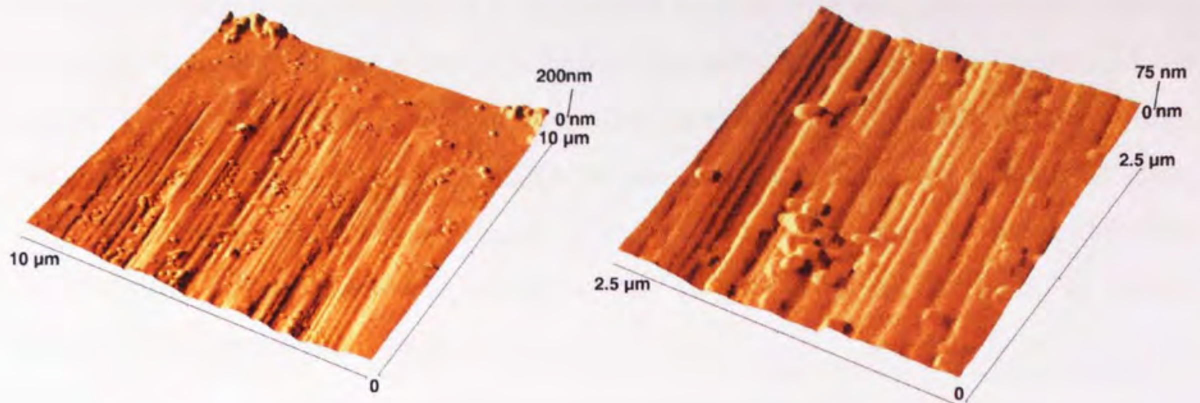

Figure 3.31 AFM micrographs of wear scar from test 10 with software shading to enhance the qualitative detail.

An AFM scan of the clean ruby ball surface is given in Figure 3.32(a). The surface of the wear scars was significantly rougher than that of the ruby counter-body. Ra values of the ruby ball and wear scars from test 10 and from test 38 were 3.0, 7.5 and 18.1 nm respectively. Single line AFM scans from: the ruby ball; the wear scar from test 10; the wear scar from test 38 and the untested surface of sample P5S7 are shown in Figure 3.32(b) for comparison.

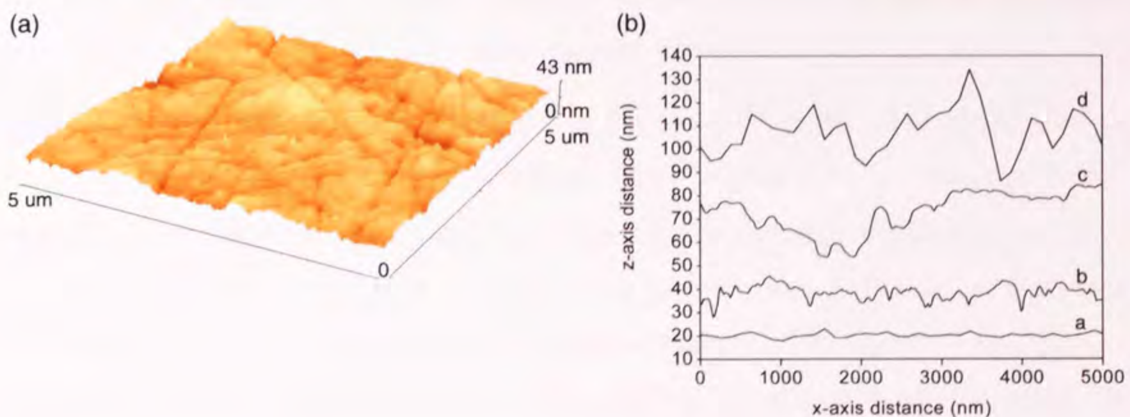

Figure 3.32 (a) AFM scan of the surface of the ruby ball (b) comparison of the surface topography of: a - untested P5S7; b – ruby ball; c – wear scar from test 10; d – wear scar from test 38.

Optical microscopy examination of the spherical ruby counter-body showed no evidence of counter-body wear after each test. A typical post test result is given in Figure 3.33, for test 30. The pattern of debris matched the pattern on the worn coating surface: there was a large quantity of debris around the perimeter and inside this there was a relatively clean zone. At the centre there was a build up of material which appeared to form a thin film over the ruby surface which was seen even after 18000 cycles and this could be readily removed by wiping with 2-Propanol.

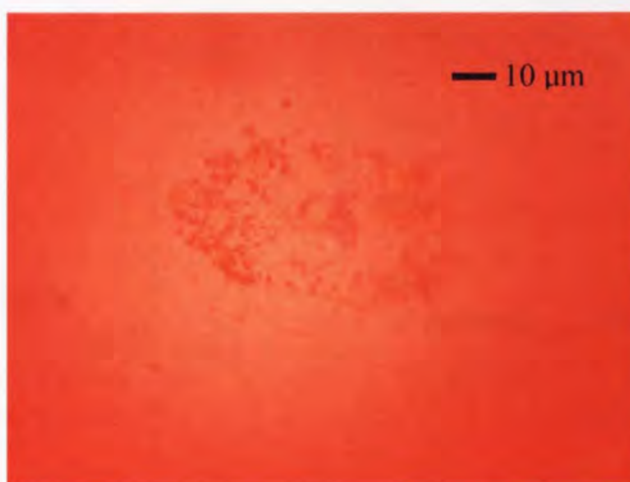

Figure 3.33 Optical microscopy image of debris and transfer film on the spherical ruby counter-body.

SEM and AES analysis was attempted at the central region of transfer film on the counter-body following testing of specimen P5S7 (Figure 3.34 (a) and (b)). Just C was detected, however significant charging of the sample occurred which caused low signal intensity. Monochromated XPS analysis of the transfer film and clean ruby surface was also attempted using a 120 µm X-ray spot size (Figure 3.34 (c) and (d)). Again, the signal intensity was low. The elements C, O and Al were positively detected. The C concentration at the transfer film was significantly higher than the adventitious C on the unworn ruby surface. No Cr was detected in the transfer film.

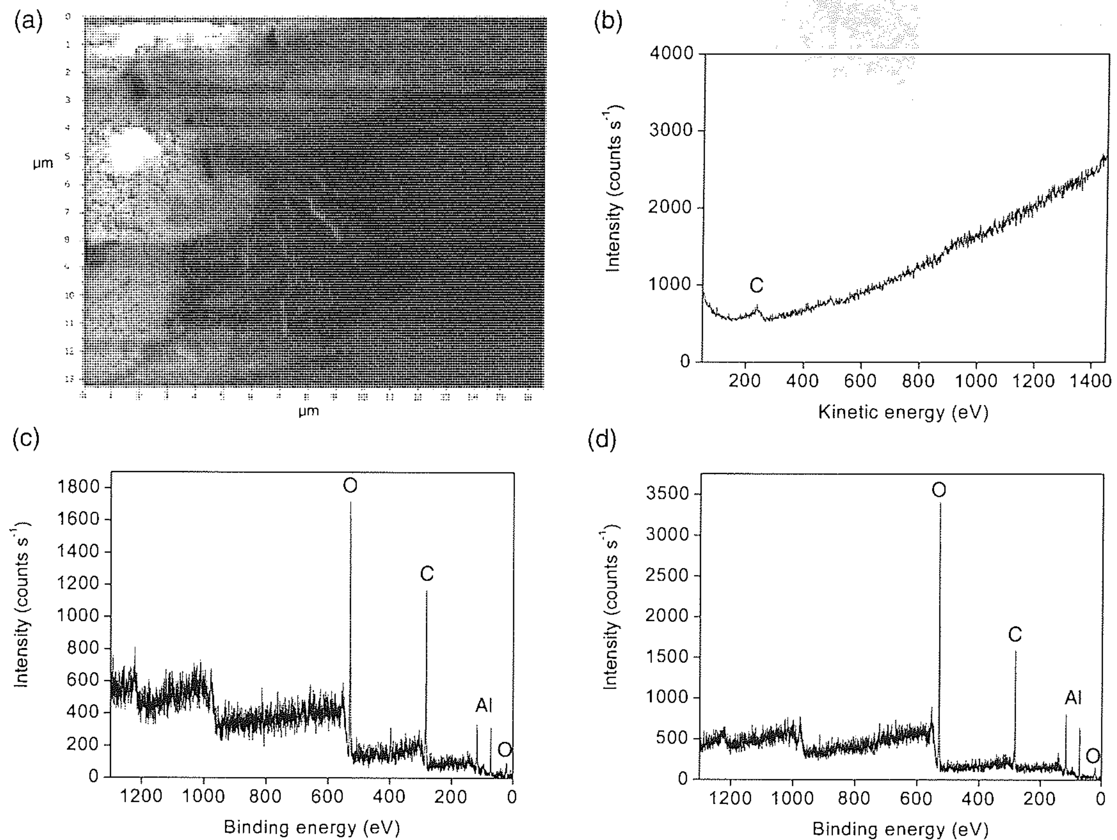

Figure 3.34 (a) SEM image of the central region of transfer film on the counter-body surface (b) AES analysis of the transfer film (c) XPS analysis of the transfer film (d) XPS analysis of the clean ruby surface.

For tests where the coating had been completely removed and the Si substrate reached, catastrophic fracture failure of the Si quickly occurred. An optical microscopy example of this is shown in Figure 3.35. An uncoated Si wafer was subjected to the wear test under the same conditions and significant fracture failure occurred after 3000 - 6000 cycles.

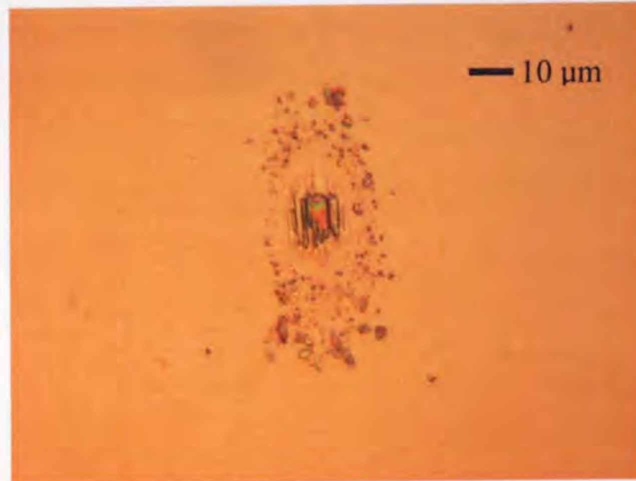

Figure 3.35 Optical microscopy image showing catastrophic failure of the Si substrate after total wear removal of the coating.

3.3.1.4 High amplitude nanowear contact conditions

As given in Table 3.12, the initial contact radius was calculated to be 2 μm and the initial mean contact pressure approximately 800 MPa based on the Hertzian contact theory. This is expected to fall rapidly as wear occurs and the spherical counter-body is supported by a larger area of contact. A first simple approximation of the change in contact radius and contact pressure as wear develops can be made by assuming that a wear scar forms that conforms to the shape of the counter-body with no consideration of elastic deformation: at 50, 100 and 150 nm wear depth the contact radii would be 3.9, 5.5 and 6.7 μm and the mean contact pressures would be 209, 105 and 71 MPa respectively. The contact radii would be expected to be greater and the mean pressure lower than these values due to elastic deformation of the coating and counter-body. From Figure 3.27 and from microscope observations of wear scars (Figure 3.29) it was clear that the total contact area was significantly greater than the measured wear zone. In order to take account of this, an empirical approach was taken: It was assumed that the clean area surrounding the wear scar indicated the extent of the contact zone. The radius of the clean area was measured from each wear test by optical microscopy and the results were plotted against average wear depth, Figure 3.36. Simply fitting the scatter plot with a straight line enabled an estimate of contact radii and contact pressure to be made: at 50, 100 and 150 nm wear

depth the contact radii were determined to be 5.2, 6.3 and 7.3 μm and the mean contact pressures 117, 80 and 60 MPa respectively.

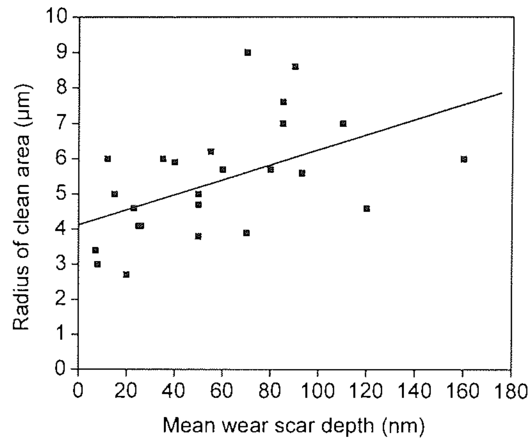

Figure 3.36 Scatter plot of mean wear depth against clean area radius.

3.3.2 Experiment to investigate the nanowear of a matrix of 150 nm coatings and the effect of four key coating process parameters

3.3.2.1 Measurement of specific wear rates and analysis of the complete data set

All AFM data of the wear scars were software processed to calculate the volume of coating material lost. During 9 of the extended period tests (out of a total of 76 data points), the coating was completely worn away and the Si substrate was exposed. In these cases the very poor tribological properties of Si resulted in large amounts of fracture damage of the substrate and therefore extremely high apparent material volume losses. In order to eliminate the error caused by the Si failure and to calculate an approximation of coating material lost due to wear, the area of the region with total coating loss was estimated by optical microscopy and this was multiplied by the nominal coating thickness. The approximated values fitted reasonably well with the other data points in the series, although it is recognised that Si wear debris could have an effect on the specific wear rate. The oscillation amplitude of the contacted counter-body was estimated to be 14 μm from the lengths of the wear scar tracks and from this the total distance travelled by the counter-body was calculated at 0.5, 2, 4 and 8 m for the 18000, 72000,

144000 and 216000 oscillation tests respectively. With knowledge of the volume of coating material lost, total distance travelled by the counter-body and the applied load, a value of specific wear rate was determined for each test. An initial analysis of the complete set of results yielded some important observations. The range of specific wear rates for all of the experimental data are given in a histogram in Figure 3.37. Given the asymmetric shape of the distribution, due to zero being a low wear rate limit, the use of a mean and standard deviation did not really capture the information from the data set. The second and third quartile (50% of the data) was bounded by the range 6 - 24 x 10^{-17} $m^3N^{-1}m^{-1}$; whilst the full range was 0.2 - 90 x 10^{-17} $m^3N^{-1}m^{-1}$.

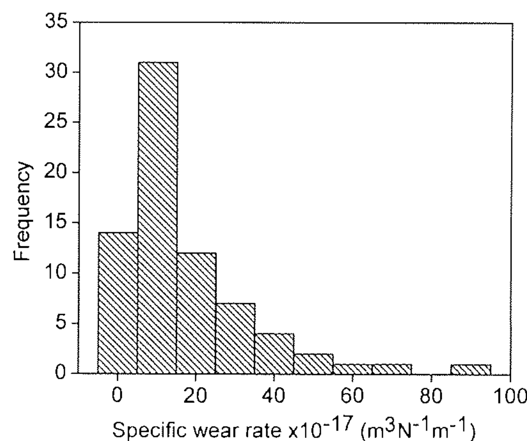

Figure 3.37 Histogram of all specific wear rate data for 150 nm coatings.

An assessment of changes to the specific wear rate with number of oscillations was made by splitting the data set into four sub-sets corresponding to the four test durations. The four data distributions are given as boxplots in Figure 3.38 for ease of comparison. From the results it can be seen that there was no significant change in specific wear rate with duration of test. After 18000 oscillations (30 minutes test duration) the nanowear process had reached a stable condition.

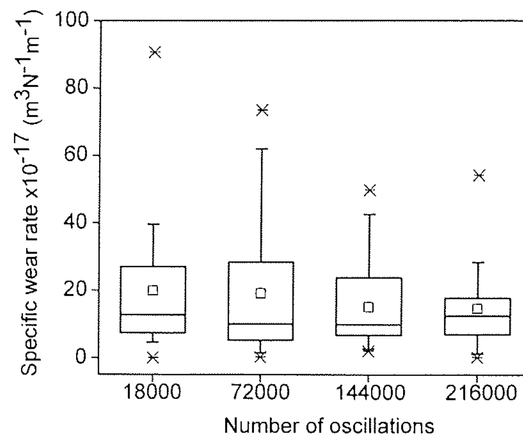

Figure 3.38 Boxplots showing the distribution of specific wear rate data against number of oscillations for 150 nm coatings. The box is defined by the 25th to 75th percentile range. The whiskers are defined by the 5th to 25th and 75th to 95th percentile ranges. The full data range is shown by the lined crosses. The median and mean are indicated by a horizontal line and small square respectively.

The individual specific wear rate values for each coating (8 in the case of tests 1-3 and 4 for all others) were averaged and the individual values were plotted against the grouped average values (Figure 3.39) in order to look for changes in the scatter of data. It was clear that there was an increase of scatter with increasing wear rate, even taking into account the greater error associated with the values that were estimated by optical microscopy.

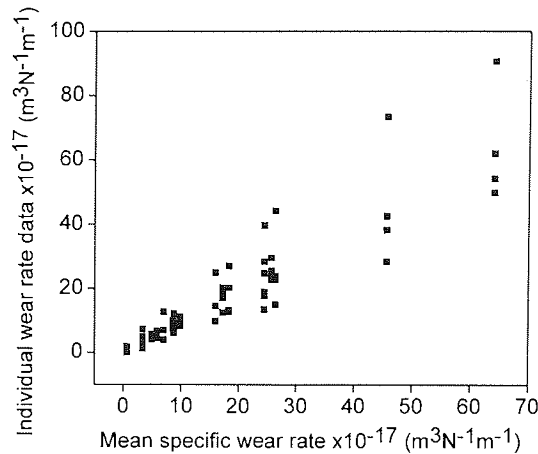

Figure 3.39 Scatter plot of individual specific wear rate measurements against group averages for each coating at 150 nm.

3.3.2.2 Statistical analysis of the effect of the four key process parameters using ANOVA

The specific wear rate results were analysed against the chosen process parameters using the ANOVA statistical procedure and the main effects results are given in Table 3.13 in a similar manner to that described in section 3.2.2.

Table 3.13 Main effects results from ANOVA analysis at 150nm.

	Ar flow (sccm)		Adhesion Layer		Cr current (A)		Bias voltage (V)	
	12	28	None	Present	0.00	0.75	40	80
Specific wear rate ($x 10^{-17} m^3N^{-1}m^{-1}$) (s = 5.8)	16	19	20	14	6	29	20	14
	(P=0.234	F=1)	(P=0.000	F=21)	(P=0.000	F=158)	(P=0.003	F=10)

ANOVA results relating to interactions between the four process control parameters are given in Table 3.14 and are displayed as in section 3.2.2.

Table 3.14 Primary interaction effects from the ANOVA analysis at 150 nm.

Parameter 1:	Ar flow			Adhesion layer		Cr current
Parameter 2:	Ad. Layer	Cr current	Bias volt	Cr current	Bias volt	Bias volt
Interaction	P = 0.494 F = 0	P = 0.916 F = 0	P = 0.000 F = 30	P = 0.000 F = 16	P = 0.103 F = 3	P = 0.607 F = 0

3.3.2.3 Correlations with the tribologically important properties of the coatings

Scatter plots showing the correlation between the nano-scale mean specific wear measurements and coating hardness, reduced modulus, H/E_r ratio, critical load, surface roughness, and thickness are given in Figure 3.40. Correlations with coating composition are given in Figure 3.41. The correlations were fitted with a straight line using a linear regression procedure and the r^2(adjusted) values are given for reference.

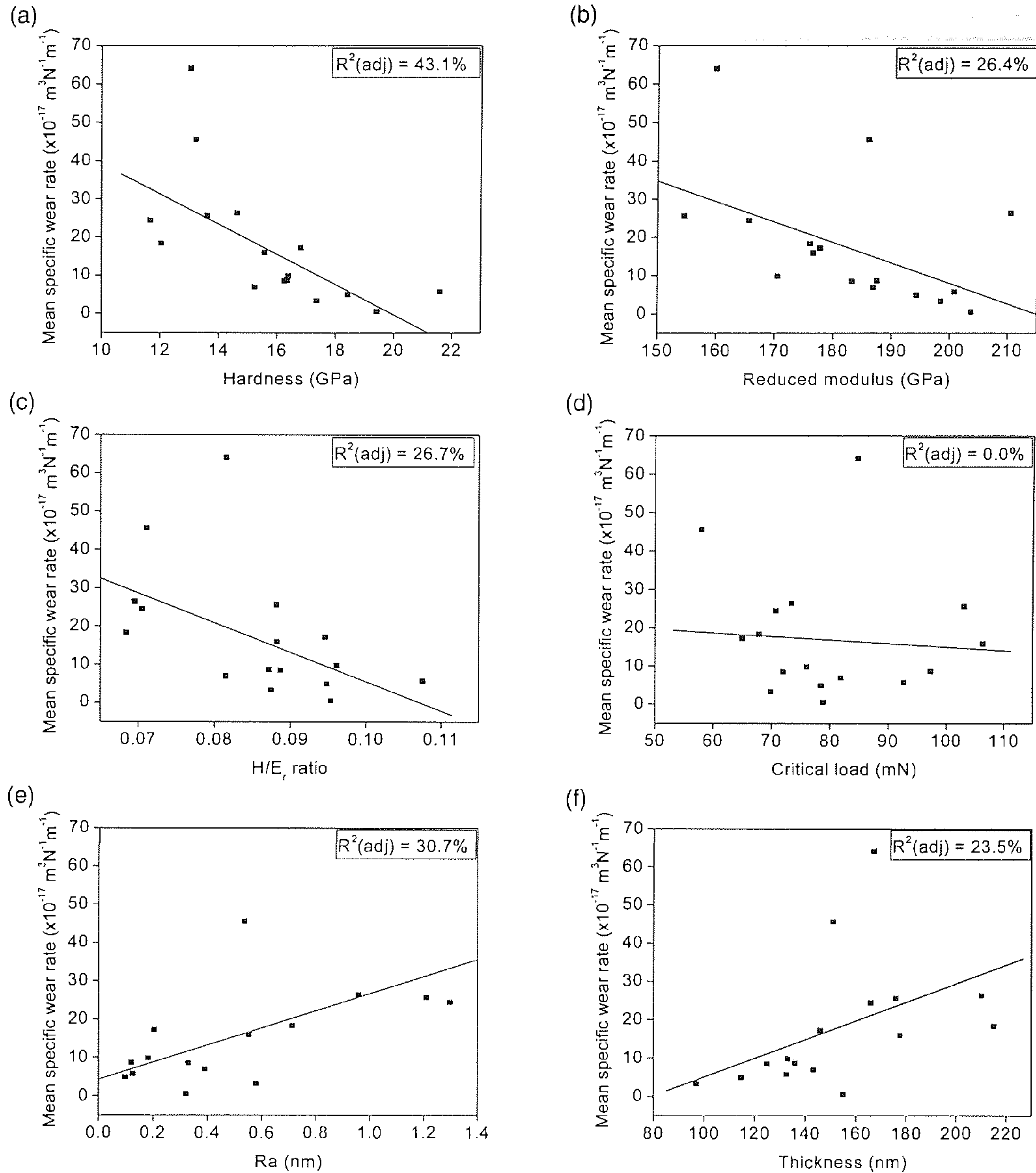

Figure 3.40 150 nm correlation plots fitted with a linear regression between mean specific wear rate and tribologically important coating properties (a) hardness (b) reduced modulus (c) H/E_r ratio (d) critical load (e) surface roughness Ra and (f) coating thickness.

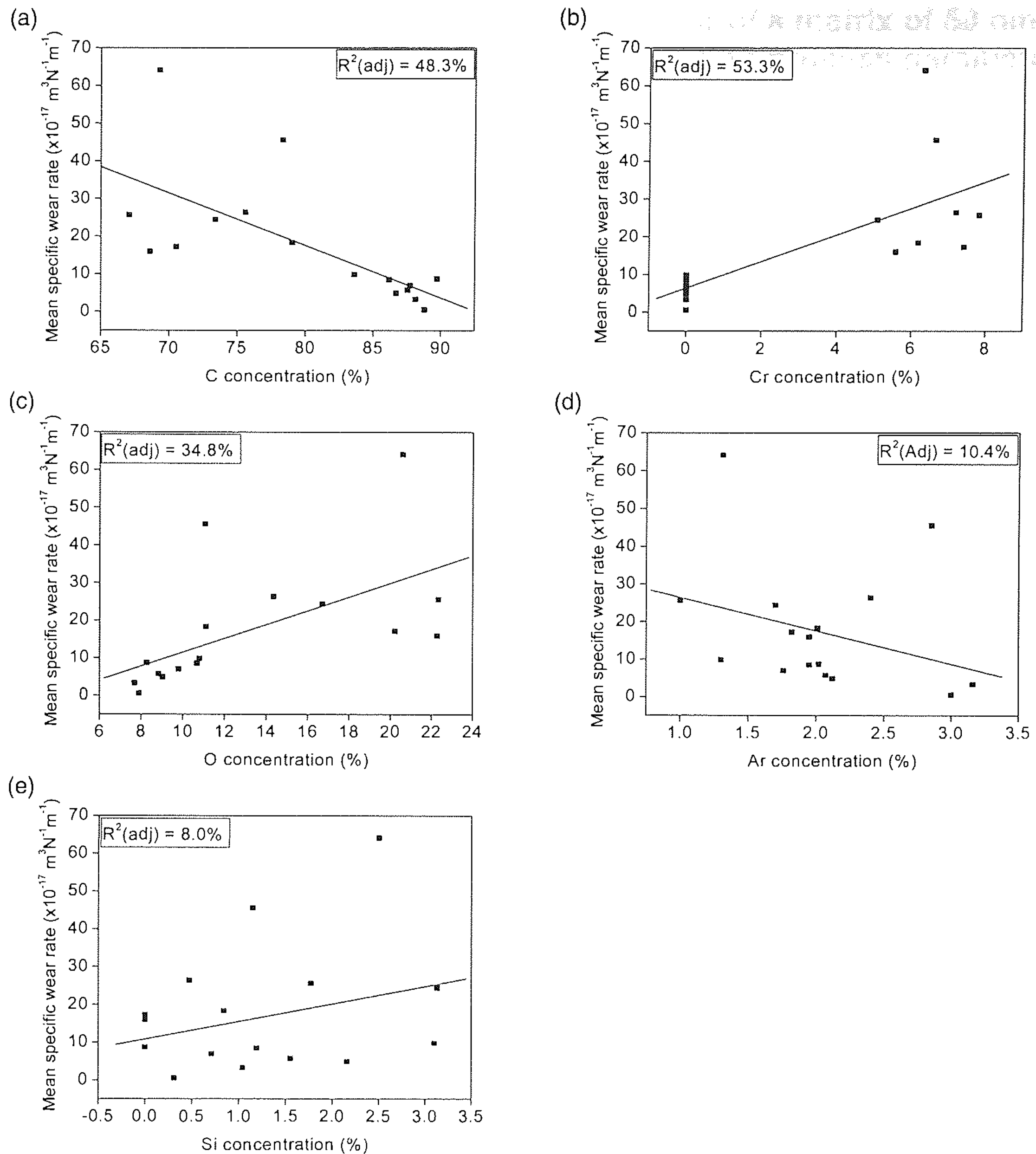

Figure 3.41 150 nm correlation plots fitted with a linear regression between mean specific wear rate and coating constituents (a) carbon (b) chromium (c) oxygen (d) argon (e) silicon.

3.3.3 Experiment to investigate the nanowear of a matrix of 50 nm coatings and the effect of four key coating process parameters

3.3.3.1 Measurement of specific wear rates and analysis of the complete data set

Measurements were made and the data was processed as described in section 3.3.2. In no tests was the coating worn down to the substrate. There was an asymmetric distribution of specific wear rate results as with the 150 nm tests and this is shown in Figure 3.42. The second and third quartile (50% of the data) was bounded by the range 7 - 18 x 10^{-17} $m^3N^{-1}m^{-1}$; whilst the full range was 2.0 - 54 x 10^{-17} $m^3N^{-1}m^{-1}$. Again the wear rates were in general very low. The rates were slightly lower and significantly less distributed than the results at 150 nm.

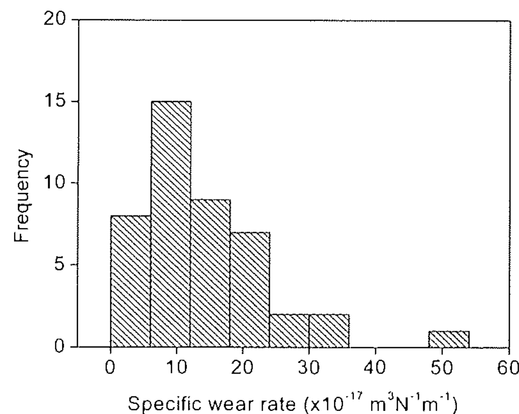

Figure 3.42 Histogram of all specific wear rate data with 50 nm films.

Boxplots were used to assess changes of wear rate with test duration as given in Figure 3.43. From the results it can be seen that there was a reduction of specific wear rate with duration of test. The tests performed at 3000 oscillations (5 minutes test duration) showed a significantly higher wear rate and data spread compared with the other tests.

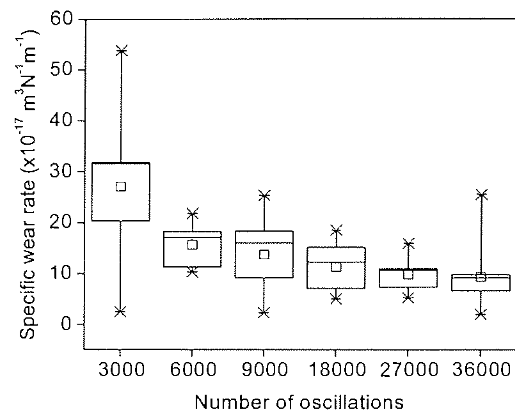

Figure 3.43 Boxplots showing the distribution of specific wear rates against number of oscillations at 50 nm. For a definition of terms see the caption to Figure 3.38.

The individual specific wear rate values for each coating were averaged and the individual values were plotted against the grouped average values (Figure 3.44). There was no clear change in data scatter with increasing wear rate as was evident with 150 nm coatings, although the range was much smaller than previous.

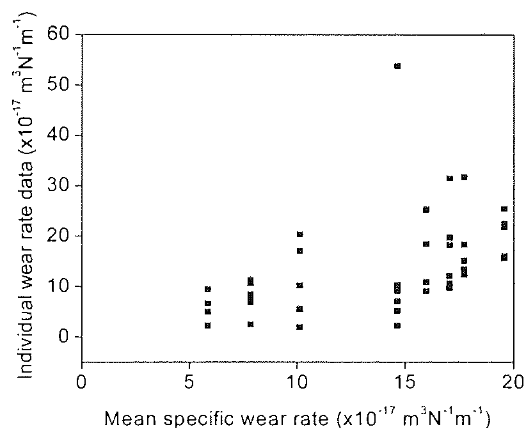

Figure 3.44 Scatter plot of individual specific wear rate measurements against group averages for each coating at 50 nm.

3.3.3.2 Statistical analysis of the effect of the four key process parameters using ANOVA

The specific wear rate results were analysed against the key coating process parameters using the ANOVA statistical procedure and the main effects results are given in Table 3.15 as previously described.

Table 3.15 Main effects results from ANOVA analysis at 50nm.

	Ar flow (sccm)		Adhesion Layer		Cr current (A)		Bias voltage (V)	
	12	28	None	Present	0.00	0.75	40	80
Specific wear rate ($x 10^{-17} m^3N^{-1}m^{-1}$) (s = 5.8)	14	14	15	13	12	16	18	10
	(P=0.778	F=0)	(P=0.693	F=0)	(P=0.200	F=2)	(P=0.007	F=8)

ANOVA results relating to interactions between the four process control parameters are given in Table 3.16 and as previously described.

Table 3.16 Primary interaction effects from the ANOVA analysis at 50 nm.

Parameter 1:	Ar flow			Adhesion layer		Cr current
Parameter 2:	Ad. Layer	Cr current	Bias volt	Cr current	Bias volt	Bias volt
Interaction	P = 0.530 F = 0	P = 0.823 F = 0	P = 0.399 F = 1	P = 0.399 F = 1	P = 0.823 F = 0	P = 0.530 F = 0

3.3.3.3 Correlations with the tribologically important properties of the coatings

Scatter plots showing the correlation between the nano-scale mean specific wear measurements and coating hardness, reduced modulus, H/E_r ratio, critical load, surface roughness, and thickness are given in Figure 3.45. Correlations with bulk coating composition are given in Figure 3.46. The correlations were fitted with a straight line using a linear regression procedure and the r^2(adjusted) values are given for reference.

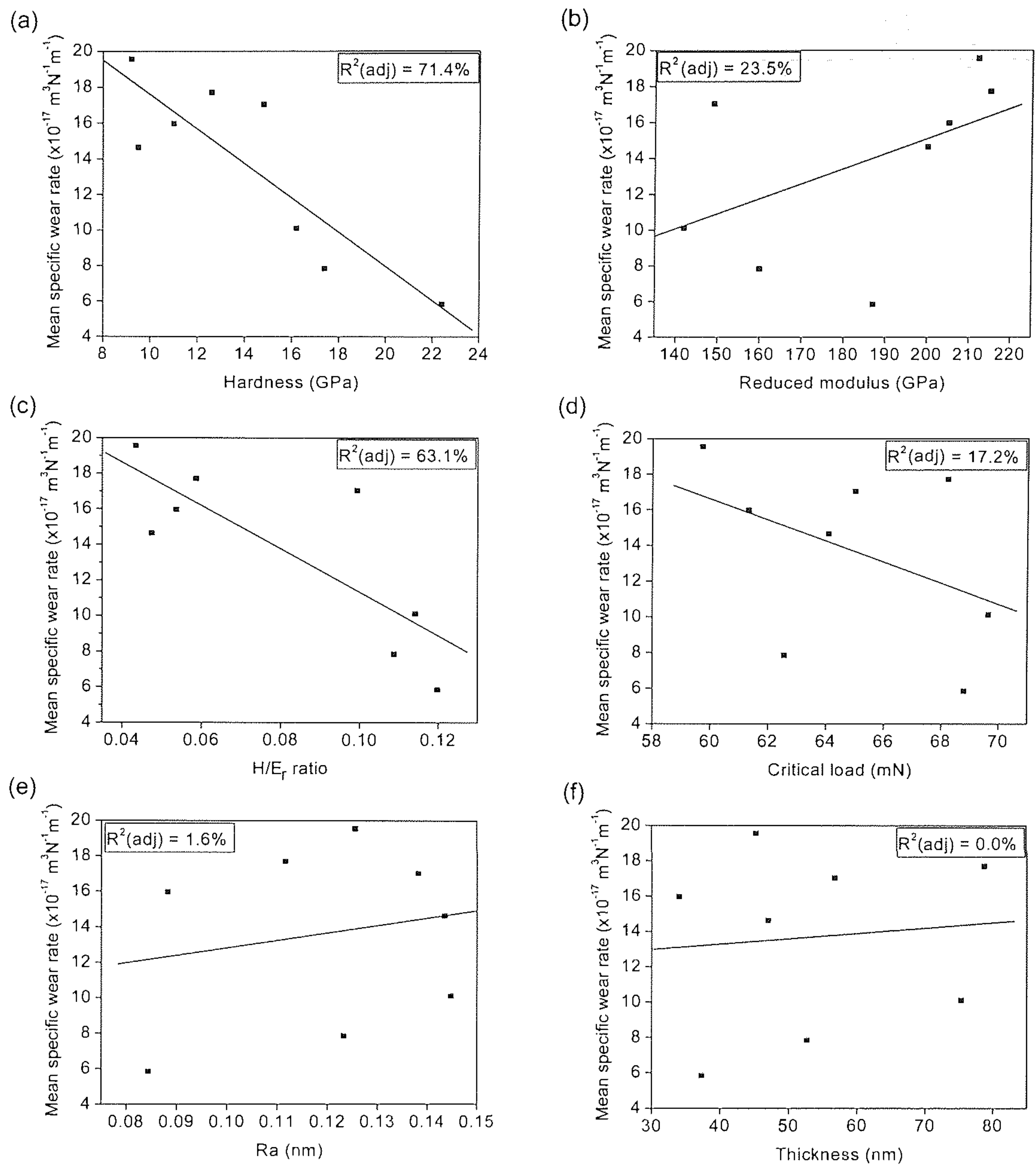

Figure 3.45 50 nm correlation plots fitted with a linear regression between mean specific wear rate and tribologically important coating properties (a) hardness (b) reduced modulus (c) H/E_r ratio (d) critical load (e) surface roughness Ra and (f) coating thickness.

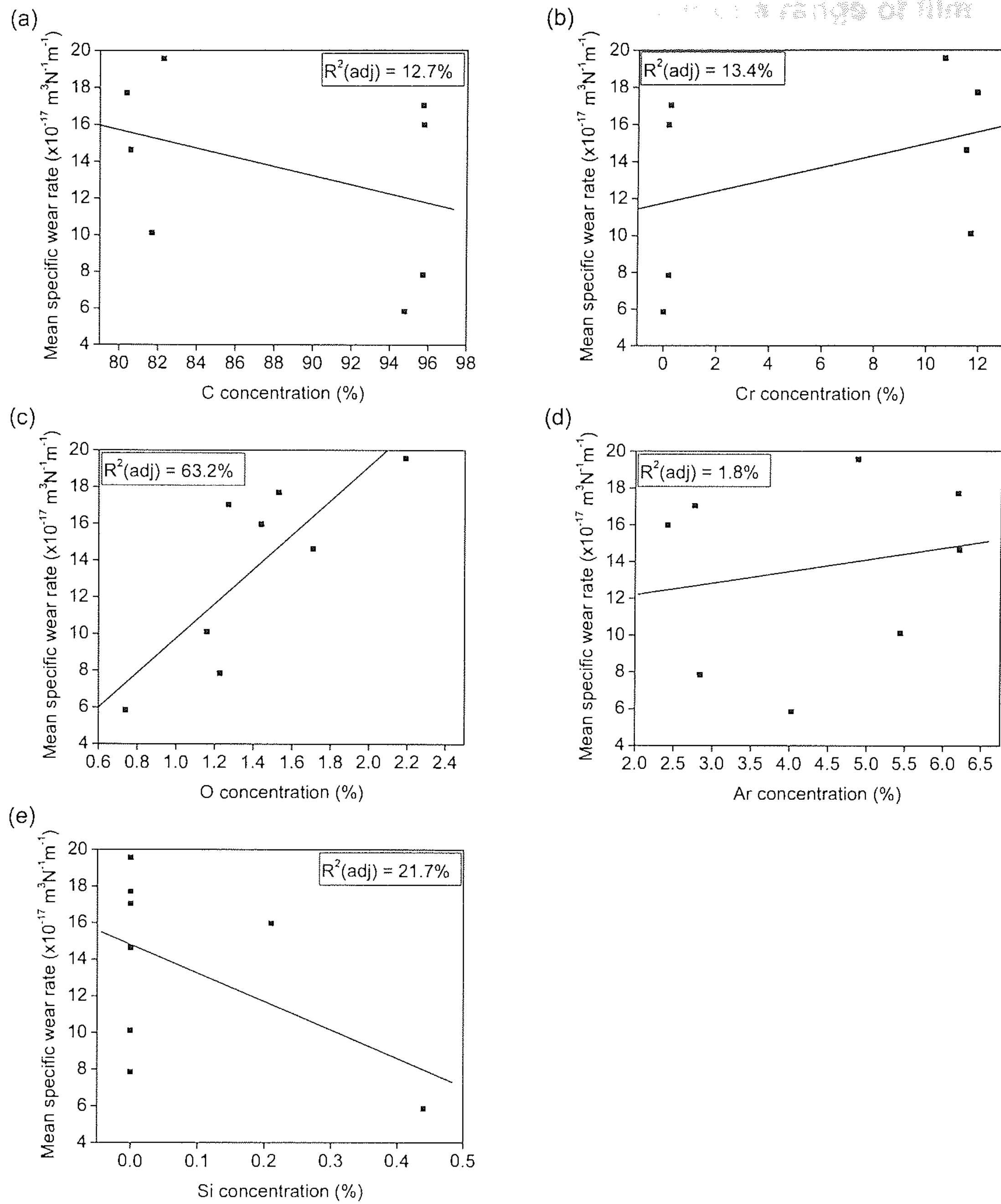

Figure 3.46 50 nm correlation plots fitted with a linear regression between mean specific wear rate and bulk coating constituents (a) carbon (b) chromium (c) oxygen (d) argon (e) silicon.

3.3.4 Experiment to investigate the nanowear of a range of film thicknesses (2000 nm to 10 nm)

Values of initial mean contact pressure were calculated from elastic contact theory and estimated from optical images (as described in section 3.3.1.4) and are given in Table 3.17.

Table 3.17 Calculated contact radius and mean contact pressure values.

Applied load (mN)	Initial contact radius (μm)	Initial mean contact pressure (MPa)
10	{2} (4.2)	{800} (180)
1	{0.9} (1.9)	{390} (90)
0.1	{0.4} (0.84))	{200} (45)
Key: {data calculated from elastic theory} (data determined empirically from optical images)		

Measurements were made and the data was processed as discussed in section 3.3.2. In no tests had the coating been worn down to the substrate. The complete data set was analysed using boxplots to investigate changes in specific wear rate with test duration. The results are shown in Figure 3.47. The measured wear rate during the first 1 minute of testing (600 oscillations) was very high with more data spread compared with tests of greater duration. The wear process stabilised after 5 minutes.

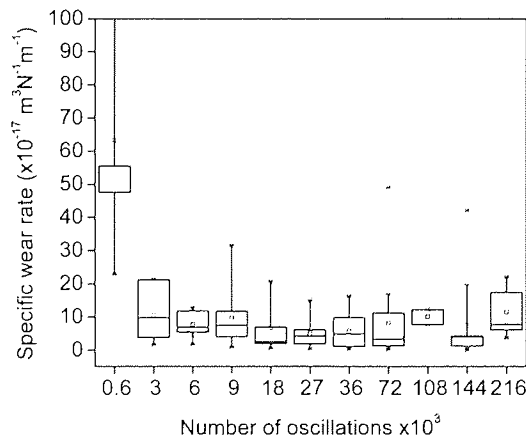

Figure 3.47 Boxplots showing the distribution of specific wear rates against number of oscillations. For a definition of terms see the caption to Figure 3.38.

The effect of applied load and coating thickness was investigated by the use of boxplots so that a comparison could be made between the distributions of replicated data sets. The one minute test results were omitted from the analysis as the wear process was a long way from a stable condition at this duration. The results are shown in Figure 3.48. The wear rate and data scatter reduced with increasing applied load and more significantly with reducing coating thickness. The thinnest coating produced the lowest wear rates, which were in the range 0.1 to 6.1 x 10^{-17} $m^3N^{-1}m^{-1}$.

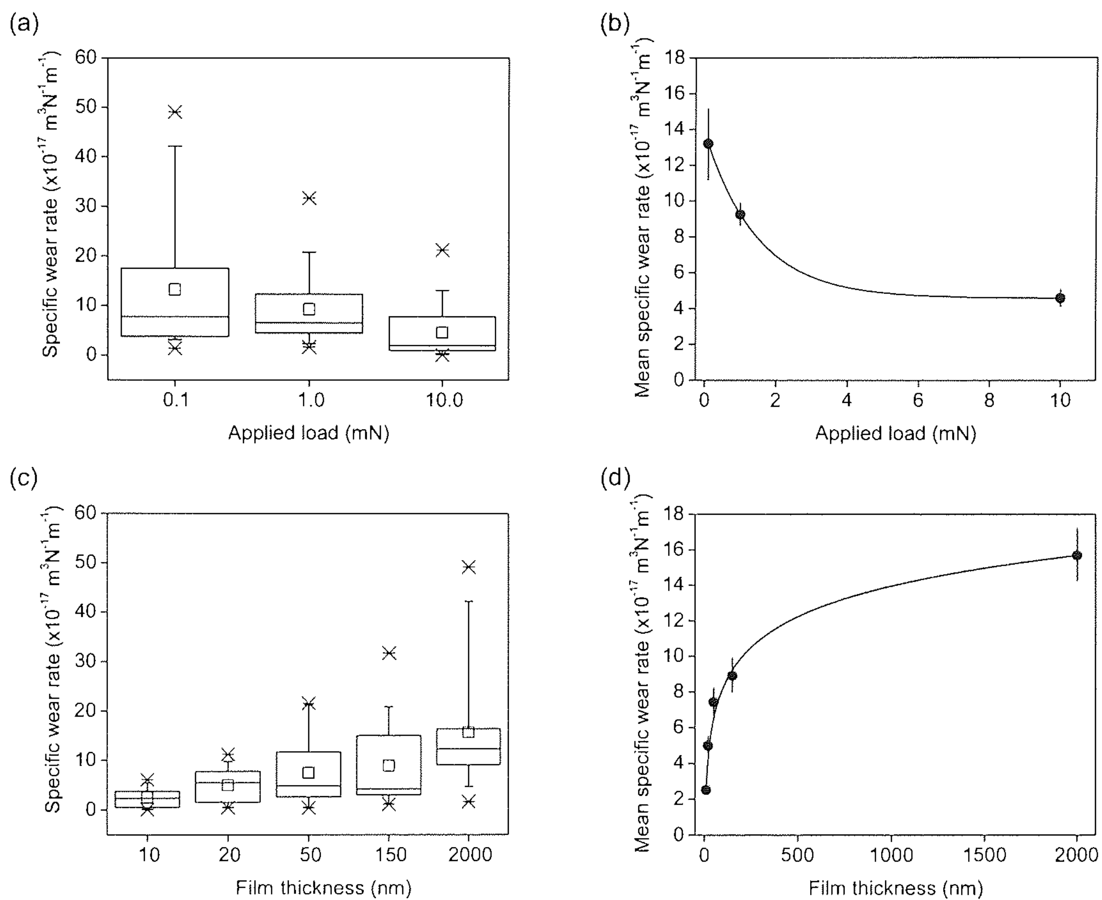

Figure 3.48 (a) boxplots showing the effect of applied load on all wear rate data (b) scatter plot showing applied load versus mean wear rate with standard error bars (c) boxplots showing the effect of thickness on all wear rate data (d) scatter plot showing thickness versus mean wear rate with standard error bars. For a definition of boxplot terms see the caption to Figure 3.38.

For comparison, an uncoated Si wafer was tested at 10.0, 1.0, and 0.1 mN load for a two hour duration (72000 oscillations). In all cases the Si surface had undergone significant fracturing (for example Figure 3.49).

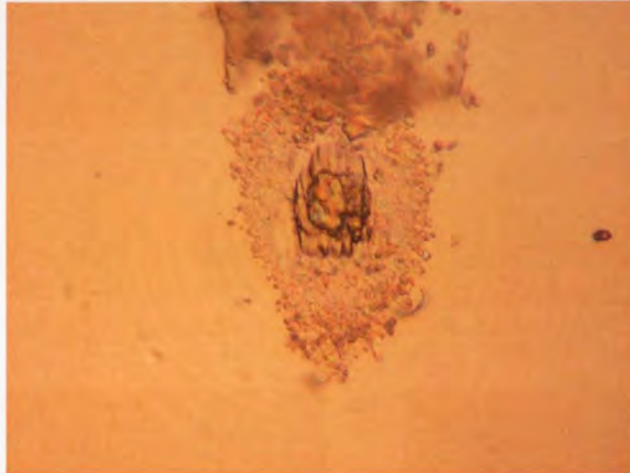

Figure 3.49 Optical microscopy image of Si wafer after a two hour wear test at 1.0 mN.

The surface topography of the 2000 nm coating provided conditions beneficial for an AFM examination of the early stages of wear development at both the highest and lowest loads (Figure 3.50). Under both loading regimes, the initial stages of wear involved asperity flattening and movement of material to fill the inter-asperity gaps. Following this initial stage, more significant asperity flattening occurred with some ploughing events under counter-body asperities or third body particles. The ploughing events increased with time until typical wear scars were formed (see Figure 3.26 and Figure 3.31).

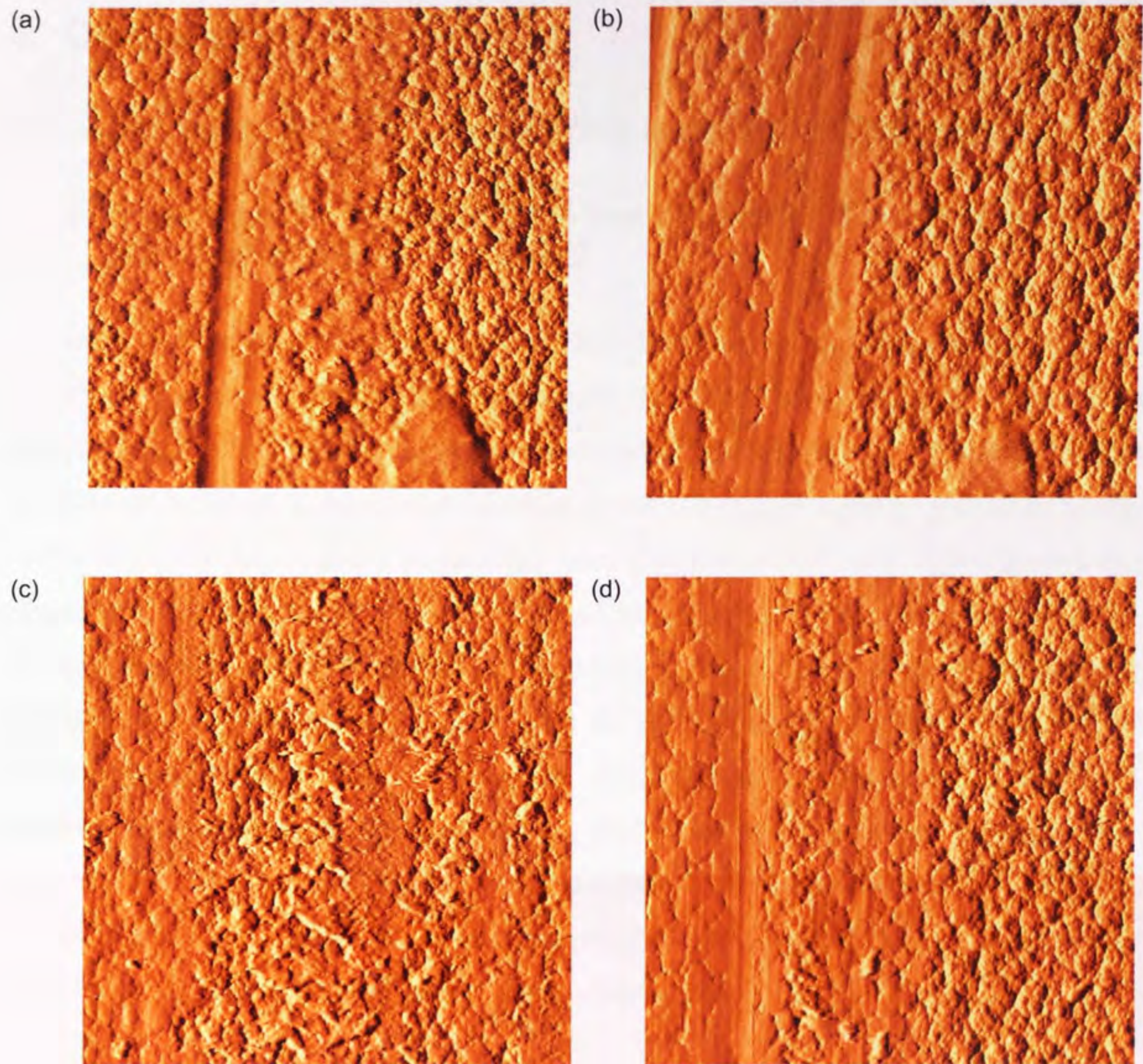

Figure 3.50 3 µm x 3 µm AFM scans of wear scars (a) 0.1 mN load for 2 hours (b) 0.1 mN load for 6 hours (c) 10 mN load for 1 minute (d) 10 mN load for 5 minutes.

4 Discussion

4.1 Low wear / low friction thin film analysis techniques

4.1.1 Experiment to investigate the use of XPS for the determination of sp^3/sp^2 bonding ratio in a-C

The large number of variables available within the sp^3/sp^2 peak fitting algorithm meant that there were many component arrangements that could be fit to the C 1s spectra (a large freedom to fit), resulting in little certainty of sp^3/sp^2 ratio results. This was the case despite constraining the component variables to realistic ranges based on published results and taking account of peak broadening from the instrument used. More knowledge concerning the component peaks is required to limit the fitting freedom and hence improve the reproducibility of results. Published results from other researchers do not clearly define the constraints used for peak fitting nor provide the full assignment of component peak characteristics. No errors were reported in the literature based on freedom to fit as discussed here, although a number of reports showed that component peak characteristics were allowed to vary from sample to sample [for example 128,131]. It is difficult to imagine that this is not a universal problem when the XPS instrument has insufficient resolution to clearly identify the sp^3/sp^2 components.

It is fundamental to the peak fitting method that C coatings with a mixture of sp^3 and sp^2 bonding yield C 1s peaks that can be represented by a combination of separate overlapped sp^3/sp^2 components. It follows from this definition that: materials that are pure sp^3 or pure sp^2 must produce the narrowest C 1s peaks; materials that are composed of a 1:1 mixture of both must have the widest peaks and materials of the same sp^3/sp^2 ratio must have the same peak width. This statement ignores the effect of C-O bonding from adsorbed atmospheric O, although this affects only the trailing tail of the peak. It is clear from Figure 3.5 that the points highlighted above were not observed in the measured data here. It is possible that the XAES D value results were also subject to significant error. This means that the three plots on Figure 3.5 may not have had the same sp^3/sp^2 ratio and hence may not be expected to overlap. However this does not explain why any plot could be narrower than graphite. This also highlights the problem that there is no a-C primary

standard, external to these techniques, with known sp^3/sp^2 ratio. Raman spectroscopy is widely used for determining sp^3/sp^2 ratio and could theoretically be used to calibrate a-C standards for subsequent use in XPS C 1s peak fitting work. The Raman method also involves a complex fitting procedure and analysis method; therefore great care would need to be taken. Schwan et al. [249] showed additional complications to the conventional two peak ('G' and 'D') model with magnetron sputtered a-C films. This suggests that the potential use of Raman to standardise sputtered a-C standards may be challenging.

It is interesting to note that when the asymmetric Ar^+ ion etched graphite peak shape (which would be expected to be similar to a 100% sp^2 coating) was used to define the shape of the sp^2 component when peak fitting, then an sp^3 component was not required. It may therefore be the case that all of the a-C coatings tested were near 100% sp^2 and the peak shape was just rather asymmetric. When peak fitting, the use of an sp^3 component may simply be to 'asymmetrise' an incorrect sp^2 component peak shape. This however seems unlikely. The lack of sp^3/sp^2 separation with the high resolution XPS instrument can be interpreted in a number of ways: there were two separate components but the high resolution XPS equipment used still did not have enough energy resolution to show them; the coatings were near 100% sp^2 and the C 1s peak showed a significant asymmetry; there were not two but several closely spaced components within the C 1s envelope of amorphous C coatings, reflecting the fact that the a-C coatings did not contain just pure ordered sp^2 and sp^3 bonding but many additional bonding environments.

A more thorough investigation is clearly required to resolve these questions, however for the purposes of this work a severe limitation was identified with the use of XPS for the determination of sp^3/sp^2 bonding ratio in a-C. Therefore the technique was only applied tentatively in the early stages of the project.

4.1.2 Investigation of material pile-up and cracking during nanoindentation experiments

From the calculated h_f/h_{max} values and the AFM scans of indentations it can be inferred that pile-up and cracking errors were not a significant problem during nanoindentation testing of the coatings used in this work. However, Si showed both pile-up and cracking at relatively deep indentations. This observation strengthens the need for limiting the

depth of indentations when testing films on Si substrates. It also suggests that significant errors may be attached to the calculations of hardness and reduced modulus values of Si under nanoindentation testing in section 3.2.5. Jung et al. [250] reported similar cracking under nanoindentation testing of Si <111> with a Berkovich indenter at 32 mN load. No cracking was observed at 9 mN load.

4.1.3 Investigation of ISE with nanoindentation experiments

The production of asymmetric data distributions from replicated nanoindentation tests at very low depth is a practical characteristic of the Oliver-Pharr method. By using an appropriate method for dealing with this type of distribution no significant change in measured hardness and reduced modulus was observed at very low indentation depth. Consequently, this approach was taken with all very low depth testing.

It is apparent that as yet no clear ISE has been identified and studied with a-C coatings in the literature (refer to the literature survey described in section 1.5.3.1.9). Where trends have been observed the possibility of this being due to errors in the nanoindentation method can not been discounted. It is therefore not surprising that relatively consistent values of hardness and reduced modulus with indentation depth was observed here when suitable care was taken with the test procedure and data replication.

4.2 Experiments to investigate the tribologically important properties of a-C coatings

4.2.1 Experiment to investigate Cr doping in a-C coatings at the nano- and macro-scale with 1 to 3 μm coatings

The XPS results suggest that P1S1 was composed of approximately equal concentrations of sp^2 and sp^3 bonded a-C, together with O. However, the assumptions involved in the sp^2 and sp^3 analysis have been brought into question in this work (refer to section 4.1.1). The O was present to a depth of around 5% of the coating thickness with a localised adsorbed O layer (possibly water vapour) on the surface. The presence of O at the depth measured implies that the coating has a more open structure near to the surface in comparison to the Cr containing films. When a small amount of Cr was included in the coating the adsorbed O layer was of low concentration and was confined to the surface. This suggests that the

inclusion of Cr produced a more compact structure at the surface. With P1S3, a slightly higher concentration of surface O was observed and this combined with the surface Cr to form Cr_2O_3. As with P1S2, very little O penetration into the subsurface region occurred which, along with the high reduced modulus for this sample, again suggests that Cr doping promotes a more compact structure at the surface. The C and Cr in the bulk of the coating occurred at a ratio 2:3, a result consistent with bulk of the coating being Cr_3C_2.

The nanoindentation tests showed similar results for P1S1 and P1S2, but P1S3 showed significantly lower hardness and higher elastic modulus. Both the nanowear and the coefficient of friction increased with increasing Cr content, consistent with observed hardness changes, although differences in coefficient of friction became negligible as wear progressed. At very high Cr content the coating was transformed from a Cr doped a-C to Cr_3C_2.

The bulk hardness of Cr_3C_2 is quoted in the literature at between 10 and 18 GPa as measured by Vickers hardness test [251] which is significantly higher than the indentation hardness value for P1S3 measured in this work. Due to the potential imperfections and deviations from the standard bulk crystal structure that may be introduced during the sputtering process, it is reasonable to expect a sputtered film to vary considerably from the standard bulk values. This can be seen from a review of published hardness and elastic modulus data from sputtered Cr_3C_2 coatings where there is a large range of results depending upon the specific coating parameters used [for example 252,253,254].

Both wear and friction were found to increase with the reduction in hardness, as expected in this mode. A reduction in coating hardness will mean that plastic wear modes (such as ploughing and shearing of the coating) become more significant. This type of wear generally results in a greater quantity of material loss and higher frictional forces. The wear tracks are less than 5% of the coating thickness in each case, hence the substrate would not be expected to contribute significantly to the degree of wear/friction at this depth and so a comparison can be confidently made despite the difference in coating thickness.

It is interesting to compare the results of this work with previous work performed on similar samples, but using test methods operating in a micro/macro range [232]. A comparison of the results is given in Table 4.1. It should be noted that all coatings described in reference [232] were prepared using the same generic process to the coatings in this work, except a thickness of 2 μm was deposited and the samples were produced on M42 tool steel using 3 C targets and 1 Cr target with a different dimensional arrangement. Total target currents are given in brackets for reference. It is acknowledged that there will be differences between the two sets of coatings, but despite this it is felt that a useful comparison of the general effects can still be drawn between a nano-scale and micro/macro-scale investigation of the use of Cr doping in sputtered a-C coatings. The nano-scale wear results have been approximated by assuming the wear track to be a parabolic prism.

Table 4.1 Comparison of nano-scale tests with micro/macro-scale tests.

	Nano-scale tests (C targets (all tests): 2 x 3.5 A) (Cr targets (no doping): 0 A) (Cr targets (low doping): 1 x 0.25 A) (Cr targets (high doping): 2 x 0.75 A)			Micro/macro-scale tests (C targets (all tests): 3 x 2.2 A) (Cr targets (no doping): 0 A) (Cr targets (low doping): 1 x 0.25 A) (Cr targets (high doping): 1 x 1.25 A)		
	Hardness Nanoindentation (GPa)	Wear Nanoscratch ($x10^{-13}$ $m^3N^{-1}m^{-1}$)	Coefficient of Friction Final nanoscratch	Hardness Microhardness (HV converted to GPa)	Wear Pin-on-disk at 10 N ($x10^{-17}$ $m^3N^{-1}m^{-1}$)	Coefficient of Friction Pin-on-disk at 10 N after 'run-in'
No doping	11.5	2.0	0.18	39	0.4	0.17
Low Cr doping	11.2	2.9	0.17	28	2.5	0.17
High Cr doping	8.4	4.1	0.18	12	5.7	0.23

The absolute values of hardness in this work were much lower than those previously measured under micro-hardness tests [232]. These published high micro-hardness measurements are difficult to understand. Hardnesses of the order of 40 GPa would not be expected for amorphous C films with low sp^3 content. The indentations in this work were less than 5% of the full coating thickness; so it would be expected that the hardness values so measured were influenced only by the physical properties of the coating with negligible effect due to the substrate. Shallow indentations rely upon accurate modelling

of the probe tip to account for deviations from an ideal shape and inaccuracies in this modelling can produce large errors in hardness. Probe tip modelling for the Berkovich indenter was carried out with great care hence there is confidence that the nano-hardness values are an accurate representation of the outer layers of the coating.

Due to the greater indentation depths involved with the micro-hardness test, the question arises as to whether the results are unduly influenced by the substrate. However, this is not likely to be the case, since the values would be expected to be lower if influenced by the tool steel substrate and show little change with changes to the coating composition. This was not the case. Thus, from reference [232] it seems reasonable to assume that (as with nano-indentation) the micro-hardness results should be wholly representative of the coating.

There can be a difference between nano-hardness results determined by the Oliver-Pharr method and those determined by direct measurement of the size of the residual impression, if the material is such that not all of the contact area under load is plastically deformed. In this case, the contact area calculated by observation of the residual hardness impression would be less than that at peak load, resulting in a higher hardness value compared to the Oliver-Pharr method where the contact area at peak load is derived from the initial gradient of the (depth/load) unloading curve [156]. Whether this can explain the magnitude of differences observed is open to debate.

It is not the case that hardness is a function of depth into the coating given the results discussed in section 4.1.3.

The general effect of increasing amounts of Cr in the coatings under both sets of tests was to produce a reduction in hardness. The magnitude of the effect in this work is much smaller than that previously reported [232]. In this work: changing from 0 to 1.5 A of the Cr sputter current reduced the hardness by 27%. For the micro-hardness tests a similar current change reduced the hardness by 59%.

Some interesting differences exist between wear results tested at the nano-scale and macro-scale. The nanowear results in this work show a clear increase in wear with increasing Cr concentration, as do the low load macro-scale pin-on-disc tests (Table 4.1).

However at higher load, the pin-on-disk test shows a more complex relationship, suggesting that in this case, wear has little dependence on Cr concentration [68,232]. The differences are due to the very different wear mechanism operative for the two conditions.

In the case of the nanowear measurements, wear is due to ploughing (plastic deformation) mechanism by a diamond indenter. After the first pass of the indenter, the depth of the tracks passed through the outer contaminant and oxygen modified regions in both P1S2 and P1S3 coatings and a similar condition was reached with P1S1 by pass number 3. This confirms that the final nanowear results were not significantly affected by these outer layers and were due to the elastic/plastic (particularly plastic) properties of the bulk coating material. Despite the very low forces applied in the nano-scale tests, this force was applied through a very sharp indenter, producing a high contact pressure and severe plastic flow; almost a single asperity mode.

The pin-on-disc wear test in comparison, had a much higher total load, but this is distributed over a large number of asperity contacts. The wear scar on the pin is typically measured at approximately 250 μm. Hence the total contact stress for the 10 N load used in the pin on disk experiments is of the order of 0.2 GPa. The initial contact pressure in the case of the nanowear tests exceeded the yield pressure of the coatings. The pressure would quickly reduce as plastic deformation occurred due to the applied load being spread over an increasing area as the indenter penetrated the material. From the AFM results of the wear track, the final contact pressure was estimated to be of the order of 10 GPa, which is expected given the hardness of the coatings. Thus, the differences between the nano- and micro-scale wear results is a function of the method of test and not related to the depth of the coating tested. The pin-on-disk test is likely to involve mainly elastic contact and adhesive transfer wear and hence the benefits imparted by Cr are attributed to these mechanisms. Wear in the case of the nano-tests involves gross plastic deformation of the coating material.

Friction, in the case of the nanowear, was dominated by the ploughing term for the first 2-3 passes as exhibited by the rapid increase in track depth at the start of the test (Figure 3.17). For later passes the ploughing effect was less dominant as the films had previously undergone plastic deformation, thus reducing the contact pressure, which is evident by the

reduction of the gradient of the track depth curves (Figure 3.17). There was a measurable difference between the frictional properties of the three coatings during the first two passes, with the higher Cr containing films exhibiting a higher coefficient of friction. This could be attributed to Cr_2O_3 on the surface of the P1S3 specimen producing a raised coefficient of friction until the indenter had penetrated through to the bulk of the coating. However, as pointed out in the wear discussion, the indenter was beyond the depth of the O layer after the first pass. It is more likely that the lower hardness of the Cr doped coatings, which enabled the indenter to penetrate more deeply into the coating, caused an enhancement of the ploughing frictional term for the early passes of those films. Convergence of results occurred with later passes when plastic deformation and hence the ploughing term no longer dominated.

In the case of the pin on disk tests, the adhesive term dominates and transfer films formed between the pin and the coating largely govern the measured coefficient of friction. Hence the effects imparted by Cr are attributed to these mechanisms and the fact that the coefficient of friction is different in the case of the carbide (P1S3) coating to the a-C P1S1 and P1S2 coatings is not surprising in view of the material differences.

Considering the very different mechanisms operative in the nano and macro-scale tests it seems to be coincidental that the measured values of coefficient of friction are so similar.

4.2.2 Experiment to investigate the effects of pulsed substrate biasing with 150 nm coatings

Substrate bias voltage was found to be the most significant of the three pulse bias parameters tested. Of the twelve coating properties measured, voltage was a significant factor in nine and was the most significant factor in six of those. For this reason bias voltage was chosen as one of the four key coating process parameters for further investigation at low thickness in the following sections. The effect of increasing voltage on the physical and mechanical properties of very thin coatings fitted with the standard model. Applying a negative bias to the substrate increases the energy of incoming ions (and atoms via collision with higher energy ions) thus increasing sputtering and possibly temperature and implantation. This has the effect of densification of the coating resulting in the observed increases in hardness and reduced modulus [53,192,255]. Work to model

film growth shows that increased surface mobility (which increases with both incoming ion/atom energy and surface temperature) results in a reduction of porous structure [87,88]. The standard structure zone diagram shows reducing chamber pressure producing higher density films as a result of less frequent collisions between particles which reduces the thermalisation of the system and hence increases the quantity and energy of high energy particles reaching the substrate [103]. The standard structure zone diagram has been modified to show the densification with increasing substrate bias voltage [62]. There is also likely to be an accompanying increase of internal compressive stress and brittleness which will ultimately cause a reduction of critical load under scratch test [53,192,255,256,257]. This was also seen in the data. Work by Yang and colleagues [231] using a similar process but with 1.5 μm films showed hardness increased with bias voltage to a maximum at 90 V and further increases of voltage produced a slightly reducing hardness, as the energy of ion bombardment becomes high enough to go beyond densification and cause some damage to the coating structure. The surface of the coatings became smoother with increasing voltage which would be expected to follow from the densification process, although this effect is also likely to reverse at higher voltages (higher ion energies) as ion bombardment begins to cause surface damage. There was also a clear correlation between O and Ar concentration in the coating and bias voltage. The Ar correlation reflects the increased implantation with bias voltage. The O correlation can be interpreted as reflecting the densification of the coating with voltage, resulting in fewer available sites for atmospheric O and/or water vapour adsorption. This is a similar mechanism to the reported correlation between chamber pressure and O content [258]. The lower chamber pressure results in an increase in the number and energy of high energy particles to the substrate and hence an increase in coating densification and therefore a reduction of available oxidisable pores.

Bias voltage pulse frequency was a significant factor in five of the twelve coating properties and was the most significant factor in one of those. The effect of increasing frequency mirrored the effects observed with bias voltage magnitude for H, Er and Lc. These results are in agreement with the observations in the literature [93,95] that show increasing pulse frequency yielding higher substrate ion current and the suggested rise in the energy and flux of particles to the substrate, for the same densification reason as that

given above. It is interesting to note however that under typical coating conditions and over the ranges 50 to 150 kHz the change in substrate current in [95] was almost immeasurable and yet there was a small but measurable effect on the coating properties here. Frequency also had a controlling effect on surface topography and in the case of peak spacing was the most significant factor. In addition to the effects discussed, there was a significant interaction of pulse frequency with the effect of bias voltage for coating hardness and surface peak height. This means that both the voltage required to produce maximum hardness/peak height and the value of the maximum hardness/peak height are functions of pulse frequency. There will be an increase of peak voltage accompanying the increase in frequency (for a constant pulse width) to maintain a constant time averaged voltage. This may explain the tendency for the frequency effects to mirror the voltage effects in terms of the nanoindentation test results, considering that here it has been demonstrated that the magnitude of the voltage pulse seems to be more important than the number of pulses in a given time. This also provides one mode of interaction between the two. However this can not be the whole answer as the effect of the interaction is to alter the shape of the voltage response and in addition, the correlation between frequency and voltage is not seen in the topographical results. Kelly et al. [93] showed that the rate of change of ion current (at the specimen) with cathodic bias voltage increased with increasing pulse frequency, confirming a voltage-frequency interaction. This work was performed with an Al target and covered the range of voltage and frequency used in the work reported here. The work by Kelly et al. [93] on the same pulse voltage unit (but working at higher voltages / frequencies and with a greater substrate to magnetron area ratio and with a small positive going pulse during the 'off time') showed that a high voltage and current swing occurred just after the voltage pulse is first switched on, producing in effect a complex series of decaying voltage pulses within the pulse envelope. If this is still present here and is a real event that is experienced within the chamber then this may play a role in the frequency effects and interactions. As the frequency is increased the rate of 'switches' will increase and so the system will be subjected to a greater degree of these highly unstable voltage swings and also as the frequency is increased the pulse duration decreases which modifies the form of the switching effects as can be seen in reference [93].

Bias voltage pulse width was a significant factor in seven of the twelve coating properties and was the most significant factor in one of those. In general, the trends were similar to increasing bias voltage magnitude for H, Er and surface roughness. The one exception to this was critical load, where an increase in pulse width produced an increase in average critical load. This means that under the right conditions, pulse width can be used to increase both hardness and critical load, unlike bias voltage in voltage control mode which tends to affect the two properties in opposition. Pulse width in fact had a much more complex effect on the coating process by interacting with many of the effects produced by voltage magnitude and frequency. As pulse width is increased from 500 to 2500 ns, the peak voltage of the pulse will increase significantly (more than for frequency when going from 50 to 150 KHz) to maintain a constant time averaged voltage, which may account for the similarity between voltage and pulse width effects and also goes some way to account for the pulse width-voltage interactions. As with frequency, the interactions take a complex form which this simple model does not fully explain. In the work reported by Kelly et al. [93] it was stated that the effects of voltage and frequency on substrate ion current, including the voltage-frequency interaction, became less marked as the duty factor was increased. Increased duty factor is effectively a reduced pulse width and hence reveals an interacting effect between pulse width, frequency and voltage. It can be speculated that the increase in peak voltage and greater off-time that a high pulse width gives, modifies the characteristics of the ion current switch-on pattern, which reference [93] has shown is also controlled by frequency and here may lie the basis for the interactions between frequency and pulse width. Also, the longer off-time will mean that the substrate is subjected to prolonged periods of electron current with the associated heating effect which has been shown to increase the mobility of surface atoms resulting in a densification effect as is evident on the standard structure zone diagram [53,103]. Increased substrate bias current at high pulse width can be observed in Table 2.3.

4.2.3 Experiment to investigate four key coating process parameters with 150 nm coatings

Cr target current was shown to have the greatest overall effect on the measured coating properties: seven significant effects were identified with six of those being of the greatest effect, from a total of eleven measured properties. Hardness reduced with increasing Cr

current (and hence increasing Cr content in the film) consistent with that reported at μm thicknesses (section 4.2.1, and ref. [232]). The softening action of Cr also produced an equivalent reduction of coating stiffness. A rise in the Cr to C ratio in the film was observed with increasing Cr target current as expected. There was also an accompanying rise in O at the surface consistent with oxidation of the Cr dopant as observed in section 4.2.1. There was a clear rise in surface roughness associated with Cr doping. This could be due to the rise in film thickness (associated with the inclusion of Cr doping) being related to increased film roughness as observed in section 3.2.5. However, the range of thickness here is very small compared with that in section 3.2.5 and consequently negligible effect would be expected. Therefore it would seem that the addition of Cr directly affects the surface roughness.

There were six significant effects identified with substrate bias voltage with two being of the greatest effect. The results for bias voltage matched those previously discussed in section 4.2.2. The significant reduction of coating thickness with increasing bias voltage is consistent with the coating densification model previously described and with increased re-sputtering of the deposited film at higher cathodic bias.

Ar flow also yielded six significant effects, although most were of less significance than those observed with Cr current and bias voltage. The results of hardness, roughness and thickness are in agreement with those observed for bias voltage. This suggests that the increased Ar availability enhanced the ion bombardment and hence densification of the film. However, a clear reduction of Ar content in the film was also detected as the Ar flow increased. This implies that a contrary mechanism was in operation, such that a greater collision of transported atoms was occurring prior to arrival at the substrate, thus reducing the quantity and energy of bombarding Ar ions. Increased Ar flow produced a large increase in the critical load under nanoscratch testing. No clear mechanism is proffered for this observation given the prior discussion. It is thought that the complex effect that changes in chamber pressure (as a result of changes in Ar flow) have on the coating system (sputtering process, material transport and deposition process), outlined in section 1.3.2, provides the reason for the complex results recorded in this work and the significant interaction observed.

Again six significant effects were identified with the use of an adhesion layer. As with Ar flow most of those were small effects when compared with Cr current and bias voltage. It can be seen that an adhesion layer provided measurable benefits to the adhesion of 150 nm coatings under nanoscratch testing. The reduction of the Si signal as recorded by XPS suggests a reduction of coating pin-holes by the adhesion layer. There was a slight increase in coefficient of friction associated with the use of an adhesion layer; however in general little information could be derived from the friction data.

Considering the obtained results and derived discussion points it is apparent that variations in the testing regime can provide an effective method of determining tribologically important coating properties and performing DOE optimisation work with 150 nm a-C coatings.

4.2.4 Experiment to investigate four key coating process parameters with 50 nm coatings

There were few results with 50 nm coatings that showed statistical significance. The errors were large relative to the differences between mean results. This was due to greater relative noise associated with the smaller measurements and (in the case of hardness and reduced modulus) the production of asymmetric data distributions negating the use of statistical methods based on normal distributions. It is likely that with increased replication of testing and coatings statistical significance could be achieved. An overall comparison between the results at 50 nm and 150 nm showed fewer trends present in the critical load, roughness and thickness data at the lower thickness. Little change in coefficient of friction was observed at both thicknesses. There was however a significant reducing trend in all of these properties with reducing film thickness. These points will be discussed in more detail in section 4.2.5.

A comparison was made between the 50 nm and 150 nm results. Overall, where trends were observed, there is general agreement between results with 50 nm and 150 nm films, suggesting no significant alteration in coating process mechanism and coating properties over this range:

Cr target current showed the same trends for all results with one major exception. This suggests that the effect of Cr, as discussed in section 4.2.3, is operative at 50 nm thickness. The main exception was reduced modulus, where a rising trend with increased Cr was seen in contrast to the falling trend with 150 nm films. No definitive reason is proposed given the errors associated with 50 nm coatings, however changes in film composition and structure with thickness are shown in the results which may provide an explanation: A comparison of surface composition shows the 150 nm films (Table 3.2) to contain more Cr than the 50 nm films (Table 3.8). A comparison of composition data following Ar^+ ion etching to 10 nm with non doped a-C shows little penetration of O with 50 nm films compared with μm scale films, suggesting a more dense structure at low thickness (refer to the discussion in section 4.2.1).

The results for bias voltage generally showed less significance than those for Cr. Trends were present in hardness, reduced modulus and Ar content results. The form was the same as those at 150 nm with, again, the exception of reduced modulus where a reversal of the trend occurred.

The results for changes to Ar flow were also of low statistical significance. Trends were detected with hardness, reduced modulus and O content which matched those observed at 150 nm. Ar also exhibited significant interactions with other coating parameters.

Hardness and reduced modulus trends with adhesion layer were of greater magnitude and opposite sign when compared with similar testing of 150 nm films. This could be due to the compositional and structural changes with film thickness as discussed above. In addition, the small indents required with 50 nm coatings involve working with more of the imperfect tip of the Berkovich indenter compared with 150 nm films, which may alter the stress field below the contact such that the adhesion layer and substrate-adhesion-coating interfaces interfere with the measured nanoindentation results. From elastic contact theory, it is known that increasing the radius of a spherical indenter in contact with a flat material under constant load serves to move the point of maximum stress deeper into the material. It is interesting to note that no reduction of XPS Si signal was observed with the introduction of an adhesion layer, suggesting that the very low thickness layer was ineffective at reducing coating pin-holing.

It is useful to consider the coefficient of friction results in more depth and discuss the reason why little useful information was produced by the NanoTest friction system. Measurable frictional forces were produced when a normal load of tens of mN was applied with a sphero-conical diamond indenter (nominal opening angle 60° and spherical end radius 4 μm). The initial mean contact pressure at this load is approximately 12 GPa by elastic contact theory. This is comparable with the yield stress of the coating and hence the frictional force will be dominated by plastic flow and ploughing (as discussed with thicker coatings in section 4.2.1). A load of 0.05 mN was used during the topography scan and frictional forces were below the limits of detection. The initial mean contact pressure at this load is approximately 1 – 2 GPa by elastic contact theory. This is a very significant pressure (too high to be relevant to MEMS micro-engineering applications) and yet no measurable frictional force was detected by the available equipment. It is apparent from these observations that the NanoTest friction system does not have the sensitivity to provide useful frictional information relevant MEMS tribology and hence to the aims of this work.

4.2.5 Experiment to investigate a range of film thicknesses (2000 nm to 10 nm)

The effect of film thickness on nanoscratch test results observed here (and in section 3.2.3 and 3.2.4) is in good agreement with that previously reported. Beake and Lau [191] showed decreasing critical load and load support with decreasing a-C film thickness. The mode of failure was also shown to change when film thickness was reduced to ≤ 20 nm: with no clear failure event evident. The model proposed by Beake and Lau included two competing factors: (i) greater film thickness (when film is harder than substrate) provides greater load support, to account for the critical load versus depth trend; (ii) greater film thickness introduces greater film stress, to account for the loss of sudden coating delamination events at low thickness. From this model it was predicted that a maximum critical load would occur with 100 nm films. Thicknesses less than this would show reducing critical load due to lower load support and thicknesses greater than this would show reducing critical load due to excessive stress. This effect is not observed here, with the 2000 nm film producing the highest critical load. By inference: coating stress may not provide a significant contribution toward nanoscratch tests in the work reported here.

However, both Beake and Lau's work and that reported here shows a clear mechanistic change with films of thickness ≤ 20 nm. From the result reported in this work with zero film thickness it is apparent that thicknesses of ≤ 20 nm offer no protection to the Si substrate under nanoscratch testing; that is, the change of nanoscratch mechanism at low thickness is in effect a change to the failure mechanism of Si. It may be the case that the plastic (ploughed) depth required for the sphero-conical indenter to create sufficient shear stress for delamination to occur is greater than 20 nm.

Consideration of the Ra results, including those in section 3.2.3 and 3.2.4, shows a clear trend of increasing surface roughness with increasing coating thickness. All films show Ra values greater than the ion etched substrate. During the early stages of film growth, the surface topography conforms relatively closely to the underlying Si substrate. As the film develops greater topographic features are introduced by the action of the film growth, suggesting some limited mobility of incoming atoms, creating 'shadowing' effects. This effect seems to be enhanced when Cr is co-deposited with the C.

No significant change in elemental composition occurred with thickness. This is in contrast to a slight decrease of surface Cr at lower thickness observed when depositing a higher Cr concentration (refer to section 3.2.3 and 3.2.4).

4.3 Experiments to investigate the nanotribology of a-C films

4.3.1 Characterisation of the sample oscillated nanoindentation nanowear process

4.3.1.1 Dynamic depth measurements with the sample oscillated nanoindentation system

Depth drifts of many tens of nm were recorded over typical test durations due to thermal drift, despite the temperature being controlled to < +/- 0.05°C. This shows that there is a large uncertainty attached to dynamic wear depth measurements from the sample oscillated nanoindentation system. A significant improvement in thermal stability is required before this apparatus can be used for continuous wear depth measurement.

4.3.1.2 Low amplitude nanowear mode (experiments 1-9)

The initial mean contact pressure is relatively high for the 200 mN test but much lower than the hardness of the coating. It is clear that the oscillation amplitude is producing a relatively small displacement of the contact when compared with the contact area. This mode of wear is consistent with that previously reported in conditions of fretting wear on hard coatings at similar initial contact pressure but larger scales of load, contact area and displacement [259]. A build up of wear debris around the edge of the contact forms which means that the high stress region is no longer located at the centre of contact, but instead an annular region of high stress forms underneath the trapped debris [199,259]. The wear pattern mirrors the distribution of stress. It is also possible that a partial slip mechanism is operating and under these conditions fatigue failures would tend to occur in a ring around the centre of contact, at the boundary between the stick-slip region where the highest alternating stresses occur [260]. This may account for the points of gross failure / coating cracking of the low load test after extended oscillation time. It is interesting to note the difference in depths at positions on the circular trench parallel and perpendicular to the oscillation. Under a partial slip mechanism, the differences can be attributed to the different types of stress produced in the coating: alternating compressive and tensile at the leading and trailing edges of the oscillated contact; and an alternating shear stress at positions parallel to the oscillation. With conditions of full slip, the parallel and perpendicular locations will certainly exhibit different rates of particle removal producing an asymmetric distribution of debris around the edge of the contact.

4.3.1.3 High amplitude nanowear mode (experiments 10-42)

The distribution of measured results shown in Figure 3.27 is similar to the simple spherical cross-section, which suggests that there may be a significant degree of abrasive wear occurring which is tending to grind the coating to the shape of the counter-body [202]. More importantly, it shows that gross fatigue or delamination events are not occurring. The results are quite scattered which may be indicative of the occurrence of more random fracture events within some of the coating formulations alongside the abrasive wear [202]. The distribution is shifted towards lower scar widths when compared

with the ideal spherical cross-section which suggests that the outer, low pressure regions of the contact are below a critical pressure for true measurable wear to occur.

Ar^+ ion XPS depth profiling of similar coatings showed that the outer layers were composed predominantly of an oxidised C film of just a few nm thickness (Figure 3.12). During the initial stages of the wear test this oxidised (and possibly moisture containing) outer layer of the coating is quickly removed from the total region of contact which is significantly larger than the area of distinct measurable wear. Similar large curls of debris from tribological studies of a-C:H films have been reported elsewhere [212]. The oxidisation process of the outer layers of the a-C coating will likely alter the atomic arrangement and density of the coating in that region, resulting in differences in the internal stress and brittleness between the bulk and the outer-layers which can account for its rapid removal [199,213]. The presence of the oxygen rich outer layer could also be accounted for by the adsorption of oxygen containing organic material from the atmosphere.

The wear scar (Figure 3.26, Figure 3.29 and Figure 3.31) is indicative of the operation of abrasive wear. Under macro-scale testing the topographical dimensions of the wear scar would be considered to be a fine polish, but relative to the size of the scar the abrasion is rather coarse. The hardness of ruby will depend on the orientation, any grain arrangement and to some extent the test method used. Sapphire, ruby and other forms of Al_2O_3 are considered to be hard and are widely used as an abrasive medium. The hardness has been reported around 25 – 35 GPa [261,262] which is higher than the hardness measured for the coatings used in this work. This means that under these conditions the ruby surface would be expected to exhibit predominantly elastic deformations and show little if any wear, which is in agreement with the AES results (Figure 3.30). The hard ruby nano-asperities will initially produce plastic deformations in the a-C coating yielding particles of coating which will further perpetuate the abrasive action as a 3-body wear process. Significant 2-body wear is possible as a result of the nano-asperities of the sapphire counter-body. However, AFM examination of typical wear scars shows considerably broader and deeper grooves than the counter-body asperities (Figure 3.32). In addition, Figure 3.26 shows clear changes in the wear patterning during scar development (particularly between 72000 and 144000 oscillations and between 144000 and 216000

oscillations) which is consistent with irregularly formed and distributed abrasive particles. The released abrasive particles are large relative to the size of the contact and are shaped and oriented such that plastic flow (ploughing) and cutting wear is occurring. With relatively high hardness coatings such as those used in this work there is a tendency for some fatigue fracturing to occur which is likely given the high degree of scatter in Figure 3.27 / Figure 3.28 and this will generate more 3-body particles. As a result of the fracture process, the abrasive particles are expected to have sharp edges and corners which will be maintained by further fracturing during abrasion, enhancing the cutting and ploughing effects [202]. In order to produce high levels of plastic flow, the abrasive particles must have a hardness value greater than the surface of the coating. There is no clear mechanism available to harden the generated abrasive particles: oxidation of the C would be expected to have a softening effect as would mechanical working of a-C coatings due to graphitisation [213,263]. There is no long-range crystal structure within bulk a-C coatings but short-range ordered 'crystallites' are expected. At the small scale employed within this work, the abrasive particles may possess some graphite crystal ordering and be anisotropic in nature with certain orientations possessing a greater hardness than that measured for the bulk of the coating. It has been shown that low rates of wear can occur even with relatively soft 3-body particles [264] as a result of a fatigue wear mechanism [199]. It is clear that the size of the particles and the grooves in the wear scar are large relative to the size of the contact when compared with macroscopic abrasive wear testing where surfaces are relatively smooth. This shows that the size of the generated abrasive particles does not scale with the reduction of external parameters such as: contact area, load, speed and slid distance and this phenomenon has been reported with adhesive wear at much larger scales [202]. Moving to very small contact areas means that the likelihood of large trapped abrasive particles (relative to the contact size) reaching the edge of the contact and being ejected is higher, which has an impact on the material removal rate. It has been shown under macroscopic wear that (for small abrasive particle size) there is a relationship between particle size and wear rate if all other conditions are constant; with larger particles producing increased wear [265,266]. From the Archard [206] model of wear, the wear constant is determined as the volume of material lost per unit sliding distance per unit load. In the case of abrasive wear, the wear constant is related to the hardness of the worn material and the fraction of surface-particle interactions that result in

further particle generation. It seems likely that a change in the particle size and number, relative to the contact area, will affect the fraction term described above, thus influencing the wear constant.

The formation of a transfer film of worn coating material on the counter-body plays an important role in reducing the overall wear rate under macro-scale testing of a-C coatings. It is not clear whether a true wear-reducing transfer film formed under the nanowear conditions here. Optical microscopy and SEM examination of the ruby counter-body clearly shows the presence of a transfer film (Figure 3.33 and Figure 3.34). The composition of the film was predominantly C with some O. It is interesting to note that no Cr was detected in the transfer film and therefore Cr may not play a role in any wear-reducing mechanism, contrary to findings at micro- / macro-scale [232,233]. Despite the limitations of AES and small area monochromatic XPS on a charging sample, one would expect to detect Cr if it was present in the transfer layer at the bulk film concentration (typically 12%). It is difficult to speculate on a mechanism whereby the Cr is segregated out of the coating during transfer film formation. It may be the case that the transfer film is formed from the low Cr outer layers of the (Cr doped) coating, with little material exchange into / out of the transfer film during wear test. It has been previously reported that no transfer film forms on a larger sapphire counter body at higher load [212].

4.3.1.4 High amplitude nanowear contact conditions

It is interesting to compare the calculations of mean contact area and pressure calculated in section 3.3.1.4 with those estimated for macro-scale pin-on-disk tests. Taking a low load pin-on-disk example of 10 N delivered to an a-C coating via a WC counter-body of radius 2.5 mm. The initial contact radius and mean contact pressure was estimated to be 50 μm and 1400 MPa respectively based on the Hertzian contact theory, changing to approximately 125 μm and 200 MPa estimated from a typical 250 μm wear track width [68,267,268].

4.3.2 Experiment to investigate the nanowear of a matrix of 150 nm coatings and the effect of four key coating process parameters

4.3.2.1 Measurement of specific wear rates and analysis of the complete data set

The measured nanowear rates were in general very low. Reported specific wear rates for similar coatings produced by Teer Coatings, tested under macro-scale pin-on-disk conditions were found to fall in the range 1 - 10 x 10^{-17} $m^3N^{-1}m^{-1}$ [68,228,231,232,268,269]. The nano-scale wear rates are generally a little higher than the macro-scale results (with similar coatings) although the order of magnitude was the same. This shows that the measured specific wear rate remains reasonably constant if the mean contact pressure is maintained while the scale of the test (contact area, amplitude, load and depth of wear) is reduced by many orders of magnitude. The pin-on-disk tests were run using hardened tool steel substrates and at a significantly greater sliding speed but a general comparison between the nano- and macro-scale results can be made. The spread of the results is much greater under nano-scale testing when compared with related work to investigate the effects of key process parameters but under macro-scale testing. It has been shown that varying Cr magnetron current and substrate biasing over a much wider range than the work described here (in addition to the substrate bias pulse frequency) using macro-scale pin-on-disk testing produced a range of specific wear rates with a (approximate) factor of 10 between the highest and lowest values [231,232]. With the work described here there is a factor of about 500 between the highest and lowest values. The greater range is not accounted for by the increase of relative experimental error associated with nano-scale work but it does show a greater sensitivity of the nanowear process to the properties of the coating.

The increased data scatter with increasing wear rate implies that in going from a low to high wear rate, the mechanism of wear may also be undergoing change. There are (at least) two possible reasons for this: (1) a greater degree of random fracture events contributing to the increasing wear rate (2) an increase in the variation of the properties (size, shape, quantity and retention time) of generated abrasive particles leading to an increasing wear rate.

4.3.2.2 Statistical analysis of the effect of the four key process parameters using ANOVA

An initial inspection of the main effects plots (Table 3.13) shows that Cr magnetron current has the greatest effect on specific wear rate with an increase of Cr magnetron current from 0 to 0.75 A producing a 5 fold increase of wear rate. Both the use of an adhesion layer and increasing the cathodic substrate bias voltage produced a reduction of wear rate. Adhesion layer, cathodic substrate bias voltage and Cr magnetron current were all found to be statistically significant control parameters for specific wear rate. Ar flow rate was not. The most notable interaction was between Ar flow rate and cathodic substrate bias voltage. At low Ar flow rate, increasing the cathodic substrate bias produced a small (but negligible) increase in wear rate. At high Ar flow rate, increasing the cathodic substrate bias produced a significant decrease in wear rate.

The primary correlation shown in Figure 3.40 is with coating hardness. The Archard model of wear reveals that the specific wear rate (or wear constant) of a surface is inversely proportional to the hardness of the surface. It is clear that the inverse relationship is maintained under nanowear testing. The addition of Cr to a-C coatings has been shown to reduce hardness, which in turn leads to increased specific wear rate as reported in this work. Published results (also used for comparison in section 4.2.1) with similar films but at 2000 nm thickness and tested under macro-scale conditions [232] showed a similar trend of reducing hardness with Cr current, although a hardness reduction of 60 % was reported for the macro-scale work compared with 25 % here, over the same Cr current range. The reported trend in macro-scale (pin-on-disk) specific wear rate in going from 0 to 0.75 A Cr target current was rising, falling and (approximately) unchanging depending on the applied load. At low load, the macro-scale wear was reported to increase by approximately 700 % compared with 383 % from the nano-scale results here, over the same Cr current range. Under nano-scale wear the incorporation of Cr in the film does not appear to provide any beneficial wear reducing properties through increased load support and enhanced transfer film properties as it does with macro pin-on-disk testing at high loads [232]. The role of the transfer film under conditions of nanowear may be less significant than under macro-scale testing given the large size of abrading particles relative to the contact area and film size.

It has been shown in this work that increasing the cathodic substrate bias voltage causes an increase in both hardness and reduced modulus of the coating, which translates into the observed reduction of specific wear rate. Published results with similar films but at 1700 nm thickness and tested under macro-scale conditions [231] showed a similar trend of increasing hardness with bias voltage, although a hardness increase of 40 % was reported for the macro-scale work compared with 28 % here over the same bias range. There was little change in reported macro-scale (pin-on-disk) specific wear rate in going from 40 to 80 V bias compared with a 30 % reduction here. No clear mechanism for the interacting influence of Ar flow rate can be shown. It is suggested that at low Ar chamber pressure there may be a limited number of Ar^+ ions available to provide a significant increase in the flux of bombarding ions with increased cathodic substrate bias, leading to the strong Ar flow – bias voltage interaction. Further work is required to fully understand this effect.

The concept of a Cr adhesion layer was developed to provide a transition between materials of different modulus, hence avoiding a concentration of shear forces at the coating-substrate interface. This is particularly effective with relatively thick C films on metal substrates. This work shows that a Cr adhesion layer provides measurable wear reduction with thin C films on Si substrates under nano-scale wear processes. If the mechanism by which the Cr layer acts to reduce the wear rate is simply by providing better adhesion of the coating to the substrate (thus reducing the chance of adhesion failure events contributing to wear) and given that the critical load value is sensitive to coating adhesion, then a correlation would be expected between critical load and specific wear rate such that a higher critical load coating would correlate with a lower wear rate result. Figure 3.40 (d) shows that this is not the case. A more thorough analysis of the data shows that the wear reducing effect of the adhesion layer is only significant with the Cr containing coatings and serves to not only reduce the mean specific wear rate but also to reduce the scatter of results.

4.3.2.3 Correlations with the tribologically important properties of the coatings

The correlation plots show the nanowear mechanism to be in agreement with the standard model developed for macroscopic wear: (i) wear is primarily dominated by film hardness

(ii) harder, stiffer (high H/E_r) coatings produce less wear. There is a positive relationship between surface roughness and wear rate which is absent from the Archard model of wear. However, the link is likely to be due to the association between Cr content and surface roughness rather than a direct roughness-wear cause and effect. A positive relationship between wear rate and large increases of surface roughness has been reported elsewhere under macroscopic testing of DLC coatings [270]. A similar relationship can be seen with coating thickness which is also likely to be due to the association between Cr content and thickness. It is interesting to note that no correlation was present between nanoscratch critical load and wear, suggesting that the nanoscratch tool is a poor predictor of nanowear properties. The relationships between wear and film composition are in agreement with the link between Cr content and hardness.

Under conditions of nanotribology, such as those described in this work, the area of contact is small when compared with micro or macro-scale testing. This means that any coating defects will have more impact on wear results at the nano-scale compared with micro- and macro-scale work. Large test areas mean that a more representative sample of the coating is used, averaging out the effects of any defects. With nanotribology, defects can be encountered or not at different locations meaning that more scatter of data is expected.

It can be seen from Figure 3.39 that there is a clear relationship between wear rate and data scatter and two possible reasons for this effect were proffered at the end of section 4.3.2.1. From the previous discussion, it is the case that coating hardness is the principle factor affecting the abrasive wear rate for the nanowear described here. The nature of fracture events within a wear process tends to be more random [202] than an abrasive, grinding wear action and so the increase in data scatter could be as a result of the wear mode gaining a greater contribution from fracture events. However, harder, stiffer coatings are usually more brittle and of lower fracture toughness, hence more likely to suffer fracturing than films which are softer and more elastic and this is the reverse trend to that observed here. So the increased scatter at high wear rate is most likely due to another reason.

A more likely explanation takes account of the abrasive particles trapped between the contact, which is fundamental to the wear action. Under 3-body abrasive wear conditions: once the wear process has stabilised and loose material has been generated, the wear action is principally occurring between the coating and the trapped abrasive particles. Any changes that occur to the quantity, size, shape, physical properties or retention time of the particles at the contact must affect the wear rate. If the generation rate, properties and retention of particles at the contact are stable then the wear rate will be stable. If this is not the case then fluctuations of wear rate would be expected. The previous discussion has shown that the wear particles do not scale with the size of the contact. Therefore with small contact area nanowear conditions, there are much fewer and larger particles (relative to the contact size) than under macro-scale conditions. The tiny contact area (typical contact radius 4 – 7 μm) means that the probability of a relatively large trapped abrading particle reaching the edge of the contact and being ejected is far more likely than with the same sized particles under a contact area many orders of magnitude larger which would have an impact on the rate of material loss and therefore the wear rate. The small number of trapped particles means that the loss (or gain) of a few particles from ejection (or formation) events would have a greater influence on the wear rate. For this reason a nano-scale abrasive wear system is expected to be more unstable than an equivalent macro-scale system and this provides a further mechanism to account for the greater scatter of results when compared with similar macro-scale pin-on-disk work. This mechanism can also explain the increasing data scatter with increasing wear rate, as lower hardness films will undergo more plastic flow and cutting wear action with a higher probability of generating larger particles, thus exacerbating the instability. The inverse relationship between material hardness and worn particle size has been reported under adhesive wear conditions [202,271].

Hardness is not the only influence. As the four process parameters are changed, this not only results in changes to the coating hardness with all other conditions remaining constant, there are accompanying alterations in the coating composition and structure which will very likely affect the quantity, size, shape and physical properties of the abrasive particles produced, which in turn will influence the wear rate and stability. Moving from low-to-high Cr current and high-to-low bias voltage produced a similar

reduction of (mean) coating hardness (25 % and 22 % for Cr and bias respectively). For Cr this change resulted in a 383 % increase of (mean) specific wear rate, whereas for bias voltage this change resulted in just a 43 % increase. It is apparent from this that there are changes occurring, as a result of Cr and/or bias alterations, which are affecting the wear mechanism in a more complex manner than just by the control of film hardness. Reference to and rearrangement of the standard Archard model given in Equation 1.24 shows that specific wear rate *Q/W* (volume of material lost per unit load per unit slid distance) is related to hardness in the following way:

Equation 4.1

$$\frac{Q}{W} = K.\frac{1}{H}$$

where *H* is hardness and *K* is the wear coefficient. Changes in Cr and/or bias not only alter *H* but may affect *K*. The wear coefficient is a constant of proportionality, however the value of *K* may alter as a function of wear conditions (for example: properties of the materials under sliding contact, temperature, humidity) and wear mode (for example: adhesive wear, abrasive wear, fatigue wear). For abrasive wear, *K* is a measure of the probability of a potential wear interaction with an asperity or abrasive particle resulting in the occurrence of an actual wear event. In moving from an undoped to an approximately 12% Cr doped a-C film, a clear change in composition has occurred which is likely to change certain material properties that are not easily captured by standard material testing methods. It has been discussed above and in section 4.3.1.3 that the nanowear process is likely to involve a combination of abrasive wear and some fatigue wear events; therefore *K* captures some contribution from both. The addition of significant Cr doping may alter the size of initial abrasive particles released from fatigue events as a result of the increased surface roughness associated with Cr doping or from the release of possible Cr_3C_2 (or other Cr-C bonded) crystallites from the film, thus influencing wear rate independently of *H*. It can be speculated that the inclusion of significant Cr doping may affect the adhesive forces retaining the nano-scale abrasive particles within the contact zone thus enhancing material removal and therefore wear. This is very speculative but

again indicates the importance of further work to investigate the properties and behaviour of released abrasive particles.

4.3.3 Experiment to investigate the nanowear of a matrix of 50 nm coatings and the effect of four key coating process parameters

4.3.3.1 Measurement of specific wear rates and analysis of the complete data set

It is clear that there was a slight reduction of wear rate with reducing film thickness (comparing the 50 nm results here with the 150 nm work). This change was accompanied by a more significant reduction of data scatter which is consistent with the wear rate – data scatter relationship discussed in section 4.3.2. This trend is more clearly observed and therefore discussed in section 4.3.4.

Test times were reduced with 50 nm films based on the prior experience with 150 nm and taking into account the reduction of material thickness. The short-time tests revealed an initially high wear rate, reducing and stabilising after approximately 18000 oscillations. The early stage results are typical of the 'running-in' process encountered with many wear systems where the wear rate falls exponentially and stabilises due to: (i) a reduction of contact pressure as the wear scar grows (ii) the formation of a lubricating transfer film (iii) blunting of the abrasive asperities / particles (iv) clogging of the gaps between asperities.

4.3.3.2 Statistical analysis of the effect of the four key process parameters using ANOVA

Overall, the effect of the four process control parameters with 50 nm coatings was in line with that found at 150 nm. This supports the findings in section 4.2.4 where it was shown that the effects of the four coating parameters (on the film properties) is broadly similar over this thickness range. However, with the exception of bias voltage, the significance of the effects of the process controls was greatly reduced at 50 nm, pointing to a possible change in wear mechanism.

Cr magnetron current again demonstrated an increasing wear effect which can be attributed to the softening influence of Cr doping, with no implied benefit to the transfer film behaviour. The significance of the effect of Cr was small in comparison to that observed at 150 nm. The applied change in Cr current produced a reduction of (mean) film hardness of approximately 25% at both 150 nm and 50 nm thickness but yielded an increase in (mean) wear of just 33% with 50 nm coatings (down from 383% with 150 nm coatings). On the other hand, substrate bias voltage produced a comparable effect on (mean) wear at both thicknesses, which was of similar magnitude to the Cr effect at 50 nm. It can be speculated that over these two thicknesses the effect of bias voltage is primarily related to hardness, whereas a complex effect involving both hardness and wear coefficient is produced by Cr (as discussed at the end of section 4.3.2.3) at the higher thickness. This becomes simplified to just a hardness relationship at the lower thickness as the probability of fatigue events is reduced (this point is expanded in section 4.3.4).

Reductions in the effect on wear of both Ar flow and adhesion layer were also present with the thinner coatings, which further indicates a wear contribution related to coating thickness.

4.3.3.3 Correlations with the tribologically important properties of the coatings

The correlation plots with hardness and *H/Er* are in agreement with those determined at 150 nm, which shows that the general nanowear mechanism at 50 nm thickness is also in agreement with the Archard model developed for macroscopic wear. As implied with regard to Cr content above, the effect of changes in both *H* and *H/Er* on wear is greatly reduced at the lower film thickness. Little correlation was observed for reduced modulus, Ra and coating thickness which reflects the reduced effect of Cr on wear and the less clear associations between Cr content and these film properties at 50 nm. On the other hand, the relationships between wear and film composition are generally maintained in going from 150 nm to 50 nm films confirming the sustained link between Cr content and film composition with thickness. Again there was no significant correlation between critical load and wear providing further support for the limited use of nanoscratch when considering nanowear.

4.3.4 Experiment to investigate the nanowear of a range of film thicknesses (2000 nm to 10 nm)

It is clear from the results that there is a strong positive-going relationship between wear rate and coating thickness. The relationship can be fitted with an exponential function with wear rate decreasing rapidly at low thickness (Figure 3.48 (d)). The results discussed in section 4.3.2 and 4.3.3 at 150 nm and 50 nm thicknesses are in agreement with this trend. As film thickness is reduced from 150 nm its effect on wear will become very large and is expected to dominate other contributions considered. This explains the reduction of significance (on wear) of the coating process parameters in going from 150 nm to 50 nm.

In a simple wear model, where it is assumed that the rate of wear remains constant along with the contact area between the touching surfaces over time and coating failure is said to occur when wear depth is equal to film thickness, it can be shown that:

Equation 4.2

$$d_f \propto \frac{t}{W_r}$$

where d_f is the slid distance to coating failure (which is proportional to the time to coating failure or number of oscillations to coating failure), t is the coating thickness and W_r is the specific wear rate of the coating. Between 10 nm and 150 nm, the specific wear rate versus thickness curve can be accurately fit (for SI units) by the expression:

Equation 4.3

$$W_r = 9.76 \times 10^{-17} e^{\frac{-1.35\times10^{-8}}{t}}$$

This is shown in Figure 4.1 (a). Inserting Equation 4.3 into Equation 4.2 and plotting the resulting curve (Figure 4.1 (b)) shows the competing effects of: (i) greater film thickness increasing the slid distance (or time) to failure by providing more material between the contact point and substrate (ii) lower film thickness increasing the slid distance (or time) to failure by reducing the wear rate.

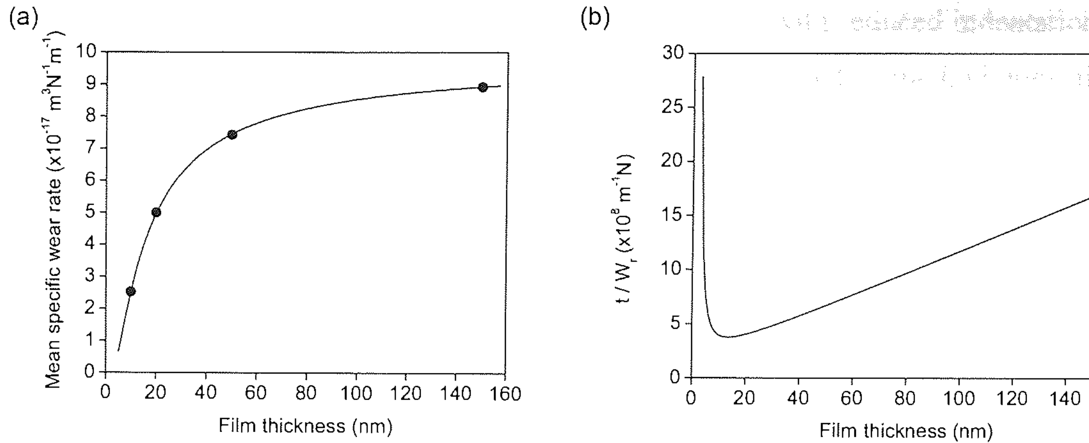

Figure 4.1 (a) Mean specific wear rate versus film thickness data fit with the expression in Equation 4.3 (b) Time or slid distance to failure versus film thickness expressed as t/w_r from Equation 4.2.

It can be seen that a minimum wear resistance to coating failure occurs with films of approximate thickness 14 nm. Thicknesses higher or lower than this will produce a greater wear resistance to coating failure. Of course this is a very simple model and it is clear that the rising trend below 14 nm thickness must peak and fall at some value below 10 nm, since the wear resistance of zero thickness (uncoated Si) has been shown to be very poor.

Bhushan and Koinkar [188] reported reduced wear and reduced deformation under nanoscratching with 5 nm and 10 nm DLC coatings in comparison to results at 25 nm. However the tribological performance of the substrate was very different to that used in the work reported here. The uncoated Ni-P substrate was shown by Bhushan and Koinkar to produce the lowest degree of wear tested, whereas here the uncoated Si substrate has been shown to produce very high levels of wear. It was speculated that reduced wear at low film thickness may be due to an increased contribution from the low wearing substrate or as a result of greater film-substrate interfacial adhesion.

Lin et al. [198] also reported reducing wear volumes with reducing coating thickness under nanoscratch testing over the range 150 to 70 nm for a-C:H coatings on Si. It was tentatively speculated that this was due to increased work of (film) adhesion and increased Young's modulus of the film with reducing thickness. However, it should be

pointed out that a significant increasing trend of modulus with reduced indentation depth was reported but it is not clear whether this could be attributed to methodological errors as summarised in section 1.5.3.1.9.

Clearly it is the initial film thickness that is important, as the results show that wear rates of thicker coatings do not exponentially decrease as the substrate is approached. It has been shown that there is little change in hardness with film thickness, therefore consideration of the Archard equation of wear (Equation 4.1) suggests that a change of the K term occurs with thickness. Under conditions of 3-body abrasive wear this implies: a reduction of the number of generated particles; a reduction in size of the particles; a change in the physical properties of the particles such that material removal is reduced. If fatigue mechanisms are primarily responsible for the initial formation of abrasive particles, it is possible that the close proximity of the film-substrate interface acts as a barrier to z-axis crack growth with thinner coatings, reducing the size and number of those particles. Also, as film thickness decreases any residual stresses in the film are expected to significantly reduce with a likely reduction of abrasive particles formed due to fatigue events. Under a sliding contact between a spherical indenter and flat surface the stress distribution is such that the zone of maximum stress is typically located significantly below the surface [272,273,274]. The depth of maximum stress is related to the coefficient of friction at the contact. For friction coefficients ≤ 0.3 the depth of maximum stress is in the rage 0.4 – 0.5 times the contact radius. This equates to a range of 1000 – 160 nm for the loads used. Hence the maximum stress is located within the 2000 nm film yet in the substrate for the other films and progressively further from the coating as the thickness is reduced. This will mean that changes of stress during oscillation cycles and stress gradients within the coating are less significant as film thickness is reduced thus lowering the probability of fatigue events and hence the initial release of abrasive particles. Of course the values given are for an ideal situation and are most appropriate for a macro-scale system, where asperities are not considered. Under nano-scale testing, asperities are large relative to the contact radius creating a more complex system. Also, with time the indenter will be supported by a wear scar rather than a simple ball-on-flat model further complicating the system. However, it is thought that this analysis still provides a possible reason for the observations made, particularly when

one considers the asperity flattening and clogging of inter-asperity gaps that occurs during the early stages of test (see Figure 3.50). With thin films, the maximum changes of stress and stress gradients will be located in the Si, which has been shown to have poor fatigue resistance under nanowear testing, however it is possible that fracture growth to the surface may be impeded by the film-substrate interface. In addition, even a thin a-C film ensures that no direct contact is made between the Si and counter-body providing some shielding from any bouncing effects as the counter-body slides across the surface.

Under the macro-scale Archard model of wear, specific wear rates are independent of applied load, assuming that the wear mode does not change. It can be seen in Figure 3.48 that at low loads this is not the case; specific wear rate increases with reducing load. This is not surprising given the very small contact areas at low load and likely sensitivity of these systems to small changes in the properties of the abrading particles as a function of load (see 4.3.2.3). A reduction of wear with increasing load has also been reported with similar coatings deposited at μm-scale thickness and tested with macro-scale pin-on-disk [231]. The deviation from Archard model was ascribed to the operation of a transfer film.

A 'running-in' pattern can be observed in the data shown in Figure 3.47, characterised by a rapid reduction of the initially high wear rate. This is consistent with the formation of a transfer film, which has been shown to be present, although its effectiveness on wear reduction is unproven. The pattern may also be attributed to the initial flattening of asperities and clogging of inter-asperity gaps as shown in the AFM scans of Figure 3.50. This is in agreement with the findings of Achanta et al. [234].

5 Conclusions and further work

The findings revealed in this work have been compared with the aims laid out at the end of the introduction (section 1.6). The conclusions given below are structured such that the progress toward the aims is made clear. Suggestions of any further work that may be required to fully meet the aims are included at the end, along with possible new areas of research inspired by these findings.

5.1 Assessment and development of an array of test methods for low wear / low friction ultra thin a-C films relevant to MEMS and micro- / nano-scale engineering systems

5.1.1 Chemical composition and structure

(i) XPS provided useful information regarding surface and bulk film compostion for all film thicknesses tested. Relationships were identified between process control parameters and film composition and nanowear. Some interference from the substrate and interlayers occurred at 10 nm film thickness, as the analysis depth was close to the coating thickness. When testing films < 10 nm the use of ARXPS is recommended to limit the analysis depth.

(ii) Fundamental problems were identified with the use of XPS C 1s peak analysis to determine sp^3/sp^2 ratio of a-C and a-C:H films, therefore this technique was limited to some tentative estimates in the early stages of the work. When no reliable spectral information is obtainable from the C-C bonding in a specimen then assumptions have to be made. It has been shown that a calculated sp^3/sp^2 ratio is strongly dependent on the chosen assumptions, thus questioning the repeatability and reproducibility of results. While a large body of research has been published providing good evidence for the effectiveness of this approach, it is the opinion of the author that this work has raised some important issues which question its validity and this requires further research.

(iii) AES and small area XPS provided some useful information about the composition of transfer films and worn surfaces but charging effects limited the usefulness. This is likely to be a common difficulty when working with nanotribology due to the small test areas

and range of suitable materials. More stable results would be produced by coating specimens with a thin conductive Au film (of just a few atoms) prior to AES/XPS testing. However this would render the article useless for any subsequent nanotribology testing.

5.1.2 Physical properties

(i) Relationships between process control parameters and surface roughness and nanowear wear were identified with AFM, although the effects of roughness became less significant with reducing depth.

5.1.3 Mechanical properties

(i) No pile-up or cracking of films examined in this work was observed.

(ii) No clear indentation size effect was observed with nanoindentation testing down to 5 nm indents, when a significant number of replicates were used and with an appropriate statistical treatment of data. Consequently, nanoindentation was successfully used to measure hardness and reduced modulus of films as thin as 50 nm; beyond the range of previously reported work.

(iii) No correlation was found between critical load results (from nanoscratch testing) and nanowear.

5.1.4 Nanotribology

(i) Under conditions relevant to MEMS, extremely low frictional forces were generated using a nanoscratch testing system coupled to a standard NanoTest friction probe. The forces were below the limits of detection of the system meaning that no useful information was produced. It would be necessary to modify the friction probe transducer or add further amplification in order to generate a measurable signal; however this may not improve the signal to noise ratio if the noise is mainly produced from specimen surface non-uniformities. A new approach to friction measurement is required which can couple to the sample oscillated nanoindentation nanowear system, for dynamic friction measurements.

(ii) Wear testing using multipass nanoscratching was capable of showing similar trends to those reported with macro-scale testing (pin-on-disk) and sample oscillated nanoindentation nanowear when plastic deformation was the primary controlling factor. The technique produced extremely high contact pressures limiting the wear mechanism to (almost) single asperity ploughing, with little specific relevance to MEMS. High absolute wear rates were produced relative to the other techniques. Given the time of each test it was impractical to undertake > 10 cycles therefore, even at completion, the wear process would not be expected to have stabilised or fully undergone any tribo-chemical changes and transfer film formation.

(iii) The sample oscillated nanoindentation nanowear system was shown to create conditions relevant to MEMS and produce measurable wear with film thicknesses down to 10 nm. It is expected that applied loads can be successfully reduced further to test a greater range of MEMS contact pressures. With some adjustments to the apparatus and possible replacement of the transducer it is expected that sliding speeds can be increased to be more in line with those expected for micro-scale motors. With impoved temperature control of the nanoindentation system, continuous monitoring of wear depth may be possible.

5.2 Application of the test methods to a series of SIP a-C and Cr doped a-C coatings

5.2.1 Use of DOE with commercially produced ultra thin coatings

(i) DOE was an effective tool for the optimisaton of commercially produced low wear / low friction films deposited at 150 nm. The effectiveness of the DOE technique was also proven with 50 nm films, however increased replication of testing and film production would be expected to improve the statistical significance of the observed effects.

5.2.2 Investigation of the effect of thickness on the properties of coatings/coating process

(i) The addition of an increasing level of Cr doping to a-C films formed an increasing amount of C-Cr bonding until the C:Cr ratio reached 2:3 (which is likely to be C_2Cr_3).

The co-deposited Cr formed Cr-O on the surface (as a result of post-deposition oxidation) and reduced the diffusion of O into the bulk.

(ii) Cr was the most effective coating process parameter for controlling film properties relevant to nanotribology over all thicknesses investigated. The general effect of Cr doping was to make films softer, more elastic and rougher. This was detrimental to tribology under nano-scale testing, irrespective of coating thickness. The magnitude of the effect of Cr current on the film properties reduced with coating thickness as did the number of significant effects identified.

(iii) The magnitude of the pulsed bias voltage was the most important of the three available pulse bias parameters. However, both pulse frequency and pulse width were shown to produce interactions with voltage magnitude (and one other) and would need to be considered for a complete optimisation process.

(iv) Bias voltage was an important parameter for controlling film properties relevant to nanotribology. The general effect of bias voltage was to harden and stiffen the films by densification, as a result of increased ion flux and ion energy during the coating process. The effect of bias voltage was beneficial to nanotribology at all thicknesses tested. The magnitude of the effect of bias voltage on the film properties reduced with coating thickness as did the number of significant effects identified.

(v) Ar flow was generally a less important control parameter compared with Cr current and bias voltage. Ar flow had complex effects on the film properties which reflects the complex effects that changes to chamber pressure has on the whole coating process. Again, the magnitude of the effects on the film properties reduced with coating thickness as did the number of significant effects identified.

(vi) The use of an adhesion layer was also less important compared with Cr current and bias voltage. An adhesion layer was shown to improve adhesion under nanoscratch testing and reduce nanowear with 150 nm films but offered no measurable improvement at 50 nm thickness.

(vii) There was little change of: film hardness, reduced modulus, composition and the ability to produce a multi-layered coating structure, with thickness.

(viii) Critical load (from nanoscratch testing) increased with film thickness due to increased load support. Films below 20 nm provided no measurable benefit to critical load over uncoated Si. Easily observable coating delamination under nanoscratch testing reduced with reduced thickness. It was speculated that insufficient plastic (ploughed) depth was achieved with ultra thin films for the sphero-conical indenter to create shear stresses capable of producing delamination before Si fracturing occurred.

(ix) The surface roughness of deposited films increased with film thickness suggesting some limited mobility of incoming atoms, creating 'shadowing' effects.

5.2.3 Investigation of fundamental tribology at the nano-scale

(i) At low oscillation amplitude (2 μm at 10 Hz) relative to contact area (2 – 5 μm) and under loads between 10 and 200 mN against a spherical ruby counter-body classic fretting wear occurred.

(ii) At high oscillation amplitude (14 μm at 10 Hz) relative to contact area (0.4 – 4 μm) and under loads between 0.1 and 10 mN against a spherical ruby counter-body full reciprocating sliding was produced and the wear mechanism changed to predominantly 3-body abrasion although the release of abrasive particles by fatigue events was also likely.

(iii) It was possible to quantify specific wear rates of films under nanowear and these were shown to be very low (10^{-16} – 10^{-18} $m^3N^{-1}m^{-1}$). There is therefore a great potential for this type of film to offer practical solutions to MEMS and micro- / nano-engineering problems.

(iv) Values of specific wear rate were of similar order of magnitude under both nanowear and macro-scale (pin-on-disk) testing, despite large differences of test condition.

(v) The nanowear results were generally consistent with the Archard model developed for macroscopic wear: hardness was the main controlling factor; wear was inversely

proportional to film hardness; wear was inversely proportional to film H/E_r ratio. There were some deviations from the standard model listed below.

(vi) Nanowear rate reduced exponentially with reducing (initial) film thickness. It was speculated that this effect may be linked to a reduction in the release of abrasive particles by fatigue events with reduced film thickness due to (i) the close proximity of the film-substrate interface acting to inhibit crack growth (ii) reduced coating residual stress with reduced film thickness (iii) the stress changes and stress gradients associated with a reciprocating sliding system being primarily located in the substrate and progressively further from the film as thickness is reduced. It would be very interesting to extend the work to test film thicknesses below 10 nm, as the exponential reduction of wear rate is expected to reach a minimum and then rise, since zero thickness (uncoated Si) demonstrated a very high wear rate.

(vii) Replicated testing of films showed that increasing specific wear rate under conditions of nanowear was associated with a greater data spread. This effect was ascribed to the small number of relatively large abrasive particles, which are involved in the wear system, leading to wear rates being sensitive to small changes in the number and properties of those particles.

(viii) Nanowear rate increased with reducing applied load and this effect was related to the sensitivity of wear rate to small changes in abrasive particle properties under conditions of very low load with accompanying small contact areas.

(ix) The properties of the abrasive particles formed during the nanowear process are important governers of the nanowear process and changes to those particles are implicated as being the cause of many of the observations noted above. Further work is required to investigate the mechanism of particle formation and to isolate, measure and hence link the properties of the particles to nanowear.

(x) A 'running in' process was present under conditions of nanowear. This is consistent with the formation of a transfer film on the counter-body and this was identified. It was not clear whether the transfer film provided a wear reduction mechanism at the nano-scale. Only C was detected in the transfer film, even when approximately 12 % Cr doping

was included in the film. Further work is required to understand the nature and effect of the nanowear transfer film. The initial nanowear stage was dominated by asperity flattening and clogging of interasperity gaps, which is also consistent with the observed 'running in' wear reducing pattern.

(xi) The coating process factors investigated provided an effective control of specific wear rate with 150 nm films, but this diminished with reducing thickness. Therefore it is expected that large changes to the process control factors are required to achieve a significant effect on wear at very low thickness. It is also expected that the specific wear rate of films < 20 nm would be mainly controlled by thickness variation.

5.2.4 Optimisation of a-C films for nanowear

(i) Film thicknesses ≥ (approx.) 20 nm:

- The process control parameters developed for μm scale thicknesses are operative but as thickness is reduced much larger changes to the control parameters may be required to have an effect.
- Nanowear is primarily dominated by film hardness, therefore promotion of high hardness will reduce wear (no Cr doping, high substrate bias voltage). However, the production of excessive coating stress may be detrimental to film adhesion.
- The use of bias pulse frequency, bias pulse width, Ar flow and an adhesion layer may be included in an optimisation sequence to balance competing priorities.

(ii) Film thickness < (approx.) 20 nm:

- The process control parameters developed for μm scale thicknesses are likely to be inoperative.
- Lower the film thickness for reduced wear rate (being aware that there will be an as yet undetermined minimum).
- Use a high hardness film.

- Film stress is likely to be insignificant for nanowear at ultra low thickness (although of course this may need to be considered for maintaining the shape of a compliant item).

5.3 Further work

5.3.1 Determination of sp^3/sp^2 ratio by XPS C 1s peak analysis

The work undertaken in this thesis has highlighted some important issues with the current use of C 1s peak analysis for the determination of sp^3/sp^2 ratios. A series of typical a-C:H and a-C films should be tested with the highest resolution equipment currently available, a synchrotron X-ray source, to identify the true structure of the C 1s peak and provide valuable information concerning the location and shape of component peaks. The results from this exercise can then be applied to laboratory XPS results and correlated with other analysis methods (C KLL D value, Raman).

5.3.2 Nanotribology

The sample oscillated nanoindentation nanowear equipment has an excellent potential for further development. Testing with loads below 0.1 mN should be undertaken to reduce the contact pressures further, covering a wider range of MEMS conditions. However, at very low loads there is a possibility of the indenter 'bouncing' rather than maintaining a constant contact. It may be necessary to modify the oscillator module so that minor adjustments to sample orientation can be made in order to optimise the perpendicular alignment and hence reduce bouncing. Alternatively a larger counter-body could be considered. Faster oscillation speeds should be investigated by increasing the supplied voltage frequency, however a reduction of amplitude is expected. A modification to the oscillator transducer may be necessary to overcome this. With improvements to the temperature stability of the nanowear chamber (and laboratory) it may be possible to fully exploit the nanoindentation unit to continuously monitor wear depth during testing. More significant development work should be undertaken to incorporate dynamic friction monitoring into the nanowear test unit to provide full nanotribometry.

The materials tested by the nanowear system should be expanded to cover a wider range, with importance to MEMS and also for fundamental nanotribology: Si, polysilicon, etched Si sidewalls, a-C:H, ta-C, organic monolayers, Au, Ni, W, tool steel, SiO_2, Cr_2O_3 and Al_2O_3. Certain key materials should be tested in a real MEMS device in order to understand the relationship with those results obtained under ideal test conditions.

The important film thickness-wear effect which was identified and quantified for the first time in this work should be further investigated. Sputtered a-C film thicknesses below 10 nm should be investigated to establish the relationship in the range 0 – 10 nm. Other materials should be tested to investigate the effect of material properties on the observed thickness-wear relationship.

The importance of wear-generated abrasive particles on nanowear has been demonstrated in this thesis. This provides a significant area for further research. Key areas of research include the formation mechanism of particles (the use of single asperity AFM testing is appropriate here), their properties (including tribo-chemical changes and formation of transfer films) and the relationship to wear rates and environmental conditions.

References

[1] DTI, Basic Technologies for Industrial Applications LINK project 'CONTACT' internal documentation, DTI reference CHBL/C/019/00024 (2004) (unpublished).

[2] L-S. Fan, Y-C. Tai, R.S. Muller, *IC-processed electrostatic micromotors*, Sens. Actuators 20(1-2) (1989) 41-47.

[3] Y-C. Tai, R.S. Muller, *IC-processed electrostatic synchronous micromotors*, Sens. Actuators 20(1-2) (1989) 49-55.

[4] W.S.N. Trimmer, K.J. Gabriel, *Design considerations for a practical electrostatic micro-motor*, Sens. Actuators 11(2) (1987) 189-206.

[5] M. Mehregany, S.D. Senturia, J.H. Lang, P. Nagarkar, *Micromotor fabrication*, IEEE Trans. Electron Devices 39(9) (1992) 2060-2069.

[6] L-S. Fan, Y-C. Tai, R.S. Muller, *Integrated movable micromechanical structures for sensors and actuators*, IEEE Trans. Electron Devices 35(6) (1988) 724-730.

[7] M.J. Madou, *Fundamentals of microfabrication: the science of miniaturization (second edition)*, CRC Press, 2002.

[8] National research council, *Microelectromechanical systems: advanced materials and fabrication methods*, National Academies Press, 1997.

[9] N. Maluf, *An introduction to Microelectromechanical Systems engineering (second edition)*, Artech House Inc, 2004.

[10] T.A. Core, W.K. Tsang, S.J. Sherman, *Fabrication technology for an integrated surface micromachined sensor*, Solid State Technol. 36 (1993) 39-47.

[11] J.A. Williams, H.R. Le, *Tribology and MEMS*, J. Phys. D: Appl. Phys. 39 (2006) R201-R214.

[12] P.F. van Kessel, L.J. Hornbeck, R.E. Meier, M.R. Douglass, *A MEMS-based projection display*, Proc. IEEE 86(8) (1998) 1687-1704.

[13] S.B. Luitjens, W. Folkerts, H.W. van Kesteren, J.J.M. Ruigrok, *Trends in digital magnetic recording: the application of thin-film heads for tape recording*, Philips J. Res. 51 (1998) 5-19.

[14] K. Komvopoulos, *Surface engineering and microtribology for microelectromechanical systems*, Wear 200 (1996) 305-327.

[15] S.H. Kim, D.B. Asay, M.T. Dugger, *Nanotribology and MEMS,* Nanotoday 2(5) 2007 22-29.

[16] S.J. Timpe, K. Komvopoulos, *An experimental study of sidewall adhesion in microelectromechanical systems*, J. Microelectromech. Syst. 14(6) (2005) 1356- 1363.

[17] W.M. van Spengen, R. Puers, I de Wolf, *On the physics of stiction and its impact on the reliability of microstructures*, J. Adhesion Sci. Technol. 17(4) (2003) 563-582.

[18] Y-P. Zhao, L.S. Wang, T.X. Yu, *Mechanics of adhesion in MEMS – a review*, J. Adhesion Sci. Technol. 17(4) (2003) 519-546.

[19] H. Guckel, J. J. Sniegowski, T. R. Christenson, F. Raissi, *The application of fine-grained, tensile polysilicon to mechanicaly resonant transducers*, Sensors Actuators A 21(1-3) (1990) 346-351.

[20] C-J. Kim, J.Y. Kim, B. Sridharan, *Comparative evaluation of drying techniques for surface micromachining*, Sensors Actuators A 64(1) (1998) 17-26.

[21] U. Srinivasan, M.R. Houston, R.T. Howe, R. Maboudian, *Alkyltrichlorosilane-based self-assembled monolayer films for stiction reduction in silicon micromachines*, J. Microelectromech. Syst. 7(2) (1998) 252-260.

[22] W.R. Ashurst, C. Yau, C. Carraro, R. Maboudian, M.T. Dugger, *Dichlorodimethylsilane as an anti-stiction monolayer for MEMS: a comparison to the octadecyltrichlorosilane self-assembled monolayer*, J. Microelectromech. Syst. 10(1) (2001) 41-49.

[23] D. Kobayashi, C-J Kim, H. Fujita, *Photoresist-assisted release of movable microstructures*, Jpn. J. Appl. Phys. 32 (1993) L1642-L1644.

[24] Y. Yee, K. Chun, J.D. Lee, C-J. Kim, *Polysilicon surface-modification technique to reduce sticking of microstructures*, Sensors Actuators A 52(1-3) (1996) 145-150.

[25] R. Banga, J. Yarwood, A.M. Morgan, B. Evans, J. Kells, *FTIR and AFM Studies of the Kinetics and Self-Assembly of Alkyltrichlorosilanes and (Perfluoroalkyl)trichlorosilanes onto Glass and Silicon*, Langmuir 11 (1995) 4393-4399.

[26] M.M. Sung, G.J. Kluth, O.W. Yauw, R. Maboudian, *Thermal Behavior of Alkyl Monolayers on Silicon Surfaces*, Langmuir 13 (1997) 6164-6168.

[27] M.R. Linford, P. Fenter, P.M. Eisenberger, C.E.D. Chidsey, *Alkyl Monolayers on Silicon Prepared from 1-Alkenes and Hydrogen-Terminated Silicon*, J. Am. Chem. Soc. 117(11) (1995) 3145-3155.

[28] W.M. van Spengen, *MEMS reliability from a failure mechanisms perspective*, Microelectronics Reliability 43 (2003) 1049-1060.

[29] K.J. Gabriel, F. Behi, R. Mahadevan, *In situ friction and wear measurements in integrated polysilicon mechanisms*, Sensors and Actuators A 184 (1990) 21–23.

[30] M. Mehregany, K.J. Gabriel, W.S.N. Trimmer, *Integrated fabrication of polysilicon mechanisms*, IEEE Trans. Electron Devices 35 (1988) 719–723.

[31] S.T. Patton, J.S. Zabinski, *Failure mechanisms of a MEMS actuator in very high vacuum*, Tribol. Int. 35(6) (2002) 373-379.

[32] M.L.W. van der Zwan, J.A. Bardwell, G.I. Sproule, M.J. Graham, *Mechanism of the growth of native oxide on hydrogen passivated silicon surfaces*, Appl. Phys. Lett. 64(4) (1994) 446-447.

[33] W. Maw, F. Stevens, S.C. Langford, J.T. Dickinson, *Single asperity tribochemical wear of silicon nitride studied by atomic force microscopy*, J. Appl. Phys. 92(9) (2002) 5103-5109.

[34] Z. Tao, B. Bhushan, *Surface modification of AFM silicon probes for adhesion and wear reduction*, Tribol. Lett. 21(1) (2006) 1-16.

[35] S.T. Patton, W.D. Cowan, K.C. Eapen, J.S. Zabinski, *Effect of surface chemistry on the tribological performance of a MEMS electrostatic lateral output motor*, Tribol. Lett. 9(3-4) (2001) 199-209.

[36] B. Bhushan, *Adhesion and stiction: mechanisms, measurement techniques and methods for reduction*, J. Vac. Sci. Technol. B 21 (2003) 2262-2296.

[37] R. Maboudian, W.R. Ashurst, C. Carraro, *Tribological challenges in micromechanical systems*, Tribol. Lett. 12(2) (2002) 95-100.

[38] K.C. Eapen, S.T. Patton, S.A. Smallwood, B.S. Phillips, J.S. Zabinski, *MEMS lubricants based on bound and mobile phases of hydrocarbon compounds: film deposition and performance evaluation*, J. Microelectromech. Syst. 14(5) (2005) 954-960.

[39] J.J. Nainaparampil, B.S. Phillips, K.C. Eapen, J.S. Zabinski, *Micro–nano behaviour of DMBI-PF$_6$ ionic liquid nanocrystals: large and small-scale interfaces*, Nanotechnology 16(11) (2005) 2474-2481.

[40] K. Holmberg, H. Ronkainen, A. Matthews, *Tribology of thin coatings*, Ceramics International 26 (2000) 787-795.

[41] S.A. Henck, *Lubrication of digital micromirror devices^{TM}*, Tribol. Lett. 3 (1997) 239-247.

[42] A.D. Romig, M.T. Dugger, P.J. McWhorter, *Materials issues in microelectromechanical devices: science engineering, manufacturability and reliability*, Acta Materialia 51 (2003) 5837-5866.

[43] D. Kim, D. Cao, M.D. Bryant, W.J. Meng, F.F. Ling, *Tribological study of microbearings for MEMS applications*, Journal of tribology - transactions of the ASME 127(3) (2005) 537-547.

[44] E.E. Flater, A.D. Corwin, M.P. de Boer, R.W. Carpick, *In situ wear studies of surface micromachined interfaces subject to controlled loading*, Wear 260 (2006) 580-593.

[45] J. Robertson, *Diamond-like amorphous carbon*, Materials Science and Engineering R 37 (2002) 129-281.

[46] J. Robertson, *Amorphous carbon*, Adv. Phys. 35(4) (1986) 317-374.

[47] M. Winter, http://www.webelements.com, Webelements Ltd and University of Sheffield, accessed 2007.

[48] J.C. Angus and C.C. Hayman, *Low pressure, metastable growth of diamond and 'diamondlike' phases*, Science 241 (1988) 913-921.

[49] B.T. Kelly, *Physics of graphite*, Applied Science Publishers, 1981.

[50] http://www.brittanica.com, Encyclopaedia Brittanica Inc, accessed 2008.

[51] T. Zaharia, *The study of ultra-low energy deposition of hydrogenated amorphous carbon thin films*, PhD thesis Aston University, 2007.

[52] http://teercoatings.co.uk, Teer Coatings Ltd, accessed 2008.

[53] W.D. Westwood, *Sputter deposition*, AVS, 2003.

[54] T.E. Sheridan, M.J. Goeckner, J. Goree, *Model of energetic electron transport in magnetron discharges*, J. Vac. Sci. Technol. A 8 (1990) 30-37.

[55] A.D. Kuypers, E.H.A. Granneman, H.J. Hopman, *A magnetic multipole reactor for high flux reactive-ion etching*, J. Appl. Phys 63 (1988) 1899-1903.

[56] T.E. Sheridan, M.J. Goeckner, J. Goree, *Pressure dependence of ionisation efficiency in sputtering magnetrons*, Appl. Phys. Lett. 57 (1990) 2080-2082.

[57] J.A. Thornton, *Magnetron sputtering: basic physics and application to cylindrical magnetrons*, J. Vac. Sci. Technol. 15 (1978) 171-177.

[58] N. Savvides, B. Window, *Unbalanced magnetron ion-assisted deposition and property modification of thin films*, J. Vac. Sci. Technol. A 4 (1986) 504-508.

[59] R.P. Howson, H.A. J'Afer, A.G. Spencer, *Substrate effects from an unbalanced magnetron*, Thin Solid Films 193-194 (1990) 127-137.

[60] W.D. Sproul, *High-rate reactive DC magnetron sputtering of oxide and nitride superlattice coatings*, Vacuum 51 (1998) 641-646.

[61] P.J. Kelly, R.D. Arnell, *Magnetron sputtering: a review of recent developments and applications*, Vacuum 56 (2000) 159-172.

[62] P.J. Kelly, R.D. Arnell, *Characterization studies of the structure of Al, Zr and W coatings deposited by closed-field unbalanced magnetron sputtering*, Surf. Coat. Technol. 97 (1997) 595-602.

[63] R.D. Arnell, P.J. Kelly, *Recent advances in magnetron sputtering*, Surf. Coat. Technol. 112 (1999) 170-176.

[64] P.J. Kelly, R.D. Arnell, *The influence of magnetron configuration on ion current density and deposition rate in a dual unbalanced magnetron sputtering system*, Surf. Coat. Technol. 108-109 (1998) 317-322.

[65] P.J. Kelly, R.D. Arnell, *The influence of deposition parameters on the structure of Al, Zr and W coatings deposited by closed-field unbalanced magnetron sputtering*, Surf. Coat. Technol. 86-87 (1996) 425-431.

[66] D.G. Teer, *Magnetron ion plating*, UK patent no. 2 258 343, USA patent no. 5 554 519, European patent no. 0 521 045, 1994.

[67] K. Laing, J. Hampshire, D. Teer, G. Chester, *The effect of ion current density on the adhesion and structure of coatings deposited by magnetron sputter ion plating*, Surf. Coat. Technol. 112 (1999) 177-180.

[68] S. Yang, X. Li, N.M. Renevier, D.G. Teer, *Tribological properties and wear mechanism of sputtered C/Cr coating*, Surf. Coat. Technol. 142-144 (2001) 85-93.

[69] V. Rigato, G. Maggioni, D. Boscarino, G. Mariotto, E. Bontempi, A.H.S. Jones, D. Camino, D.G. Teer, C. Santini, *Ion beam analysis and Raman characterisation of coatings deposited by cosputtering carbon and chromium in a closed field unbalanced magnetron sputter ion plating system*, Surf. Coat. Technol. 116-119 (1999) 580-584.

[70] J.J. Zhang, M.X. Wang, J. Yang, Q.X. Liu, D.J. Li, *Enhancing mechanical and tribological performance of multilayered CrN/ZrN coatings*, Surf. Coat. Technol. 201 (2007) 5186-5189.

[71] M. Gubisch, Y. Liu, L. Spiess, H. Romanus, S. Krischok, G. Ecke, J.A. Schaefer, Ch. Knedlik, *Nanoscale multilayer WC/C coatings developed for nanopositioning:Part I. Microstructures and mechanical properties*, Thin Solid Films, 488 (2005) 132-139.

[72] P. Zhang, L. Wang, X. Nie, *Tribological properties of a-C/Cr(N) coatings in micro- and nano-scales*, Surf. Coat. Technol. 201 (2007) 5176-5181.

[73] R.V. Stuart, G.K. Wehner, *Energy Distribution of Sputtered Cu Atoms*, J. Appl. Phys. 35 (1964) 1819-1824.

[74] S. Berg, I.V. Katardjiev, *Preferential sputtering effects in thin film processing*, J. Vac. Sci. Technol. A 17 (1999) 1916-1925.

[75] S. Schiller, K. Goedicke, J. Reschke, V. Kirchoff, S. Schneider, F. Milde, *Pulsed magnetron sputter technology*, Surf. Coat. Technol. 61 (1993) 331-337.

[76] M. Scherer, J. Schmitt, R. Latz, M. Schanz, *Reactive alternating current magnetron sputtering of dielectric layers*, J. Vac. Sci. Technol. A 10 (1992) 1772-1776.

[77] P. Frach, U. Heisig, Chr. Gottfried, H. Walde, *Aspects and results of long-term stable deposition of Al2O3 with high rate pulsed reactive magnetron sputtering*, Surf. Coat. Technol. 59 (1993) 177-182.

[78] D.A. Glocker, *Influence of the plasma on substrate heating during low-frequency reactive sputtering of AlN*, J. Vac. Sci. Technol. A 11 (1993) 2989-2993.

[79] W.D. Sproul, M.E. Graham, M.S. Wong, S. Lopez, D. Li, R.A. Scholl, *Reactive direct current magnetron sputtering of aluminum oxide coatings*, J. Vac. Sci. Technol. A 13 (1995) 1188-1191.

[80] J.W. Bradley, H. Backer, P.J. Kelly, R.D. Arnell, *Time-resolved Langmuir probe measurements at the substrate position in a pulsed min-frequency DC magnetron plasma*, Surf. Coat. Technol. 135 (2001) 221-228.

[81] J.W. Bradley, H. Backer, P.J. Kelly, R.D. Arnell, *Space and time resolved Langmuir probe measurements in a 100 kHz pulsed rectangular magnetron system*, Surf. Coat. Technol. 142-144 (2001) 337-341.

[82] R.D. Arnell, P.J. Kelly, J.W. Bradley, *Recent developments in pulsed magnetron sputtering*, Surf. Coat. Technol. 188-189 (2004) 158-163.

[83] H. Backer, P.S. Henderson, J.W. Bradley, P.J. Kelly, *Time resolved investigation of plasma parameters during deposition of Ti and TiO2 films*, Surf. Coat. Technol. 174-175 (2003) 909-913.

[84] P.J. Kelly, C.F. Beevers, P.S. Henderson, R.D. Arnell, J.W. Bradley, H. Backer, *A comparison of the properties of titanium based films produced by pulsed and DC magnetron sputtering*, Surf. Coat. Technol. 174-175 (2003) 795-800.

[85] P.S. Henderson, P.J. Kelly, R.D. Arnell, H. Backer, J.W. Bradley, *Investigation into the properties of Ti based films deposited using pulsed magnetron sputtering*, Surf. Coat. Technol. 174-175 (2003) 779-783.

[86] J. S. Colligon, *Applications of ion-beam-assisted deposition*, Mater. Sci. Eng. A 139 (1991) 199-206.

[87] K-H. Muller, *Monte Carlo calculation for structural modifications in ion-assisted thin film deposition due to thermal spikes*, J. Vac. Sci. Technol. A 4 (1986) 184-188.

[88] J.A. Thornton, *The microstructure of sputter-deposited coatings*, J. Vac. Sci. Technol. A 4 (1986) 3059-3065.

[89] D.J. Srolovitz, A. Mazor, B.G. Bukiet, *Analytical and numerical modeling of columnar evolution in thin films*, J. Vac. Sci. Technol. A 6 (1988) 2371-2380.

[90] G.S. Bales, A. Zangwill, *Macroscopic model for columnar growth of amorphous films by sputter deposition*, J. Vac. Sci. Technol. A 9 (1991) 145-149.

[91] L.J. Friedrich, S.K. Dew, M. Brett, T. Smy, *Thin film microstructure modelling through line-segment simulation*, Thin Solid Films 266 (1995) 83-88.

[92] Y. Lifshitz, S.R. Kasi, J.W. Rabalais, W. Eckstein, *Subplantation model for film growth from hyperthermal species*, Phys. Rev. B41 (1990) 10468-10480.

[93] P.J. Kelly, R. Hall, J. O'Brien, J.W. Bradley, G. Roche, R.D. Arnell, *Substrate effects during mid-frequency pulsed DC biasing*, Surf. Coat. Technol. 142-144 (2001) 635-641.

[94] Window B, Savvides N, *Charged particle fluxes from planar magnetron sputtering sources*, J. Vac. Sci. Technol. A 4 (1986) 196-202.

[95] K.E. Cooke, J. Hampshire, W. Southall, D.G. Teer, *The industrial application of pulsed DC bias power supplies in closed field unbalanced magnetron sputter ion plating*, Surf. coat. Technol. 177-178 (2004) 789-794.

[96] W.D. Westwood, *Calculation of deposition rates in diode sputtering systems*, J. Vac. Sci. Technol. 15 (1978) 1-9.

[97] T. Motohiro, *Applications of Monte Carlo simulation in the analysis of a sputter-deposition process*, J. Vac. Sci. Technol. A 4 (1986) 189-195.

[98] P. Sigmund, *Theory of Sputtering. I. Sputtering Yield of Amorphous and Polycrystalline Targets*, Phys. Rev. 184 (1969) 383-416.

[99] P.J. Kelly, R.D. Arnell, *The influence of substrate temperature on the properties of Al, Zr and W coatings deposited by closed-field unbalanced magnetron sputtering*, Vacuum 49 (1998) 43-47.

[100] J.S. Colligon, V. Vishnyakov, R. Valizadeh, S.E. Donnelly, S. Kumashiro, *Study of nanocrystalline TiN/Si_3N_4 thin films deposited using a dual ion beam method*, Thin Solid Films 485 (2005) 148-154.

[101] R. Gago, O. Sanchez-Garrido, A. Climent-Font, J.M. Albella, E. Roman, J. Raisanen, E. Rauhala, *Effect of the substrate temperature on the deposition of hydrogenated amorphous carbon by PACVD at 35 kHz*, Thin Solid Films 338 (1999) 88-92.

[102] H. Nakazawa, T. Kawabata, M. Kudo, M. Mashita, *Structural changes of diamond-like carbon films due to atomic hydrogen exposure during annealing*, Appl. Surf. Sci. 253 (2007) 4188-4196.

[103] J.A. Thornton, *Influence of apparatus geometry and deposition conditions on the structure and topography of thick sputtered coatings*, J. Vac. Sci. Technol. 11 (1974) 666-670.

[104] D.G. Teer, *Carbon coatings method and apparatus for applying them and articles bearing such coatings*, USA patent no. 6 726 993, 2004.

[105] *Statguide (electronic version 5.1.2600.2180)*, Minitab Inc State College PA, 2003.

[106] *e-Handbook of statistical methods (electronic version)* http://www.itl.nist.gov/div898/handbook/, NIST USA, accessed 2007.

[107] *Electronic Statistics Textbook (Electronic Version)* http://www.statsoft.com/textbook/stathome.html, StatSoft Inc Tulsa OK, accessed 2005.

[108] R.D. Evans, J.Y. Howe, J. Bentley, G.L. Doll, J.T. Glass, *Influence of deposition parameters on the composition and structure of reactively sputtered nanocomposite TaC/a-C:H thin films*, J. Mater. Res. 20(9) (2005) 2583-2596.

[109] D. Briggs, M.P. Seah, *Practical surface analysis - second edition - volume 1 Auger and X-ray photoelectron spectroscopy*, John Wiley and Sons, 1990.

[110] J.F. Watts, J. Wolstenholme, *An introduction to surface analysis by XPS and AES*, Wiley, 2003.

[111] P.J. Cumpson, M.P. Seah, *Elastic scattering corrections in AES and XPS II estimating attenuation lengths and conditions required for their valid use in overlayer/substrate experiments*, Surf. Interface Anal. 25 (1997) 430-446.

[112] J.C. Lascovich, R. Giorgi, S. Scaglione, *Evaluation of the sp^2/sp^3 ratio in amorphous carbon structure by XPS and XAES*, Appl. Surf. Sci. 47 (1991) 17-21.

[113] J.C. Lascovich, S. Scaglione, *Comparison among XAES, PELS and XPS techniques for evaluation of sp^2 percentage in a-C:H*, Appl. Surf. Sci. 78 (1994) 17-23.

[114] S.T. Jackson, R.G. Nuzzo, *Determining hybridization differences for amorphous carbon from the XPS C1s envelope*, Appl. Surf. Sci. 90 (1995) 195-203.

[115] J. Schafer, J. Ristein, R. Graupner, L. Ley, U. Stephan, Th. Frauenheim, V.S. Veerasamy, G.A.J. Amaratunga, M. Weiler, H. Ehrhardt, *Photoemission study of amorphous carbon modifications and comparison with calculated densities of states*, Phys. Rev. B 53 (1996) 7762-7774.

[116] K.C. Pandey, *New dimerized-chain model for the reconstruction of the diamond (111)-(2 × 1) surface*, Phys. Rev. B 25 (1982) 4338-4341.

[117] R. Klauser, J.M. Chen, T.J. Chuang, L.M. Chen, M.C. Shih, J.C. Lin, *The interaction of oxygen and hydrogen on a diamond C(111) surface: a synchrotron radiation photoemission, LEED and AES study*, Surf. Sci. 356 (1996) L410-416.

[118] S. Rey, F. Antoni, B. Prevot, E. Fogarassy, J.C. Arnault, J. Hommet, F. le Normand, P.Boher, *Thermal stability of amorphous carbon films deposited by pulsed laser ablation*, Appl. Phys. A 71 (2000) 433-439.

[119] J. Diaz, S. Anders, X. Zhou, E.J. Moler, S.A. Kellar, Z. Hussain, *Analysis of the π^* and σ^* bands of the x-ray absorption spectrum of amorphous carbon*, Phys. Rev. B 64 (2001) 125204.

[120] F. le Normand, J. Hommet, T. Szorenyi, C. Fuchs, E. Fogarassy, *XPS study of pulsed laser deposited CN_x films*, Phys. Rev. B 64 (2001) 235416.

[121] R. Haerle, A. Pasquarello, A. Baldereschi, *First-principle study of C 1s core-level shifts in amorphous carbon*, Comput. Mater. Sci. 22 (2001) 67-72.

[122] R. Haerle, E. Riedo, A. Pasquarello, A. Baldereschi, *sp^2/sp^3 hybridization ratio in amorphous carbon from C 1s core-level shifts: X-ray photoelectron spectroscopy and first-principles calculation*, Phys. Rev. B 65 (2001) 045101.

[123] D.R. McKenzie, *Tetrahedral bonding in amorphous carbon*, Rep. Prog. Phys. 59 (1996) 1611-1664.

[124] C. Gao, Y.Y. Wang, A.L. Ritter, J.R. Dennison, *Nature of carbon-carbon bonding in evaporated and ion-sputtered (diamondlike) amorphous carbon from (e, 2e) spectroscopy*, Phys. Rev. Lett. 62 (1989) 945-948.

[125] R.C. Haddon, L.E. Brus, K. Raghavachari, *Rehybridization and π-orbital alignment: the key to the existence of spheroidal carbon clusters*, Chem. Phys. Lett. 131 (1986) 165-169.

[126] P. Ruffieux, O.Groning, M. Bielmann, P. Mauron, L. Schlapbach, P. Groning, *Hydrogen adsorption on sp^2-bonded carbon: Influence of the local curvature*, Phys. Rev. B 66 (2002) 245416.

[127] Y.V. Butenko, S. Krishnamurthy, A.K. Chakraborty, V.L. Kuznetsov, V.R. Dhanak, M.R.C. Hunt, L. Šiller, *Photoemission study of onionlike carbons produced by annealing nanodiamonds*, Phys. Rev. B 71 (2005) 075420.

[128] J. Diaz, G. Paolicelli, S. Ferrer, F. Comin, *Separation of the sp^3 and sp^2 components in the C1s photoemission spectra of amorphous carbon films*, Phys. Rev. B 54 (1996) 8064-8069.

[129] P. Merel, M. Tabbal, M. Chaker, S. Moisa, J. Margot, *Direct evaluation of the sp^3 content in diamond-like-carbon films by XPS*, Appl. Surf. Sci. 136 (1998) 105-110.

[130] J. Diaz, S. Anders, X. Zhou, E.J. Moler, S.A. Kellar, Z. Hussain, *Combined near edge x-ray absorption fine structure and x-ray photoemission spectroscopies for the study of amorphous carbon thin films*, Journal of electron spectroscopy and related phenomenon 101-103 (1999) 545-550.

[131] E. Riedo, F. Comin, J. Chevrier, F. Schmithusen, S. Decossas, M. Sancrotti, *Structural properties and surface morphology of laser-deposited amorphous carbon and carbon nitride films*, Surf. Coat. Technol. 125 (2000) 124-128.

[132] S. Doniach, M. Sunjic, *Many-electron singularity in x-ray photoemission and x-ray line spectra from metals*, J. Phys. C 3 (1970) 285-291.

[133] J.C.W. Folmer, D.K.G. de Boer, *XPS core level line shapes in metallic compounds: A probe for the nature of the electrons at the Fermi level*, Solid State Communications 38 (1981) 1135-1138.

[134] T.T.P. Cheung, *X-ray photoemission of carbon: lineshape analysis and application to studies of coals*, J. Appl. Phys. 53 (1982) 6857-6862.

[135] T.T.P. Cheung, *X-ray photoemission of polynuclear aromatic carbon*, J. Appl. Phys. 55 (1984) 1388-1393.

[136] L Calliari, *AES and core level photoemission in the study of a-C and a-C:H*, Diamond Relat. Mater. 14 (2005) 1232-1240.

[137] S. Haq, D.L. Tunnicliffe, S. Sails, J.A. Savage, *Assessment of nondiamond carbon levels present in chemical vapor deposited diamond by analysis of the plasmon loss features of x-ray photoelectron spectra*, Appl. Phys. Lett. 68 (1996) 469-471.

[138] G. Speranza, N. Laidani, *Measurement of the relative abundance of sp^2 and sp^3 hybridised atoms in carbon based materials by xps: a critical approach part I*, Diamond Relat. Mater. 13 (2004) 445-450.

[139] G. Speranza, N. Laidani, *Measurement of the relative abundance of sp^2 and sp^3 hybridised atoms in carbon based materials by xps: a critical approach part II*, Diamond Relat. Mater. 13 (2004) 451-458.

[140] S.C. Seo, D.C. Ingram, *Fine structures of valence-band, x-ray-excited Auger electron, and plasmon energy loss spectra of diamondlike carbon films obtained using x-ray photoelectron spectroscopy*, J. Vac. Sci. Technol. A 15 (1997) 2579-2584.

[141] M.S. Hague, H.A. Naseem, J.L. Schultz, W.D. Brown, S. Lal, S. Gangopadhyay, *Comparison of infrared, Raman, photoluminescence, and x-ray photoelectron spectroscopy for characterizing arc-jet-deposited diamond films*, J. Appl. Phys. 83 (1998) 4421-4429.

[142] G. Speranza, L. Calliari, N. Laidani, M. Anderle, *Semi-quantitative description of C hybridization via s- and p-partial density of states probing: an electron spectroscopy study*, Diamond Relat. Mater. 9 (2000) 1856-1861.

[143] Y. Mizokawa, T. Miyasato, S. Nakamura, K. Geib, C. Wilmsen, *The C KLL first derivative XPS spectra as a fingerprint of the carbon state and the characterisation of diamond like carbon films*, J. Vac. Sci. Technol. A 5 (1987) 2809-2813.

[144] S. Craig, G.L. Harding, R. Payling, *Auger lineshape analysis of carbon bonding in sputtered metal-carbon thin films*, Surf. Sci. 124 (1983) 591-601.

[145] J. Zemek, J. Zalman, A. Luches, *XAES and XPS study of amorphous carbon nitride layers*, Appl. Surf. Sci. 133 (1998) 27-32.

[146] Y. Lifshitz, *Pitfalls in amorphous carbon studies*, Diamond Relat. Mater. 12 (2003) 130-140.

[147] A. Fuchs, J. Scherer, K. Jung, H. Ehrhardt, *Determination of sp^2/sp^3 carbon bonding ratio in a-C:H including irradiation damage by factor analysis of Auger electron spectra*, Thin Solid Films 232 (1993) 51-55.

[148] Y. Mizokawa, T. Miyasato, S. Nakamura, K.M. Geib, C.W. Wilmsen, *Comparison of the CKLL first-derivative auger spectra from XPS and AES using diamond, graphite, SiC and diamond-like-carbon films*, Surf. Sci. 182 (1987) 431438.

[149] D.R. Tallant, J.E. Parmeter, M.P. Siegal, R.L. Simpson, *The thermal stability of diamond-like carbon*, Diamond Relat. Mater. 4 (1995) 191-199.

[150] *TopoMetrix User's Manual version 3.05 85-10086 rev. C*, TopoMetrix, 1996.

[151] *A practical guide to SPM*, Veeco Instruments Inc, 2005.

[152] *User's guide to autoprobe M5*, ThermoMicroscopes, 1992-2000.

[153] A.C. Fischer-Cripps, *Nanoindentation*, Springer-Verlag New York Inc, 2002.

[154] S.J. Bull, *Nanoindentation of coatings (topical review)*, J. Phys. D Appl. Phys. 38 (2005) R393-R413.

[155] M.F. Doerner, W.D. Nix, *A method for interpreting the data from depth-sensing indentation instruments*, J. Mater. Res. 1 (1986) 601-609.

[156] W.C. Oliver, G.M. Pharr, *An improved technique for determining hardness and elastic modulus using load and displacement sensing indentation experiments*, J. Mater. Res. 7 (1992) 1564-1583.

[157] *Metallic materials – Instrumented indentation test for hardness and materials paramenters ISO 14577 Part 1 – Test method, ISO 12577 Part 2 – Verification and calibration of machines, ISO 12577 Part 3 – Calibration of reference blocks*, ISO Central Secretariat Geneva, 2002.

[158] H. Hertz, *On the contact of elastic solids (in German)*, J. Reine Angew. Math. 92 (1881) 156-171.

[159] A.E.H. Love, *Stresses produced in a semi-infinite solid by pressure on part of the boundary*, Philos. Trans. R. Soc. A 228 (1929) 377-420.

[160] A.E.H. Love, *Boussinesq's problem for a rigid cone*, Quart. J. Math. (Oxford Series) 10 (1939) 161-175.

[161] I.N. Sneddon, *The relation between load and penetration in the axisymmetric boussinesq problem for a punch of arbitrary profile*, Int. J. Engng. Sci. 3 (1965) 47-57.

[162] J. Woirgard, J.-C. Dargenton, *An alternative method for penetration depth determination in nanoindentation measurements*, J. Mater. Res. 12 (1996) 2455-2458.

[163] M. Martin, M. Troyon, *Fundamental relations used in nanoindentation: Critical examination based on experimental measurements*, J. Mater. Res. 17 (2002) 2227-2234.

[164] R.B. King, *Elastic analysis of some punch problems for a layered medium*, Int. J. Solids Structures 23 (1987) 1657-1664.

[165] J.C. Hay, A. Bolshakov, G.M. Pharr, *A critical examination of the fundamental relations used in the analysis of nanoindentation data*, J. Mater. Res. 14 (1999) 2296-2305.

[166] M. Troyon, L. Huang, *Correction factor for contact area in nanoindentation measurements*, J. Mater. Res. 20 (2005) 610-617.

[167] K. Herrmann, N.M. Jennett, W. Wegener, J. Meneve, K. Hasche, R. Seeman, *Progress in determination of the area function of indenters used for nanoindentation*, Thin Solid Films 377-378 (2000) 394-400.

[168] K.J. Van Vliet, L. Prchlik, J.F. Smith, *Direct measurement of indentation frame compliance*, J. Mater. Res. 19 (2004) 325-331.

[169] K. Herrmann, K. Hasche, F. pohlenz, R. Seeman, *Characterisation of the geometry of indenters used for the micro- and nanoindentation method*, Measurement 29 (2001) 201-207.

[170] J. C. Sánchez-López, C. Donnet, J. L. Loubet, M. Belin, A. Grill, V. Patel, C. Jahnes, *Tribological and mechanical properties of diamond-like carbon prepared by high-density plasma*, Diamond Relat. Mater. 10 (2001) 1063-1069.

[171] A. Bolshakov, W.C. Oliver, G.M. Pharr, Mater. Res. Soc. Symp. Proc. 436 (1996) 141.

[172] A. Bolshakov, G.M. Pharr, *Influences of pile-up on the measurement of mechanical properties by load and depth sensing indentation techniques*, J. Mater. Res. 13 (1998) 1049-1058.

[173] G.M. Pharr, *Measurement of mechanical properties by ultra-low load indentation*, Mater. Sci. Eng. A 253 (1998) 151-159.

[174] R. Rabe, J.-M. Breguet, P. Schwaller, S. Stauss, F.-J. Haug, J. Patscheider, J. Michler, *Observation of fracture and plastic deformation during indentation and scratching inside the scanning electron microscope*, Thin Solid Films 469–470 (2004) 206–213.

[175] S.V. Hainsworth, T.F. Page, Mater. Res. Soc. Symp. Proc. 436 (1997) 171–176.

[176] S.V. Hainsworth, M.R. McGurk, T.F. Page, *The effect of coating cracking on the indentation response of thin hard-coated systems*, Surf. Coat. Technol. 102 (1998) 97–107.

[177] J.L. Hay, M.E. O'Hern, W.C. Oliver, *The importance of contact radius for substrate-independent property measurement of thin films*, Mater. Res. Soc. Symp. Proc. 522 (1998) 27-32.

[178] S. Soare, S.J. Bull, A. Horsfall, J.M.M. dos Santos, A.G. O'Neill, N.G. Wright, *Assessment of Aluminium Metallization by Nanoindentation*, Mater. Res. Soc. Symp. Proc. 750 (2003) 83–88.

[179] T.Y. Tsui, J. Vlassak, W.D. Nix, *Indentation plastic displacement field: Part II. The case of hard films on soft substrates*, J. Mater. Res. 14 (1999) 2204-2209.

[180] T.Y. Tsui, J. Vlassak, W.D. Nix, *Indentation plastic displacement field: Part I. The case of soft films on hard substrates*, J. Mater. Res. 14 (1999) 2196-2203.

[181] A.M. Korsunsky, M.R. McGurk, S.J. Bull, T.F. Page, *On the hardness of coated systems*, Surf. Coat. Technol. 99 (1998) 171-183.

[182] S.J. Bull, *Nanoindentation of coatings (topical review)*, J. Phys. D: Appl. Phys. 38 (2005) R393-R413.

[183] E. Liu, X. Shi, H.S. Tan, L.K. Cheah, Z. Sun, B.K. Tay, J.R. Shi, *The effect of nitrogen on the mechanical properties of tetrahedral amorphous carbon films deposited with a filtered cathodic vacuum arc*, Surf. Coat. Technol. 120/121 (1999) 601–606.

[184] W.D. Nix, H. Gao, *Indentation size effects in crystalline materials: a law for strain gradient plasticity*, J. Mech. Phys. Solids 46 (1998) 411-425.

[185] W.D. Nix, *Elastic and plastic properties of thin films on substrates: nanoindentation techniques*, Mater. Sci. Eng. A234-236 (1997) 37-44.

[186] L. Huang, K. Xu, J. Lu, B. Guelorget, H. Chen, *Nano-scratch and fretting wear study of DLC coatings for biomedical application*, Diamond Relat. Mater. 10 (2001) 1448-1456.

[187] P. lemoine, J.F. Zhao, J.P. Quinn, J.A. McLaughlin, P. Maguire, *Hardness measurements at shallow depths on ultr-thin amorphous carbon films deposited onto silicon and Al2O3-TiC substrates*, Thin Solid Films 379 (2000) 166-172.

[188] E. Martinez, J.L. Andujar, M.C. Polo, J. Esteve, J. Robertson, W.I. Milne, *Study of the mechanical properties of tetrahedral amorphous carbon films by nanoindentation and nanowear measurements*, Diamond Relat. Mater. 10 (2001) 145-152.

[189] J.F. Lin, P.J. Wei, J.C. Pan, C-F Ai, *Effect of nitrogen content at coating film and film thickness on nanohardness and Young's modulus of hydrogenated carbon films*, Diamond Relat. Mater. 13 (2004) 42-53.

[190] B. Bhushan, V.N. Koinkar, *Microscale mechanical and tribological characterization of hard amorphous carbon coatings as thin as 5 nm for magnetic disks*, Surf. Coat. Technol. 76-77 (1995) 655-669.

[191] B.D. Beake, S.P. Lau, *Nanotribological and nanomechanical properties of 5-80 nm tetrahedral amorphous carbon films on silicon*, Diamond Relat. Mater. 14 (2005) 1535-1542.

[192] X. Li, B. Bhushan, *Micromechanical and tribological characterization of hard amorphous carbon coatings as thin as 5 nm for magnetic recording heads*, Wear 220 (1998) 51-58.

[193] S.J. Bull, E.G. Berasetegui, *An overview of the potential of quantitative coating adhesion measurement by scratch testing*, Tribol. Int. 39 (2006) 99-114.

[194] B.D. Beake, V.M. Vishnyakov, R. Valizadeh, J.S. Colligon, *Influence of mechanical properties on the nanoscratch behaviour of hard nanocomposite* TiN/Si_3N_4 *coatings on Si*, J. Phys. D: Appl. Phys. 39 (2006) 1392-1397.

[195] P.A. Steinmann, Y. Tardy, H.E. Hintermann, *Adhesion testing by the scratch test method: The influence of intrinsic and extrinsic parameters on the critical load*, Thin Solid Films 154 (1987) 333–349.

[196] H.S. Park, D. Kwon, *An energy approach to quantification of adhesion strength from critical loads in scratch tests*, Thin Solid Films 307 (1997) 156-162.

[197] B.D. Beake, A.A. Ogwu, T. Wagner, *Influence of experimental factors and film thickness on the measured critical load in the nanoscratch test*, Mater. Sci. Eng. A 423 (2006) 70-73.

[198] J.F. Lin, C.C. Wei, Y.K. Yung, C-F. Ai, *The affects of hydrogenated carbon films with different film thicknesses and nitrogen content on specimen mechanical properties, scratch critical load, adhesion work and tribological behaviour*, Diamond Relat. Mater. 13 (2004) 1895-1906.

[199] R.D. Arnell, P.B. Davies, J. Halling, T.L. Whomes, *Tribology principles and design applications*, Macmillan education Ltd, Basingstoke, 1991.

[200] G. Amontons, *On the resistance originating in machines (in French)*, Mem. Acad. Roy. (1699) 206-222.

[201] C.A. Coulomb, *The theory of simple machines (in French)*, Mem. Math. Phys. Acad. Sci. 10 (1785) 161-331.

[202] E. Rabinowicz, *Friction and wear of materials*, Wiley, London, 1966.

[203] F.P. Bowden, D. Tabor, *The friction and lubrication of metals*, OUP Oxford, Pt. 1 1950 and Pt. 2 1964.

[204] J.A. Greenwood, J.B.P. Williamson, *Contact of nominally flat surfaces*, Proc. Roy. Soc. A 295 (1966) 300-319.

[205] J.T. Burwell, *Survey of possible wear mechanisms*, Wear 1 (1957) 119-141.

[206] J.L. Archard, *Contact and rubbing of flat surfaces*, J. Appl. Phys. 24 (1953) 981–988.

[207] J. Halling, *A contribution to the theory of mechanical wear*, Wear 34 (1975) 239-249.

[208] I.V. Kragelsky, *Friction and wear*, Butterworths, London, 1965.

[209] N.P. Suh, *The delamination theory of wear*, Wear 25 (1973) 111-124.

[210] N.P. Suh, *An overview of the delamination theory of wear*, Wear 44 (1977) 1-16.

[211] R.D. Arnell, J.W. Midgley, D. Teer, *The development of surface orientations on rubbed pyrolytic carbon and their relation to the friction and wear*, Brit. J. Appl. Phys. 1 (11) (1968) 1543-1548.

[212] R. Hauert, *An overview on the tribological behaviour of diamond-like carbon in technical and medical applications*, Tribol. Int. 37 (2004) 991-1003.

[213] C. Donnet, *Recent progress on the tribology of doped diamond-like and carbon alloy coatings: a review*, Surf. Coat. Technol. 100-101 (1998) 180-186.

[214] J.E. Sundgren, H.T.G. Hentzell, *A review of the present state of art in hard coatings grown from the vapor phase*, J. Vac. Sci. Technol. A 4 (1986) 2259-2279.

[215] D.S. Kim, T.E. Fischer, B. Gallois, *The effects of oxygen and humidity on friction and wear of diamond-like carbon films*, Surf. Coat. Technol. 49 (1991) 537-542.

[216] C. Donnet, M. Belin, J.C. Auge, J.M. Martin, A. Grill, V. Patel, *Tribochemistry of diamond-like carbon coatings in various environments*, Surf. Coat. Technol. 68-69 (1994) 626-631.

[217] A. Erdemir, C. Bindal, J. Pagan, P. Wilbur, *Characterization of transfer layers on steel surfaces sliding against diamond-like hydrocarbon films in dry nitrogen*, Surf. Coat. Technol.76-77 (1995) 559-563.

[218] A. Erdemir, C. Bindal, G.R. Fenske, C. Zuiker, P. Wilbur. *Characterization of transfer layers forming on surfaces sliding against diamond-like carbon*, Surf. Coat. Technol. 86–87 (1996) 692-697.

[219] Y. Liu, A. Erdemir, E.I. Meletis, *An investigation of the relationship between graphitization and frictional behavior of DLC coatings*, Surf. Coat. Technol.86-87 (1996) 564-568.

[220] H. Fukui, M. Irie, Y. Utsumi, K. Oda, H. Ohara. *An investigation of the wear track on DLC (a-C:H) film by time-of-flight secondary ion mass spectroscopy*, Surf. Coat. Technol. 146–147 (2001) 378-383.

[221] A. Grill, *Tribology of diamondlike carbon and related materials: an updated review*, Surf. Coat. Technol. 94-95 (1997) 507-513.

[222] H. Ronkainen, J. Linkonen, J. Koskinen, S. Varjus, *Effect of tribofilm formation on the tribological performance of hydrogenated carbon coatings*, Surf. Coat. Technol. 79 (1996) 87-94.

[223] C. Donnet, J. Fontaine, A. Grill, T. le Mogne, *The role of hydrogen on the friction mechanism of diamond-like carbon films*, Tribol. Lett. 9 (2000) 137-142.

[224] C. Donnet, A. Grill, *Friction control of diamond-like carbon coatings*, Surf. Coat. Technol. 94–95 (1997) 456-462.

[225] J. Fontaine, C. Donnet, A. Grill, T. le Mogne, *Tribochemistry between hydrogen and diamond-like carbon films*, Surf. Coat. Technol. 146–147 (2001) 286-291.

[226] A.A. Voevodin, M.S. Donley, J.S. Zabinski, J.E. Bultman, *Characterization of transfer layers on steel surfaces sliding against diamond-like hydrocarbon films in dry nitrogen*, Surf. Coat Technol. 76 - 77 (1995) 559-563.

[227] A.A. Voevodin, A.W. Phelps, J.S. Zabinski, M.S. Donley, *Friction induced phase transformation of pulsed laser deposited diamond-like carbon*, Diamond. Relat. Mater. 5 (1996) 1264-1269.

[228] D. Camino, A.H.S. Jones, D. Mercs, D.G. Teer, *High performance sputtered carbon coatings for wear resistant applications*, Vacuum 52 (1999) 125-131.

[229] C.D. Martino, F. Demichelis, A. Tagliaferro, *Characteristics of a-C:H:Si films deposited by r.f. sputtering under various deposition conditions*, Diamond Relat. Mater. 3 (1994) 547-550.

[230] X.T. Zeng, *Unbalanced magnetron sputtered carbon composite coatings*, J. Vac. Sci. Technol. A 17 (1999) 1991-1995.

[231] S. Yang, D. Camino, A.H.S. Jones, D.G. Teer, *Deposition and tribological behaviour of sputtered carbon hard coatings*, Surf. Coat. Technol. 124 (2000) 110-116.

[232] S. Yang, D.G. Teer, *Investigation of sputtered carbon and carbon-chromium multi-layered coatings*, Surf. Coat. Technol. 131 (2000) 412-416.

[233] S. Yang, X. Li, N.M. Renevier, D.G. Teer, *Tribological properties and wear mechanism of sputtered C/Cr coating*, Surf. Coat. Technol. 142-144 (2001) 85-93.

[234] S. Achanta, D. Drees, J-P. Celis, *Friction and nanowear of hard coatings in reciprocating sliding at milli-Newtons loads*, Wear 259 (2005) 719-729.

[235] S. Sundararajan, B. Bhushan, *Micro/nanotribology of ultra-thin hard amorphous carbon coatings using atomic force / friction force microscopy*, Wear 225-229 (1999) 678-689.

[236] N.S. Tambe, B. Bhushan, *Nanoscale friction-induced phase transformations of diamond-like carbon*, Scripta Materialia 52 (2005) 751-755.

[237] S. Tsuchitani, R. Kaneko, S. Hirono, *Effects of humidity on nanometer scale wear of a carbon film*, Tribol. Int. 40 (2007) 306-312.

[238] B. Wei, K. Komvopoulos, *Nanoscale indentation hardness and wear characterization of hydrogenated carbon thin films*, Trans. ASME J. Tribol. 118 (1996) 431-438.

[239] B.K. Gupta, B. Bhushan, *Mechanical and tribological properties of hard carbon coatings for magnetic recording heads*, Wear 190 (1995) 110-122.

[240] X. Li, B. Bhushan, *Micro/nanomechanical and tribological characterization of ultrathin amorphous carbon coatings*, J. Mater. Res. 14 (1999) 2328-2337.

[241] M.G. Lim, J.C. Chang, D.P. Schultz, R.T. Howe, R.M. White. *Polysilicon microstructures to characterize static friction*, Proc IEEE Workshop on Micro Electro Mechanical Systems Napa Valley CA (1990) 82-88.

[242] D.C. Senft, M.T. Dugger, *Friction and wear in surface micromachined tribological test devices*, Proc. SPIE 3224 (1997) 31-38.

[243] M.P. de Boer, D.L. Luck, W.R. Ashurst, R. Maboudian, A.D. Corwin, J.A. Walraven, J.M. Redmond, *High performance surface micromachined inchworm actuator*, J. Microelectromech. Syst. 13 (2004) 63-74.

[244] K.H. Lau, K.Y. Li, *Correlation between adhesion and wear behaviour of commercial carbon based coatings*, Tribol. Int. 39 (2006) 115-123.

[245] J.F. Zhao, P. Lemoine, Z.H. Liu, J.P. Quinn, P. Maguire, J.A. McLaughlin, *A study of microstructure and nanomechanical properties of silicon incorporated DLC films deposited on silicon substrates*, Diamond Relat. Mater. 10 (2001) 1070-1075.

[246] P. Patsalas, M. Handrea, S. Logothetidis, M. Gioti, S. Kennou, W. Kautek, *A complementary study of bonding and electronic structure of amorphous carbon films by electron spectroscopy and optical techniques*, Diamond Relat. Mater. 10 (2001) 960-964.

[247] C.K. Park, S.M. Chang, H.S. Uhm, S.H. Seo, J.S. Park, *XPS and XRR studies on microstructures and interfaces of DLC films deposited by FCVA method*, Thin Solid Films 420-421 (2002) 235-240.

[248] C.D. Wagner, A.V. Naumkin, A. Kraut-Vass, J.W. Allison, C.J. Powell, J.R. Rumble Jr, *NIST XPS standard reference database 20 version 3.4 (web version) http://srdata.nist.gov/xps/*, NIST USA, accessed 2005.

[249] J. Schwan, S. Ulrich, V. Batori, H. Ehrhardt, *Raman spectroscopy on amorphous carbon films*, J. Appl. Phys. 80 (1996) 440-447.

[250] Y-G. Jung, A. Pajares, R. Banerjee, B. R. Lawn, *Strength of silicon, sapphire and glass in the subthreshold flaw region*, Acta Materialia 52 (2004) 3459–3466.

[251] J.F. Shackelford, W. Alexander, J.S. Park, *CRC materials science and engineering handbook 2nd edition*, CRC Press, London, 1994.

[252] Y.L. Su, T.H. Liu, C.T. Su, S.H. Yao, W.H. Kao, K.W. Cheng, *Wear of CrC-coated carbide tools in dry machining*, J. Mater. Process Technol. 171 (2006) 108-117.

[253] Y.L. Su, T.H. Liu, C.T. Su, J.P. Yur, W.H. Kao, S.H. Yao, *Tribological characteristics and cutting performance of* $Cr_{x\%}C$*-coated carbide tools*, J. Mater. Process Technol. 153/154 (2004) 699-706.

[254] A. Paul, J. Lim, K. Choi, C. Lee, *Effects of deposition parameters on the properties of chromium carbide coatings deposited onto steel by sputtering*, Mater. Sci. Eng. A 332 (2002) 123-128.

[255] B. Bhushan, X. Li, *Nanomechanical characterisation of solid surfaces and thin films*, Int. Mater. Rev. 48(3) (2003) 125-164.

[256] H. Windischmann, *An intrinsic stress scaling law for polycrystalline thin films prepared by ion beam sputtering*, J. Appl. Phys. 62 (1987) 1800-1807.

[257] H. Windischmann, *Intrinsic stress in sputtered thin films*, J. Vac. Sci. Technol. A 9 (1991) 2431-2436.

[258] A. Okamoto, T. Serikawa, *Magnetron-sputtered silicon films for gate electrodes in MOS devices*, J. Electrochem. Soc. 134 (1987) 1479-1484.

[259] S. Fouvry, P Kapsa, H. Zahouani, L. Vincent, *Wear analysis in fretting of hard coatings through a dissipated energy concept*, Wear 203-204 (1997) 393-403.

[260] I.M. Hutchings, *Tribology: friction and wear of engineering materials*, Edward Arnold, London, 1992.

[261] R.W. Rice, *Mechanical properties of ceramics and composites grain and particle effects*, Marcel Dekker Inc, New York, 2000.

[262] A. Krell, S. Schadlich, *Depth sensing hardness in sapphire and in sintered sub-µm alumnina, International journal of refractory metals and hard materials*, 19(4) (2001) 237-243.

[263] Y. Liu, A. Erdemir, E.I. Meletis, *Influence of environmental parameters on the frictional behaviour of DLC coatings*, Surf. Coat. Technol. 94/95 (1997) 463-468.

[264] R.C.D. Richardson, *The wear of metals by relatively soft abrasives*, Wear 11(4) (1968) 245-275.

[265] T.O. Mulhearn, L.E. Samuels, *The abrasion of metals: a model of the process*, Wear 5(6) (1962) 478-498.

[266] B.W.E. Avient, J. Goddard, M. Wilman, *An experimental study of friction and wear during abrasion of metals*, Proc. Roy. Soc. A258 (1960) 159-180.

[267] G.M. Wilson, S.O. Saied, S.K. Field, *Mechanical and physical properties of C and C-Cr sputter coatings measured at the nano-scale*, Thin Solid Films 515 (2007) 7820-7828.

[268] J. Stallard, D. Mercs, M. Jarratt, D.G. Teer, P.H. Shipway, *A study of the tribological behaviour of three carbon-based coatings, tested in air, water and oil environments at high loads*, Surf. Coat. Technol. 177-178 (2004) 545-551.

[269] V. Fox, A. Jones, N.M. Renevier, D.G. Teer, *Hard lubricating coatings for cutting and forming tools and mechanical components*, Surf. Coat. Technol. 125 (2000) 347-353.

[270] J. Jiang, R.D. Arnell, *The effect of substrate surface roughness on the wear of DLC coatings*, Wear 239 (2000) 1-9.

[271] D.F. Moore, *Principles and Applications of Tribology*, Pergamon Press, Oxford, 1975.

[272] G.M. Hamilton, *Explicit equations for the stresses beneath a sliding spherical contact*, Proceedings of the Institution of Mechanical Engineers 197C (1983) 53-59.

[273] G.M. Hamilton, *Erratum to explicit equations for the stresses beneath a sliding spherical contact*, Proceedings of the Institution of Mechanical Engineers 197C (1983) 282.

[274] G.M. Hamilton, L.E. Goodman, *The stress field created by a sliding circular contact*, Journal of Applied Mechanics 88 (1966) 371-376.

6 Appendix – Publications

1. G.M. Wilson, S.O. Saied, S.K. Field, *Mechanical and physical properties of C and C-Cr sputter coatings measured at the nano-scale*, Thin Solid Films 515 (2007) 7820-7828.

2. G.M. Wilson, J.L. Sullivan, *The effects of pulsed substrate biasing on thin amorphous carbon coatings: a statistical design of experiment study*, J. Phys. D: Appl. Phys. 40 (2007) 5438-5445.

3. G.M. Wilson, J.F. Smith, J.L. Sullivan, *A nanotribological study of thin amorphous C and Cr doped amorphous C coatings*, Wear xxx (2008) xxx–xxx (available online).

4. G.M. Wilson, J.F. Smith, J.L. Sullivan, *A DOE nanotribological study of thin amorphous carbon-based films*, Tribol. Int. xxx (2008) xxx–xxx (accepted for publication June 2008).

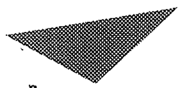
Aston University

Content has been removed due to copyright restrictions